NOVA SCHOOL OF SCIENCE & TECHNOLOGY

DEPARTAMENT OF CHEMISTRY

MARIA ALEXANDRA GOMES LÚCIO

BSc in Applied Chemistry

Development of Metal-organic Frameworks as Versatile Materials for Applications in Crystal Structure Determination and Photocatalysis

MASTER IN BIOORGANIC CHEMISTRY

NOVA University Lisbon
September, 2024

NOVA SCHOOL OF SCIENCE & TECHNOLOGY

DEPARTAMENT OF CHEMISTRY

DEVELOPMENT OF METAL-ORGANIC FRAMEWORKS AS VERSATILE MATERIALS FOR APPLICATIONS IN CRYSTAL STRUCTURE DETERMINATION AND PHOTOCATALYSIS

MARIA ALEXANDRA GOMES LÚCIO

BSc in Applied Chemistry

Adviser: Clara Sofia Barreiro Gomes
Researcher, NOVA University Lisbon

Co-advisers: Sandra Maria Nunes Gago
Researcher, NOVA University Lisbon

Examination Committee:

Chair: Luísa Maria da Silva Pinto Ferreira,
Assistant Professor with Habilitation, NOVA University Lisbon

Rapporteurs: Luís Manuel Cunha Silva,
Researcher, Faculdade de Ciências da Universidade do Porto

Adviser: Clara Sofia Barreiro Gomes,
Researcher, NOVA University Lisbon

MASTER IN BIOORGANIC CHEMISTRY

NOVA University Lisbon
November, 2024

Development of Metal-organic Frameworks as Versatile Materials for Applications in Crystal Structure Determination and Photocatalysis

To my family,

ACKNOWLEDGEMENTS

After the completion of this work, I am most grateful for all the help provided by my advisers, Dr. Clara Gomes and Dr. Sandra Gago, for all the support, insights, teachings and overall help to make me a better professional in the field. I would also like to thank and acknowledge Dr. Vitor Rosa for the guidance in the laboratory. I am most grateful to all the Organometallic and Coordination Chemistry group and the Photochemistry and Supramolecular Chemistry Research group for receiving me. Thank you to the Department of Chemistry, NOVA Faculty of Sciences and Technology and NOVA University of Lisbon for all the learning, growth and experience it provided over the last five years.

I would like to especially thank my colleagues of this last academic year at the lab: Beatriz Machado, Diogo Costa, Maria Vaz, António Lampreia, Inês Mendes, Jorge Maçãs and Rodrigo Rodrigues, for the company and laughs that always manage to lift the spirits.

Most of all, I am most grateful for my family and friends for supporting me all throughout this journey, for all the love and encouragement given. I couldn't have done this without them. And a special thank you to my three dogs (who can't read but will receive treats as a "thank you") for giving emotional support in August when I was at home writing.

Finally, I would like everyone who is reading this dissertation for devoting your time. Independent of the size that this contribution may have in the field, I hope that we can all learn and expand this area's general knowledge.

"Somewhere, something incredible is waiting to be known." (Carl Sagan).

ABSTRACT

Structural characterization of non-crystallizable compounds is an impending issue needing to be solved. With single-crystal X-ray diffraction (SCXRD), the absolute configuration of structures can be determined. However, obtaining single crystals is not always an easy procedure. The introduction and development of the Crystalline Sponge Method (CSM), which requires the encapsulation of guest molecules into the pores of a crystalline metal-organic framework (MOF), was a big step in structural determination through SCXRD.

MOFs are a popular class of materials due to their large pores and high-specific surface area, making them ideal candidates for a wide range of applications, including gas storage and as (photo-)catalysts. In addition, gaseous hydrogen is a promising candidate as a green and sustainable alternative energy source. Therefore, the use of MOFs as photocatalysts to produce hydrogen from water splitting is becoming a widely a hot topic for researchers.

In this work, we developed Zr- and Zn-MOFs for their application as crystalline sponges and as photocatalysts for hydrogen production through water splitting. The synthesized materials were characterized by diffuse reflectance spectroscopy (DRS), infrared (FTIR), and when possible, by powder and single-crystal X-ray diffraction (PXRD and SCXRD, respectively).

A new Zn-MOF bearing three triazine-tripyridine (tpt) ligands and triflate substituents was obtained. However, SCXRD studies showed that this new material displayed a small size pore when compared to the original material employed in the CSM. In addition, when attempting the preparation of the new Zn-MOF, two polymorphs of a cationic Zn-complex consisting of two tpt, two water and two methanol substituents were obtained. Within the CSM studies, the crystal structure of *o*-isopropylaniline and of propargyl alcohol, both liquid compounds at room temperature, were achieved. An unreported Zr-O cluster and promising results in the photocatalytic hydrogen production with our MOF-systems, using two different aqueous sacrificial agent solutions were also obtained.

Keywords: Metal-Organic Frameworks, Photocatalysis, Hydrogen Production, Structural Determination, Crystallography, Crystalline Sponge Method.

RESUMO

A caracterização estrutural de compostos não cristalizáveis é um problema pendente que necessita de uma solução. Com a difração de raios-X de cristal único (SCXRD), a configuração absoluta de estruturas pode ser determinada, mas a obtenção de cristais únicos não é um procedimento fácil. A introdução e desenvolvimento do Método da Esponja Cristalina (CSM), que requer o encapsulamento de moléculas de um composto *guest* nos poros de uma estrutura metal-orgânica (MOF) cristalina, foi um grande passo na determinação estrutural por SCXRD.

O hidrogénio gasoso é um candidato promissor como uma fonte de energia alternativa, verde e sustentável ao sistema de hidrocarbonos atual. Além disso, os MOFs são um material popular devido aos seus poros largos e área de superfície altamente específica, daí terem sido apontados como potenciais fotocatalisadores para a produção de hidrogénio.

Neste trabalho desenvolvemos Zr- e Zn-MOFs para a sua aplicação como esponjas cristalinas e fotocatalisadores na produção de hidrogénio através da divisão da água. Os materiais sintetizados foram caracterizados por espectroscopia de refletância difusa (DRS) e de infravermelho (IV), assim como, quando possível, difração de raios-X de pó (PXRD) e de cristal único (SCXRD).

Um novo Zn-MOF com três triazinas-tripiridinas (TPT) e substituintes triflato foi obtido. No entanto, estudos por SCXRD mostram que este novo material apresentava um poro pequeno comparativamente à esponja original da CSM. Adicionalmente, aquando da preparação do novo Zn-MOF, dois polimorfos de um complexo catiónico de Zn, consistindo em duas TPT, duas águas e dois substituintes metanol, foram obtidos. Dentro dos estudos de CSM, a estrutura cristalina da *o*-isopropilanilina e do álcool propargílico, ambos líquidos à temperatura ambiente, foram alcançadas. Um *cluster* de Zr-O por reportar e resultados promissores na produção de hidrogénio por fotocatálise com o nosso sistema de MOFs, usando dois agentes sacrificiais aquosos diferentes, também foram conquistados.

Palavras-Chave: Estruturas Metal-Orgânicas, Fotocatálise, Produção de Hidrogénio, Determinação Estrutural, Cristalografia, Método da Esponja Cristalina.

CONTENTS

LIST OF FIGURES

LIST OF TABLES

LIST OF EQUATIONS

List of Annexes

SYMBOLS AND ABBREVIATIONS

1D	One-dimensional
2D	Two-dimensional
3D	Three-dimensional
ε	Molar extinction coefficient
API	Active Pharmaceutical Ingredient
AQE	Apparent Quantum Efficiency
ATA	2-aminoterephthalic acid
BDC	Biphenyl-4,4′-dicarboxylic acid
BHT	Benzenehexathiolate
BIAN	Bis(imino)acenaphthene
bipy	4,4′-bipyridine
BTC	1,3,5-benzenetricarboxylate
CB	Conduction Band
CIF	Crystallographic Information File
CMF	Crystalline Molecular Flask
CMOF	Chiral Metal-Organic Framework
CP	Coordination Polymer
CS	Crystalline Sponge
CSD	Cambrige Structural Database
CSM	Crystalline Sponge Method
d	Duplet

dd	Duplet of duplets
DCM	Dichloromethane
DMF	Dimethylformamide
DMSO	Dimethylsulfoxide
DRS	Diffuse Reflectance Spectroscopy
eq	Equivalent
EtOH	Ethanol
eV	Electronvolt
FTIR	Fourier-Transform Infrared Spectroscopy
I_0	Incident photon flux
IR	Infrared
IUPAC	International Unit of Pure and Applied Chemistry
J	Coupling constant
HER	Hydrogen Evolution Reaction
HOMO	Highest Occupied Molecular Orbital
HSAB	Hard/Soft Acid/Base
LUMO	Lowest Unoccupied Molecular Orbital
m	multiplet
Me	Methyl
MeCN	Acetonitrile
MeOH	Methanol
MOF	Metal-Organic Framework
NCS	Isothiocyanate
NMP	N-Methyl-2-pyrrolidone
NMR	Nuclear Magnetic Resonance
OTf	Triflate (trifluoromethanesulfonate)
PCP	Porous Coordination Polymer
PL	Photoluminescence
POM	Polyoxometalate
ppm	Parts Per Million

PSD	Post Synthetic Deprotection
PSM	Post Synthetic Modification
PXRD	Powder X-Ray Diffraction
q	Quadruplet
QD	Quantum Dots
r.t.	Room temperature
s	singlet
SA	Sacrificial Agent
SBU	Secondary Building Unit
SCXRD	Single Crystal X-Ray Diffraction
t	triplet
TA	Terephthalic acid
TPT	2,4,6-tri-4-pyridyl-1,3,5-triazine
UV	Ultraviolet
UV/Vis	Ultraviolet/Visible spectroscopy
VB	Valence Band
XPS	X-ray Photoelectron Spectroscopy
XRD	X-ray Diffraction
δ	Chemical shift
η	Yield (represented in percentage, %)
λ	Wavelength
υ	Wavenumber

1

INTRODUCTION

Structural determination has seen major advances throughout the years in techniques such as nuclear magnetic resonance (NMR) spectroscopy, but the usage of X-ray crystallography (XRD) remains the most detailed and complete analysis nowadays as it gives us the angles, planes and chirality of the molecule all at once. Albeit it being extremely useful, single-crystal X-ray diffraction (SCXRD) requires, as the name states, a single-crystal of the sample, which can be extremely difficult to obtain, especially for certain compounds that aren't crystallizable, like some natural products, agrochemicals, and active pharmaceutical ingredients (APIs) due to their isolation in very small quantities or to being a liquid/oil at room temperature, which leads to another problem – the structural characterization of non-crystals. Moreover, the structural elucidation is particularly crucial in medicinal uses for chiral compounds because their structure is directly related to their properties and function, like in the case of ecadotril. The (*S*)-ecadotril shows cardiovascular activity, while the (*R*)-ecadotril has an intestinal antisecretory action [2], meaning that isomers and stereochemistry are extremely important in the compound's activity, so its absolute determination is of the upmost importance.

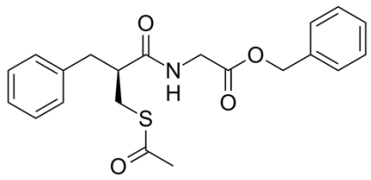

Figure 1. Chemical structure of (S)-ecadotril.

Additionally, in this century, environmental pollution and global warming are another impending issue plaguing the Human's future development and survival. The over-usage of fossil fuels is leading scientists to start looking for alternative energy sources that are green, sustainable, and, especially, renewable. Hydrogen is, therefore, a promising candidate, especially if generated by water splitting – a plentiful resource –, using photo or electrocatalysis as its mean of production.

1.1 MOFs

Metal-organic frameworks, abbreviated as MOFs, are a class of micro/mesoporous hybrid materials with high specific surface area and porosity[3], [4]. They consist of metal ions or clusters, serving as lattice nodes, and polydentated organic ligands performing as linkers. This imparts a three-dimensional (3D) network structure to MOFs, which may or may not be crystalline, and provides them with a unique chemical and structural tunability (**Figure 2**) [5], [6]. According to the official International Unit of Pure and Applied Chemistry (IUPAC) adopted terminology [7], they fall under the sub-class of coordination networks, originating from a broader class of coordination polymers (CPs), and their official definition is articulated as "a coordination network with organic ligands containing potential voids". These analogous structures formed by metals and multidentate organic ligands showed promise due to their more precise rational design, where it is possible to manipulate its shape and size and functionalize its pores with different groups to establish more connections [8], [9].

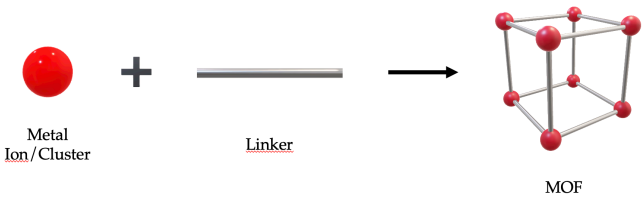

Figure 2. Basic geometric construction of a MOF through metal-ligand coordination bonds.

Therefore, for a solid to be denominated a MOF, it must be geometrically well-defined, possess strong bonding, inorganic clusters, and organic ligands as linkers, which are available for further modification [10].

1.1.1 History of MOFs

In 1994, Yaghi and Li reported the first MOF, a copper(I) chloride and 4,4'-bipyridine (bipy) 3D compound which was described as the following: "(…) these sheets are interlocked with other sheets to form a three-dimensional, neutral network containing a two-dimensional, intersecting system of channels of smaller aperture" [11]. The MOF denomination surged later, in 1995, as the first porous CP in another article. In that paper, a MOF using copper(II) nitrate and bipy, forming large rectangular pores, and cobalt(II) nitrate and 1,3,5-benzenetricarboxylate (BTC) linkers, originating pink, cubic crystals was reported [12]. Later in 1995, Yaghi reported the first Zn-MOF, MOF-5, composed of zinc(II) nitrate and 1,4-dicarboxylate (BDC) [13].

Earlier MOFs were primarily composed of divalent metals, such as Zn^{2+}, due to their inexpensiveness and propensity to great porosity, making them promising for various applications. Some examples of Zn-MOFs are MOF-5 and ZIF-8 (**Figure 3**). However, these types of MOFs also showed instability under harsh conditions.

From then on, MOFs employing other types of transition metals, such as zirconium (UiO-66), copper (HKUST-1), iron (MIL-53), titanium (COK-69), and others (**Figure 3**), surged

to be applied in various applications from gas storage to drug delivery, playing with the different combinations of metals, their respective counterions and organic linkers, which led to endless possibilities of new structures.

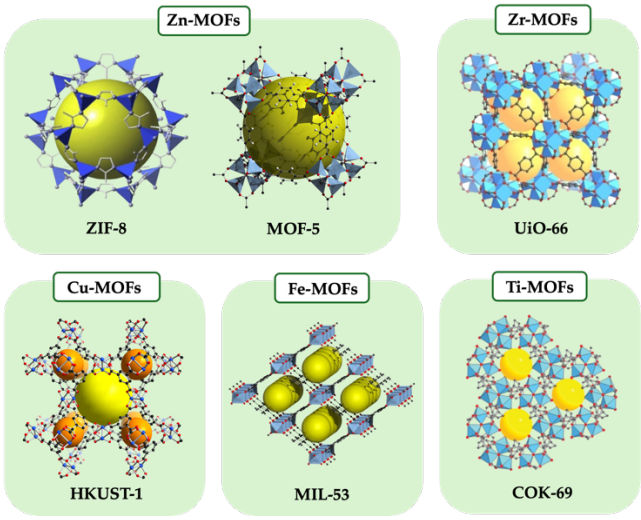

Figure 3. Examples of metal-organic frameworks with various metals.

The design of new MOFs requires an in-depth comprehension of molecular and intramolecular interactions within the intricate three-dimensional structure, ensuring the attainment of desired physical and chemical properties. Moreover, it demands nearly precise control over the techniques used for both synthesis and crystal analysis [14].

1.1.2 Physical Properties

The metal cation nodes and organic electron-donor linkers within MOFs are connected via coordinative metal-ligand interactions and electrostatic attraction, thereby forming secondary building units (SBUs) that dictate the network symmetry [15]. MOFs share structural similarities with zeolites, featuring interconnected 3D porous architectures characterized by various topologies and dimensions. However, unlike zeolites, MOFs are not entirely inorganic, affording them greater synthetic flexibility.

The pores within MOFs are usually rigid and maintain their structure without collapsing upon solvent removal or the addition of another liquid. This adaptability in pore size and topology is easily achievable due to their versatile coordination chemistry and the wide availability of different linkers [16]. Consequently, MOFs are highly regarded for their ability to instill functionality through the careful selection of appropriate linkers and metal nodes.

The synthesis of MOFs faces a challenge due to this wide array of available ligands, characterized by differences in size, shape, and constituent atoms. These ligands can strongly influence their structural attributes, as they contribute to different flexibilities, stabilities, and atomic compositions that enable the formation of diverse interactions such as hydrogen bonds. Flexible ligands, as opposed to rigid ones, offer greater degrees of freedom, potentially resulting in unpredictable crystal structures. This intricate interplay between metal ions and ligands is pivotal in determining the overall characteristics of MOFs.

Organic ligands commonly used in MOFs include N- or O-donor groups, such as carboxylates and imidazolates, although phosphonates and sulfonates are also employed [17].

In ligands, it is vital for them to possess a certain degree of rigidity to determine the framework's robustness. In 2014, Liu et al. rationalized that the length of the ligand is correlated with the activation energy of the ligand dissociation, thereby influencing the decomposition of the MOF [17]. Given two ligands, one longer and one shorter, and assuming that the displacement of the ligands' terminals in the transition states is the same for both cases, the shorter and more rigid ligand would be bent at a larger angle, leading to a higher activation energy of dissociation and higher inertness of the framework's scaffold.

In the case of the metal nodes, they are especially particular due to their ability to adopt various coordination geometries, which is closely tied to the resulting network topology and dimensions. Transition metals are commonly used in MOFs, primarily due to their synthetic and structural versatility, stemming from an assorted range of coordination numbers, geometries, and oxidation states. This versatility enhances the flexibility and adaptability of MOFs, allowing for a broad spectrum of structural possibilities and functional applications.

The connectivity between metal nodes and ligands directly impacts the decomposition of MOFs. Higher connectivity suppresses ligand dissociation, thus preventing decomposition and enhancing the MOF stability, as well as a faster ligand repair. Therefore, more connections favor the generation of stable MOFs [19].

The strategic selection of the SBUs enables precise control over the size of the pore, allowing it to form microporous, as well as mesoporous frameworks. These various combinations of nodes and ligands make the number of MOFs possible to construct immeasurable, but their application is dependent mostly on their stability.

1.1.3 Chemical Properties

These frameworks are dynamic systems capable of undergoing facile changes upon external stimuli, such as temperature and pressure. They exhibit a long list of beneficial structural features associated with their properties and potential applications. Among these favorable features are their high porosity and large pore volume. Additionally, they possess a large specific surface area and high thermal stability, attributed to the presence of strong bonds, leading them to withstand temperatures ranging from 250°C to 500°C.

Given the rapid advancement in the chemistry of MOFs, a spectrum of properties can be manipulated, designed, and optimized to align with their prospective applications, including the adjustment of pore size, shape, and surface area. In average, the porosity of a MOF is above 50% of the crystal volume and its surface area can go up to 10000 m^2/g, which exceeds the typical porous material. When used as a microporous material, it's taken advantage of the high surface areas through the increase of van der Waals interactions, which are required to uptake weakly interacting gases [20], and the tunability of MOF pore dimensions is exploited to control the relative rates of adsorption and transport through the pores.

The stability of MOFs is influenced by numerous factors, including the operating environment, the metal ion or cluster, organic ligands, coordination geometry, pore surface hydrophobicity, and various others [21]. However, the strength of the coordination bonds supporting the framework is believed to be crucial for maintaining said stability. Strong coordination bonds are essential for the prevention of the framework collapsing when guest molecules are included in its pores. Consequently, the ability to predict MOF stability can be approximated by assessing the strength of these bonds. Metal-ligand bond strengths tend to be positively correlated to metal cations' charges and negatively correlated with their ionic radius. Moreover, charge density, arising from the combination of charge and radius effects, plays a crucial role. Therefore, when ligands and the coordination environment are constant, high-valent metal ions with high charge densities typically forge stronger coordination bonds, resulting in a more stable framework. This resonates with Pearson's hard/soft acid/base (HSAB) principle, which elucidates that "hard" acids prefer to bind "hard" bases and vice versa. In the context of MOFs, the "hard" acids are the high-valent metal ions with high charge densities, such as Zr^{4+} [17].

Besides thermodynamic stability, the overall stability of MOFs can also be affected by kinetic factors. This phenomenon is exemplified in the Zr-MOFs, such as UiO-66, UiO-67, and UiO-68, which share the same cluster but vary in linker lengths (**Figure 4**). Thermodynamically, these MOFs should have similar stability due to their comparable bond strengths. However, experimental findings contradict this expectation, revealing decreased stability with the increase in the length. Therefore, it is inferred that kinetic stability is influenced by the rigidity of the linkers. Also, the higher the connectivity leads to a bigger suppression of ligand dissociation, thereby concluding that both the rigidity and flexibility of the ligand are important for the robustness of a MOF.

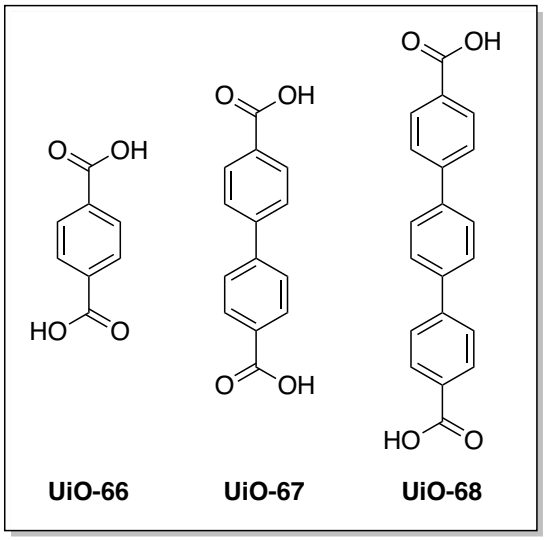

Figure 4. Linkers used in **UiO-66**, **UiO-67** and **UiO-68**.

Stable MOFs are vital across various domains, such as catalysis [22], biomedicine [23], sensing [24], or as photocatalysts for water splitting and CO_2 reduction [25], in which it is imperative that the MOF framework remains stable in aqueous solutions containing acid, base,

or coordinating anions [26]. In acidic conditions, the primary cause of MOF degradation is the competition of protons and metal ions for the coordinating linkers. MOFs containing high-valency metal ions coordinated through strong bonds with carboxylate-based ligands of low pK_a exhibit excellent stability in acids. Conversely, MOFs with low-valency metal ions and high pK_a azolate ligands are prone to degradation due to the strong affinity of azolate ligands for protons, leading to decomposition. In basic conditions, linker replacement by hydroxide groups competes with metal cations in the clusters, making the MOFs with low-valency metal ions and azolate ligands more stable, as they have a relatively lower affinity to hydroxide ions [27], [28]. When it comes to coordinating anions like F^- and CO_3^{2-}, they can be particularly destructive, because these anions can be considered "hard" Lewis bases, strongly interacting with the high-valency metal ions.

MOFs can also exhibit instability under vacuum or pressure conditions, which poses a risk to their industrial and engineering applications. This is mainly attributed to their mechanical stability, which can lead to partial collapse of the pores or phase exchange [29]. To avoid this issue, a common procedure is to perform solvent exchange using solvents with lower surface tension, followed by evacuation for the MOF activation.

The stability of MOFs in water or aqueous media is extremely important for a diverse range of applications. One approach to enhancing this ability is by introducing hydrophobic groups, such as methyl groups, onto the ligands, due to the hydrophobic surfaces and interfaces effectively hinder water molecules from attacking the inorganic clusters [19]. Additionally, methyl groups serve as electron donors, increasing the electron density of both the central and terminal benzene rings in the ligand. This elevated electron density of the carboxyl O atoms further strengthens the Zr-O bond, in the case of Zr-MOFs. However, a challenge with this introduction is that it typically results in narrower pores, leading to further condensation of water vapor at lower pressures.

Based on these findings, it was proposed that methyl groups augment the hydrophobicity of the materials, thereby raising their stability in aqueous solutions [30].

1.2 Zr-MOFs

Zr-MOFs have experienced major growth throughout the years due to their high stability and versatility, with the discovery of UiO-66 being one of the biggest accomplishments in MOF chemistry [21].

Zr-MOFs have outstanding chemical, mechanical, and thermal stability (up to 500℃), therefore they are of major interest in diverse areas such as gas adsorption, catalysis, or electrochemistry. The high stability can be attributed to the strong metal-carboxylate bonds and the metal clusters' high degree of connectivity. They are very stable in water and aqueous solutions, either acidic or alkaline, as well as in organic solvents while maintaining their crystallinity at high pressures. The stability of a complex can also be decided according to Pearson's HSAB theory, where the Zr^{4+} is a "hard" Lewis acid, due to their high charge, bond polarization, and charge to radius ratio (Z/R), turning the high oxidation state into a key feature.

These characteristics make the Zr(IV) nodes have a strong affinity for the O atoms in carboxylate-based ligands, which are "hard" Lewis bases. In the case of UiO-66, the terephthalic acid is a hard Lewis base with the high-valent metal ion, Zr^{4+}, as a hard Lewis acid, forming a strong coordination bond and, thus, a more stable framework. These strong Zr^{4+} interactions contribute to the chemical stability and their need for more ligands to balance off the charge leading to a higher connection number, which prevents the attack of guests, as previously mentioned.

Most Zr-MOFs are obtained as polycrystalline powders, requiring synchrotron PXRD data with complicated Rietveld refinement to obtain its structure. Polycrystalline powder refers to a material composed of numerous small crystalline particles, often referred to as grains or crystallites, randomly oriented within the powder. Each crystalline particle exhibits a well-defined crystal structure, but the orientation of these structures varies throughout the material. Polycrystalline powders are commonly used in various scientific and industrial applications, including materials science, catalysis, pharmaceuticals, and electronics. They are particularly useful for their uniformity, high surface area, and ease of handling. The crystallinity was poor due to the polarization of the Zr-O bonds to have a covalent character, which would slow down the ligand exchange. So, as to "promote" these polycrystalline powders to single crystals, modulated synthesis was introduced in Zr-MOF synthesis [31], [32].

Within Zr-MOFs, the discovery of UiO-66 was an important milestone, and it was firstly synthesized in 2008 by Lillerud and co-workers, with a chemical formula of $[Zr_6O_4(OH)_4(TA)_6]$ (TA=terephthalic acid) [33]. Due to their remarkable stability in water and acidic conditions, this MOF has attracted a great deal of attention. The Zr(IV) centers form high nuclearity SBUs with the organic linker, the terephthalic acid (TA) or derivatives. This high nuclearity is attributed to tetravalent metal cations forming strong covalent bonds creating a stable framework. Each Zr center in the SBU coordinates to eight oxygen atoms, four from the carboxylates and four from the μ_3-O or μ_3-OH groups. The six Zr atoms form a regular octahedron SBU, linked by 12 TA or 2-aminoterephthalic acid (ATA) molecules, defining two different types of cages: a supertetrahedron and a superoctahedron, which have different diameters (8 and 11Å), accessible through 6Å triangular windows (**Figure 5**).

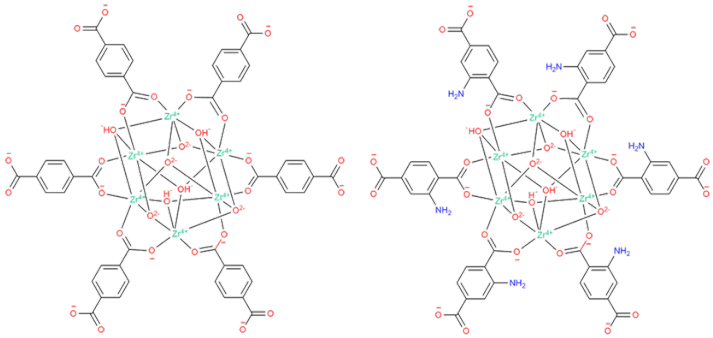

UiO-66 UiO-66-NH_2

Figure 5. Structures of **UiO-66** and **UiO-66-NH_2**.

The amino-functionalized version of this MOF (UiO-66-NH_2) is known for its exceptional stability, especially hydrothermal, where metal-ligand bond strength seems to be vital for the determining of that stability. For example, UiO-66 was proven to be capable of being suspended in water at 100ºC for 4H without suffering any structural modification.

In 2011, Schaate et al. introduced the modulated synthesis method for the preparation of Zr-MOFs with adjustable particle sizes [34]. By incorporating modulators into the standard synthesis, they successfully formed UiO-66-NH_2 crystals, which were subsequently analyzed by SCXRD. This groundbreaking study provided the first-ever single-crystal structure of a Zr-MOF. The only challenge encountered was a reduction in the connection number to 8-connected Zr-clusters, but this modification did not compromise the stability of the compound. This technique regulates the coordination equilibrium through the addition of a compound, the modulator, which is usually an acid and has similar chemical functionality as the ligand, so it allows the enhancement of crystallinity and reproducibility of the desired product. This depletes a competitive reaction, modulating the nucleation and crystal growth rates, while the selective regulation of coordinative interactions in one of the coordination modes allows for the crystals morphology control [31], [35]. Furthermore, this coordination modulation proves an improvement in synthesis reproducibility and tunability of the crystal features. This method is especially useful in Zr-MOFs synthesis to obtain single-crystals, instead of a polycrystalline powder.

This modulated synthesis technique was later applied for the formation of other Zr-MOFs, enhancing the crystallinity of the materials by augmenting their crystal size.

1.3 Zn-MOFs

Zinc is an endogenous low-toxic, low-cost, easily attainable transition metal, which presents as an ideal candidate for MOFs, due to the great porosity and surface area of its frameworks [36]. According to the HSAB principle, the divalent metal ions, such as Zn^{2+}, are "soft" acids, which can be assembled in a MOF with "soft" azolate ligands, like imidazolates, pyrazolates, and triazolates. These azolate ligands are usually deprotonated so that the coordination to the metal occurs, but, contrary to what happens to carboxylic acids, the azoles are known as bases and behave as sp^2 N-donors.

Due to Zn-based MOFs' characteristics, their usage has become ideal candidates for application in biological systems. Therefore, they are currently in study for various biomedical applications, such as drug delivery [37], imaging [38], sensing [39] and nanoencapsulations, due to its biocompatibility. Zn-MOFs have also been researched for heterogeneous catalysis, CO_2 fixation [40], alkylation of aromatic compounds, and others (**Figure 6**).

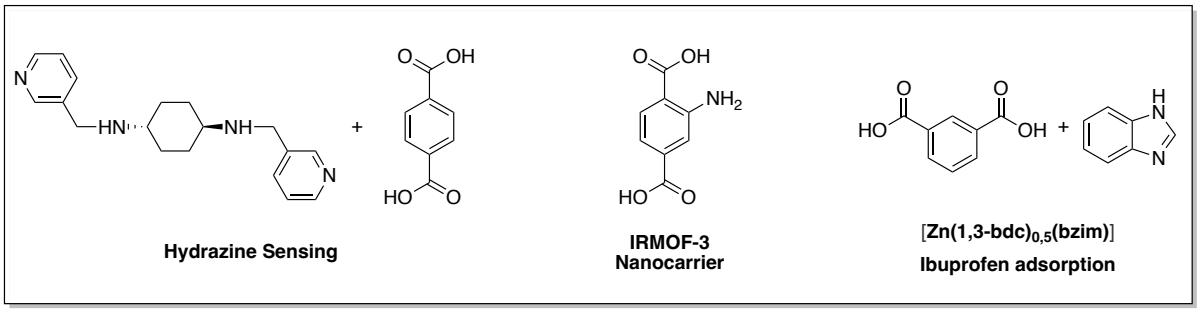

Figure 6. Ligands used in Zn-MOFs applied in sensing, nanocarrying and drug adsorption [37], [39].

Zn-based MOFs have also shown an incredible catalytic activity in reactions such as the conversion of CO_2 into valuable chemicals, due to their suitable morphology and active sites. Another example in which these materials were used as catalysts were in the studies performed by Kalhor et al. where they use CuO nanoparticles supported in Zn-MOFs for Cu-AAC reactions, in which the MOFs showed promising results [41].

In 2007, Li et al. reported a new Zn-MOF, $[ZnI(TPT)_2(TA)]_n$, and the asymmetric unit shows the zinc metal center connected to two TPT molecules, an iodide and a TA molecule, forming a distorted trigonal bipyramide geometry [42]. The TPT acts as a bidentate ligand linking to the Zn(II) atoms, forming zigzag chains, while both carboxylates from the TA ligands coordinate in a monodentate way, which act as μ_2-bridge linking the Zn(TPT)I chains, conferring pores to the framework. Along the *b*-axis, hexagonal nano-channels can be observed with the dimensions of 1.23 nm x 1.63 nm. The amino-derivative analogue for this MOF was reported in 2011 by Tan et al. using ATA instead of TA with the same coordination and geometry. Both compounds were not tested previously for structural determination using the Crystalline Sponge Method (CSM), nor for photocatalysis.

1.4 Design and Synthesis of MOFs

1.4.1 Crystal Engineering

In 1955, Pepinsky surged with the term "Crystal Engineering" [43], and it was used in 1971 by G. M. J. Schmidt in the context of organic solid-state photochemistry [44]. However, in 1988, the concept was broadened by Desiraju to include a myriad of solid-state chemistry and defined crystal engineering as "*the understanding of intermolecular interactions in the context of crystal packing and the utilization of such understanding in the design of new solids with desired physical and chemical properties*" [45]. In the past decade, crystal engineering has become a major research and rapidly developed area, growing with the advances in the understanding of supramolecular chemistry and intermolecular interactions, since it studies the design of new solid-state materials with desired and predefined properties, being considered a multidisciplinary area bounding materials, supramolecular and solid-state chemistry.

The engineering happens through the study and further manipulation of intermolecular interactions, such as hydrogen or coordination bonds. Those interactions control the molecular arrangement inside the crystal lattice, therefore controlling the properties of the material. So, an increased understanding of those will help predict the crystalline material packing and its properties [46]. Also, a better comprehension of structure-function relationships can also express a superior control of crystal engineering and new future possibilities can be unraveled.

CPs have a great potential, so its crystal engineering would be a great way to obtain new compounds to test in optical, electrical, and mechanical applications, for example. The CPs are supramolecular assemblies of metal ions/clusters and organic ligands coordinated through coordination bonds – which are the strongest of intermolecular interactions and have better directionality, thereby the prediction should be easier –, but there is always structural uncertainty, since we cannot guarantee if solvent molecules or counter ions will participate in the CP, originating crystal polymorphism or even complexes. Crystal polymorphism is the phenomenon where the same molecules can interact differently depending on the intermolecular arrangements, crystallizing into more than one structure. Desiraju revealed that polymorphism can be strongly solvent-dependent, and that the frequency of polymorphs is not uniform in all substance categories.

This structural uncertainty could present in two different situations when starting from the same reagents: (1) both the network structures and chemical compositions are different, or (2) the network structures have differences, but they have the same chemical composition. In the first case, the crystals are clearly different when observed, so crystal engineering can be expected to be difficult due to the high versatility of the self-assembly system. But in the second case, supramolecular isomerism can be identified, classifying the compounds as supramolecular isomers, which should possess equal chemical compositions in both the coordination framework and the whole crystal [47].

The supramolecular isomerism translates to the existence of more than one type of network for the same molecular building blocks and occurs mostly due to simple crystallization system, simplifying the composition control. The smallest change to the crystal growth conditions can lead to the formation of different crystalline phases in molecular crystals. In the CPs, this applies in a harsher way, since they are constructed by bonds that are stronger and more directional, inferring the crystallization in very complex multicomponent systems. Moulton and Zaworotko categorized supramolecular isomerism into 4 classes: (1) structural – different superstructures, but same network components [48], (2) conformational – different conformation of flexible ligands, (3) optical – different chirality, and (4) catenane – different degree and manner of interpenetration and interweaving, providing variations in the structure and properties [49]. Polymorphism can be considered a type of supramolecular isomerism, but the contrary is not observed. Since the CPs are very complex, their construction isn't easy, but it also should not be viewed as a problem as it is an invaluable occasion for the self-assembly and crystal growth process study. Therefore, the study of structural isomerism could be one of the major steps in perfecting the CPs crystal engineering.

There is also a distinction to make when talking about crystal engineering and crystal structure prediction. The former is less precise and deals mostly with new phases, while the latter is precise – with defined space groups and packing details – and deals with known molecules or compositions of those [50].

The Cambridge Structural Database (CSD) was established in 1965 and is a repository for 3D structural data of organic, metal-organic, and organometallic data, compiled in a crystallographic information file (.cif). Chemists and crystallographers can deposit cif files of newly obtained structures on the database for others to consult and compare to their own data. In 2024, CSD has already over 1.25 million curated entries, with over 53,000 being new structures reported only in 2023. The CSD can be used as a research tool to study the intermolecular interactions that create a particular pattern, repeating themselves in various crystal structures, and use that information to design new materials.

Crystal engineering epitomizes a paradigm for the design of new solid-state supramolecular structures characterized by predictable stoichiometry and architecture.

1.4.2 Postsynthetic Modifications

The framework can undergo "post-synthetic modifications" (PSM), which serve as a significant supplement to the classic one-pot MOF synthesis. PSM allows for precise adjustment of MOF properties by exchanging, modifying, or completely removing linker or node components. This process enables the enhancement of MOF functionality or application through the introduction of different functional groups.

The ability to alter the surface chemistry of a MOF is key to its uniqueness as a porous material, offering control over crystallographic phases and crystallite size/morphology. By carefully selecting synthetic parameters, such as building the MOF with redox-inactive nodes or employing more rigid linkers, electrochemical stability can be improved. These modifications result in MOFs exhibiting superior thermal and chemical stability [5]. The additional stability of these MOFs provides them an advantage over the previous labile ones, as they can withstand harsh modifications while retaining their porosity and crystallinity [51]. This versatility makes PSM a valuable tool for tailoring MOFs to specific applications and advancing their potential in various fields.

There are various techniques for PSM (**Figure 7**), but they can be divided into three areas, distinguishable for its breakage or formation of a certain type of chemical bonds: (a) covalent PSM – the most common one –, (b) dative PSM, and (c) postsynthetic deprotection (PSD).

Covalent PSM involves creating a new covalent bond through the alteration of a component in a heterogeneous, postsynthetic manner – usually in a MOF, the target is the ligand. Dative PSM, on the other hand, entails the formation of a dative bond with a component, wherein the ligand is introduced to the framework coordinating the SBU [52]. In PSD, a chemical bond within an intact framework is cleaved as a result of a reaction, unveiling a chemical functionality, and yielding materials with altered properties.

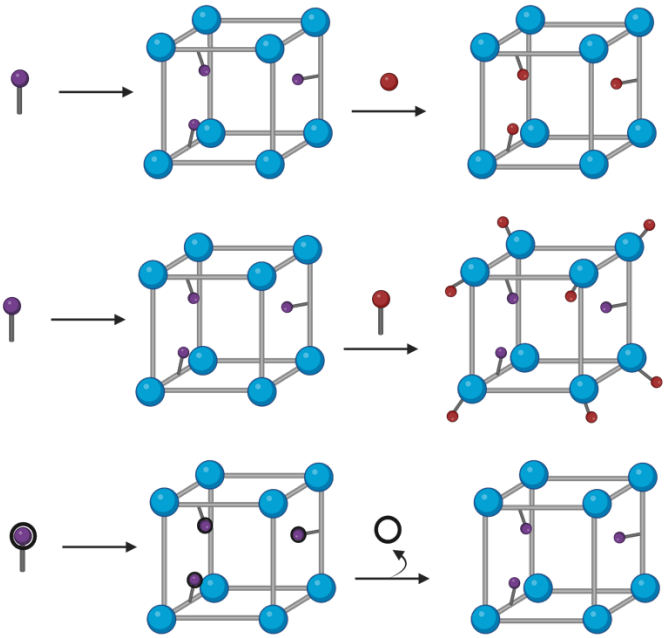

Figure 7. Generic schemes for PSM (Adapted from [51]).

An additional and excellent approach to producing previously inaccessible MOFs is through postsynthetic ligand metal ion exchange. In this method, the presence of inert metal bonds within the framework plays a crucial role in dampening the ionic exchange between the ligand and the metal, thereby facilitating controlled and selective exchanges.

PSM can be a great alternative in synthetizing MOFs with new functionalities, greater stability and processability, expanding the potential of the frameworks, but its study is still in progress. These techniques appear benefic and with an anticipated expansion due to the requirement of MOFs in industrial scale, but they will entail the adoption of green chemistry principles to become an environmentally friendly synthesis [53].

1.5 Characterization and Application of MOFs

1.5.1 Characterization Techniques

Many characterization techniques are available nowadays, from NMR to infrared spectroscopy (IR), but only a few are sensitive enough to employ on MOFs. In this case, the solution NMR could not be used due to MOFs' low (or absent) solubility in organic solvents, so the only option for performing NMR in these compounds is solid-state NMR. IR only provides data about the functional groups present in the structure, not the actual molecular disposition.

Overlooking the questions presented in other methods, X-ray diffraction can provide direct information on the 3D structure at the atomic level, determining atom connectivity of a single crystal – but it cannot provide the chemical formula, so it must be known beforehand [54]. Therefore, SCXRD provides the most trustworthy evidence of a molecular structure. As

mentioned before, the problem arising from using this technique is the necessity to obtain high-quality crystalline compounds. To solve this issue, methods have been evaluated for the structural elucidation of non-crystallizable compounds, like the case of the Crystalline Sponge Method. Enhancing the data quality acquired through the CSM has been a major concern and has been tackled from various angles, like the usage of synchrotron radiation as an X-ray source [55].

In SCXRD, there are obstacles hindering the acquisition of high-resolution data and accurate crystal structures, including structural and thermal disorder. To mitigate these issues, data is often collected at cryogenic temperatures where thermal disorder is minimized, enabling the diffraction of X-ray at higher angles. This is normally applied to crystals of small and large molecules, as well as MOFs [56].

Crystal analysis has been very impactful in the discovery of new MOFs and their properties, successfully evidencing the main absorption sites [57], pore-occupying species [54], and others.

Since some MOFs are hard to crystallize into single-crystals and are polycrystalline powders, the usage of powder X-ray diffraction (PXRD) is an available technique to understanding the sample composition. When the conditions of Bragg's Law ($n\lambda = 2d \sin\theta$) are satisfied, the sample is submitted to the incision of X-rays and the interaction between both produces constructive interference and a diffracted ray. It is a non-destructive technique, which makes a phase analysis to distinguish between an amorphous and crystalline material, and its data can be used for a diverse range of measurements, such as qualitative and quantitative analyses, crystal structure, crystallite size and microstrain, etc. Besides those qualities, it also presents some challenges, for example, the amorphous phases cannot be identified, it is a time-consuming procedure due to each step being subjected to potential user errors and the user must have previous knowledge on structural solution from PXRD [58]. Therefore, to obtain structures from PXRD, it is necessary to computationally solve it since we obtain one-dimensional (1D) diffraction data, which needs to be transformed into the 3D. This does not occur in SCXRD, where we obtain the data already in 3D form, making the solution of PXRD data harder and very time consuming. From this, we can also assume that the dataset needs to have high resolution, since the three dimensions of reciprocal space are "compressed" into the 2θ diffraction angle, resulting in an accentuated overlap of peak diffraction, then leading to a direct accurate prevention of the 2θ peak positions and intensities' determination. Therefore, if not accurate, the determination of unit cell and space group cannot be done, and structure solution will become unprobeable [59].

For the photocatalytic application, diffuse reflectance spectroscopy (DRS) is a type of absorption spectroscopy, which evaluates the reflection of light by a material [60]. It is an important technique to evaluate the spectral characteristics of a solid sample. This is important for our work since we are interested in photocatalysts that are active in the visible-light area. This type of spectroscopy is used for solid inhomogeneous materials and the Kubelka-Munk approximation is the most widely applied in order to obtain a wavelength (nm) vs. F(r), where

the F(r) is the remission function obtained through the resolution of the Kubelka-Munk function for the ratio of absorption to scatter [61].

$$R_\infty = 1 + \frac{a_0}{r_0} - \sqrt{\frac{a_0^2}{r_0^2} + 2\frac{a_0}{r_0}} \Leftrightarrow F(R_\infty) \equiv \frac{(1-R_\infty)^2}{2R_\infty} = \frac{a_0}{r_0}$$

Equation 1. Kubelka-Munk equation and resolution.

X-ray photoelectron spectroscopy (XPS) indicates the elemental composition, chemical state and the overall electronic structure and density of electronic states within or in the surface of a material. With this technique, it is observable what atoms are bonded to other atoms, especially what metals are bonded to. Since it is a photoemission spectroscopy, the sample is irradiated with an X-ray beam, originating an electron population spectrum. If laboratory X-rays are used, XPS can detect all elements apart from hydrogen and helium, with a detection limit of parts per thousand. An XPS spectrum is a plot of the number of electrons detected at a specific binding energy, and each peak represents the electronic configuration of the electrons within an atom.

1.5.2 Crystalline Sponge Method

The CSM was discovered by Fujita *et al.* in 2013 [62] and has its origin rooted in the classical host-guest complexes – the clathrates [63]. It entails the formation of a crystalline porous framework – **host** –, termed crystalline molecular flask (CMF), that can be classed as a MOF [64] or a porous CP [65], with a pore big enough to encapsulate a non-crystallizable organic molecule – **guest** – so its definite structure can be obtained through XRD analysis (**Figure 8**) [66]. CMFs possess a distinctive trait that distinguishes them from most MOFs/PCPs: their remarkable ability to withstand structural deformation in solid-state without compromising the crystallinity. This feature amplifies their capacity to uptake guest molecules with a high likelihood of ordering [55].

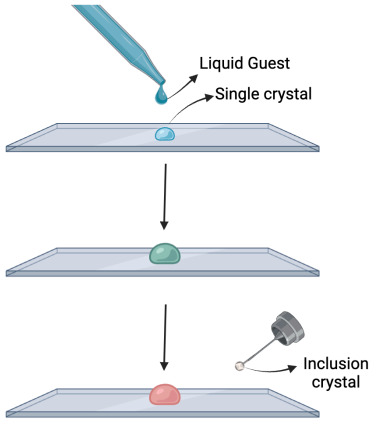

Figure 8. Guest inclusion in the host sponge (Adapted from [54]).

The first examples designed by Fujita and co-workers to be used as crystalline sponges for structure elucidation consisted of a CoMOF, $\{[(Co(NCS)_2)_3(TPT)_4]\bullet x(solvent)\}_n$ (TPT = tris(4-pyridyl)-1,3,5-triazine), and a ZnMOF, $\{[(ZnI_2)_3(TPT)_2]\bullet x(solvent)\}_n$.

The ZnMOF was preferred over the CoMOF because they are less symmetrical, leading to an easier elucidation of the guest molecules.

The original protocol involved layering a solution of ZnI_2 in methanol over a TPT solution in nitrobenzene for 7 days at room temperature, followed by solvent exchange to cyclohexane for another 7 days at 50 ºC. However, this resulted in crystal imperfections due to the extended preparation time, solvent exchange, and high temperature. In 2015, Clardy et al. [67] introduced an enhanced protocol for the sponge's formation, reducing the synthesis and encapsulation time to three days, and replacing nitrobenzene with chloroform as the solvent, facilitating the formation of higher-quality crystals.

The encapsulation of the guest molecules occurs when the sponge is soaked in an inert solvent (where the guest is dissolved in) or in the neat guest solution, maximizing the exchange between the guest and the solvent[67].

One of the advantages of the method is that the original Fujita sponge has heavy atoms (Zn and I) in its framework, facilitating the determination of the absolute configuration of the guest molecule – chirality included – since host-guest interactions are established [68]. Another advantage is its application in nanogram-microgram quantities, with the possibility of being combined with spectroscopic [69], [70] and chromatographic techniques [71], [72]. However, certain limitations are to be expected, such as a variation of robustness across multiple crystalline morphologies, prompting refinements of the initial method. Regrettably, not all have been addressed, including the necessity for high-quality crystals, poor stability in polar solvents, and relatively small pores (with an approximate cross-section of $8\ x\ 5\ Å^2$) [73], [74].

Several factors are involved when the objective is to obtain a high-quality crystal. The quality is assessed based on its diffracting power, small thermal movement, and complete occupancy of all the atoms with no disorder [75].

Alternative potential sponges must satisfy several criteria, considering the limitations of the original method, which remains in use. The criteria are as follows: (a) the pore size should be large enough to accommodate the guest, yet not overly large to weaken the interaction between host and guest, (b) the environment within the pore should exhibit a strong affinity for the guest molecules, (c) the structure must possess low symmetry to induce anisotropy, as highly symmetric frameworks increase the likelihood of guest molecule disorder, and (d) the host should demonstrate some flexibility to adjust its conformation, enabling the accommodation of various substrates [76].

The pores (or confined spaces) in the crystalline sponge (CS) work better when they can establish strong supramolecular interactions with the guest molecules. The strength of those interactions determines the degree of order exhibited by the guest inside the pre-formed CS. The confinement within the crystalline sponge's pore is restrictive, effectively selecting a single isomer from isomeric mixtures to enter, with external triggers capable of inducing further interconversion [77]. These confinement effects substantially alter the physicochemical properties of both host and guest molecules [78], [79].

Other MOFs were tried as sponges, such as $\{[(ZnBr_2)_3(TPT)_2]\bullet x(\text{solvent})\}_n$ and the $\{[(ZnCl_2)_3(TPT)_2]\bullet x(\text{solvent})\}_n$, but both present a lower void space occupation, do not

necessitate unit cell expansion and their symmetry drops to a $P2_1$ symmetry. Besides MOFs, Costa et al. reported using a polyoxometalate (POM) assembled from a semirigid macrocycle tetraimine and ethyl acetate as a CS for the determinations of several compounds' structures, but being an organic framework, the absolute determination was not possible [80]. Chiral MOFs were also attempted to be used as CSs and the analysis was based on comparing the guest's chirality to the relative stereochemistry of the known chirality of the host framework. Zaworotko et al. used $[Co_2(\text{-man})_2(bipy)_3](NO_3)_2]$ (man=mandelate) as a chiral MOF (CMOF), with the pre-installed chirality from the (*S*)-mandalete molecules. Coordination cages and biological frameworks were also possibilities developed throughout the years to circumvent the limitations that the regular Fujita's zinc sponge presents [81].

Nowadays, the CSM has evolved beyond its original application for the structural elucidation of molecules. It has matured to the extent of elucidating a mechanism [82], [83] and encompassing the solid-gas interface.

1.6 Photocatalysis for Hydrogen Production

The evolution of organic photochemistry began in the 1960s and matured in the 1980s, enabling a deep understanding of the processes initiated upon light absorption. Initially, the photochemical studies were conducted in solution. As time progressed, research has evolved towards utilizing surface and confined spaces. This advancement allowed for greater selectivity over desired pathways and offers a greater control over reactivity, addressing a previous difficulty [84]. The primary intermediates involved are often very short-lived excited states, which may react virtually without an activation energy barrier [85].

The use of porous materials, which provide three-dimensional confinement of intermediates, emerged from earlier conducted two-dimensional (2D) photochemistry studies. The porosity of these compounds facilitates mass transfer from the exterior to the interior of a particle, enabling reactions to occur within the nanometric rigid cavities, which possess specific properties, such as polarity. Consequently, the porous solid acts as a rigid matrix, confining the reaction to a restricted space. As so, zeolites were chosen as the preferred material due to their large pores and surface area. However, since they can't undergo direct photoexcitation, they play a mostly passive role. So, considering the structural resemblance between zeolites and MOFs, the latter were seen as the next frontier for the evolution of photocatalysis, a field that began to develop in the late 1970s.

Solar energy is a renewable resource that has gathered prodigious attention for the purpose of environmental remediation. Photocatalysis is a promising pathway for the conversion of solar energy to chemical energy, in a clean, green, and renewable way. In the beginning, it focused on the degradation of pollutants in low concentration in water and in air, but later progressed to other uses, such as the generation of hydrogen as an energy source.

1.6.1 Hydrogen

Hydrogen is the simplest element, corresponding to the first element on the periodic table, and the most abundant in the Universe.

In 1766, the English chemist, Henry Cavendish, demonstrated that hydrogen as flammable gas, and was distinct from other combustible gases due to its density, while also confirming later that when hydrogen was burned, water was formed. Later, in 1800, Nicholson and Carlisle discovered that the breakage of a water molecule with an electric current generated hydrogen and oxygen. This process was denominated electrolysis [86].

Hydrogen has a very simple structure, so its properties can be theoretically calculated easily, which leads to most theoretical models being based on it and applied further for more complex atoms.

Various fuels were proposed for addressing future environmental and energy crisis, such as reformulated gasoline or diesel, methanol, and ethanol, compressed natural gas and hydrogen, with the latter offering the best conditions, opposed to fossil fuels which are unevenly distributed. This can be done with almost zero emissions of air pollutants or greenhouse gases [87]. Therefore, the use of hydrogen as an energy source would help combat the environmental crisis around hydrocarbon-based fuels, so the full fuel-cycle emissions (production, transmission, and usage of a fuel) can be reduced substantially when compared to conventional systems.

Due to problems that occurred in the past, such as the hydrogen bomb, some people still find the use of hydrogen as a future fuel concerning, so its safety may be assured before proceeding for its globalization. It has several properties that can influence its use as a fuel, being those the following: (a) it is a low-density diatomic gas at ambient conditions, so it must be compressed at high pressure or liquefied to be stored in a sizable volume, (b) has low volumetric energy density, which poses a challenge for its storage on vehicles, (c) it can interact differently with materials because it is an easy-to-diffuse, small molecule, so it's more probable to leak, (d) it requires special steels or other materials that cannot suffer embrittlement, since H_2 can diffuse into metals, (e) it has the highest heating value per kilogram, which means that water is produced in the reaction and the higher the heating value, the higher the hydrogen-to-carbon ratio (H/C), (f) hydrogen is non-toxic, (g) it has a wider range of flammability and detonability limits, which can be quite dangerous, and, last but not least, (h) it has a lower ignition energy than for methane or gasoline. With these properties, we can conclude that hydrogen is safer than gasoline in some of the points, but in others there are some potential concerns, such as the higher likelihood for a leak and the possibility of finding an ignition source. It also has a faster flame velocity, which means the hydrogen-air mixtures can quickly escalate to a full-blown explosion. Therefore, it is preferable for hydrogen storage and refueling to be outdoors or in a well-ventilated space. A hydrogen-caused fire is very worrying since the flame is nearly invisible and radiates little heat, so its detection can be problematic during daytime, if there is no infrared detector or a special heat sensitive paint to indicate.

The economics behind hydrogen production is not the driving force for this switch to happen, because the costs, such as implementation, production, delivery, and refuel, are very similar to those for other-synthetic fuels, except in the costs for the hydrogen transportation, which are projected to be higher than for gasoline, besides having a need for special material-made container. Besides that, the overall cost for the total life cycle of transportation is predicted to be comparable to today's gasoline vehicles. Then, the implementation of hydrogen is not dependent on economic reasons.

H_2 is a very promising candidate as a new energy source and has been enthusiastically pursued as a replacement for the current hydrocarbon economy. But developing a hydrogen infrastructure is still seen as a daunting problem, even if H_2 production systems are already available and widely in use, such as hydrogen cells and storage techniques. But building a large-scale hydrogen production system would require many decades to be developed, as well as a high distribution pipeline system. Iceland, which is a region who depends entirely on imported oil, is evaluating a hydrogen economy, having announced their intention to make the switch by 2030 through electrolysis.

1.6.2 Water Splitting Through Visible-light Photocatalysis

In 1972, Fujishima and Honda demonstrated the feasibility of water splitting under ultraviolet (UV) light with the semiconductor TiO_2, sparking a widespread investigation in semiconductor photocatalysts [88]. Given that UV radiation constitutes only about 4% of sunlight, there is a need to evaluate other semiconductors must be appraised for the absorption of visible ($400\ \text{nm} < \lambda < 800\ \text{nm}$) or infrared light ($\lambda > 800\ \text{nm}$), which are approximately 53% and 43% of sunlight, respectively.

To obtain a great photocatalyst, a few features must be key: a long lifetime of the excited state, absorb in visible and/or infrared light, high yielding charge separation states, and good charge mobility.

The photocatalytic process has three phases: (1) the photosensitizer or photocatalyst absorbs photons from the incident light – ideally sunlight –, (2) the excited state becomes a charge separation state, which promotes the electrons from the valence band (VB) to the conduction band (CB), generating holes in the valence band and a mobile electron – electron-hole pairs –, which are highly reactive, and (3) these electron-hole pairs can participate in redox reactions, the electron in the conduction band can reduce or react with absorbed species on the photocatalyst surface, while the holes in the valence band can oxidize molecules or react with other absorbed species [89]. Throughout the reaction, the photocatalyst doesn't suffer any chemical changes. When using a single photocatalyst, the CB's bottom level needs to be more negative that the reduction potential of H^+/H_2 (0 V), while the VB's top level must be more positive than the oxidation potential of O_2/H_2O (1.23 V) [90].

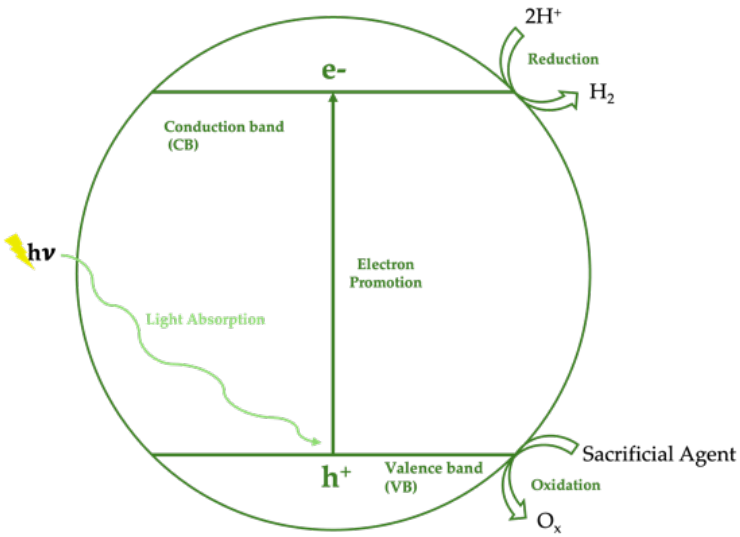

Figure 9. Photocatalytic hydrogen production by water splitting, using a sacrificial agent.

In photocatalytic water splitting (**Figure 9**), the water molecules are reduced by the electrons produced by the hydrogen (H_2), while the oxidation of the same molecules by the holes produces oxygen (O_2), and, since it is an uphill reaction, the Gibbs free energy increases by 237 $kJmol^{-1}$. Simultaneous to these reactions occurs the recombination of the photoexcited carriers, which means that the charge separation and the redox reaction on the surface must happen within their lifetime for a successful water splitting. Therefore, to make that process smoother, photocatalysts are usually modified with appropriate cocatalysts and/or a sacrificial (SA) agent is added. The cocatalyst promotes the carrier transfer and separation of photoinduced charge carriers (ex. Pt, Pd, Au) and the sacrificial agent, using electron donors (ex: methanol, triethylamine, Na_2S/Na_2SO_3), can act as hole scavengers avoiding the charge recombination.

In water splitting, there are two types of processes (**Figure 10**): (1) one-step water splitting – only one photocatalyst used –, and (2) two-step water splitting, also known as "Z-Scheme" – two catalysts used –, named after the photosynthesis process in plants [91]. In the Z-Scheme, one photocatalyst stages the reduction of H_2O to H_2 and oxidation of the reduced redox mediators, while the other performs the oxidation of H_2O to O_2, and they are combined by using a shuttle redox couple in the solution, but it can occur even in the absence of those.

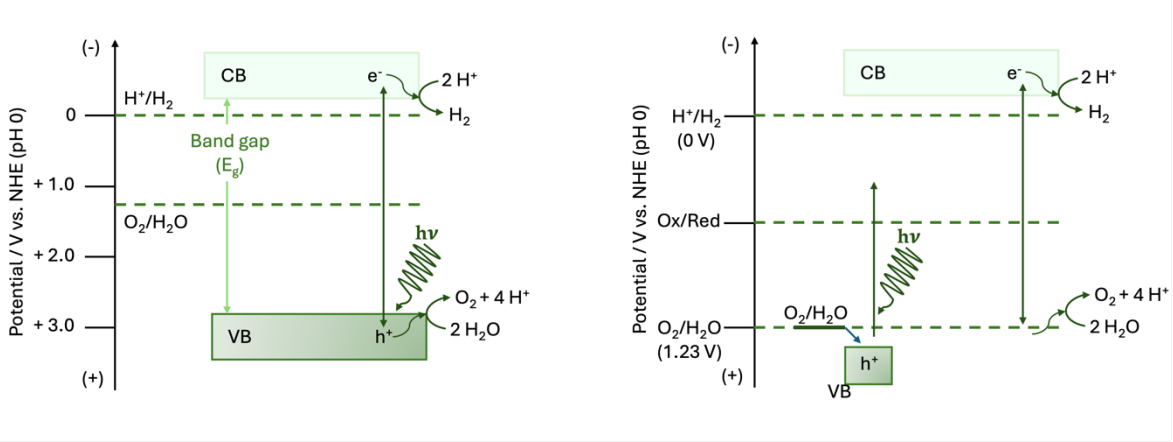

Figure 10. Types of water splitting processes: (a) One step excitation and (b) Two step excitation.

One-set photocatalysts have a higher quantum efficiency, but lower solar-to-hydrogen efficiency, with the disadvantage of producing a mixture of H_2 and O_2. While the Z-scheme produces the gases separately, both quantum and solar-to-hydrogen efficiencies are low. Therefore, this technique reduces the necessary energy for photocatalysis, but double the photons are needed for the efficient use of visible light.

1.6.3 MOFs as Photocatalysts

MOFs have emerged as ideal candidates for this application due to their tunable pore size, versatile properties, and easily modifiable functionality – but especially for their ultra-specific surface area (over 6000 $m^2\ g^{-1}$), which is imperative in the enhancement of water splitting activity [92], [93]. MOFs perform as heterogeneous catalysts and are highly sought after for their recyclability and facile separation, while also improving product selectivity [94].

The entirety or the pore of MOFs (**Figure 11**) can perform as hosts to load materials and maximize the catalytic activity, which is also enhanced by the synergetic host-guest effects. Those synergetic effects are strong enough to diminish the decrease in surface area caused by the encapsulation.

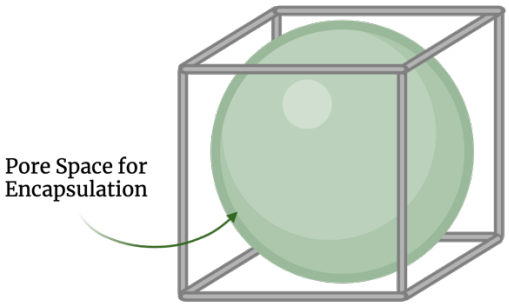

Figure 11. MOFs' porous nature.

The metal nodes in MOFs are the key factor for its catalytic performance, so their selection is important. This effect has been more significant in electrocatalysis, so Marinescu et

al coordinated benzenehexathiolate (BHT) frameworks with Co, Fe, and Ni metal nodes to test in hydrogen evolution reactions (HER) – the Co-BHT showing the best results [95]. Lin and co-workers also developed a work in electrocatalysis with the ligand 4-(5-(pyridine-4-yl)-4H-1,2,4-triazol-3-yl) benzoic acid, using Co, Cu, and Zn-Co remained the one with highest activity [96]. Besides the metal node having influence on the catalytic activity, the ligand can also play an important role, since, if it is functionalized, it can change the electronic density of the metal nodes or the efficiency to capture light. The addition of certain functional groups is beneficial for the enhancement of its absorbability range, such as NH_2 groups, which leads to an increase of 1.2 eV of the HOMO, without influence on the LUMO. The effects of other groups and diamine groups were also studied for the MIL-125, concluding that the latter was the better one based on the theory of conventional semiconductor catalysis, that states that the narrower the band gap, the more efficient the response to visible light is [97].

Xamena and co-workers applied this ligand effect study to UiO-66 and UiO-66-NH_2 to evaluate their performance in photocatalytic hydrogen production under UV-light [98]. The electron-donating group – NH_2 – has a negative σ_m value, so the electron density around the inorganic clusters is increased and so is the separation and transfer of the photogenerated charge carriers. The UiO-66-NH_2 had a visibly intensive absorption band between 300 and 440 nm that guarantees its better efficiency when compared to the regular UiO-66. It was also reported by Matsuoka that electron-withdrawing groups, such as NO_2 and halides, have the opposite effects, having lower visible-light absorbility, even if they are more active [99].

Dang et al. reported a ZnMOF using 4,4'-dibenzoic acid-2,2'-sulfone and 4,4'-azopyridine as ligands in a 1:1:1 ration for the visible-light driven hydrogen production. The SA's systems tried were H_2O and DMF/H_2O mixtures in different ratios. They firstly used the MOF as a photocatalyst in water, irradiated the solution, the MOF was recovered and washed, and then added to a fresh solution of Na_2S/Na_2SO_3 and illuminated again. These experiments revealed promising results in the utilization of ZnMOFs as photocatalysis for HER [99].

Since some MOFs can present semiconductor-like behavior, the difficulty with their usage as photocatalysts is that only a selection of them is capable of absorbing visible light.

In the classical photocatalysis, the photocatalyst is excited by the incident light with energy (E_{light}) larger than the band gap (E_{gap}), generating the electron-holes pair, but in MOFs it can happen differently, where the electron transitions can also occur from the HOMO – highest occupied molecular orbital – to the LUMO – lowest unoccupied molecular orbital. The incident light was restricted to UV light with a short wavelength ($\lambda < 365$ nm) for the successful excitation of MOFs (**Figure 12**). But, as mentioned before, MOFs responsive to visible light ($\lambda > 400$ nm, or $E_{light} < 3.1$ eV) are more desirable [100].

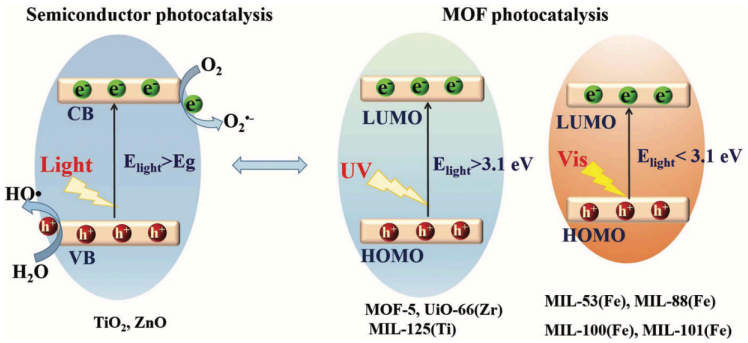

Figure 12. Photocatalysis for Semiconductors *vs.* MOFs (Reproduced from [100])

There are already some hydrogen production methods, the conventional ones – such as steam reforming, coal gasification, and water electrolysis –, the advanced ones – such as "closed thermochemical cycles" –, but alternatives with milder, more sustainable conditions, with the minimal liberation of pollutants and greenhouse gases, are still being evaluated, like the use of solar energy – one of the objectives of this work.

1.6.4 Small-scale Photocatalysis for H_2 Production

The most widely studied photocatalysts have wide band gaps – like the case of TiO_2, that is UV-responsive –, meaning they have no response to visible-light. This fact led to a global search for visible-light-responsive photocatalysts, with narrower band gaps, like sulfide-based materials, such as CdS and $Zn_xCd_{1-x}S$. Since CdS has been proven as an efficient photocatalysis for H_2 production, it still presented its own limitations for a global application like photocorrosion under visible light irradiation and the quick recombination of photo-generated charge carriers. Also, ZnS is known for its rapid generation of the electron-hole pairs upon photoexcitation, shows high activity under UV-light irradiation for H_2 production, and highly negative reduction potentials, but it also has a too large band gap, avoiding the visible-light responsive zone [101], [102]. So, as to solve those issues, $Zn_xCd_{1-x}S$ have been regarded as a viable method due to easily tunable band gap and band edge position, which vary with the change of the molar ratio of ZnS and CdS [103]. Therefore, the previously studied 3:2 CdS/ZnS photocatalyst was used as reference material, but cadmium is a known environmental pollutant, harmful for Humans, besides that to achieve high crystallinity, it usually requires high temperature and the use of a platinum cocatalyst – which is expensive.

To substitute cadmium photocatalysts, zinc is a cheaper and safer alternative, with higher crystallinity in milder conditions. Therefore, in this work, we will be using zinc and zirconium-based MOFs as possible photocatalysts in visible-light since both are more abundant in Earth's crust than Cd.

In the small-scale hydrogen production setup, the photocatalytic reactions are carried out in a closed-circulation system or in an open flow system. The closed-circulation system is generally equipped with a vacuum or flow system at atmospheric pressure and the photocatalyst sample is dispersed in the aqueous solution with an SA. The system is then evacuated

with an inert gas to eliminate the air in the solution and to keep the gas composition homogeneous, avoiding boiling the reaction solution under illumination at a reduced pressure. Alternatively, in the open flow system, the inert gas flows continuously through the headspace of the reactor. In both systems, gaseous products are analyzed by gas chromatography to avoid air contamination, but, in this work, the H_2 production was followed using a graduated pipette through the rise of the solution and applying ideal gas equation ($PV = nRT$) for the calculation of H_2 quantities.

In practice, the pressure affects the photocatalytic activity – at higher pressures, the activity is decreased due to slower formation of bubbles and desorption of product gases, which induces a problem for solar water splitting at ambient pressure – the water reformation.

1.7 Objectives

Following the work of Fujita and co-workers [54] on the development of the CSM and considering the current limitations of the existing CSs and the importance of finding ways to easily elucidate the structure of non-crystallizable compounds, the main aim of this work is to synthesize Zr- and Zn-MOFs with improved properties that can increase the efficiency, sensitivity and applicability of the CSM for structural elucidation of complex molecules and challenging samples. In addition, the synthesized materials will also be tested as potential photocatalysts for the production of hydrogen from water splitting, using a SA to help reduce the charge recombination and increase the photocatalytic activity.

To improve the efficiency and applicability of the CSM, materials with larger pores will be designed and synthesized using organic linkers with variable lengths and functional groups, where rigid molecules will be preferred over flexible structures. In addition, the structural determination of non-crystallizable organic compounds is another aim for this work.

In the case of the materials' application as photocatalysts for hydrogen production via water splitting, using visible light irradiation, one of the requirements is that these materials must absorb light in the visible region of the spectrum. Therefore, ligands with extended π systems will be used in the design and synthesis of the Zr- and Zn-photocatalysts.

In order to make synthetic processes more sustainable, whenever possible, green chemistry techniques, such as mechanochemistry, microwave-assisted reactions and hydrothermal synthesis will be employed.

2

RESULTS AND DISCUSSION

The carboxylate and azolate ligands were synthesized using various techniques. The ligands were then trialed as linkers for MOF formation with various zinc(II) salts, zirconium(IV) chloride or zirconium(IV) oxychloride octahydrate. The characterization of the MOFs and complexes obtained are described in the corresponding subsection. Previously reported MOFs that were not previously tested as crystalline sponges and/or as photocatalysts for the hydrogen production from water splitting were also synthesized.

MOFs comprising different metals, prepared at Faculdade de Ciências da Universidade do Porto, were assessed as photocatalysts in our hydrogen production system. Their photochemical characterization through UV/Vis DRS to evaluate their light-absorption properties was also performed.

2.1 Synthesis and Characterization

2.1.1 Ligands

2.1.1.1 Synthesis of Ligands

Ligands were the first synthesis' step for the obtention of MOFs. Thus, we synthesized six distinct ligands (**Figure 13**) with imine bonds, terminal carboxylic acids or terminal amines using different techniques.

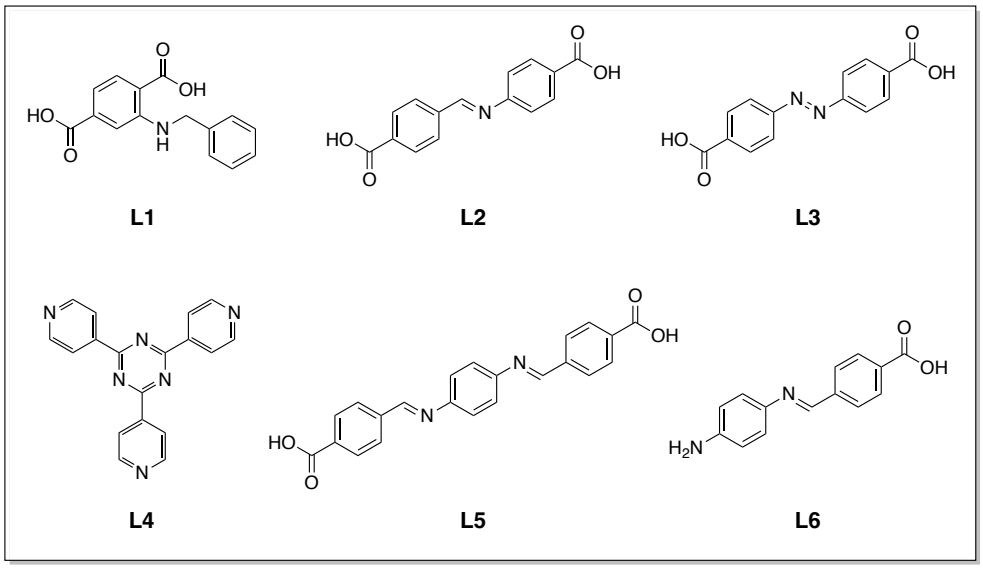

Figure 13. Synthesized ligands (**L1-L6**).

We started by attempting to synthesize **L1** (**Figure 14**), following Chatz-Giachia et al.'s protocol [104] but with a slight modification, obtaining a bright orange solid with good yield. This is not in accordance with the reported literature where it yielded a yellow solid.

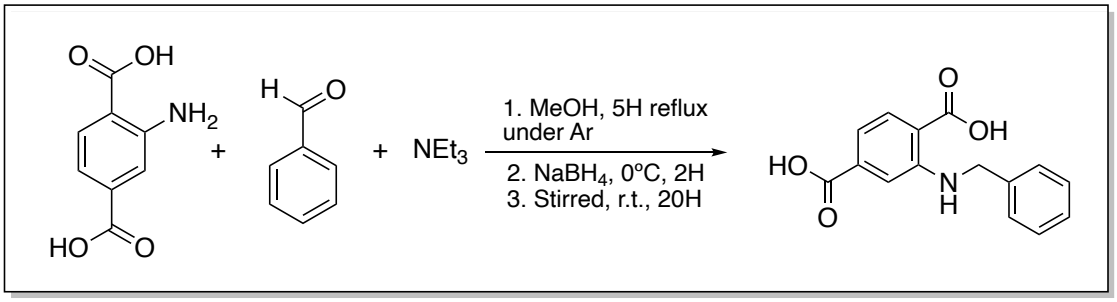

Figure 14. Synthesis of **L1** following the reported protocol: 2.8 eq. 2-aminoterephthalic acid, 2.5 eq. benzaldehyde and 4 eq. triethylamine.

Following this method, a yellow solution correspondent to the intermediate Schiff base should have been obtained, but, in fact, a deep red solution was obtained right after the addition of triethylamine. When evaporated, this solution turned into an oil of the same color, but the NMR didn't correspond to the expected product – therefore, it was impossible to obtain the intermediate on its own (**Figure 15**). The crystals formed from the oil corresponded to a triethylammonium salt having 2-aminobenzene-1,4-dicarboxylate as the counterion. When the synthesis was followed without attempting the isolation of the imine derivative, we were able to obtain **L1**, whose characterization was in agreement with the previously reported [104].

The impediment in the formation of **L1**'s imine-derivative is due to their poor stability in aqueous media, with the reaction being reversible in those conditions. The presence of water in the dimethylsulfoxide (DMSO) for the NMR could reverse the reaction and yield solely the initial reagents.

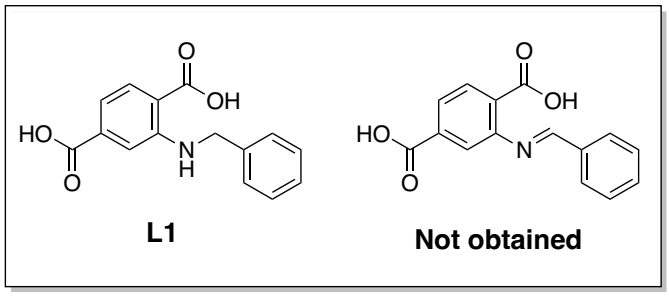

Figure 15. L1 and the unobtained Schiff base intermediate.

After the obtaining **L1**, we followed the procedure reported by Yuan et al. to attain **L2** (**Figure 16**) [105].

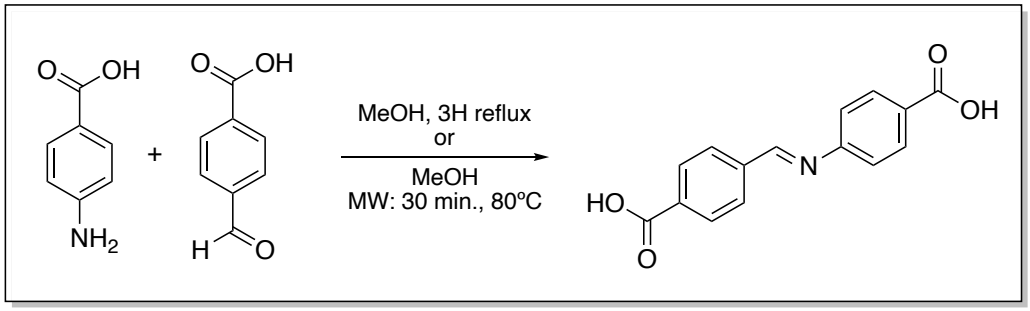

Figure 16. Two synthetic procedures for the obtention of **L2**: 1 eq. of each reactant.

We couldn't obtain the desired compound through the reported method, as in the ^{1}H NMR, the signals of the reagent, the 4-formylbenzoic acid could be seen, so either the reaction was not complete or due to its reversibility in the presence of water, the imine was not stable and reverted to the reagents. Therefore, we tried to adapt the regular 3H reflux procedure into a microwave-assisted one, converting it into a 30-minute synthesis with a good yield of the eggshell white solid. In the ^{1}H NMR for the microwave synthesis, no traces of 4-formylbenzoic acid were found (**Figure A.2** in the **Annexes**).

The salmon pink solid **L3** (**Figure 17**) was synthesized following the protocol by Li et al. in a good yield [106].

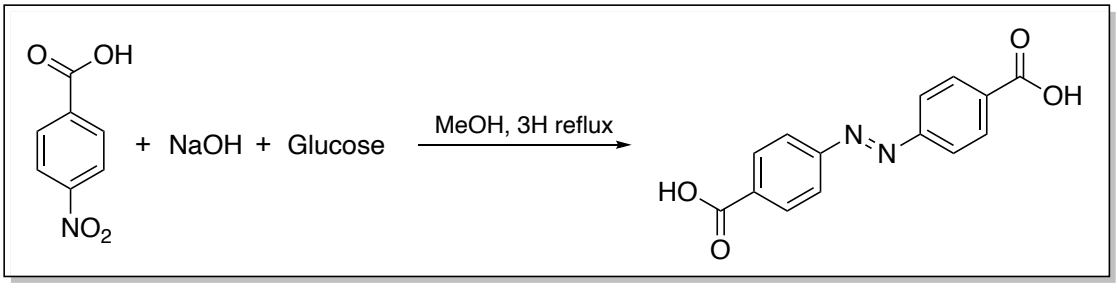

Figure 17. Synthesis of **L3** using Li's procedure: 1 eq. of *p*-nitrobenzoic acid, 15.2 eq. of sodium hydroxide, and 7.6 eq. of glucose.

The 2,4,6-tri-4-pyridyl-1,3,5-triazine (**TPT** or **L4**, **Figure 18**) was previously synthesized in our lab and was used to conduct these experiments after a ^{1}H NMR was performed to confirm if it was still pure.

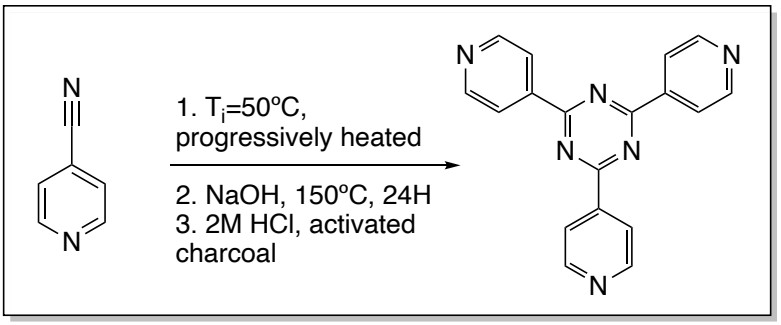

Figure 18. Synthesis of **L4**/**TPT**:

With the aim of augmenting the length of the ligands, but still checking for group effects, compounds **L5** and **L6** (**Figure 19** and **20**), the mono- and disubstituted products from the reaction, were obtained using *p*-phenylenediamine and 4-formylbenzoic acid. The disubstituted **L5** was obtained by two different methods: firstly, we tried a conventional 3H reflux which yielded the desired product. However, since the procedure by Ghamari Kargar et al. has milder conditions, such as no temperature and lower reaction time, we decided to use it [107].

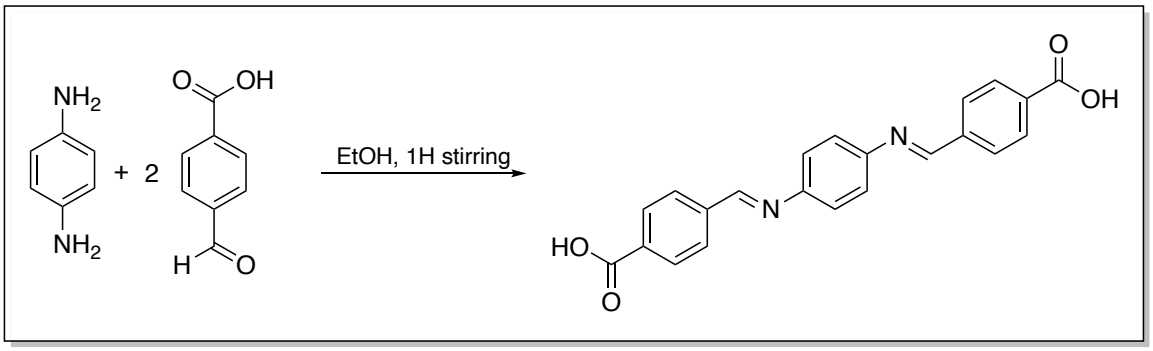

Figure 19. Synthesis of **L5**: 1 eq. of p-phenylenediamine and 2 eq. of 4-formylbenzoic acid.

In the literature, only a patent was found for **L6**. Adding a 1:1 proportion of 4-formylbenzoic acid and *p*-phenylenediamine, the aldehyde will only react in one amine position, leading to the monosubstituted ligand. **L6** was obtained using the same protocol as in **L5**, and both were obtained with good yields.

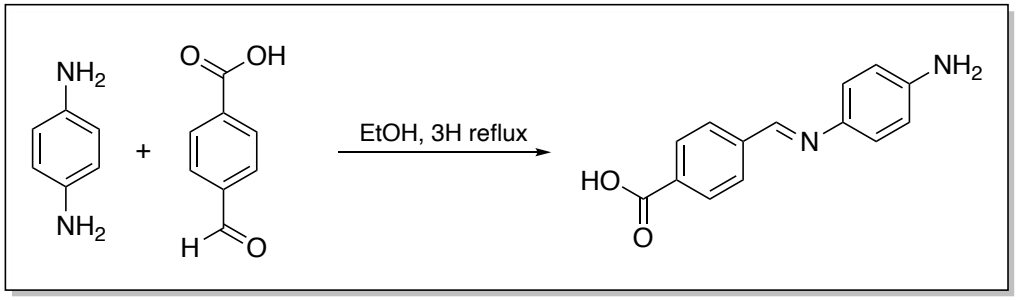

Figure 20. Synthesis of **L6**: 1 eq. of p-phenylenediamine and 1 eq. of 4-formylbenzoic acid.

2.1.1.2 Structural Characterization of the Ligands

2.1.1.2.1 NMR Analysis

The ^{1}H NMR spectra for the ligands were obtained to confirm the structural details. All the ligands' NMR spectra were obtained in deuterated DMSO, with its characteristic signal at 2.50 ppm. A broad signal correspondent to water also appeared at around 3.40 ppm.

For compound **L1** (Full spectrum - **Figure A.1** in **Annexes**), it was expected to obtain eight signals, including those of the carboxylic acids and the amine. The carboxylic acids and amine's signals are not represented due to the chemical exchange with the water present on the DMSO.

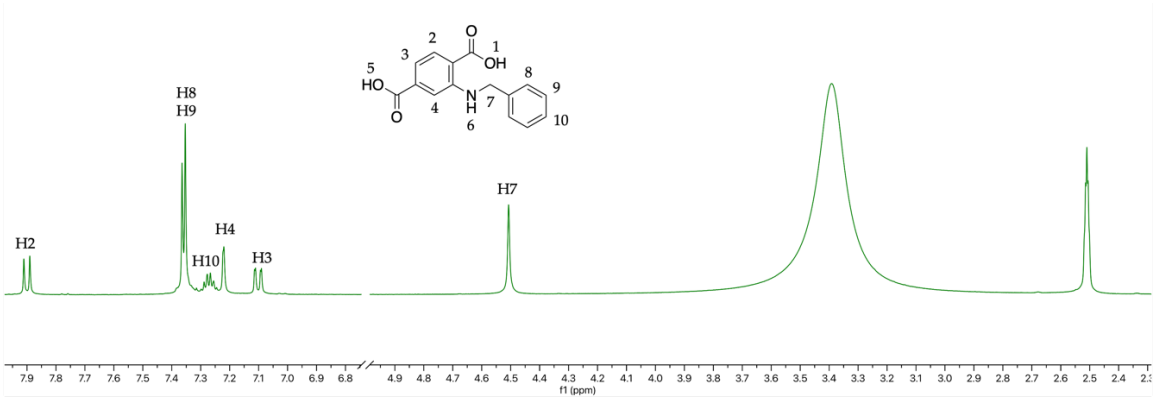

Figure 21. ^{1}H NMR (DMSO-*d6*) spectrum for **L1**.

In **Figure 21**, it is observable in the spectrum for **L1** the duplet at 7.90 ppm, integrating for 1 proton, which corresponds to H2 since it is closer to both the carboxylic acid and the amine groups, therefore the protons will be more deshielded and more downfield. In the aromatic area, there are two multiplet signals: the one corresponding to four protons at 7.35 ppm is attributed to H8 and H9, as they are chemically equal, and the other at 7.27 ppm, integrating for one proton, which we can correlate to H10. H4 is attributed to the singlet at 7.22 ppm and H3 to the duplet of duplets at 7.10 ppm, both integrating to one proton each. Additionally, in the aliphatic zone, the singlet integrating to two protons at 4.51 corresponds to H7, as it is bonded to an amine.

For **L2** and **L3** (**Figure A.2** and **A.3** in **Annexes**), the differences are observable in **Figure 22**.

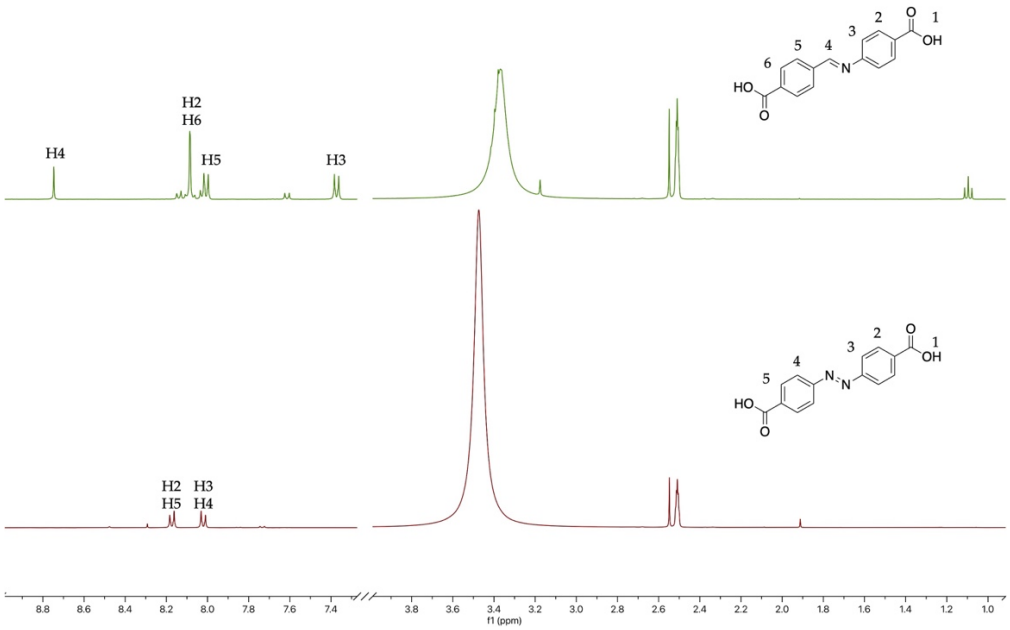

Figure 22. ^{1}H NMR (DMSO-*d6*) spectra of **L2** (top, green) and **L3** (bottom, red).

The protons in **L2**'s aromatic rings have different chemical shifts due to their chemical inequality, while in **L3** the molecule is symmetrical, therefore the protons have the same chemical environment.

For **L2**, the singlet for the C-H proton (H4) from the imine signal appears at 8.75 ppm. The 8.08 ppm multiplet, integrating to four protons, can be attributed to H2 and H6 due to their similar nature (being near a carboxylic acid), and the multiplet at 8.00 ppm, integrating to two protons, can be assigned to H5. Since H3 is closer to the electron-donor nitrogen from the imine, it will be more shielded, therefore it was appointed to the duplet signal integrating for 2 protons at 7.37 ppm. It is also noticeable in the spectrum the signals for one of the reagents, the 4-formylbenzoic acid, at 7.60 ppm and 10.11 ppm (observable in the full spectrum) due to the overtime decomposition of the ligand in DMSO.

Displayed on **L3**'s spectra are two major signals: two duplets at 8.17 ppm and 8.02 ppm, both integrating to four protons each. The first signal may be attributed to H2 and H5 due to their proximity to electron-withdrawing OH from the carboxylic acid groups and the second can be assigned to H3 and H4 for being closer to the N=N bond.

The other signals at 1.09 ppm and 3.17 ppm in **L2** is from dichloromethane and methanol, respectively, and in **L3** at 1.90 ppm is acetic acid.

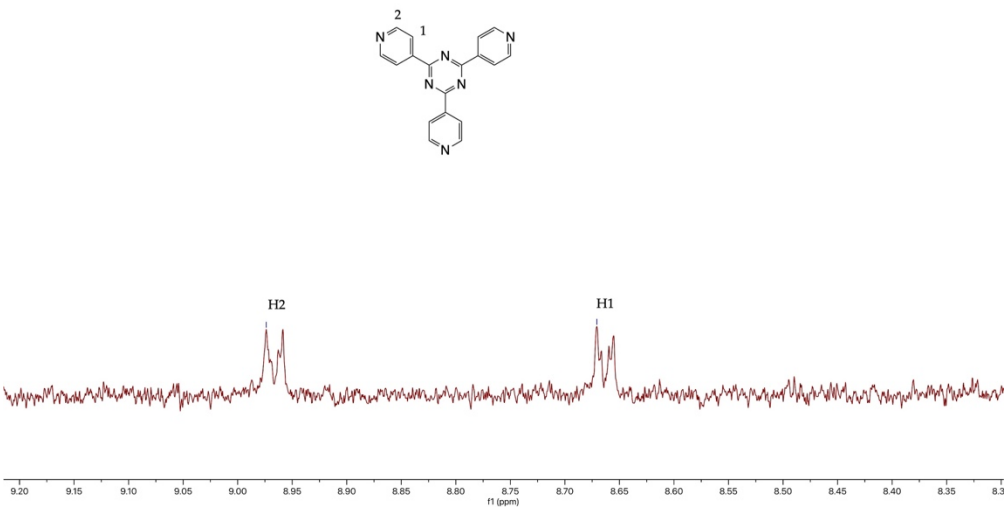

Figure 23. ^{1}H NMR (DMSO-*d6*) spectrum of TPT.

L4's, better known as TPT, spectrum (**Figure A.4** in **Annexes**) is represented in **Figure 23** in less detail – meaning without the solvent's peaks. TPT is a symmetric molecule, therefore, it will only show two doublet signals above 8.00 ppm due to the protons' proximity to the nitrogen atoms. This speculation is confirmed with doublet signals at 8.97 ppm and 8.67 ppm, both integrating to two protons.

The **L5**'s spectrum (**Figure A.5** and **A.6** in **Annexes**) is comparable to **L6**'s, as former is the disubstituted and the latter is the monosubstituted products of the same reaction, in different stoichiometry (**Figure 24**).

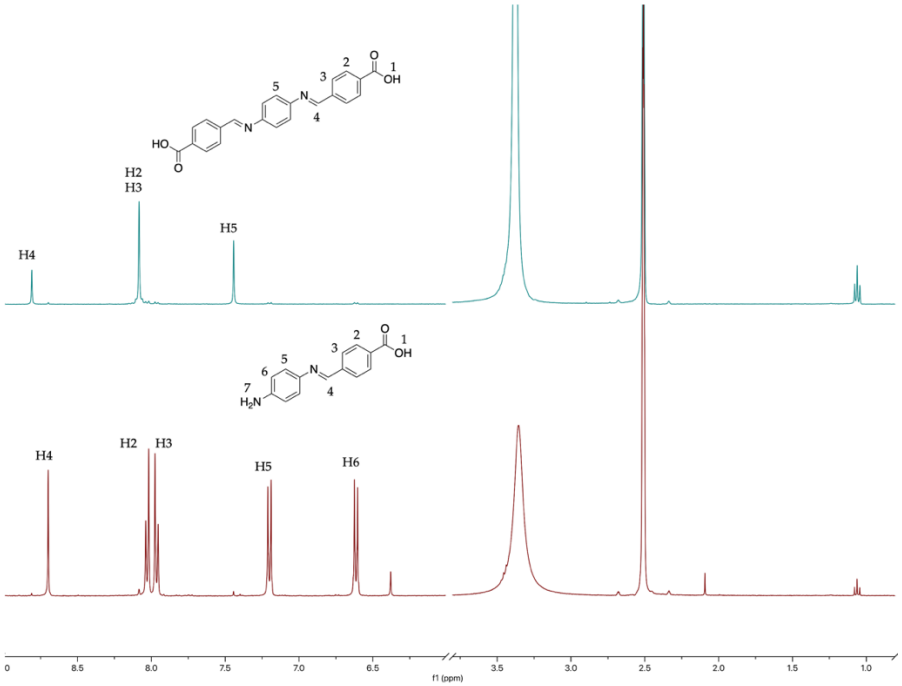

Figure 24. ^{1}H NMR (DMSO-*d6*) spectra of **L5** (top, blue) and **L6** (bottom, red).

Since **L5** is a symmetric molecule, hence only four signals are expected from hydroxyl groups from the carboxylic acids (which don't show up due to chemical exchange), the *ortho*

and *meta* protons of the aromatic rings in the extremities, the protons from the center ring, which are all chemically equal, and from the iminic C-H protons. All of those are displayed in **Figure 24** (top). The singlet at 8.81 ppm, integrating for two protons, corresponds to iminic C-H protons, the protons from the extremities' rings appear at 8.08 ppm in a singlet signal that integrates to eight protons, and the 7.44 ppm singlet that integrates for four protons is attributed to the center ring protons.

As to **L6**, five signals should be observable, besides the hydroxyl and amine protons. The singlet at 8.70 ppm for one proton represents the iminic C-H, the two duplets of duplets at 8.02 and 8.00 correspond to the two aromatic protons close to the carboxylic acid and the two protons closer to the iminic carbon, respectively. At 7.21 ppm, the duplet corresponding to two protons are from the protons closer to the iminic nitrogen, while the duplet at 6.62 ppm is the duplet from the two protons near the amine group.

The signal at 2.09 ppm in **L6**'s spectrum is from the acetone present in the NMR tube and the signal at 1.06 ppm in both spectra is from the dichloromethane.

2.1.1.2.2 FTIR Spectroscopy Analysis

The obtention of the functional groups present in the molecule through IR spectroscopy is fundamental since the materials formed will not be soluble in organic solvents, hence the need for a way to confirm what was formed. Since the ligands have carboxyl or amine groups that will bond the metals in a MOF, the bond vibrations represented in the bands from IR allows for a thorough analysis to check if a M-O or M-N bond (M = metal) is formed or if the hydroxyl or amine groups' band disappear. In **Figure 25** is represented the spectra for all the ligands, except for TPT.

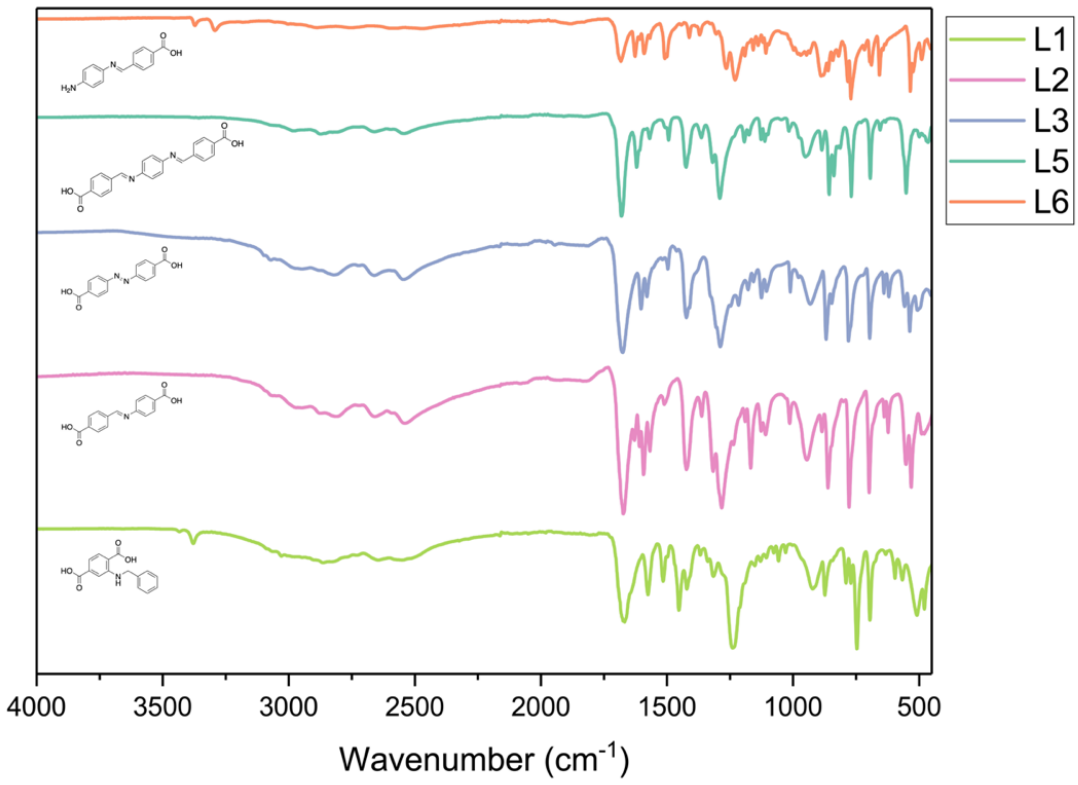

Figure 25. FTIR spectra for ligands **L1-L6** (in reverse order).

For **L1** (**Figure A.7** in **Annexes**), the FTIR spectrum was obtained and confirmed with the previously described in the literature. The characteristic amine group double bands at 3360-3510 cm^{-1} are the major indicator for the desired product formation, pointing the loss of a hydrogen by the nitrogen by the band at 3506 cm^{-1} decreasing significantly in intensity when compared to the other one at 3369 cm^{-1}. The hydroxyls from the carboxyl groups are represented through broad peaks at 2860 and 2642 cm^{-1}, while the carbonyls are at 1670 cm^{-1}. Primary amines usually present a N-H bending band at 1580-1650 cm^{-1} that in the 2-aminoterephthalic acid appears at 1622 cm^{-1}, but its absence is noticeable in **L1**'s spectrum, further confirming the formation of the secondary amine. It also has the N-H stretching band at 1242 cm^{-1}.

As for **L2** and **L3** (**Figure 26** and **Figures A.8** and **A.9** in **Annexes**, respectively), the differences between the iminic and non-iminic compound can be seen. The IR data obtained for both ligands coincide with the literature [108], [109].

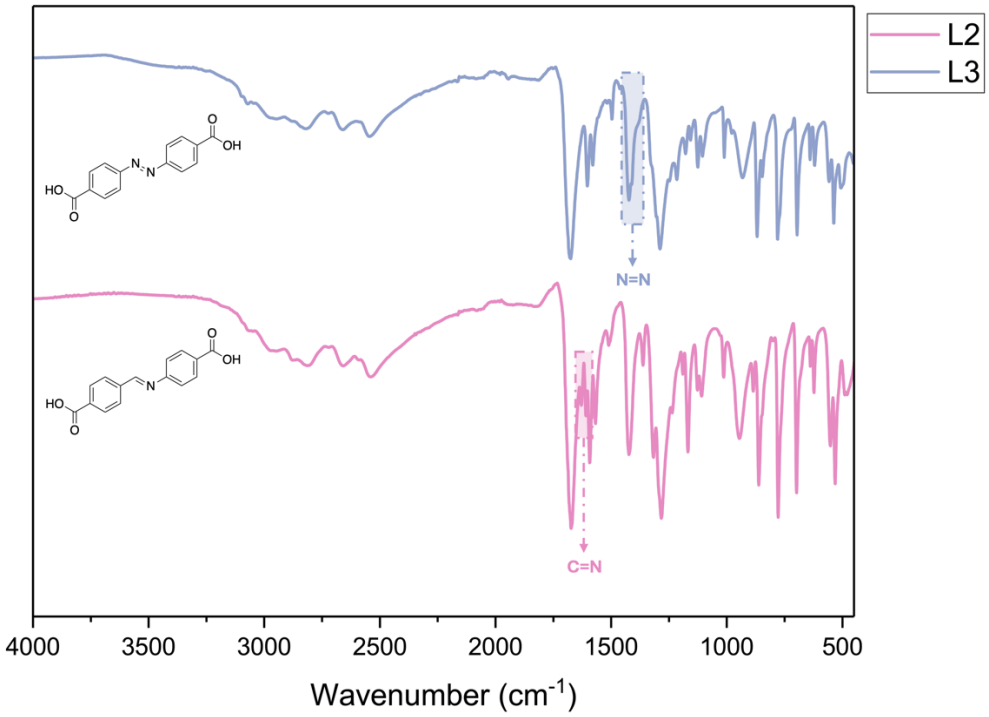

Figure 26. Comparison of the FTIR spectra for **L2** and **L3**.

In the Schiff base ligand **L2** (pink, bottom), both the appearance of a new band at 1629 cm^{-1} correspondent to the formation of an iminic C=N bond and the disappearance of the double bands at 3500-3400 cm^{-1}, characteristic to the NH_2 group from the 4-aminobenzoic acid, can explain the obtention of the desired compound.

In the azo compound **L3** (muted blue, top), the formation of the new N=N band can be observed with the broadening and close to double peaking of the band at 1443 cm^{-1} and the absence of the N-O stretching band from the 4-nitrobenzoic acid at 1540 cm^{-1}.

The common important bands belong to the carboxylic acids, such as the broad O-H bands at 2850-2535 cm^{-1} and the strong C=O band at 1675 cm^{-1}.

Another set of comparable molecules are the **L5** and **L6** (**Figures A.10** and **A.11** in **Annexes**), the di- and monosubstituted aromatic compounds, represented in **Figure 27**.

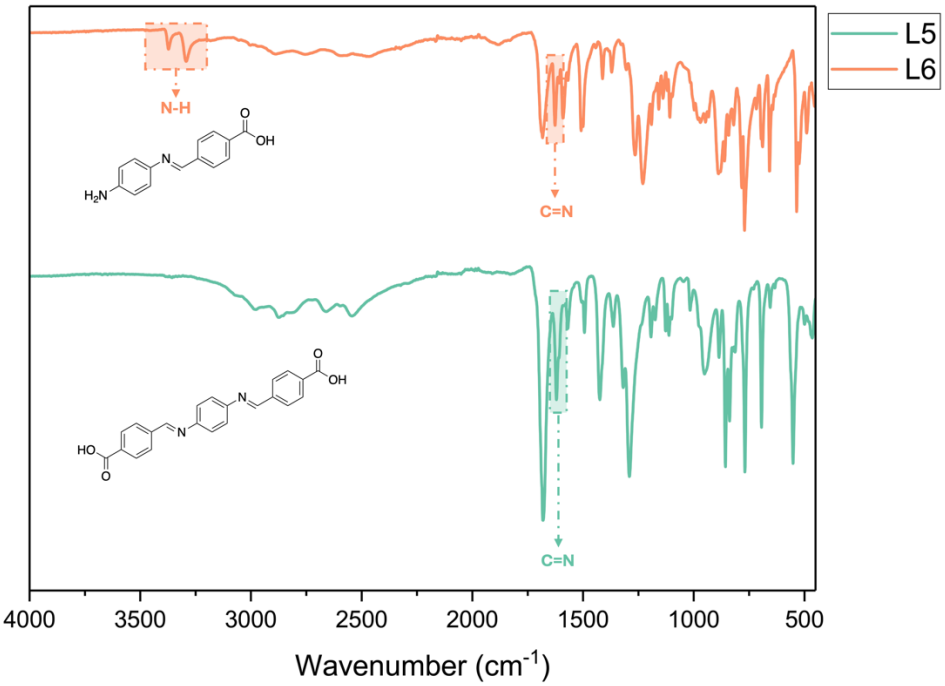

Figure 27. Comparison of the FTIR spectra for **L5** and **L6**.

The formation of the disubstituted iminic compound **L5** (mint, bottom) is confirmed by the absence of the NH_2 group characteristic double peaks at ~3500 cm^{-1} and the appearance of the C=N band at 1620 cm^{-1}.

The monosubstituted **L6** (orange, top) has the C=N band at 1623 cm^{-1} and the NH_2's double peaks at 3292 and 3371 cm^{-1}.

The intensity of the C=O from the carboxylic acid band at 1680 cm^{-1} has double the size in **L5** due to the presence of two groups, when compared to the one of **L6**. The broad bands at 2300-3000 cm^{-1} from the hydroxyl groups are also present in both.

2.1.2 Reported MOFs

Reported MOFs were synthesized to test for their application as crystalline sponges or as photocatalysts in hydrogen production through water splitting.

2.1.2.1 Synthesis of the Reported MOFs

The synthesis of the MOFs began with Fujita's sponge – the most used MOF for CSM. The Fujita's sponge, $[(ZnI_2)_3(TPT)_2]_n$, was synthesized following Clardy and coworkers' procedure [67]: a chloroform solution of TPT was added to a tube, then layered with a methanol solution of zinc iodide (ZnI_2). The tube was closed and left to grow crystals for three days. The scheme of the reaction is represented in **Figure 28**.

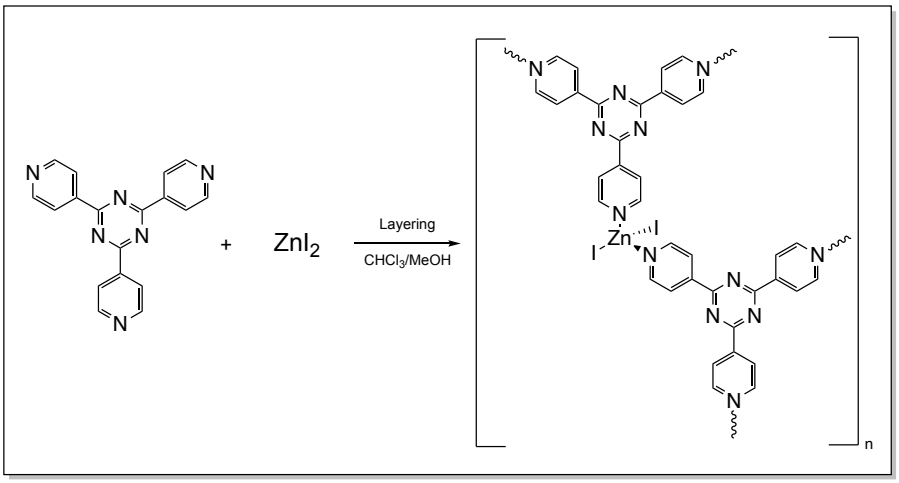

Figure 28. Reactional scheme for the synthesis of Fujita's sponge: 1 eq. of ZnI_2 and 1 eq. of TPT.

The Zr-MOFs, **UiO-66** and **UiO-66-NH$_2$**, were synthesized using Taddei et al.'s [110]and Solís et al.'s procedures [111], respectively. The former was synthesized by adding 1.25 mmol of each reagent, $ZrCl_4$ and TA, in 10 mL DMF to a glass vial. Acetic acid and water were also added to the vial to act as modulators. The vessel was microwaved for 30 minutes at 120ºC, and the product was washed and dried. For the synthesis of the latter, 0.6 mmol of the reagents, $ZrOCl_2$ and ATA, in 17.2 mL DMF were added to the microwave glass vial and magnetically stirred. Acetic acid and HCl 37% were added as modulators and the solution was stirred before being placed in the microwave for 30 min at 140ºC.

The $[ZnI(TPT)_2(TA)]_n$ (**MOF1**) and the $[ZnI(TPT)_2(ATA)]_n$ (**MOF2**) were synthesized using the protocols by Tan et al. [112], with slight alterations (**Figure 29**). 1.5 mmol of zinc iodide, 0.75 mmol of TA or ATA, and 0.75 mmol of TPT were added to the Teflon-line autoclave with 75 mL of distilled water and 126 or 210 μL of triethylamine, respectively. The autoclave was put in an oven and heated to 160 ºC for 36H (**MOF1**) or 72H (**MOF2**). **MOF1** yielded a mixture of colorless crystals and a yellow powder, while **MOF2** yielded red crystals with a brick red powder.

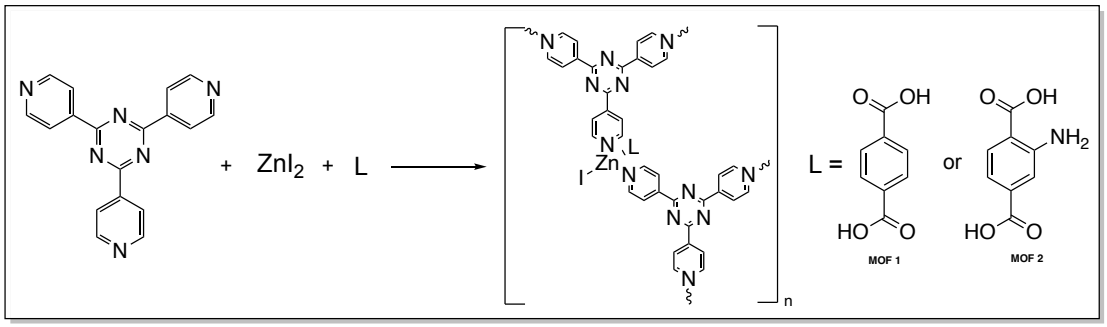

Figure 29. Reactional scheme for the synthesis of **MOF 1** and **MOF 2**: 1.5 eq. of ZnI_2 and 0.75 eq. of TA or ATA, respectively.

All the materials (in exception of Fujita's sponge, which was only characterized by SCXRD) were characterized by FTIR and PXRD, so we could guarantee the obtention of desired compound, while DRS was also performed to evaluate the light absorption range of each

one. The Zn-MOFs were also analyzed by SCXRD, as they yielded high quality single crystals, to confirm their absolute determination.

2.1.2.2 Characterization of the Reported MOFs

2.1.2.2.1 FTIR Spectroscopy Analysis

The reported MOFs were characterized by FTIR to identify the functional groups present in the overall structure. This was best used for the Zr-MOFs (**UiO-66** and **UiO-66-NH$_2$**) because crystals were not obtained.

For **UiO-66** and **UiO-66-NH$_2$** (**Figure A.11** and **A.12** in **Annexes**), the obtained spectra (**Figure 30**) was compared to the literature.

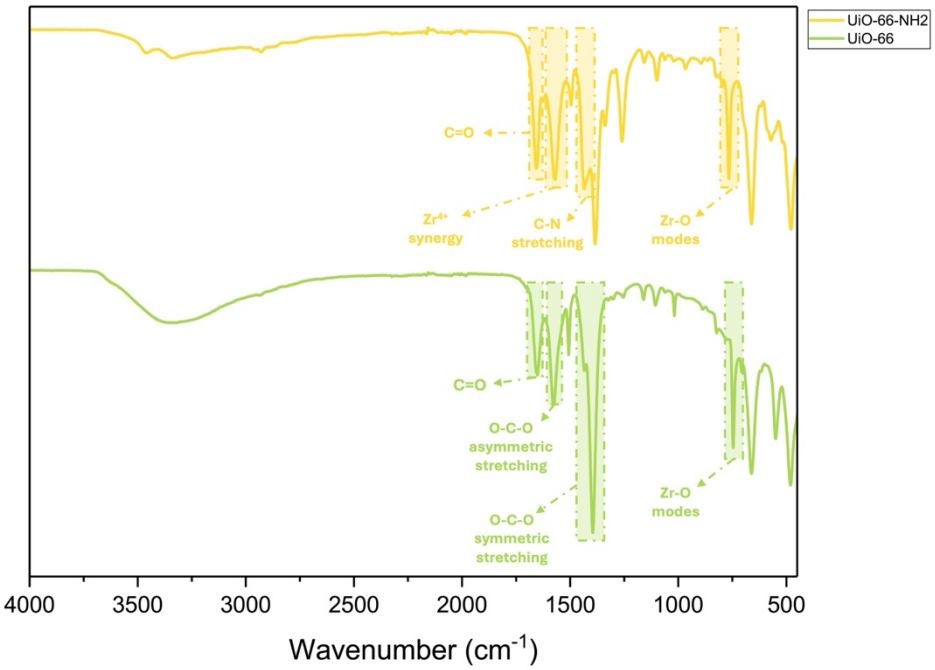

Figure 30. FTIR spectra for **UiO-66** and **UiO-66-NH$_2$**.

The synthesized **UiO-66** (lime green, bottom) was compared to the description reported by Jin et al. [113].The bands at 1660, 1580/1380, and 1506 cm^{-1} correspond, respectively, to the C=O bond from the carboxylate, the O-C-O asymmetric/symmetric stretching vibrations, and the C=C stretching vibration from the benzene ring, all from the terephthalic acid ligand. At 746 cm^{-1} appears the Zr-O modes, at 661 cm^{-1} the O-H bending band, and at 549 and 481 cm^{-1} the symmetric and asymmetric Zr-(OC) stretching bands [114].

The spectra obtained for the **UiO-66-NH$_2$** (yellow, top) was compared to Liu et al. [115]. The bands at 1657 and 1570 cm^{-1} are attributed to the C=O from the carboxyl groups and Zr^{4+} synergetic effects. At 1495 cm^{-1} is the N-H bending vibration, while at 1435 and 1260 cm^{-1} are both C-N stretching vibrations. The Zr-O modes are at 765 cm^{-1}, the O-H bending at 661 cm^{-1}, and the symmetric and asymmetric Zr-(OC) bands appear at 571 and 478 cm^{-1}.

The FTIR spectra obtained for **MOF1** and **MOF2** (**Figure A.13** and **A.14** in **Annexes**) are represented in **Figure 31**. These compounds could not be compared to the literature, since no FTIR report was found.

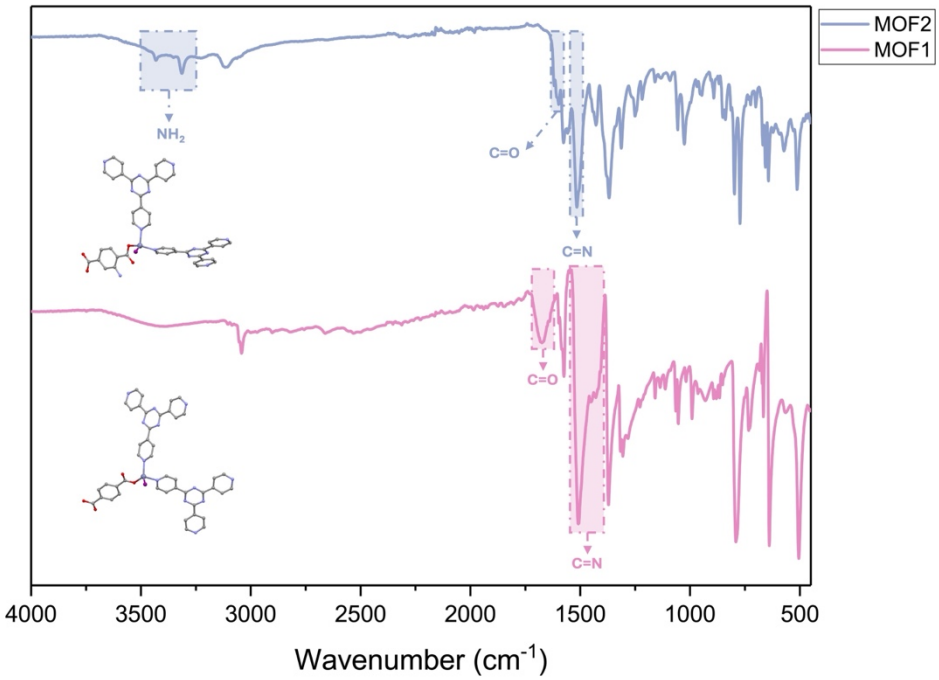

Figure 31. FTIR spectra for **MOF1** and **MOF2**.

In **MOF1** (pink, bottom), the TA ligand presents a band at 1673 cm^{-1} attributed to the C=O from the carbonyl group, confirming that the ligand is connected to the metal, since the protonated carboxyl groups' C=O band appear at 1730-1700 cm^{-1}. At 1574 cm^{-1}, the band is larger at the base, which means that it corresponds to both the C=C stretching vibration from the TPT rings and the C-O asymmetric stretching vibration from the TA. The same happens for the 1506 and 1372 cm^{-1} bands, where the former corresponds to the C=C stretching of the benzene ring in TA and C=N stretching vibration for TPT, while the latter is attributed to the ring deformation C-C mode for the TPT and symmetric stretching vibrations of the C-O in TA. The bands at 1000-400 cm^{-1} belong to the Zn-O modes.

For **MOF2** (muted blue, top), the spectrum should be similar to **MOF1**, since the only difference is the presence of a $-NH_2$ group from ATA, whose bands appear at 3431 and 3312 cm^{-1}.

2.1.2.2.2 PXRD Analysis

The PXRD diffractograms was traced for the reported MOFs, **UiO-66** and **MOF1**. It was not possible to trace the PXRD for **UiO-66-NH_2** and **MOF 2**, due to the lack of material quantity.

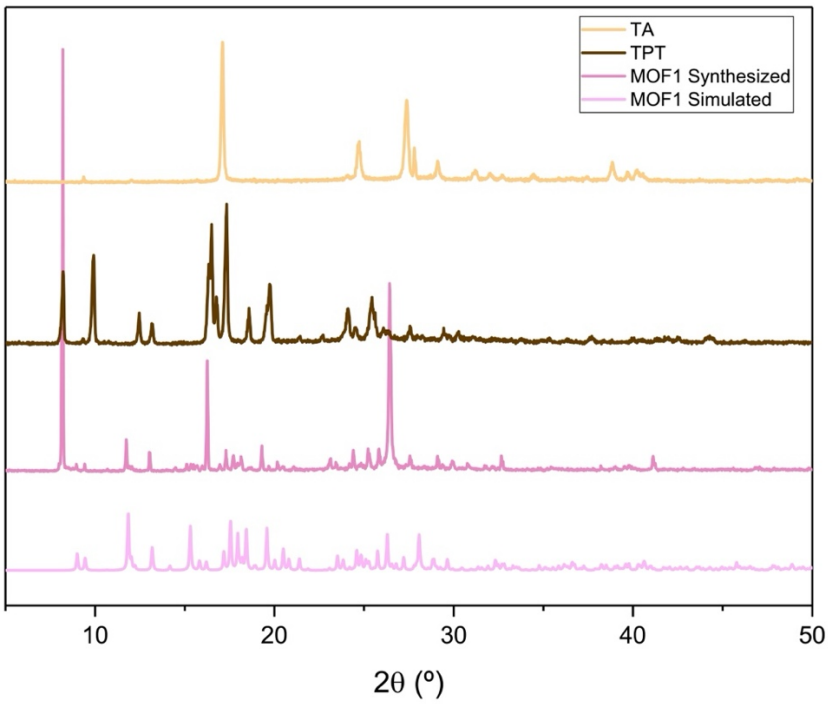

Figure 32. PXRD for **MOF1** simulated, **MOF1** synthesized and their ligands' diffractograms.

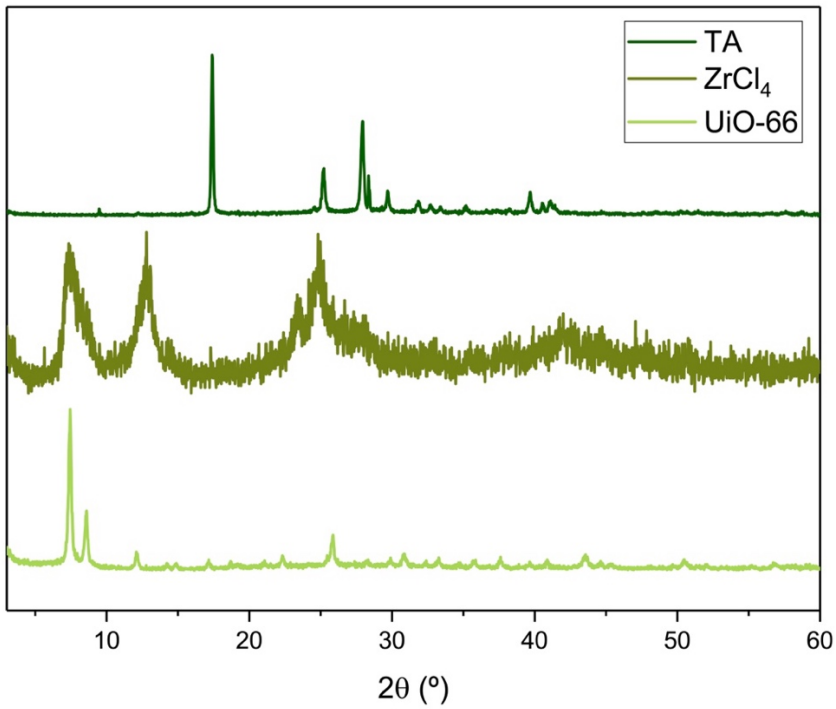

Figure 33. Comparison between PXRD data from **UiO-66** and the reagents.

In **Figure 32**, we can see both the PXRD diffractograms for **MOF1** simulated (lighter pink, bottom) and the synthesized **MOF1** (darker pink, top), while in **Figure 33**, we can observe the diffractogram for **UiO-66** in comparison to $ZrCl_4$ and TA, the precursors, and in **Figure 33** the same for **MOF1** compared to TPT and TA.

As observable, some of the peaks present in the simulated **MOF1** are not visible or are represented less intensely in the synthesized MOF1. The sample of **MOF1** used for the PXRD and photocatalysis can justify this difference, as it was used a less crystalline sample (more microcrystalline) instead of the bigger, higher quality crystals sample.

The **UiO-66** has peaks from 7º to 56º, with unique intense peaks at 7.45º, 12.08º, 22.40º and 50.46º. There are peaks belonging to TPT at 8.57º, 17.11º, 25.84º, 30.80º, 43.44º and 45.38º and some belonging to TA at 28.28º, 29.88º, 39.63º and 40.79º. According to the literature, the characteristic peaks for **UiO-66** are the 7.2º, 8.5º, 14.1º, 14.7º and 25.5º corresponding to the lattice planes (111), (200), (311), (222) and (600), respectively [116].

However, there was no previous report of a PXRD analysis for **MOF1**, so the comparison can only be established with the ligands, namely the TPT as the ZnI_2 is hygroscopic. **MOF1** has unique and good-sized peaks at 11.91º, 18.05º, 19.65º, 20.55º, 22.57º, 26.33º, 29.93º, 30.61º and 42.01º, and two around 50º at 48.05º and 55.50º with lower intensity. TPT matches the peaks at 8.22º, 13.24º, 16.54º 17.60º, 24.88º and 25.72º, while TA matches the ones at 28.13º, 29.69º, 31.47º and 33.38º. As we don't had access to the PXRD for ZnI_2, no further conclusions can be taken about matching peaks.

2.1.2.2.3 UV-Vis DRS Analysis

UV-Vis diffuse reflectance spectroscopy records the light reflected from the sample, as solids reflect two types of light when a monochromatic light is applied: the specular reflected light and the diffuse reflected light. The spectrophotometer detects both types and the reflectance obtained is the ratio between the intensity of the reflected light by the sample and by the standard. The standard used is usually barium sulfate ($BaSO_4$), as it has a transmittance close to 100%. This technique is generally used for materials and nanocomposites with surfaces that are not completely smooth and reflective.

After the obtention of the relative diffuse reflectance (r) spectra, the Kubelka-Munk transformation was applied, as to acquire a way to correlate the absorption with the diffuse reflectance, using **Equation 2**.

$$f(K) = \frac{(1-R)^2}{2R} = \frac{K}{S}$$

Equation 2. Kubelka-Munk function.

Where f(K) is the Kubelka-Munk function, R is absolute diffuse reflectance, K is the absorption coefficient and S is the scattering coefficient.

The UV-Vis DRS analysis of the materials was essential to have a prior idea of the wavelength range where each compound absorbs, before submitting the material to the hydrogen production system. The band gap was also calculated using Tauc's plot for each material.

The Transformed Kubelka-Munk function ($f(K)$) of the DRS spectra for **UiO-66** and **UiO-66-NH_2** are represented in **Figure 34**. The difference in color is easily observed, as the former is a white powder, and the latter has a brick-red tone.

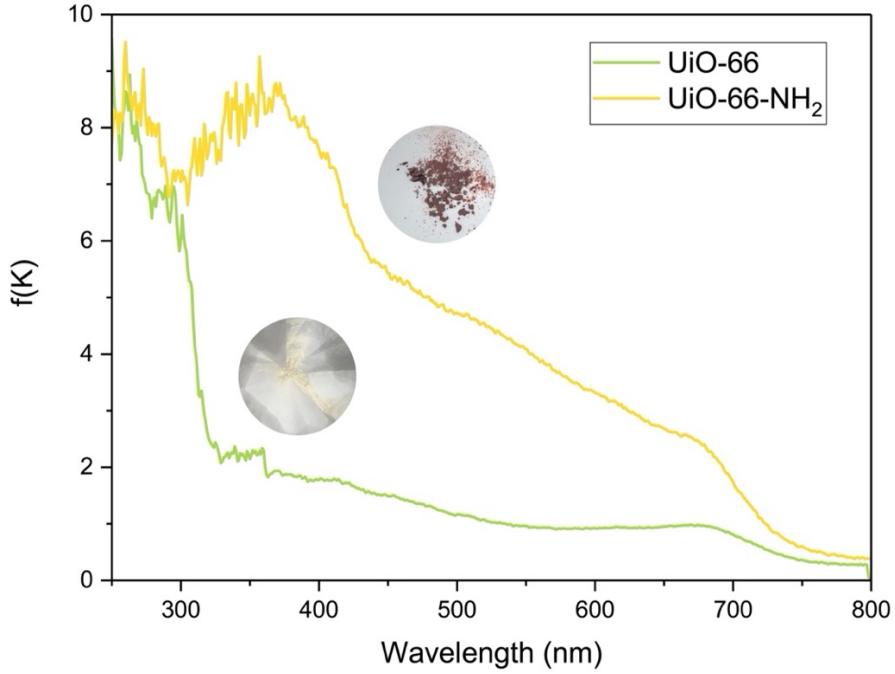

Figure 34. Transformed Kubelka-Munk UV-Vis DRS spectra for **UiO-66** and **UiO-66-NH₂**.

UiO-66 absorbs mostly in the UV range, with very low absorption in the visible zone, while **UiO-66-NH₂** absorbs in broader area, from the UV until the low region of the visible light (around 450 nm) and has a lower absorption until 670 nm.

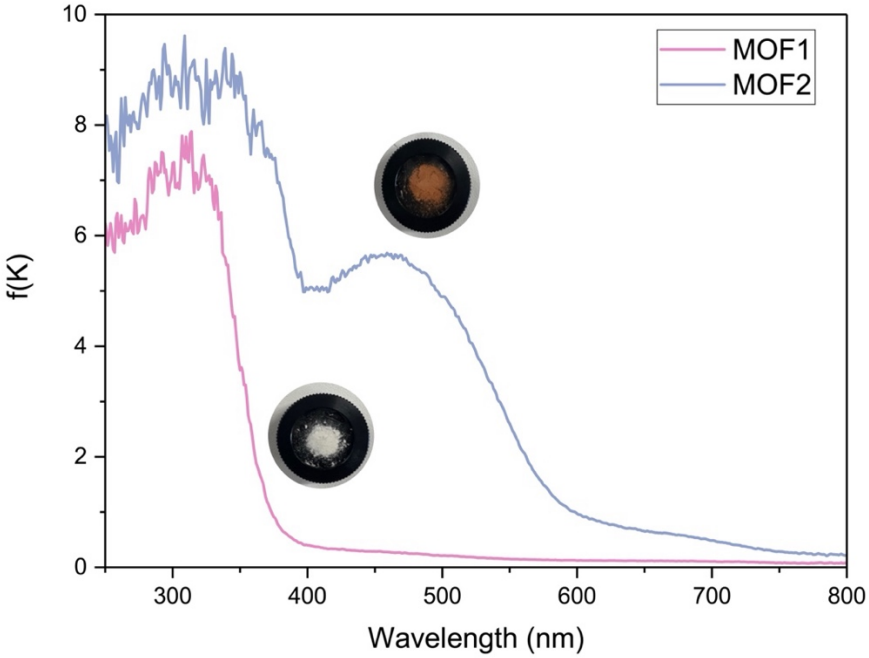

Figure 35. Transformed Kubelka-Munk UV-Vis DRS spectra for **MOF1** and **MOF2**.

In **Figure 35**, it is observable that **MOF1** absorbs from 250 to 380 nm – only in the UV range –, while **MOF2**, with its amine group, absorbs up to 600 nm, corresponding to the UV and visible areas.

In solid-state photochemistry, the band gap of a photocatalyst represents the energy range where no electronic states exist, corresponding to the energy necessary to promote an electron from the VB to the CB. Thus, it determines the photocatalyst's light absorption and its catalytic efficiency. Ideally, a semiconductor photocatalyst should have a band gap around 2.0 eV [117], so the electrons and holes can overcome kinetic barriers, but still be able to harvest majority of solar light. To obtain these values, the band gaps were calculated applying the Tauc's plot method to the DRS data.

After applying the Transformed Kubelka-Munk ($F(K)$), we obtained the values for $(F(K)h\nu)^2$ (in which h is the Planck constant and ν is the frequency) and traced a graph using those *versus* the energy (eV). In that graph, a tangent to the inflection point of the curve (corresponding to the minimum energy needed to excite an electron) is drawn until it reaches the horizontal axis. The point where those two meet gives the value of the band gap.

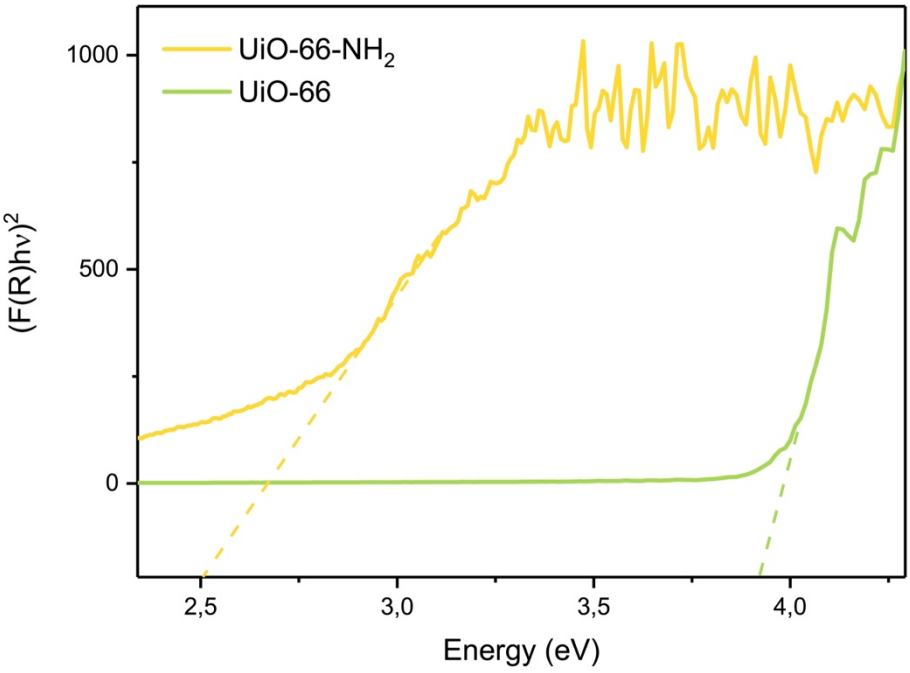

Figure 36. Tauc's plot for **UiO-66** and **UiO-66-NH$_2$**.

In the Tauc's plot (**Figure 36**) of $(f(R)hv)^2$ *vs.* energy (eV), we can extrapolate the values for the band gaps of **UiO-66** and **UiO-66-NH$_2$**, which are 3.92 eV and 2.50 eV, respectively, with **UiO-66-NH$_2$** being close to the ideal value. When comparing these values with Belver et coworkers' article [118], the value for **UiO-66-NH$_2$** is spot-on, but for **UiO-66** presents a slight shift of 0.10 eV. The difference between the amine-functionalized and normal MOF's values confirms that the NH_2 group narrows the band gap, thus instilling an enhancement of the photocatalytic activity.

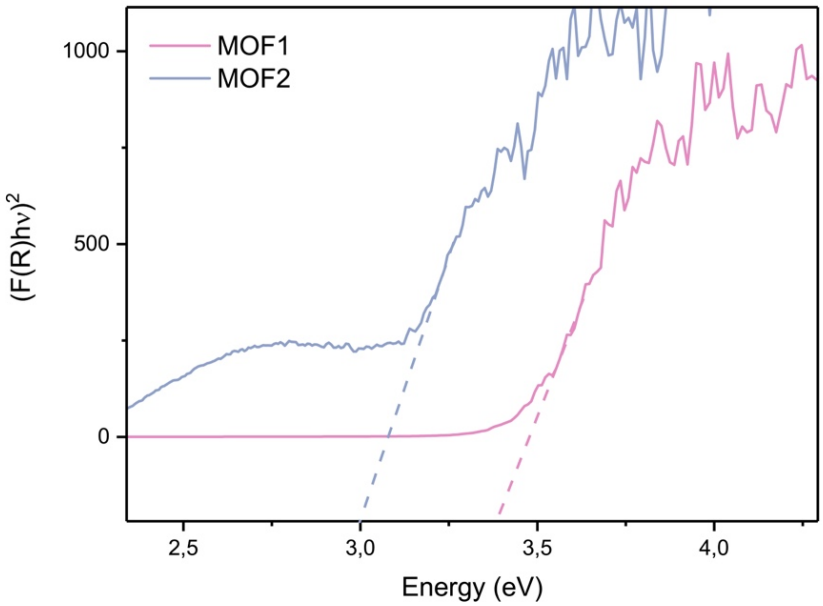

Figure 37. Tauc's plot for **MOF1** and **MOF2**.

For **Figure 37**'s Tauc's plot, the values for the band gaps are 3.34 eV for **MOF1** and 2.95 eV for **MOF2**. Again, we can see that the value for the amine-functionalized compound, **MOF2**, is much better and closer to ideal one, making it a better candidate as a photocatalyst for hydrogen production through water splitting. No literature values were found for these MOFs, as they were never tested for photocatalyzed hydrogen production.

To sum up, in **Table 1**, are represented the values obtained for each MOF and the literature values.

Table 1. Band gaps for the reported MOFs.

Material	Experimental Band Gap Value (eV)	Literature Band Gap Value (eV)
UiO-66	3.92	3.82
UiO-66-NH_2	2.50	2.50
MOF1	3.34	--
MOF2	2.95	--

2.1.2.2.4 SCXRD Analysis

The SCXRD analysis can only be performed when reasonable sized, high-quality crystals are formed, as mentioned above. Thus, those were only obtained for the Zn-MOFs, since

the Zr-MOFs, **UiO-66** and its amine-functionalized derivative, only yielded microcrystalline powders.

The crystals for Fujita's sponge were obtained using the diffusion layering technique, where a dissolved ligand is layered carefully with the metal salt dissolved in a different but miscible solvent at room temperature. For **MOF1** and **MOF2**, the crystals were obtained using the hydrothermal synthesis method, where crystals are formed in aqueous media at high temperatures and high vapor pressures.

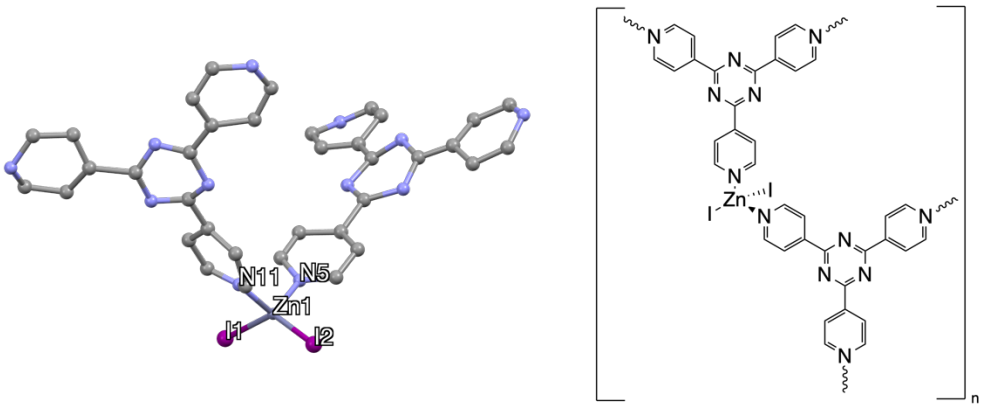

Figure 38. Mercury representation of Fujita's sponge (left), with hydrogen atoms and chloroform molecules omitted for clarity, and its structural representation (right).

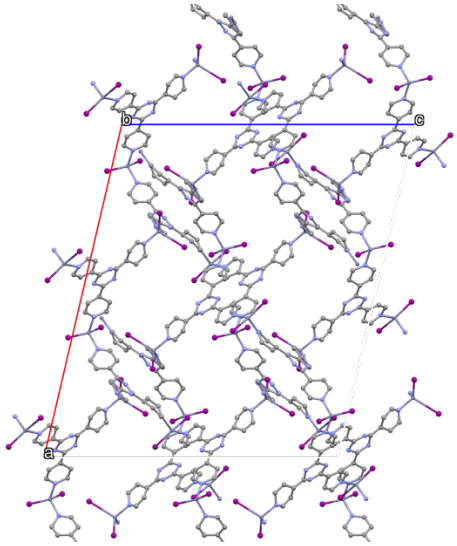

Figure 39. Mercury representation of the packing for Fujita's sponge along the *b*-axis.

Fujita's MOF (**Figure 38**) is very well-known, especially to use in the CSM, and it was obtained through diffusion layering. This crystalline framework crystallized in the monoclinic system, *C*2/c space group. The zinc metal center is connected to two TPT ligands and two iodides, conferring a distorted tetrahedral geometry around the metal center, as shown in **Table 2**, where the selected angles are different from the expected 109.5°. the expected value for a pure tetrahedral geometry. **Figure 39** shows its packing along the *b*-axis, highlighting its

pores, where guest compounds can be encapsulated thus allowing the material to perform as a crystalline sponge.

Table 2. Selected bond lengths and angles for Fujita's sponge.

Fujita's Sponge			
Bond Length (Å)		**Angles (°)**	
Zn-N^5 **Zn-N^{11}**	2.0208 2.0532	**I^1-Zn-N^5** **I^1-Zn-N^{11}** **I^2-Zn-N^5** **I^2-Zn-N^{11}**	94.85 101.29 112.59 103.05
Zn-I^1 **Zn-I^2**	2.4769 2.2359	**I^1-Zn-I^2** **N^{11}-Zn-N^5**	130.95 114.04

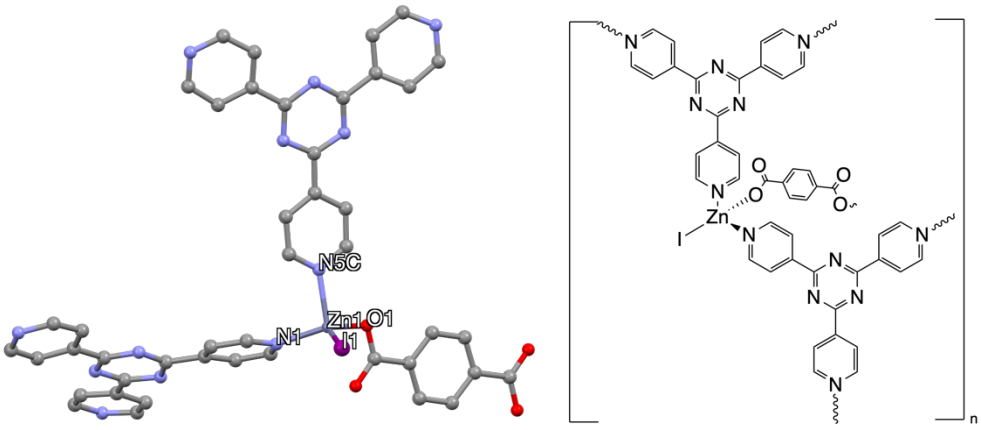

Figure 40. Mercury representation of **MOF1** (left), with hydrogen atoms omitted for clarity, and its structural representation (right).

MOF1 originated colorless block crystals from a hydrothermal synthesis. **Figure 40** shows the asymmetric unit of **MOF1** – a coordination polymer –, which crystallized in the monoclinic system, $P2_1/n$ space group. The asymmetric unit shows zinc as the metal center connected to two TPTs, one TA and an iodide atom. This molecule has a slightly distorted tetrahedral geometry, due to its angles not being exactly 109.5°, but not differing by much (**Table 3**).

Table 3. Selected bond lengths and angles for **MOF1**.

MOF1			
Bond Lengths (Å)		**Angles (º)**	
Zn-N^{1}	2.052(4)	**I^{1}-Zn-N^{1}**	114.6(1)
Zn-N^{5C}	2.090(4)	**I^{1}-Zn-N^{5C}**	105.3(1)
Zn-O^{1}	1.933(3)	**O^{1}-Zn-N^{1}**	115.3(1)
Zn-I^{1}	2.5313(8)	**O^{1}-Zn-N^{5C}**	96.7(1)
C^{19}-O^{1}	1.276(6)	**N^{1}-Zn-N^{5C}**	100.3(1)
C^{19}-O^{2}	1.226(7)	**I^{1}-Zn-O^{1}**	119.8(1)

Also, the carboxylic groups from the TA molecule could have localized (C=O and C-O^{-}) or delocalized ([O-C-O]$^{-}$) bonds. The table above shows that the value for the C=O (C-O^{2}) is higher than for the C-O^{1} connected to the metal, therefore, we can conclude that the bonds are localized.

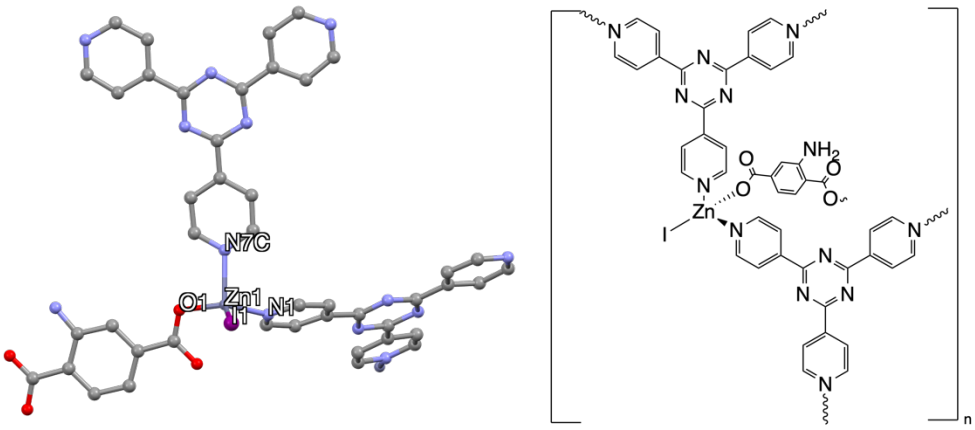

Figure 41. Mercury representation of **MOF2** (left), with hydrogen atoms omitted for clarification, and its structural representation (right).

MOF2 was synthesized through solvothermal methods and yielded red block crystals forming a coordination network (**Figure 41**). The zinc center is connected to two TPT, an ATA and an iodide in a distorted tetrahedral geometry configuration, as observable in the angle values reported on **Table 4**. The compound also crystalized in monoclinic system, but in the standard setting of the $P2_1/n$ space group seen in **MOF1** – the $P2_1/c$ space group.

Table 4. Selected bond lengths and angles for **MOF2**.

MOF2			
Bond Lengths (Å)		**Angles (º)**	
Zn-N^{1} **Zn-N^{7C}**	2.052(6) 2.087(6)	**I^{1}-Zn-N^{1}** **I^{1}-Zn-N^{7C}**	113.4(2) 106.6(2)
Zn-O^{1} **Zn-I^{1}**	1.936(7) 2.525(1)	**O^{1}-Zn-N^{1}** **O^{1}-Zn-N^{7C}**	117.2(2) 96.1(2)
C^{17}-O^{1} **C^{17}-O^{2}**	1.25(1) 1.24(1)	**N^{1}-Zn-N^{7C}** **I^{1}-Zn-O^{1}**	100.4(2) 118.7(2)

The carboxylic acid bonds in this compound have similar values, thus the bonds are delocalized.

As these compounds are candidates for application as crystalline sponges, the pore sizes were evaluated, coming to the conclusion that both **MOF1** and **MOF2** are microporous materials, suggesting that their use as crystalline sponges will be unsuccessful.

2.1.2.3 New Materials Synthesized

The materials synthesized were attributed a designation according to the metal (A for zinc and B for zirconium), according to the ligands used (1, 2, 3, 4, …) and according to the method and proportions used in that specific synthetic attempt (a, b, c, …). The attribution given to an attempt does not indicate that a new material was synthesized, some originated only reagents, which is discussed below the data confirming that fact.

2.1.2.3.1 Synthesis of New Materials

The objective of this work is not only the application of MOFs, but also the synthesis of new ones, if achievable, as MOFs are not the easiest of materials. Both Zn- and Zr-materials were synthesized.

Therefore, we made several attempts to obtain new MOFs, using Fujita's technique and proportions as inspiration, following the tables below. The green squares on the table indicate that the ligand was used in the synthesis of the corresponding compound, while the red squares indicates that it wasn't used. The compounds reference is represented in the left column and the ligands in the top line of the table.

Table 5. Synthesis of materials with ZnI_2 as the metal source.

Compound/Ligand[1]	TPT	BDC	bipy	TA	ATA	L1	L2	L3	L5	L6	Result
A1											**Fujita's Sponge**
A2											**MOF1**
A3											**MOF2**
A4											
A5											
A6											
A7											
A8											

[1] The ligands used for each material synthesis are represented in green, while the ligands not used for in that material are represented in red.

The synthesis attempts for the formation of the new materials were performed through various methods, such as conventional solution-based, mechanochemistry, solvo- and hydrothermal, and microwave-assisted reactions.

A1, **A2** and **A3** were described in section **2.1.2 Reported MOFs**. For the obtention of compound **A4** hydrothermal, microwave-assisted, diffusion layering and mechanochemistry methods were used, with the conditions represented in **Table 6**.

Table 6. Methods and conditions for the synthesis of **A4**.

Method	$n(ZnI_2)$ (mmol)	n(TPT) (mmol)	n(L2) (mmol)	T (°C)	Solvent(s)	Time	Physical Appearance
Hydrothermal	0.35	0.20	0.15	160	H_2O	72H	Beige microcrystalline powder **A4a**
Solvothermal	0.35	0.20	0.15	120	DMF	72H	White powder **A4b**
Microwave-assisted	0.35	0.20	0.15	140	H_2O	30 min.	White powder **A4c**

Diffusion Layering	0.15	0.08	0.08	r.t.	No	1H	Pale yellow powder **A4d**
Mecanochemistry	0.35	0.20	0.15	r.t.	No	1H	Bright yellow powder **Mix**

The hydrothermal (**A4a**), solvothermal (**A4b**) and microwave-assisted (**A4c**) methods were the most efficiently used for the synthesis of **A4**. The difference between the hydro and solvothermal route was the solvent and temperature of the oven. We couldn't get any crystals from the diffusion layering and the precipitate was only a mixture of reagents. The mechanochemistry attempt originated a yellow powder, corresponding to a physical mixture of the reagents.

To obtain **A5**, the conditions in **Table 7** were followed.

Table 7. Methods and conditions for the synthesis of **A5**.

Method	**n(ZnI_2) (mmol)**	**n(TPT) (mmol)**	**n(BDC) (mmol)**	**T (°C)**	**Solvent(s)**	**Time**	**Physical Appearance**
Hydrothermal	0.35	0.20	0.15	160	H_2O	72H	Eggshell white powder **A5a**
Microwave-assisted	0.35	0.20	0.15	140	H_2O	30 min.	White powder **A5b**
Microwave-assisted	0.15	0.08	0.08	140	DMF	20 min.	White powder **A5c**

All the samples originated from the synthetic methods were white, as well as all the reactants. Therefore, the characterization methods were fundamental to determine what was formed, as no visual clue was given.

Table 8. Methods and conditions for the synthesis of **A6**.

Method	n(ZnI_2) (mmol)	n(TPT) (mmol)	n(L5) (mmol)	T (°C)	Ultra-sounds	Sol-vent(s)	Time	Physical Appearance
Sol-vother-mal	1	0,5	0,25	120	Yes	DMF	24H	**TPT**
Hydro-thermal	1	0.5	0.25	160	Yes	H_2O	24H	Microcrys-talline pow-der **A6a**
Hydro-thermal	1	0.5	0.25	160	Yes	H_2O	48H	White pow-der **A6b**
Hydro-thermal	1	0.5	0.25	145	Yes	H_2O	36H	Yellowish powder **A6c**
Micro-wave-as-sisted	0.24	0.12	0.06	140	Yes	DMF	30 min.	**TPT**
Micro-wave-as-sister	0.24	0.12	0.06	140	Yes	H_2O	45 min.	Brown solid **A6d**

Our attempts to synthesize the **A6** compounds gave different sample aspects, so a careful analysis of the characterization techniques is important. The expected product is reported to be obtained through the microwave-assisted method using distilled water as a solvent with sonification and a hold-time of 45 minutes at 140°C.

Table 9. Methods and conditions for the synthesis of **A7**.

Method	n(ZnI_2) (mmol)	n(L5) (mmol)	T (°C)	Ultra-sounds	Sol-vent(s)	Time	Physical Appearance
Layering	0.10	0.20	r.t.	No	MeOH / DMF	72H	Yellowish crystals
Layering	0.10	0.20	r.t.	No	MeOH / $CHCl_3$	72H	**L5**

Heating	0.20	0.15	130	Yes	DMF/ NMP	72H	Dark brown powder **A7a**

The synthesis of these **A7** compounds was obtained through diffusion layering only but using different solvents, and through high pressure and temperature heating. The layering using the MeOH/DMF solvent system produced yellow block crystals in 1 out of 4 tubes, which we tried to analyze by SCXRD. The analysis was not completed due to a complication: when the time came to place the loop in the machine, the crystals would "jump" out, as it was not possible to fix them in the loop. In the heating procedure, the compound originated, **A7a**, is amorphous when analyzed by PXRD, but presents a FTIR spectrum different from the reagents.

Compounds **A8** were synthesized following the conditions in **Table 10**.

Table 10. Methods and conditions for the synthesis of **A8**.

Method	**n(ZnI_2) (mmol)**	**n(L6) (mmol)**	**T (°C)**	**Ultra-sounds**	**Sol-vent(s)**	**Time**	**Physical Appearance**
Layering	0.1	0.2	r.t.	Yes	MeOH / $CHCl_3$	72H	**L6**

Various attempts to obtain **A8** through diffusion layering were made, performing modifications to the synthesis to try to obtain crystals. In one of the experiments, the chloroform solution of **L6** was heated, sonicated and filtered, while in other, the solution was heated, sonicated and triethylamine was added. These procedures didn't originate crystals, and the obtained powders corresponded to **L6**.

Table 11. Synthesis of materials with $Zn(OTf)_2$ as the metal source.

Ligand[1]	**TPT**	**BDC**	**bipy**	**TA**	**ATA**	**L1**	**L2**	**L3**	**L5**	**L6**	**Result**
A9											**MOF3**
A10											
A11											
A12											

[1] The ligands used for each material synthesis are represented in green, while the ligands not used for in that material are represented in red.

A9's methods and conditions are described in **Table 12**.

Table 12. Methods and conditions for the synthesis of **A9**.

Method	n(Zn(OTf)$_2$) (mmol)	n(TPT) (mmol)	T (°C)	Solvent(s)	Time	Physical Appearance
Layering	0.03	0.02	r.t.	MeOH/ $CHCl_3$	72H	Colorless Crystals **MOF3&A9a&A9b**

The synthesis using **A9**'s reagents was all performed by diffusion layering, but two different compounds were obtained: a new MOF (**MOF3**) – $[Zn(TPT)_3(OTf)_2]_n$ – and a cationic complex with two different polymorphs (**A9a** and **A9b**) with the same synthesis conditions. X-ray diffraction data were collected for structural determination for each derivative.

Table 13. Methods and conditions for the synthesis of **A10**.

Method	n(Zn(OTf)$_2$) (mmol)	n(TPT) (mmol)	n(L2) (mmol)	T (°C)	Solvent(s)	Time	Physical Appearance
Layering	0.15	0.08	0.08	r.t.	MeOH/ $CHCl_3$	72H	Yellow powder **A10a**
Solvothermal	0.30	0.15	0.15	120	DMF	72H	Brown solid **A10b**
Hydrothermal	0.90	0.45	0.45	160	H_2O	72H	Brown microcrystalline solid **A10c**

For the synthesis of the **A10** compounds, three methods were trialed to obtain a new MOF (**Table 13**). The solvothermal and hydrothermal present different results in the FTIR analysis, one presenting the iminic band from the **L2** ligand, while the other did not. The layering compound did not form crystals, but a powder was deposited at the bottom, which was later analyzed and gave some interesting results.

Table 14. Methods and conditions for the synthesis of **A11**.

Method	n(Zn(OTf)$_2$) (mmol)	n(L5) (mmol)	T (°C)	Ultra-sounds	Sol-vent(s)	Time	Physical Appearance
Micro-wave-as-sisted	0.30	0.30	120	Yes	H_2O	30 min.	Yellow solid **A11a**
Layering	0.10	0.10	r.t.	No	MeOH /DMF	72H	Greenish yellow solid **A11b**
Layering	0.10	0.10	r.t.	No	MeOH / $CHCl_3$	72H	Yellowish brown solid **A11c**

From these attempts (**Table 14**), two different FTIR spectra were obtained, and the same happened for the microwave-assisted material, concluding with the obtention of three distinct materials.

Table 15. Methods and conditions for the synthesis of **A12**.

Method	n(Zn(OTf)$_2$) (mmol)	n(L6) (mmol)	T (°C)	Sol-vent(s)	Time	Physical Appearance
Layering	0.10	0.20	r.t.	MeOH/ DMF	72H	Dark pow-der **A12**

A12 was only synthesized using the diffusion layering methodology. Some tubes had diethyl ether added to them to see if any crystals were formed, but unfortunately, none did. When left to dry at open air, microcrystalline powder precipitated, allowing us the possibility to characterize it through FTIR and PXRD.

Table 16. Synthesis of materials with $Zn(NO_3)_2$ as the metal source.

Ligand[1]	TPT	BDC	bipy	TA	ATA	L1	L2	L3	L5	L6	Result
A13											
A14											
A15											
A16											
A17											

[1] The ligands used for each material synthesis are represented in green, while the ligands not used for in that material are represented in red.

Exchanging the metal source to $Zn(NO_3)_2$, the synthesis of five new compounds was attempted.

Table 17. Methods and conditions for the synthesis of **A13**.

Method	n(Zn(NO$_3$)$_2$) (mmol)	n(TPT) (mmol)	T (°C)	Solvent(s)	Time	Physical Appearance
Layering	0.20	0.15	r.t.	MeOH/$CHCl_3$	72H	Colorless crystals
Hydrothermal	0.38	0.19	160	H_2O	72H	Clear solution

A13 was synthesized through diffusion layering using a system of MeOH/$CHCl_3$ and by hydrothermal synthesis. The latter originated a clear solution that, after evaporation, didn't yield any precipitate.

Table 18. Methods and conditions for the synthesis of **A14**.

Method	n(Zn(NO$_3$)$_2$) (mmol)	n(TPT) (mmol)	n(ATA) (mmol)	T (°C)	Ultrasounds	Solvent(s)	Time	Physical Appearance
Hydrothermal	0.38	0.30	0.12	160	No	H_2O	72H	Light brown microcrystalline solid **A14a**
Hydrothermal	1.10	0.78	0.42	160	No	H_2O	72H	Light brown solid **A14b**

Micro-wave-assisted	0.34	0.17	0.08	140	No	H_2O	30 min.	Light pink solid **A14c**
Layer-ing	0.18	0.09	0.08	r.t.	No	MeOH / $CHCl_3$	72H	Dark pink solid **A14d**
Heat-ing	0.20	0.10	0.10	130	Yes	DMF / NMP	48H	Brown solid **A14e**
Heat-ing	0.30	0.15	0.08	110	Yes	DMF / H_2O	72H	Light pink solid **A14f**

Using four different techniques, the preparation of **A14** was attempted. All the hydrothermal attempts generated a solid with the same aspect, even with the changing ratios, but gave different FTIR spectra.

Table 19. Methods and conditions for the synthesis of **A15**.

Method	**n(Zn(NO_3)$_2$) (mmol)**	**n(ATA) (mmol)**	**T (°C)**	**Sol-vent(s)**	**Time**	**Physical Appearance**
Sol-vother-mal	1.73	1.73	120	DMF	72H	White pow-der **A15a**
Sol-vother-mal	1.73	1.73	120	DMF	72H	White pow-der **A15b**

The synthesis of **A15** was only tried through solvothermal method twice, originating two compounds with different characterization but very similar in appearance.

Table 20. Methods and conditions for the synthesis of **A16**.

Method	n(Zn(NO$_3$)$_2$) (mmol)	n(bipy) (mmol)	n(ATA) (mmol)	T (°C)	Sol-vent(s)	Time	Physical Appearance
Sol-vother-mal	1.73	0.87	0.87	160	H_2O	72H	Light brown solid **A16**
Layering	0.10	0.10	0.10	r.t.	H_2O/ MeOH/ EtOH	72H	**ATA**

A16's synthesis was not successful in obtaining the desired material, but it gave us an amorphous material through solvothermal synthesis. The layering did not work in this system, as the 2-aminoterephthalic acid precipitated after only a few minutes.

Table 21. Methods and conditions for the synthesis of **A17**.

Method	n(Zn(NO$_3$)$_2$) (mmol)	n(bipy) (mmol)	n(L1) (mmol)	T (°C)	Sol-vent(s)	Time	Physical Appearance
Layering	0.20	0.10	0.10	r.t.	H_2O/ MeOH/ EtOH	72H	Orange crystals

A17 yielded orange crystals at the bottom of the tube by diffusion layering, but there was not a chance to analyze them through SCXRD.

Table 22. Synthesis of materials with $ZnCl_2$ as the metal source.

Lig-and[1]	TPT	BDC	bipy	TA	ATA	L1	L2	L3	L5	L6	Result
A18											
A19											

[1] The ligands used for each material synthesis are represented in green, while the ligands not used for in that material are represented in red.

A few attempts to get a MOF were also performed with $ZnCl_2$ as the metal source, but it proved to be harder to work with than the other three, so only two combinations were performed.

Table 23. Methods and conditions for the synthesis of **A18**.

Method	n($ZnCl_2$) (mmol)	n(ATA) (mmol)	T (°C)	Sol-vent(s)	Time	Physical Appearance
Layering	0.20	0.10	r.t.	H_2O/ MeOH	72H	**ATA**
Micro-wave-as-sisted	0.60	0.60	140	DMF	30 min.	Dark brown solid **A18a**
Micro-wave-as-sisted	0.60	0.60	160	H_2O	30 min.	**ATA**

A18 was synthesized through diffusion layering and microwave-assisted methods, the latter twice: once in DMF and another in H_2O, which didn't achieve the desired product since it was only ATA. The layering also didn't yield anything other than ATA at the bottom of the tubes.

Table 24. Methods and conditions for the synthesis of **A19**.

Method	n($ZnCl_2$) (mmol)	n(bipy) (mmol)	n(ATA) (mmol)	T (°C)	Sol-vent(s)	Time	Physical Appearance
Layering	0.1	0.20	0.10	r.t.	H_2O/ MeOH/ EtOH	72H	Brown crys-tal
Micro-wave-as-sisted	0.56	0.28	0.42	120	DMF	30 min.	Orange powder **A19a&A19 b**

Compound **A19** was synthesized by diffusion layering and microwave-assisted techniques. Small and low-quality crystals were obtained using the first method and it was not possible to analyze them by SCXRD, while when using the microwave, a white powder was obtained through filtration and an orange powder precipitated in the washed phases. Both compounds have different FTIR data.

Table 25. Synthesis of materials with $ZrCl_4$ or $ZrOCl_2$ as the metal source.

Ligand[1]	TPT	BDC	bipy	TA	ATA	L1	L2	L3	L5	L6	Result
B1											
B2											
B3											
B4											
B5											
B6											

[1] The ligands used for each material synthesis are represented in green, while the ligands not used for in that material are represented in red.

The obtention of Zr-MOFs was also attempted, using the same methods as those applied to the zinc ones. The synthesis of **B1** and **B2** is described in subchapter **2.3. Reported MOFs**.

Table 26. Methods and conditions for the synthesis of **B3**.

Method	n($ZrCl_4$) or n($ZrOCl_2$) (mmol)	n(bipy) (mmol)	n(ATA) (mmol)	T (°C)	Solvent(s)	Time	Physical Appearance
Solvothermal	2.00	1.00	1.00	120	DMF	72H	Brick red solid **B3a**
Microwave-assisted	0.60	0.60	0.60	120	DMF + Acetic Acid + 37% HCl	30 min.	Light brown powder **B3b**
Microwave-assisted	0.50	0.25	0.25	100	DMF + 37% HCl	30 min.	Peach powder **B3c**
Microwave-assisted	0.50	0.25	0.25	140	H_2O + 37% HCl	30 min.	Colorless block crystals **B3d**
Layering	0.05	0.05	0.05	r.t.	H_2O/ MeOH/ EtOH	72H	Yellow solid **B3e**

Mecha-nochem-istry	2.60	1.30	1.30	r.t.	-	2H	Purplish powder **B3f**

The synthesis of **B3** was performed by almost all the techniques: diffusion layering, microwave-assisted, mechanochemistry and solvothermal. The solvothermal gave an orange gel, that was washed with DMF and DCM, originating a solid, which was analyzed by PXRD and FTIR. The microwave-assisted samples synthesized in DMF gave almost identical spectra, while the aqueous solution originated a clear orange solution, which was precipitated with a 1:1 diethyl ether/pentane and originated colorless block crystals, later analyzed by SCXRD and with a very different FTIR spectrum.

Table 27. Methods and conditions for the synthesis of **B4**.

Method	**n($ZrCl_4$) or n($ZrOCl_2$) (mmol)**	**n(ATA) (mmol)**	**n(L1) (mmol)**	**T (°C)**	**Sol-vent(s)**	**Time**	**Physical Appearance**
Layering	0.15	0.20	0.20	r.t.	Various	72H	Yellow sol-ids

B4 was synthesized by diffusion layering but using various combinations of solvents to try to obtain crystals. All the attempts originated either gels or a mixture of reagents. The combinations of the solvents were: **(1)** H_2O/MeOH/EtOH, **(2)** EtOH/MeOH, **(3)** H_2O/MeOH, **(4)** DMF/EtOH, **(5)** H_2O/EtOH, and **(6)** H_2O/DMF.

Table 28. Methods and conditions for the synthesis of **B5**.

Method	**n($ZrCl_4$) or n($ZrOCl_2$) (mmol)**	**n(TPT) (mmol)**	**n(L1) (mmol)**	**T (°C)**	**Sol-vent(s)**	**Time**	**Physical Appearance**
Layering	0.22	0.08	0.08	r.t.	MeOH/ $CHCl_3$	72H	Colorless needle crys-tals and yel-low solid

Due to the low quantity of **L1** synthesized, only diffusion layering was tried as the synthesis of this material, as it consumes less quantity than the other techniques. Only on one of the tubes crystals were formed, which appeared to be TPT, but it also had yellow powder at the bottom. In the other ones, only the TPT precipitated.

Table 29. Methods and conditions for the synthesis of **B6**.

Method	n($ZrCl_4$) (mmol)	n(L6) (mmol)	T (°C)	Ultra-sounds	Sol-vent(s)	Time	Physical Appearance
Micro-wave-as-sisted	0.45	0.45	120	Yes	H_2O + Acetic Acid	30 min.	Orange solid **B6a**
Layering	0.10	0.20	r.t.	No	MeOH/ $CHCl_3$	72H	Yellow solid **B6b**

The synthesis of this material was performed by two methods: diffusion layering and microwave-assisted. The microwave-assisted mixture was filtered and gave a microcrystalline fluffy solid, but, when it was washed with methanol, the compound dissolved, which meant it was not a MOF. A ^{1}H NMR was performed in DMSO, and the spectrum corresponded to 4-formylbenzoic acid, a precursor for **L6**. This means that during the microwave reaction the ligand decomposed into one of the reagents.

2.1.2.4 Characterization of New Materials

All the materials described here were characterized by FTIR and PXRD, and, when possible, ^{1}H NMR and SCXRD. For most compounds, no crystal was obtained, so the analysis and conclusions taken from the FTIR and PXRD spectra are merely speculative, as no definitive conclusion for the composition can be obtained.

2.1.2.4.1 Characterization of A4

The compound expected for **A4** is represented in **Figure 42** and they were characterized by FTIR spectroscopy and PXRD.

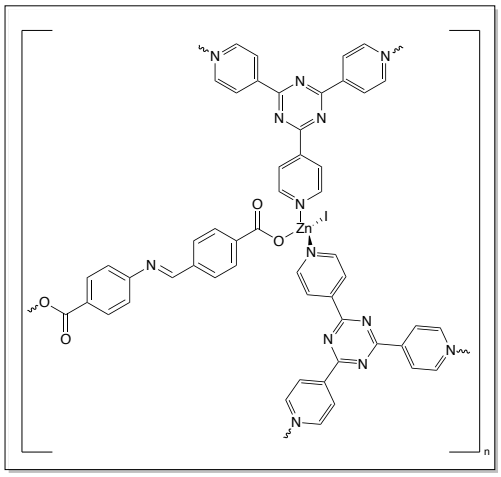

Figure 42. Expected structure for the **A4** compounds.

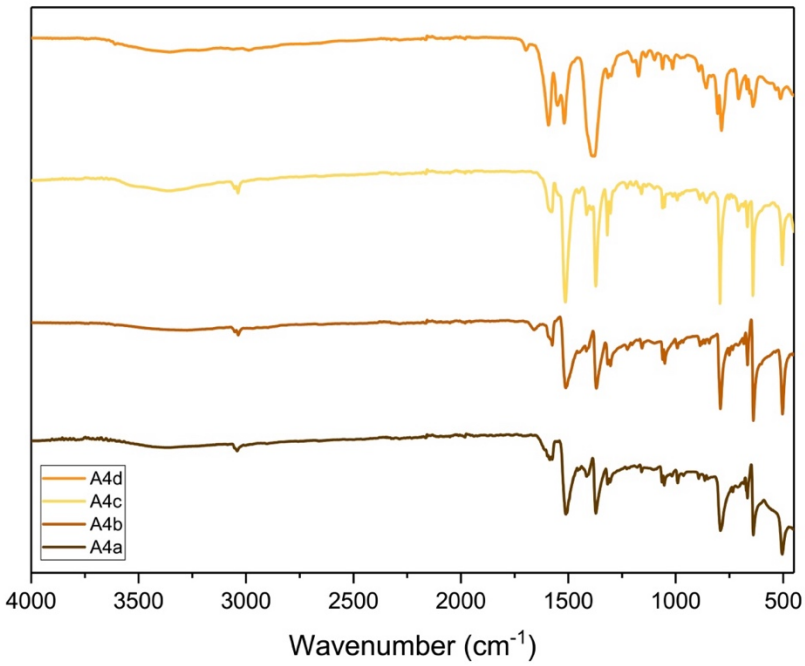

Figure 43. FTIR spectra for the synthesized **A4** compounds.

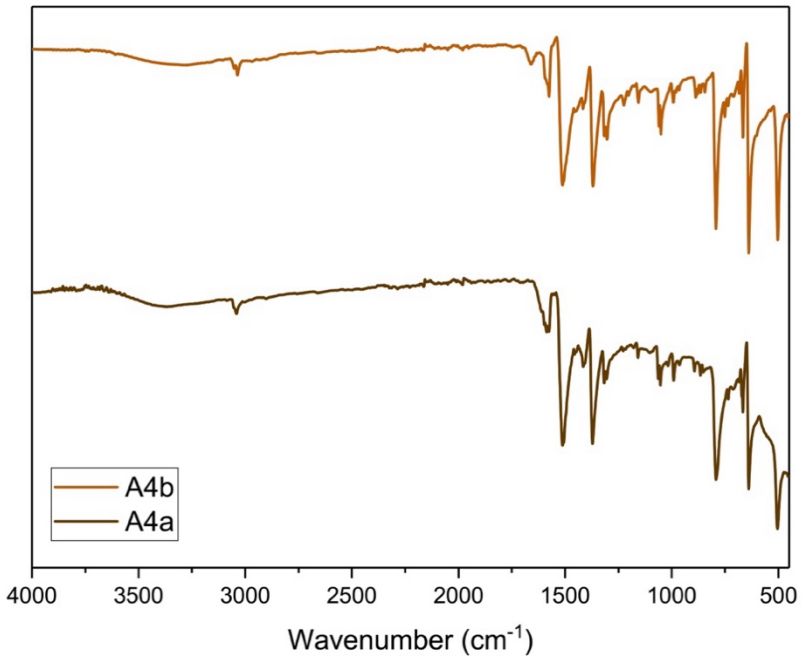

Figure 44. FTIR spectra for **A4a** (hydrothermal) and **A4b** (solvothermal).

The iminic C=N band appears in the **L2** at around 1630 cm^{-1}, but it usually appears in the 1690-1620 cm^{-1} range, so in the product it can deviate. In **Figure 43**, it is observable that the only band in this range is from the solvothermal compound, **A4b**, at 1658 cm^{-1}, which isn't very intense. In **A4a** (1603 and 1577 cm^{-1}), **A4b** (1590 and 1575 cm^{-1}) and **A4c** (1595 and 1575 cm^{-1}), the bands around 1605-1580 cm^{-1} are broad, so they can be attributed to two groups: the

C=O from the **L2**'s carbonyl group and the C-O asymmetric vibration, respectively, since there is no hydroxyl bands, indicating a bonding of **L2** to the metal. These three compounds also show the characteristic TPT bands at around 3030 cm^{-1}, which **A4d** doesn't. The C-O symmetric bands for compounds **A4a**, **A4b**, **A4c** and **A4d** appear at 1372, 1370, 1372 and 1380 cm^{-1}, respectively.

The Zn-O and Zn-N bands usually appear from 1000 to 450 cm^{-1}. We can see no new bands in the region for the hydrothermal **A4a** nor the solvothermal **A4b**, but we can observe the formation of some in the microwave-assisted **A4c** (856, 709 and 450 cm^{-1}) and diffusion layering **A4d** (708, 565, 525 and 450 cm^{-1}).

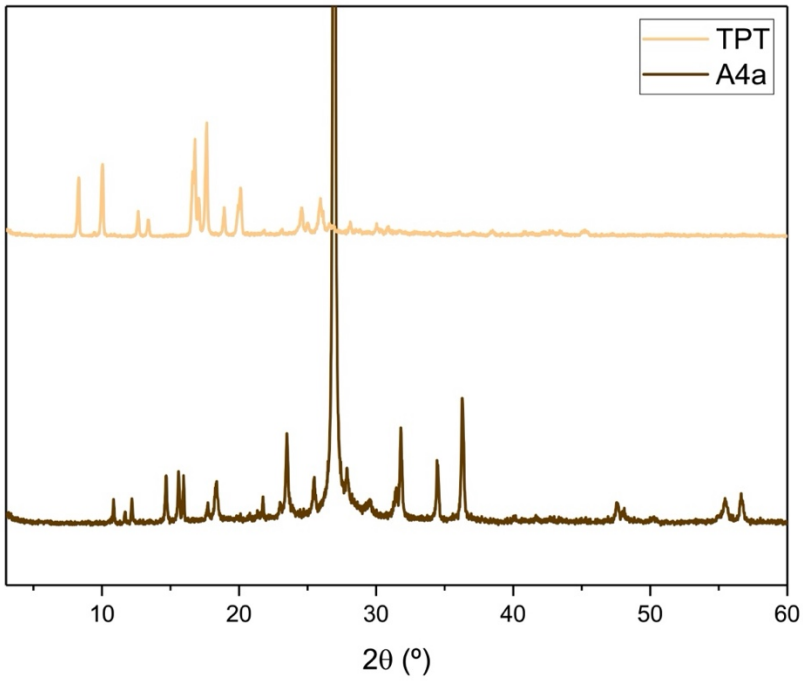

Figure 45. PXRD diffractogram for **A4a** in comparison with TPT ligand.

By the analysis of the PXRD (**Figure 45**), the sample of **A4a** is crystalline and differs a lot from the TPT's diffractogram, but this information cannot be confirmed for **L2** nor ZnI_2 as no data was possible to be collected due to lack of quantity or the need to use inert atmosphere for the measurement of ZnI_2, due to its high hygroscopicity. Usually, inorganic materials have peaks up to higher angles, closer to 60º, while in organic materials these are more visible at lower angles.

A4a has its most intense peaks at 23.49º, 27.10º, 31.80º and 36.29º and no peaks overlap with TPT's. This compound also has peaks after 40º at 47.59º, 48.02º, 55.50º and 56.63º, which indicates the presence of a metal.

PXRD data was not collected for **A4b**, **A4c** and **A4d** due to lack of time.

2.1.2.4.2 Characterization of A5

The expected structure for the **A5** is in **Figure 46** and, starting by the FTIR analysis, we could spot differences between the three samples, as observable in **Figure 47**.

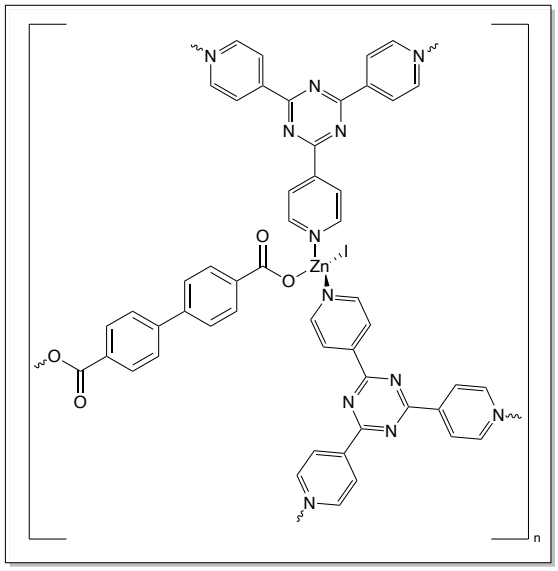

Figure 46. Expected structure for the **A5** compound.

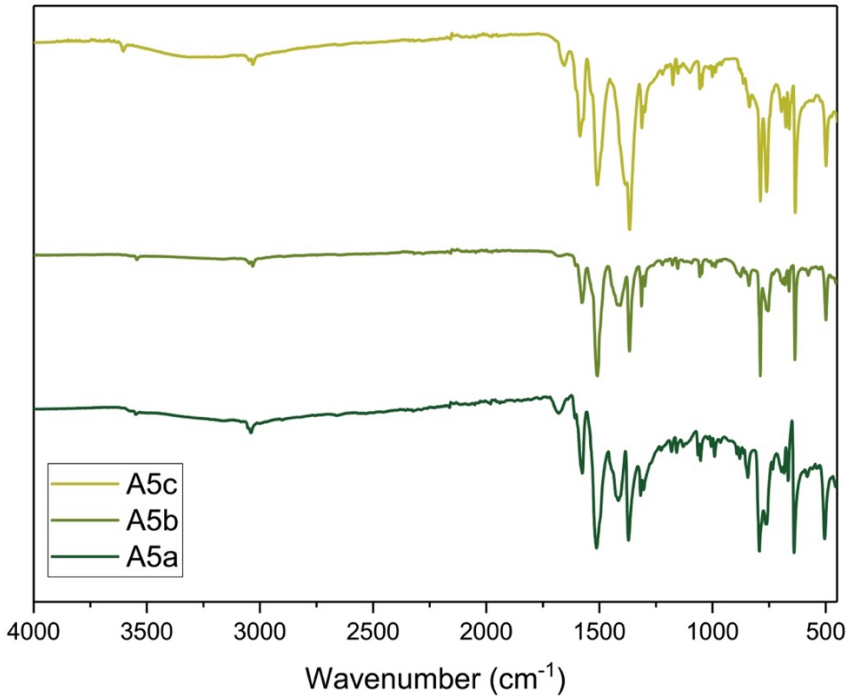

Figure 47. FTIR spectra for the **A5** compounds.

The BDC ligand does not have major defining bands due to their lack of substituents besides the carboxylic acid groups, so the presence of a C=O and C-O asymmetric and symmetric vibration bands are expected. All the compounds possess the characteristic 3040-3030 cm^{-1} bands from the TPT ligand, and all have the formation of a new band at around 3600-3540 cm^{-1}, more specifically, 3548, 3550 and 3610 cm^{-1} for **A5a**, **A5b** and **A5c**, respectively. ZnI_2 has a band in the 3600 cm^{-1} region. Therefore, we can confirm the presence of a Zn-I bond in the synthesized materials. As it is observable from **Figure 47**, the hydro microwave-assisted doesn't have a well-defined band at 1670-1660 cm^{-1}, while this is visible in the other two. This

band corresponds to the C=O from the carboxylic acids in the BDC ligand. The bands from 1590 to 1565 cm^{-1} correspond to the asymmetric C-O bond vibrations bound to the metal. From 1515-1510 cm^{-1}, the band represents both the C=C stretching vibrations from the benzene rings in BDC and the C=N stretching vibration from the TPT rings. The band at 1375-1360 cm^{-1} represents the C-O symmetric vibrations from the BDC. **A4a** and **A4b** have new bands in the 1000-450 cm^{-1} zone, while **A4c** does not have any. **A4a** has the new bands at 778, 584 and 453 cm^{-1} and **A4b** at 765, 581 and 458 cm^{-1}, probably corresponding to the Zn-O and Zn-N bond formation.

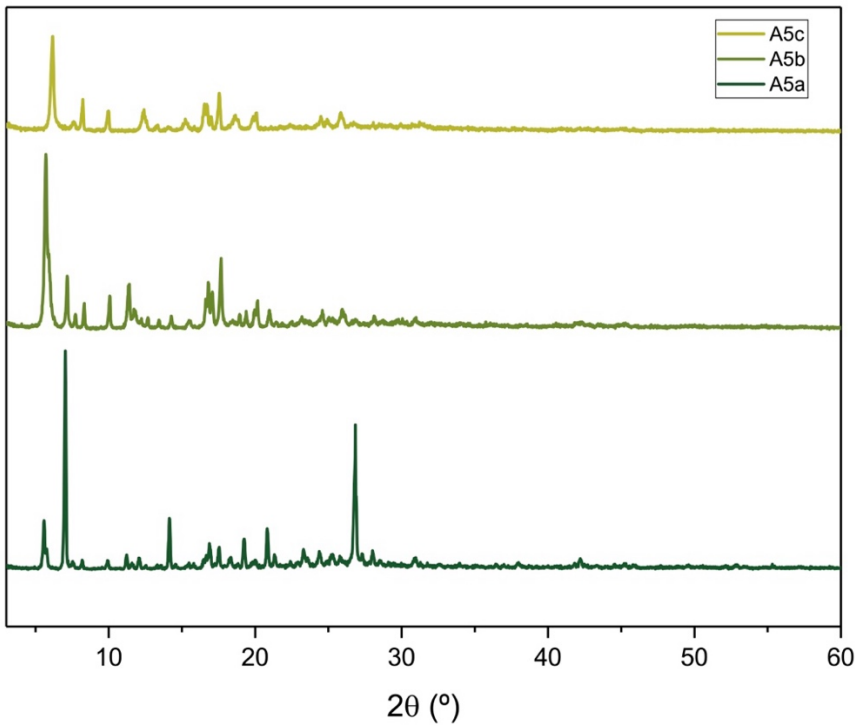

Figure 48. PXRD diffractogram for the **A5** compounds.

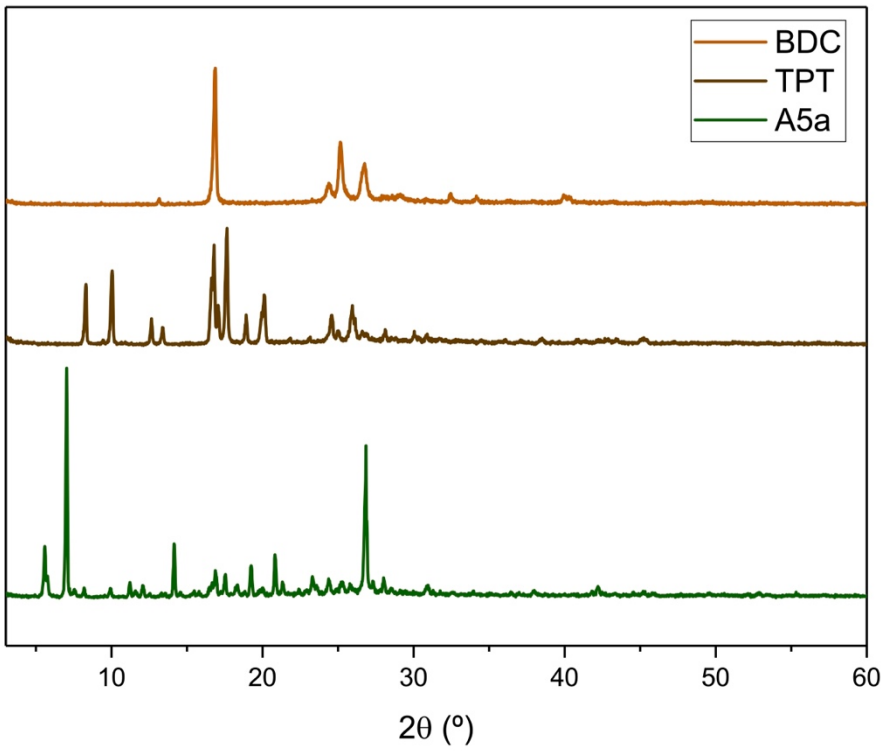

Figure 49. Comparison between PXRD data for **A5a** and reagents.

In the PXRD (**Figure 48**), we can confirm that all the samples are crystalline and so we went to confirm if they are a physical mixture of the reagents. In **Figure 49** is represented **A5a** in comparison to the reagents, except for ZnI_2. The other compounds' comparison is reported in the Annexes (**Figures A.74** and **A.75**).

Compound **A5a** has an easily observable new peak at 5.58º, which initially suggests that it is not a physical mixture of reagents. There are a few peaks that are very close to overlapping with some from TPT (8.22º, 9.96º, 20.06º, 31.00º and 45.30º) and from BDC (16.87º, 24.40º and 25.33º). **A5a** has intense unique peaks at 14.14º, 19.26º, 20.84º, 26.84º and 28.02º, and peaks after 50º, such as 42.04º and 52.94º.

For **A5b** most peaks belong either to TPT or BDC, but some are unique and intense, such as 5.68, 7.18, 11.34 and 16.62º. For this compound, no peak is above 50º, which probably indicates it's not a metalorganic compound.

Finally, **A5c** has some intense peaks at 6.15º, 8.22º, 12.34º and 16.56º, which are all unique to the compound, and no peaks above 35º. The compound also has peaks correspondent to TPT (8.22º, 18.71º, 20.09º, 24.91º and 30.98º, for example) and to BDC (13.28º, 16.93º, 24.47º and 29.03º).

2.1.2.4.3 Characterization of A6

The **A6** compounds were analyzed firstly by FTIR spectroscopy, with the spectra represented in **Figure 51**. The structure expected is in **Figure 50**.

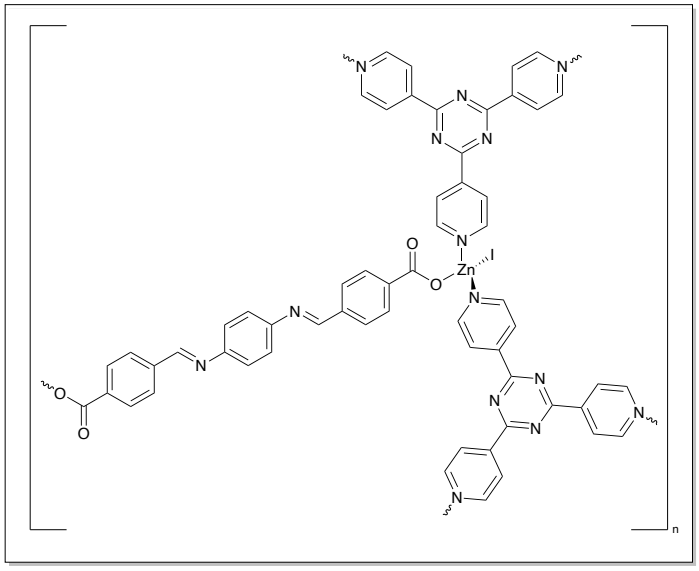

Figure 50. Expected structure for **A6** compound.

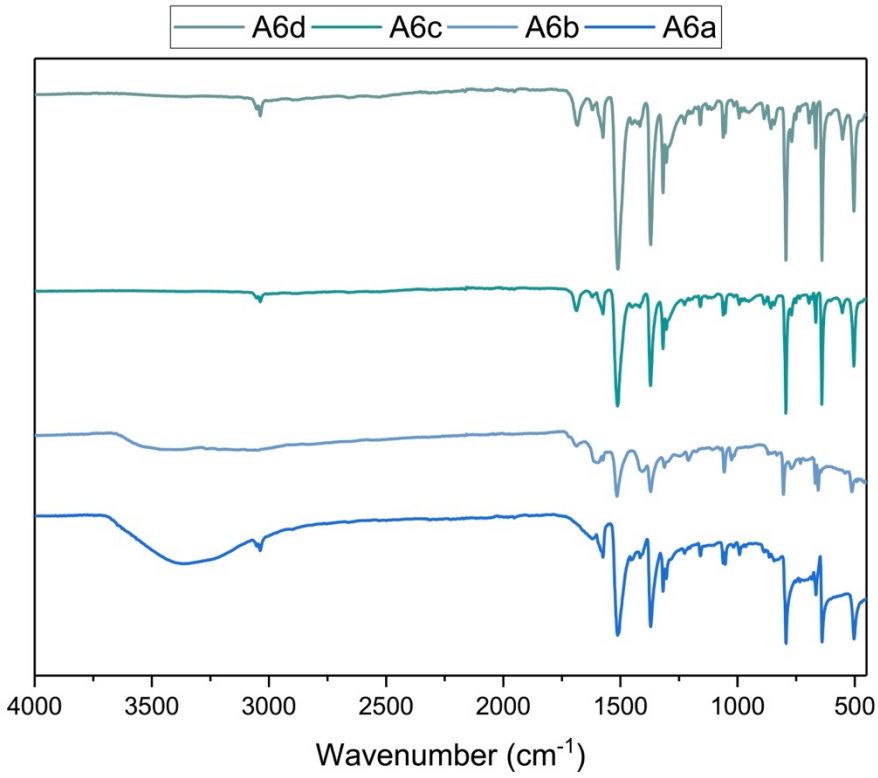

Figure 51. FTIR spectra for the **A6** compounds.

In the FTIR spectra (**Figure 51**), we can observe directly that **A6c** and **A6d** overlap near perfectly and that **A6b** is the only one which does not have the characteristic TPT bands at 3030 cm^{-1}. Compound **A6a** has no band in the 1685-1670 cm^{-1}, while **A6b** has one at 1670, **A6c** at 1678 and A6d at 1683 cm^{-1}, correspondent to the carbonyl groups from **L5**'s carboxylic acids. Another important band is the one around 1620 cm^{-1} representing the iminic C=N bond from **L5**, which is present in **A6a** and **A6b**. The band at 1590-1570 cm^{-1} is from the asymmetric C-O

stretching vibrations and the ones at 1380-1370 cm^{-1} from the symmetric ones. None of the compounds had new bands in the 1000-450 cm^{-1}.

The FTIR is the first technique to be performed as we had easier access to the spectrometer and a shorter collection time. The PXRD was later traced to confirm if the compounds are a physical mixture of reagents or not.

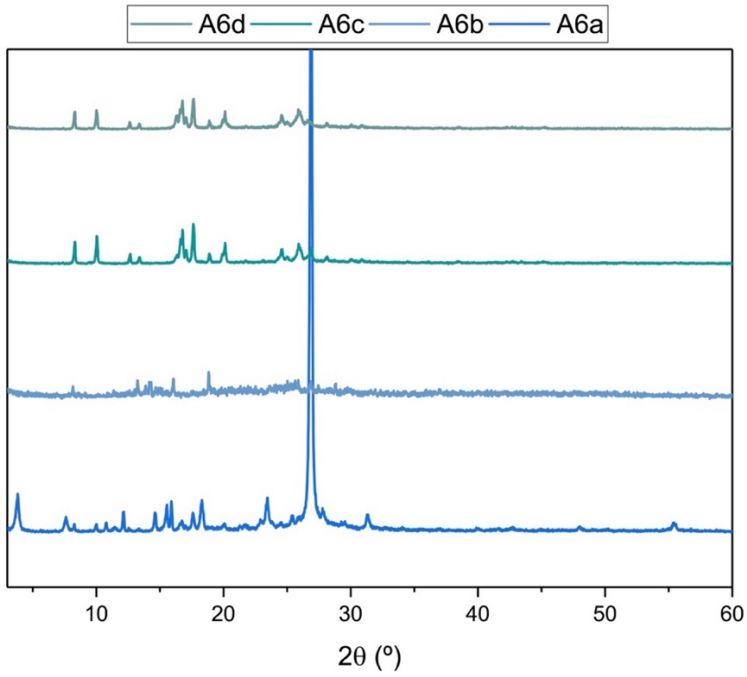

Figure 52. PXRD diffractograms for the **A6** compounds.

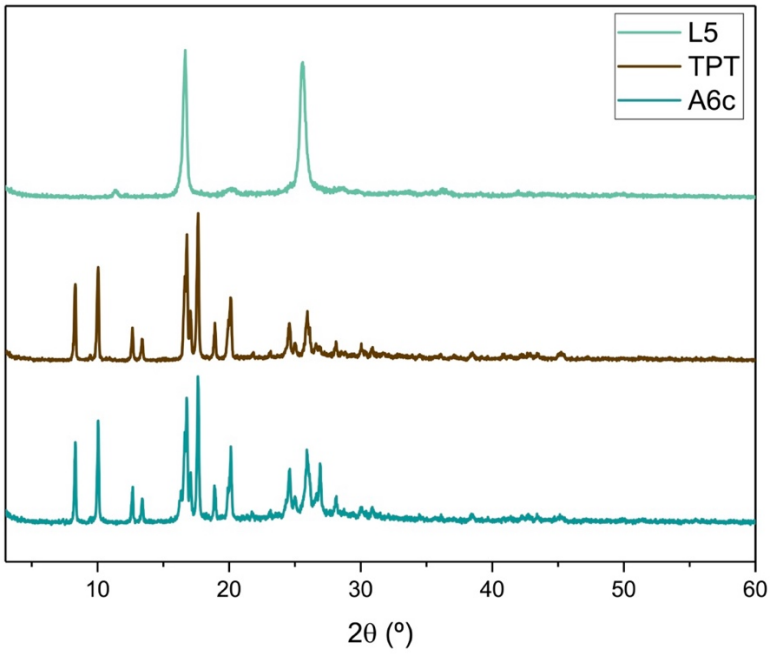

Figure 53. Comparison between the PXRD data from **A6c** and reagents.

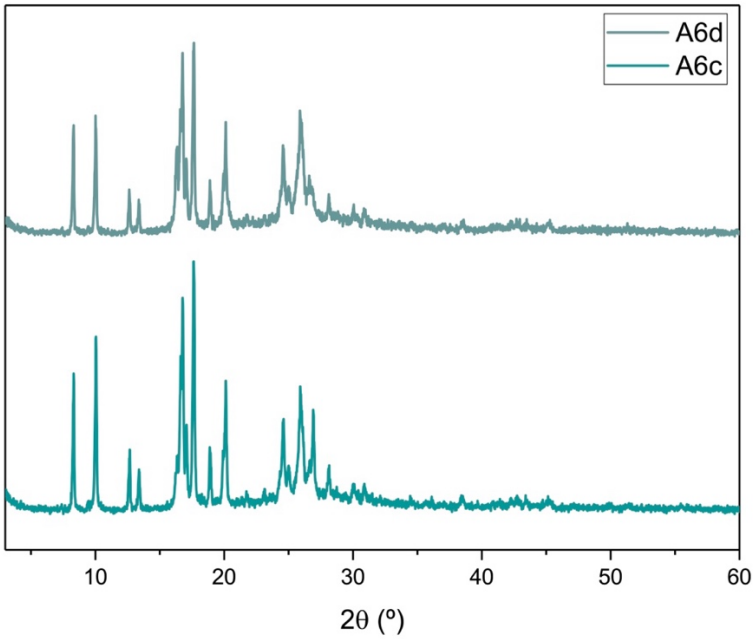

Figure 54. Comparison between the PXRD diffractogram for **A6c** and **A6d**.

From the PXRD data (**Figure 53**), we can confirm that the hydrothermal **A6c** and the microwave-assisted **A6d** originated the same compound (**Figure 54**). All the samples are crystalline, and **A6b** has a low crystallinity. Comparisons to the reagents were established for **A6c** (and subsequentially, **A6d**) due to **A6a** having a large intensity peak at 27° disturbing the normalization of the spectrum, but the peaks are still described below.

A6a has its own unique peaks, like 3.82°, 12.14°, 15.54°, 15.93°, 23.42° and 31.31°, and has similar peaks to TPT, such as 8.29°, 10.05°, 16.79°, 20.15° and 29.61°, and to **L5** at 11.56°

and 25.82º. Low-definition peaks are found at 48.15º and 55.58º – this can indicate the presence of the metal in the structure.

A6b is an amorphous compound, which means it won't have any diffraction peaks.

By **Figure 54**, we can conclude that the diffractogram of **A6c** is the same as TPT's, so if **A6c** is equal to **A6d**, **A6d** is also TPT. Since the FTIR spectra for compounds **A6c** and **A6d** was traced first, it indicates the presence of new bands, meaning a new compound may have been formed. However, after the PXRD analysis, we can confirm that, in fact, no new materials were formed.

2.1.2.4.4 Characterization of A7

Represented in **Figure 55** is the expected structure of **A7** and in **Figure 56** is the FTIR spectrum for the **A7a** compound.

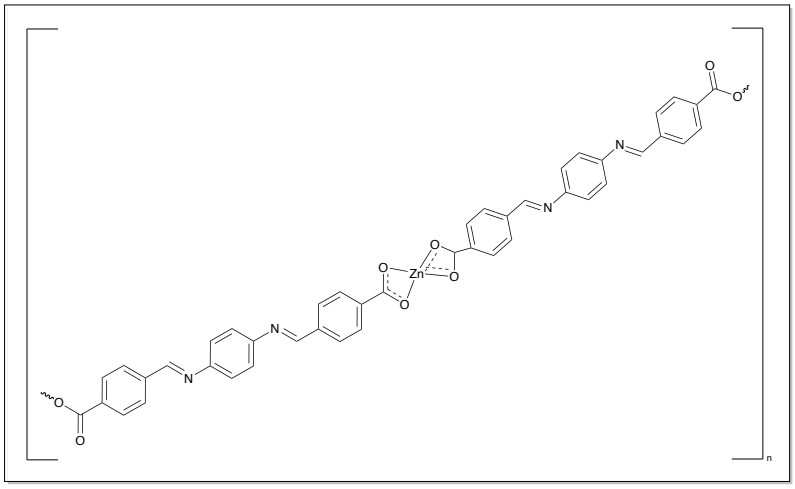

Figure 55. Expected structure for **A7** compound.

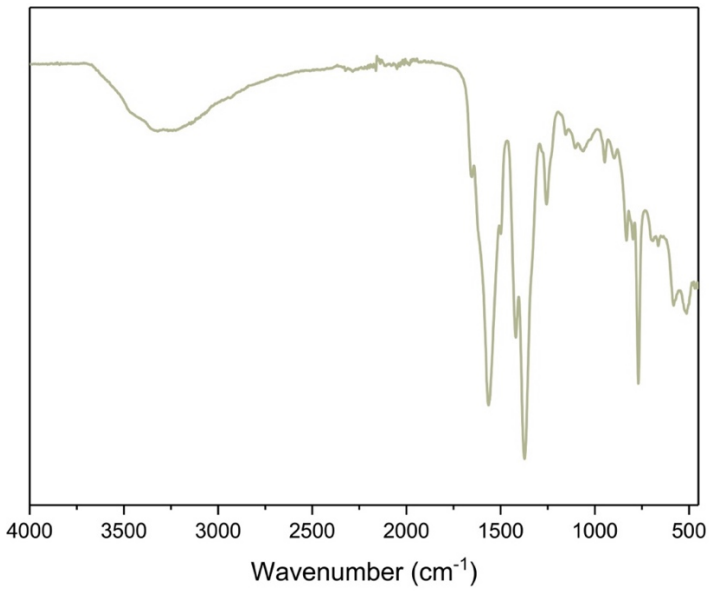

Figure 56. FTIR spectrum for **A7a**.

In the spectrum, the important bands are the 1652, 1563, and 1373 cm^{-1}. The first corresponds to the carbonyl group from **L5**, the second is very wide and has "slope" at 1621 cm^{-1}, which is from the iminic C=N, but it also corresponds to the asymmetric C-O stretching vibration, and the third band is from the symmetric C-O stretching vibration. Then, there are two new bands at 581 and 512 cm^{-1} that can be associated to the formation of Zn-O bonds.

The PXRD showed that the compound is an amorphous material, as it had no bands (**Figure A.58** in **Annexes**), and no further conclusions can be drawn.

2.1.2.4.5 Characterization of A9

The SCXRD data was collected for these compounds and are represented in **Figure 57, 58** and **59**.

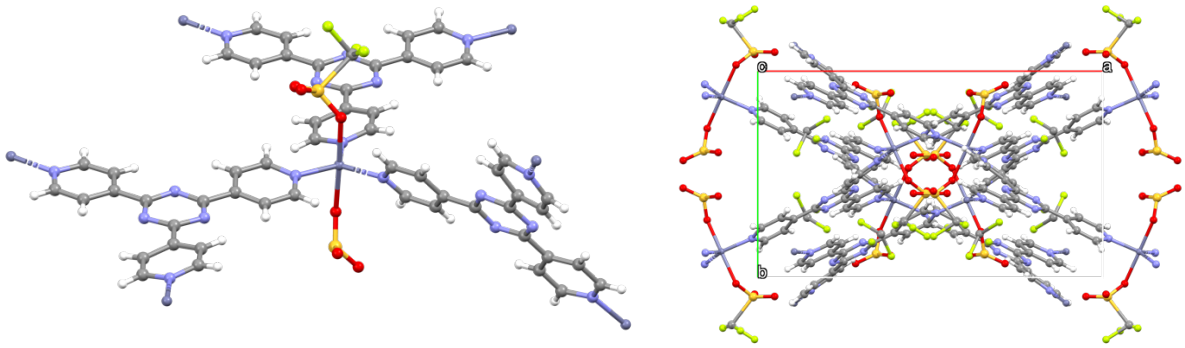

Figure 57. Mercury representation of **MOF3** (left) and its packing along the *c*-axis (right).

The MOF, **MOF3**, and the cationic complexes, **A9a** and **A9b**, were crystallized using the diffusion layering method with chloroform and methanol as the solvents. The three of them crystallized in the monoclinic system, but in different space groups, with **MOF3** in the $C2/c$, **A9a** in the $P2_1/c$, and **A9b** in the $P2_1/n$ space groups. As the data shows, the chemical composition of **A9a** and **A9b** is the same, but their space groups are different, indicating they are polymorphs – compounds that are equal in composition but crystallize in different crystal forms and supramolecular arrangements.

MOF3 forms a new and unreported coordination network composed of the metal center connected to five other atoms, which, in this case, is a zinc center connected to three TPT molecules and two triflate molecules, creating a slightly distorted trigonal bipyramid geometry, with the TPT molecules in the equatorial positions, while the triflates are in the axial positions. This can be proven by the angles formed between the ligand's connecting atoms and the metal center reported in **Table 30**.

Table 30. Selected bond lengths and angles for **MOF3**.

MOF2			
Bond Lengths (Å)		**Angles (°)**	
Zn-N^1	2.006(7)	**N^1-Zn-N^4**	123.7(3)
Zn-N^4	2.014(6)	**N^4-Zn-N^5**	120.4(3)
Zn-N^5	2.017(7)	**N^1-Zn-N^5**	115.9(3)
Zn-O^1	2.169(8)	**N^1-Zn-O^1**	92.0(3)
Zn-O^4	2.160(8)	**N^1-Zn-O^4**	86.5(3)
		O^1-Zn-O^4	177.7(3)

The pore dimensions for this molecule were evaluated and the new MOF appears to be microcrystalline.

A9a and **A9b** have the same composition and identical chemical formula (**Figure 59**), but crystallized in different space groups, which makes them polymorphs. This fact can be observed by the SCXRD data for each compound and will be represented in **Figure 60**.

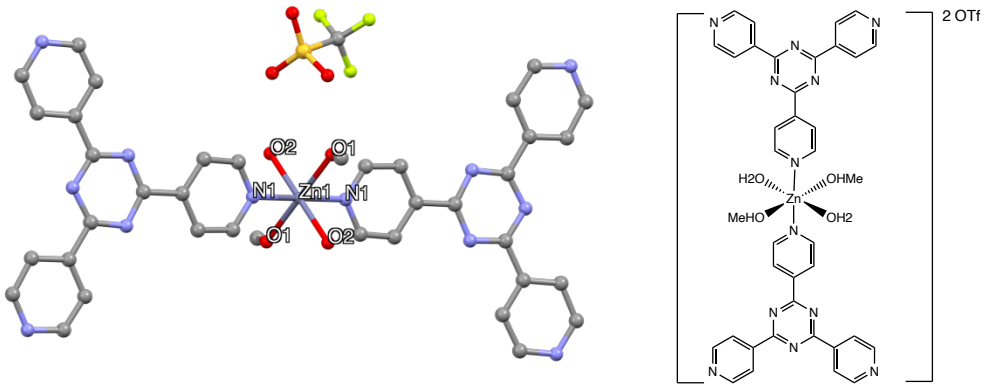

Figure 58. Mercury representation (left) and schematic representation (right) of **A9a** and **A9b**. The hydrogens are omitted for clarity.

As mentioned before, the difference between the **A9a** and **A9b** compounds is their space group, which can be observed in their packing in **Figure 60**. The cationic complexes were formed through diffusion layering and their structure comprehends a zinc center connected to two methanol and two water molecules in the equatorial plane and two TPT molecules in the axial plane.

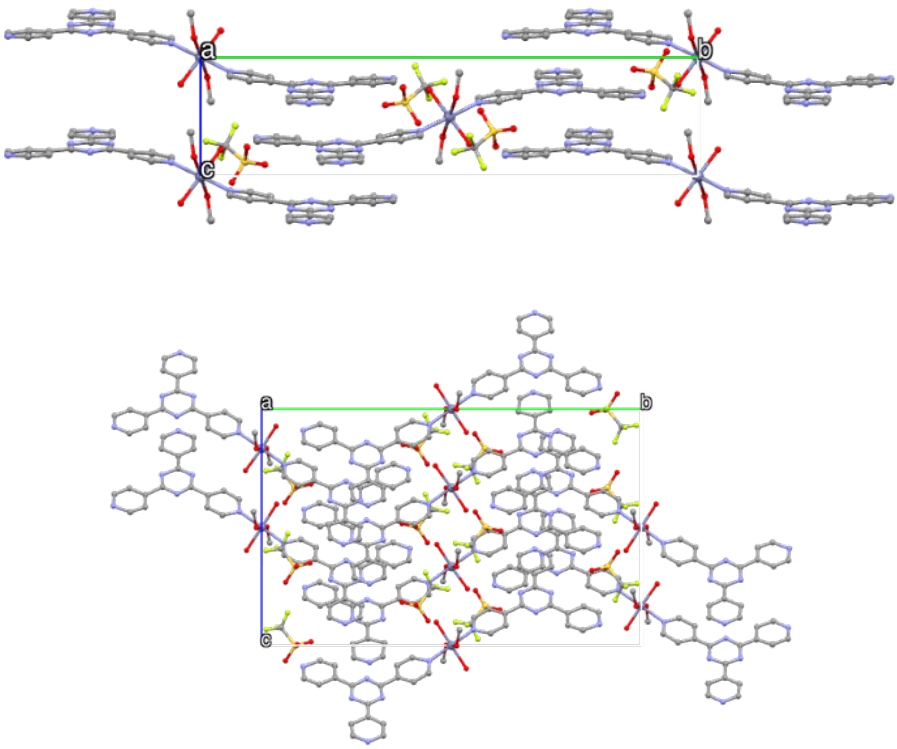

Figure 59. Mercury representation of **A9a** (top) and **A9b** (bottom) of their packing along the *a*-axis.

Both compounds are monoclinic systems, but **A9a**'s space group is in the $P2_1/c$ and **A9b** is in the $P2_1/n$. Since the zinc atom is connected to six atoms, the geometry for **A9a** is octahedral and for **A9b** is slightly distorted octahedral, with the selected bond lengths and angles are represented in **Table 31**.

Table 31. Selected bond lengths and angles between the atoms of **A9a** and **A9b**.

A9a				**A9b**	
Bond Lengths (Å)		**Angles (°)**		**Bond Lengths (Å)**	**Angles (°)**
Zn-N¹	2.144	**N¹-Zn-O¹** **N¹-Zn-O²** **O¹-Zn-O²**	90.30 90.20 90.85	2.16(1)	89.30 91.5(4) 90.1
Zn-O¹ **Zn-O²**	2.138 2.094	**N¹-Zn-N¹** **O¹-Zn-O¹**	180.00 180.00	2.065 2.14(1)	179.8(5) 176.88

These cationic complexes, **A9a** and **A9b**, display cationic moieties that are somewhat related to two neutral complexes previously reported in the literature: (a) a complex with a ferrous center connected to two thiocyanates, two methanol molecules and two TPTs, with the CSD Refcode AREHAG [119], and (b) a complex with a cobalt center bonded to the same

molecules as the ferrous complex, with the CSD Refcode ZUFZEI [120]. Both these complexes have a co-crystallized molecule of methanol in their asymmetric unit. Similar to our cation complexes, they have the TPT molecules in the equatorial planes and the methanol and thiocyanates in the axial one, conferring them an octahedral geometry.

2.1.2.4.6 Characterization of A10

The expected structure for **A10** is in **Figure 60** and the FTIR spectra of these compounds are represented in **Figure 61**.

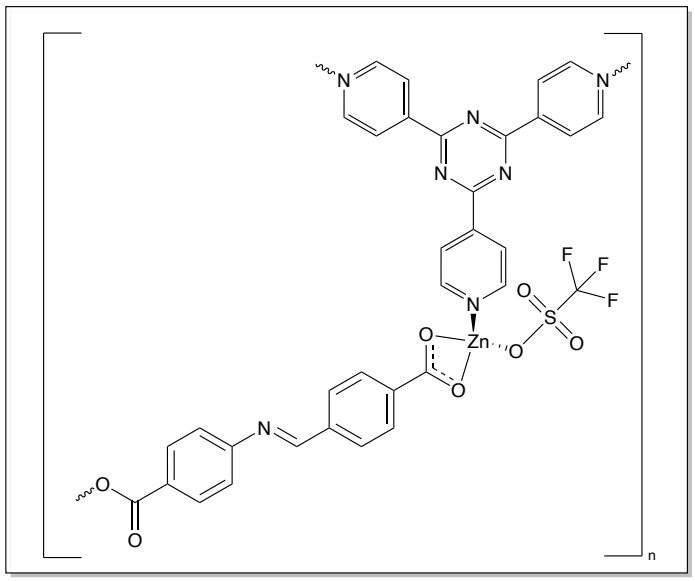

Figure 60. Expected structure for **A10** compounds.

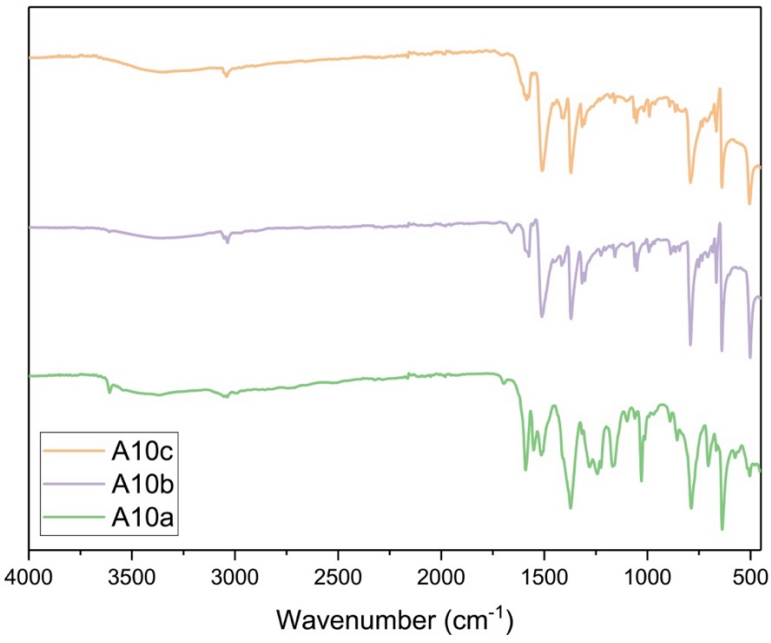

Figure 61. FTIR spectra for the **A10** compounds.

Firstly, we can confirm the presence of TPT in the products as they all have characteristic bands at 3030 cm^{-1}. **A10a** has a band at 3806 cm^{-1} that may be a trace of methanol's hydroxyl group from the diffusion layering. At 1698, 1658 and 1696 cm^{-1}, are the carbonyl bands from **L2**'s carboxylic acids for **A10a**, **A10b** and **A10c**, respectively. **A10b** has a broad band at 1585-1575 cm^{-1} that can be associated to the deviated iminic C=N band of **L2** and to the asymmetric C-O stretching vibration. The latter can also be observed in the other two spectra but at 1590 cm^{-1} for **A10a** and 1586 cm^{-1} for **A10c**, which do not have the former iminic band, meaning they probably don't have **L2** in their composition. The C=C benzene ring vibration and C=N stretching from the TPT rings appear at 1515, 1513 and 1511 cm^{-1} for **A10a**, **A10b** and **A10c**. In the same compound order, appears the symmetric C-O stretching vibration at 1374, 1370 and 1371 cm^{-1}. While compound **A10c** has no new band below 1000 cm-1, **A10a** has at 573 cm^{-1} and **A10b** at 707 cm^{-1}.

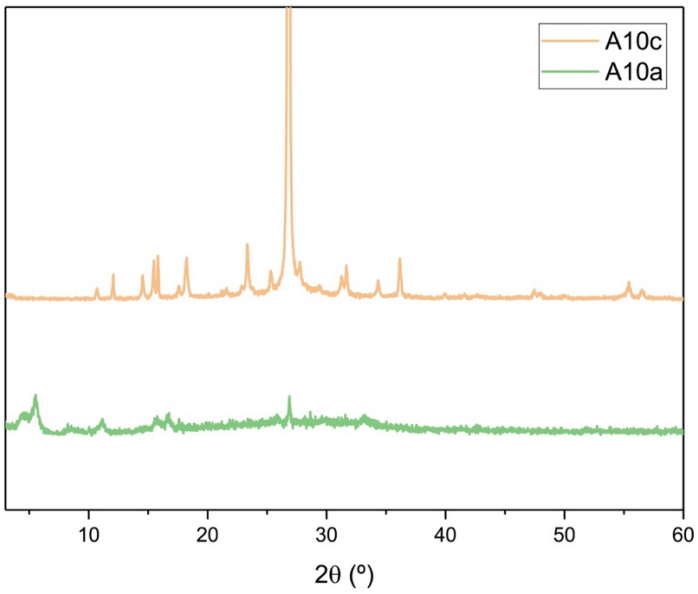

Figure 62. PXRD diffractograms for compounds **A10a** and **A10c**.

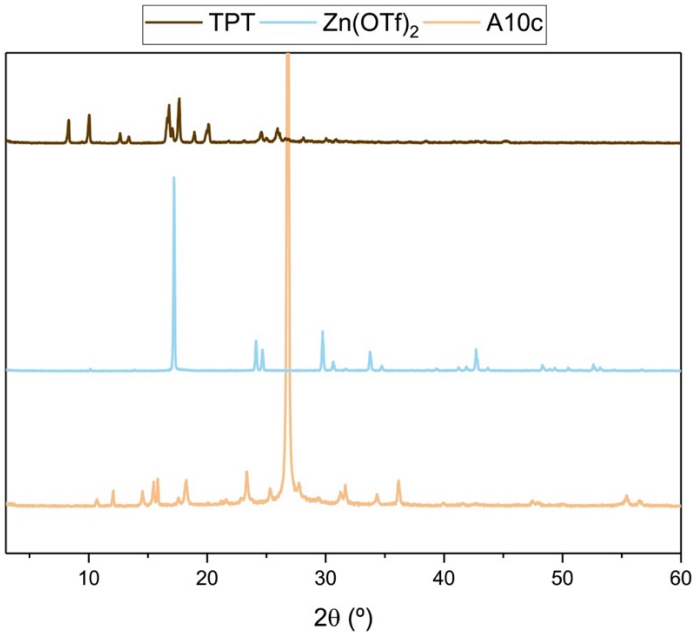

Figure 63. Comparison between the PXRD diffractograms for compound **A10c** and reagents.

Since the amount of **A10b** was not enough for PXRD analysis, only **A10a** and **A10c**'s data was collected. Analyzing the diffractograms (**Figure 62**), we can conclude that **A10a** has very low crystallinity and **A10c** is crystalline.

In compound **A10a**, the few peaks detectable are at 4.60º, 5.52º, 11,20º, 15.72º, 16.71º, 26,86º and 33.09º, with the penultimate peak belonging to TPT. The rest cannot be compared to **L2** because no diffractogram was traced for it due to a lack of compound quantity.

Sample **A10c** has some peaks that relate to the TPT (17.62º and 26.80º) and a single peak related to the $Zn(OTf)_2$ at 56.59º. We cannot be sure which peaks belong to **L2**. But the prospects seem to point to a metalorganic material with peaks above 50º. There are also intense peaks at 15.50º, 15.80º, 18.20º, 23.38º, 36.14º and 55.36º.

2.1.2.4.7 Characterization of A11

A11's structure is represented in **Figure 64** and characterized by FTIR and PXRD since it didn't yield any crystals.

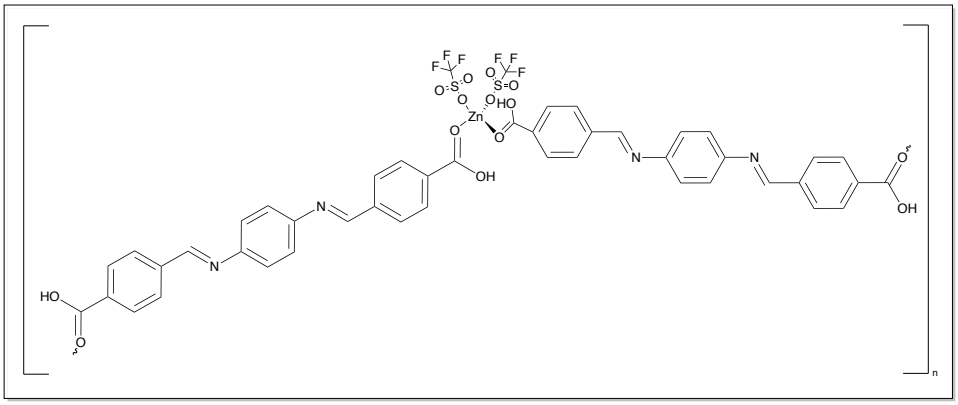

Figure 64. Expected structure for **A11** compounds.

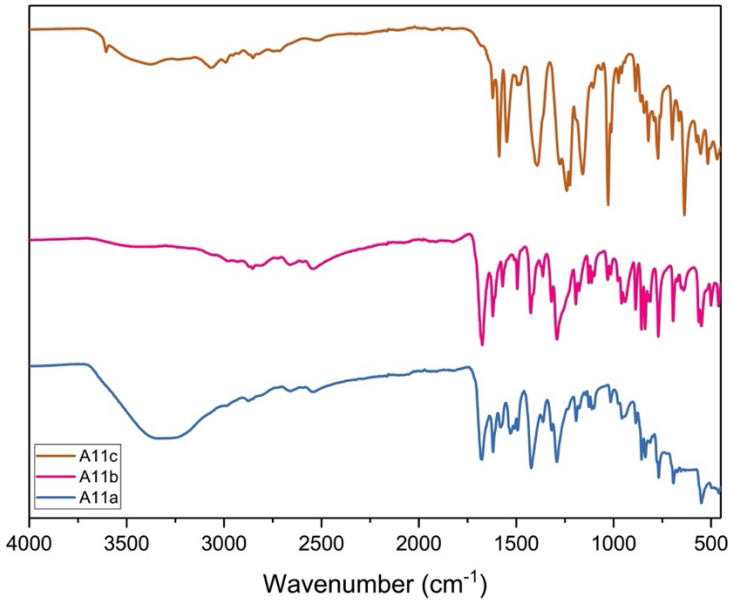

Figure 65. FTIR spectra for the **A11** compounds.

In **Figure 65** is represented the FTIR spectra for **A11**. For **A11a**, we have a 1676, 1620, 1580, 1360 and 1234 cm^{-1} bands which correspond to the carbonyl from the carboxylic acids of **L5**, the C=N bonds from the iminic groups, the asymmetric C-O stretching vibrations, the symmetric C-O vibrations and the S=O from the triflate groups, respectively. Those bands definitions also apply for **A11b** with the bands at 1674, 1619, 1570, 1363 and 1267 cm^{-1}. But, for **A11c**, we can observe a new band at 3606 cm^{-1} that possibly indicates the presence of methanol, representing its hydroxyl group and a lack of C=O band, indicating the possibility of a carbonyl reduction. At 1621 cm^{-1} is the iminic C=N bond, and, assuming a connection to zinc, at 1588 and 1391 cm^{-1} is the asymmetric and symmetric C-O stretching vibrations. From 1000 to 450 cm^{-1}, **A11a** has new bands at 670 and 640 cm^{-1}, **A11b** at 940, 656, 643 and 573 cm^{-1}, and **A11c** at 790 and 650 cm^{-1}.

According to this data, **A11c** appears to be the equal to the structure proposed for **A7** (**Figure 55**), **A11a** and **A11b**, similar between each other, are closer to the structure proposed in **Figure 64**.

The PXRD data for **A11a** in comparison to the reagents is represented in **Figure 66**.

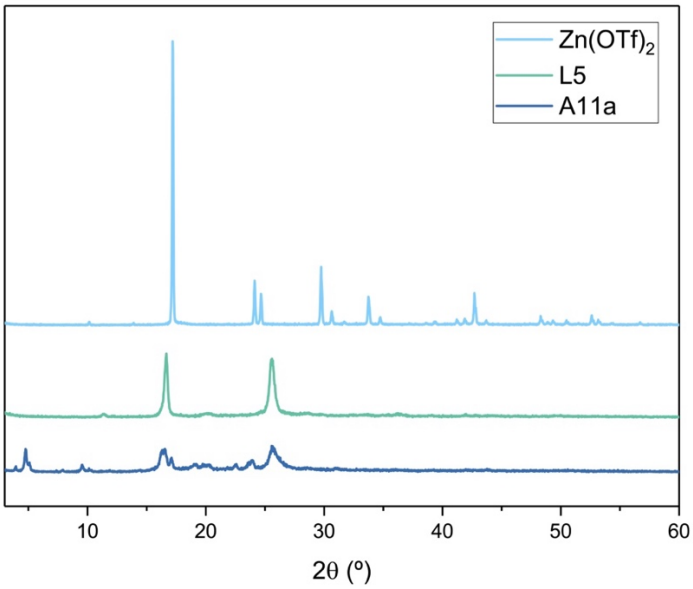

Figure 66. Comparison between the PXRD diffractograms for compound **A11a** and reagents.

Due to the very small quantity of solid obtained from the diffusion layering technique, compounds **A11b** and **A11c** could not be analyzed through PXRD. **A11a** is crystalline, as we can see from its diffractogram, and different from the reagents, with new bands.

A11a, the microwave sample, has intense peaks at 9.51°, 16.25°, 16.48°, 17.09°, 23.83° and 25.64°, of which 16.49° and 25.64° corresponds to **L5**, as well as the not intense peak at 20.19°. It also has one peak related to $Zn(OTf)_2$ at 17.09°. Due to the lack of peaks after 50°, it is unprobeable that the material has a metal in its composition. These results mean that **A11a** is not a physical mixture of the ligands.

2.1.2.4.8 Characterization of A12

The only compound obtained for **A12** has its FTIR and PXRD data collected and its structure in **Figure 67**.

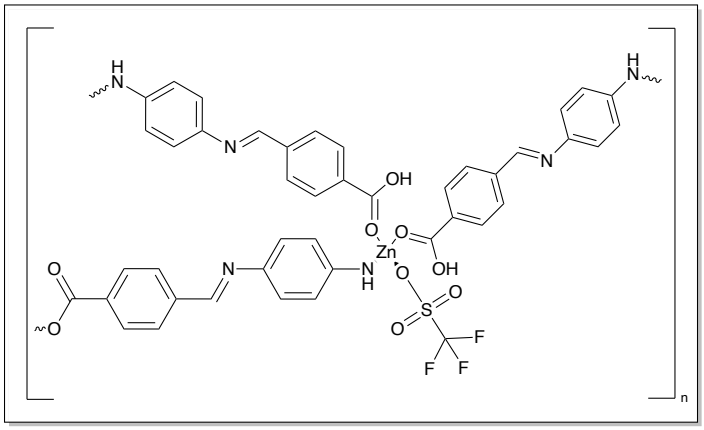

Figure 67. Expected structure for the **A12** compounds.

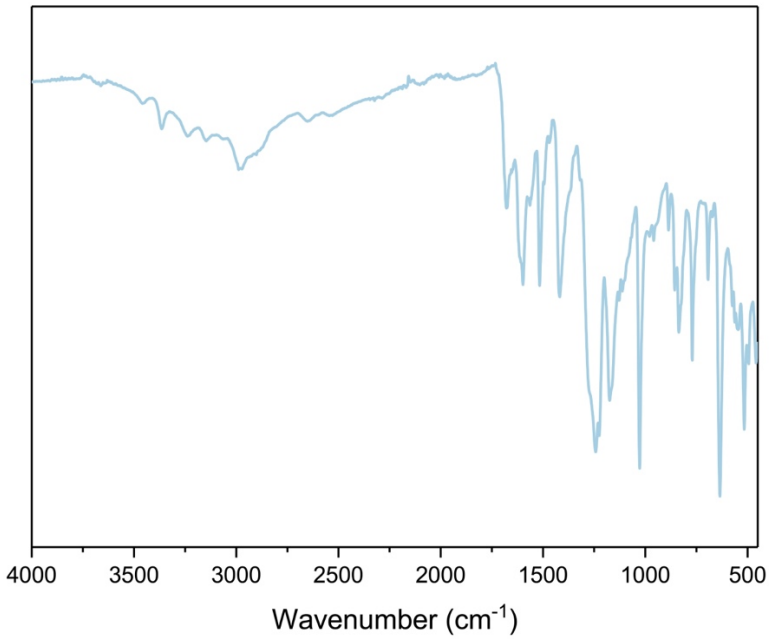

Figure 68. FTIR spectrum for compound **A12**.

In **Figure 68**, we can infer that the band at 3353 cm^{-1} belongs to the N-H stretching from **L5**'s newly formed secondary amine. The presence of only one of the two N-H bands indicates the nitrogen formed a bond to zinc. The bands at 1681, 1608, 1583 and 1416 cm^{-1} correspond to the C=O, the iminic C=N, the asymmetric C-O and symmetric C-O stretching vibrations. The new band at 1236 cm^{-1} is representative of the S=O bands from the triflate groups. There is also the formation of new bands below 1000 cm^{-1}, one at 856 cm^{-1} and other at 659 cm^{-1}.

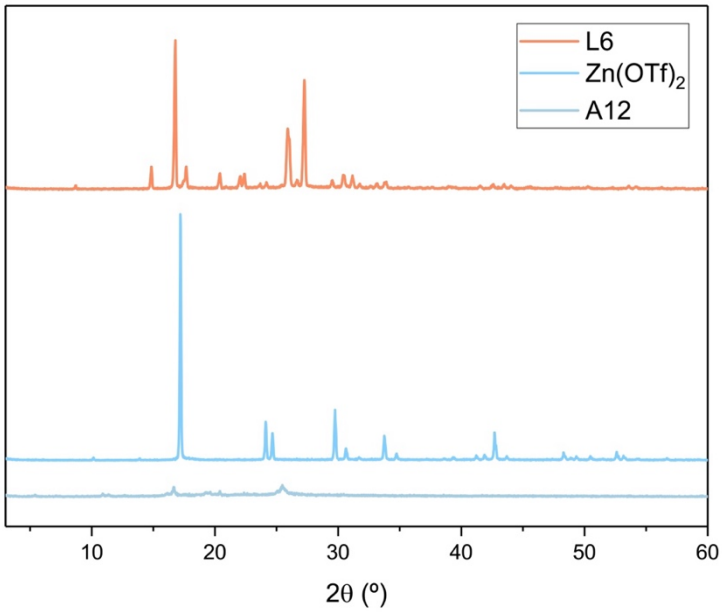

Figure 69. Comparison between the PXRD spectra for compound **A12** and reagents.

As mentioned above, we can confirm **A12**'s low crystallinity from the barely defined peaks, which are not intense, with the most intense being the last one at 25.51°. There are two peaks related to **L6** at 16.66° and 20.39°. The diffractogram for **A12** doesn't appear to be a physical mixture of the reagents and the compound did not dissolve in DMSO, DMF, MeOH nor diethyl ether. Thus, this can indicate that a polymeric compound was formed since both reagents are soluble in DMSO and this one is not.

2.1.2.4.9 Characterization of A14

The expected structure (**Figure 70**), the FTIR spectra (**Figure 71**) and PXRD diffractograms (**Figure 72**) for compounds **A14** are represented below.

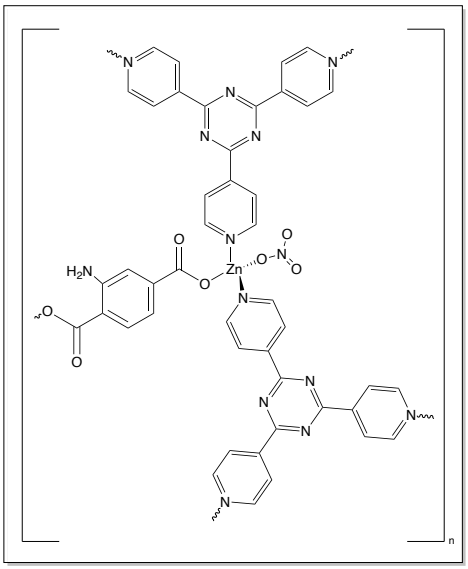

Figure 70. Expected structure for the **A14** compounds.

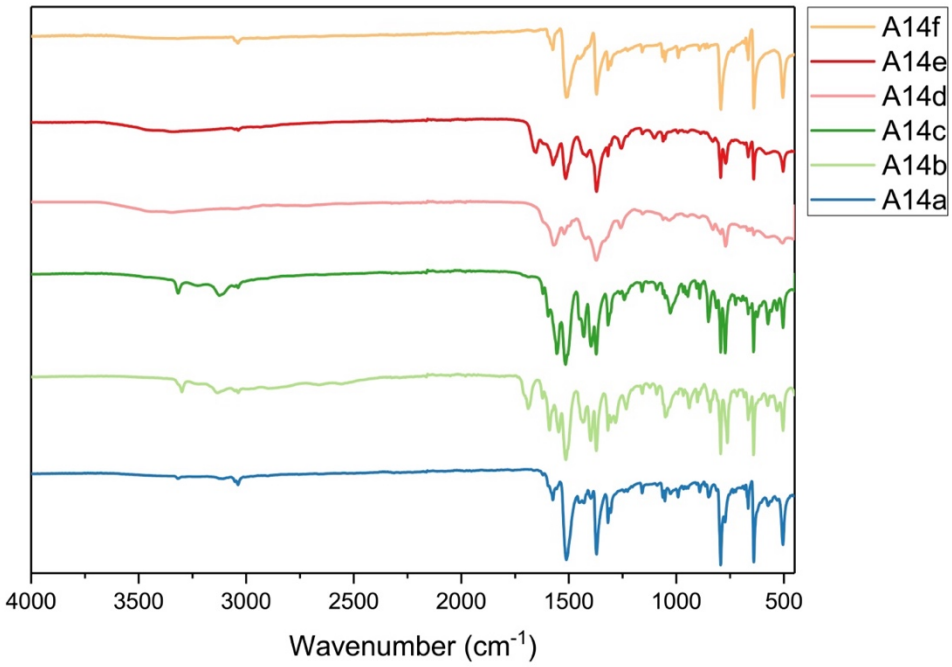

Figure 71. FTIR spectra for the **A14** compounds.

All the **A14** samples observed in the FTIRs of **Figure 71** have the TPT characteristic bands present, even though some are roughly defined. Compound **A14a** appears to have only one NH band at 3316 cm^{-1} from the ATA NH_2 group, **A14b** has those bands at 3299 and 3131 cm^{-1}, **A14c** at 3316 and 3221 cm^{-1}, which the other three compounds do not have in their spectra.

A14a has a small band at 1620, which is supposed to correspond to C=O from ATA, as well as the C-O asymmetric and symmetric bands at 1575 and 1397 cm^{-1}. It also has a band corresponding to the $Zn(NO_3)_2$ at 1243 cm^{-1}. Below the 1000 cm^{-1}, this compound has new bands at 772, 571 and 530 cm^{-1}.

For the hydrothermal **A19b**, the FTIR resembles a mixture of reagents, as it has a band at 1690 cm^{-1} and, in the free ATA ligand, the C=O group appear at 1670 cm^{-1} – which was attributed at 1623 cm^{-1} for the bound ligand in **A19b**'s spectrum. The C-O asymmetric and symmetric bonds are at 1591 and 1397 cm-1 and there is a new band at 1281 cm^{-1}, corresponding to an N-O bond from the nitrate. New bands in the 1000-450 cm^{-1} region are located at 763, 719 and 533 cm^{-1}.

Compound **A14c** has the important bands at 1620, 1596, 1396, 1248 cm^{-1}, which correspond, respectively, to the C=O vibration, C-O asymmetric and symmetric, and N-O bond from the nitrate. This compound also presents new bands at 814, 724, 623, 574 and 532 cm^{-1}.

For the layering compound, **A14d**, it possesses the C=O band at 1620 cm^{-1}, the C-O asymmetric and symmetric at 1569 and 1376 cm^{-1} and a new band at 1258 cm^{-1} from the N-O. Below 1000 cm^{-1}, new bands at 829 and 701 cm^{-1} were formed.

A14e does not have the NH_2 bands from the ATA ligand. The lack of this group indicates it is either connected to the metal or the ATA does not appear in the structure. The last sentence is debunked by the other bands in the compound, especially the ones at 1620 (C=O stretching

vibration), 1575 (C-O asymmetric) and 1373 cm^{-1} (C-O symmetric) from the ATA. There are two new bands: one at 1254 cm^{-1} for the N-O bond and one at 770 cm^{-1}.

Compound **A14f** is a special case, as its spectrum looks to be very similar to TPT's, but PXRD confirmed it was not pure TPT, so let's assume it is a physical mixture of reagents, therefore, it has no new bands.

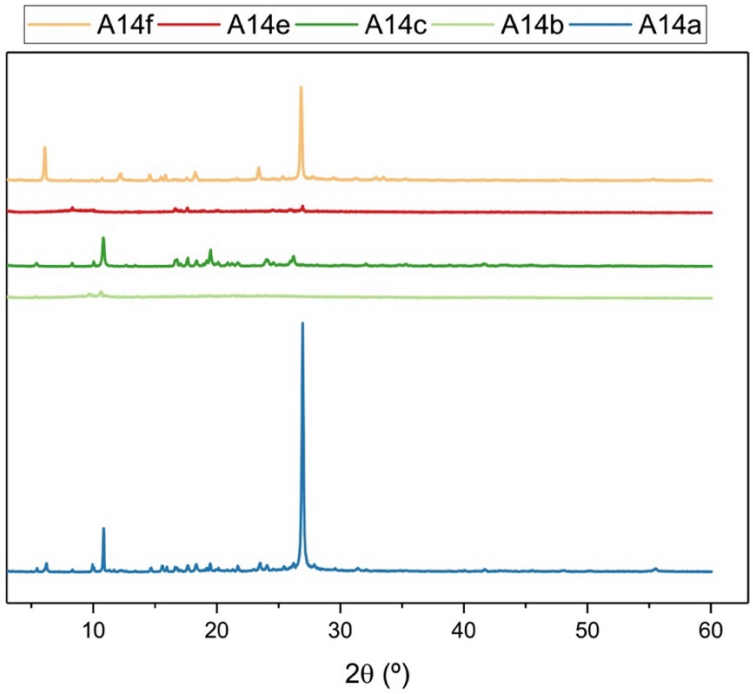

Figure 72. PXRD diffractogram for the **A14** compounds.

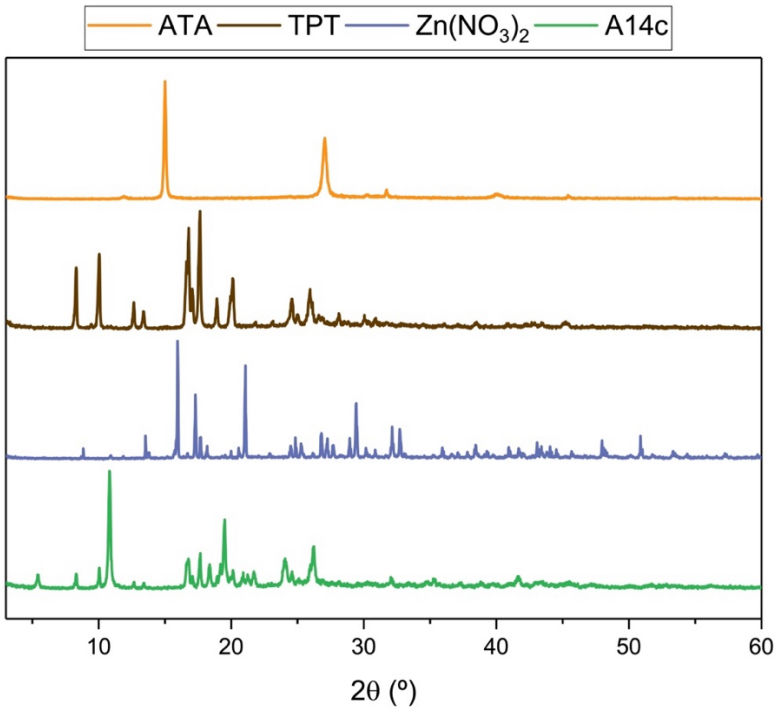

Figure 73. Comparison between the PXRD diffractograms for compound **A14c** and reagents.

In **Figure 72** is represented the PXRD spectra for five out of the six **A14** compounds and in **Figure 73** is represented the PXRD data for compound **A14c** in comparison to the reagents. That comparison was also made for the remaining compounds (**A14a** and **A14f**), being presented in the **Annexes A.76** to **A.77**.

Compound **A14a** is crystalline and has unique intense peaks at 6.20º, 9.94º, 10.85º, 18.34º, 19.45º, 23.55º and 55.44º. The other intense peaks belong to $Zn(NO_3)_2$ at 26.21º and 27.07º, with other peaks at 15.97º, 16.60º, 17.63º, 21.29º, 24.65º, 25.47º, 27.89º, 29.59º, 32.09º, 41.78º and 47.96º. It also has peaks in common with ATA at 11.71º and 31.45º and with TPT at 8.35º, 13.32º, 17.05º, 20.15º, 21.68º, 23.05º and 45.44º. The other unique peaks are medium to low intensity and vary from 5.44º to 50.36º.

A14b and **A14e** have low crystallinity, therefore, only present a few peaks. The first has peaks at 5.31º, 9.60º and 10.58º, which are all unique. The second has no unique peak, all of them matching either one of the three reagents, meaning the sample is a physical mixture of the reagents.

For **A14c**, we have unique and intense peaks at 10.83º, 19.51º and 24.06º, and some medium to low intensity ones at 5.42º, 18.36º, 19.18º, 20.90º, 37.39º and 38.90º. Peaks at 8.35º, 10.03º, 12.63º, 13.37º, 16.77º, 17.09º, 20.15º, 21.70º and 43.40º belong to TPT, the ones at 17.67º, 21.23º, 24.69º, 26.20º, 35.38º and 41.55º to $Zn(NO_3)_2$. The peak at 30.05º is the only one that corresponds to ATA. No peaks are above 50º.

The analysis of the **A14f** diffractogram indicates that it has two unique and intense peaks at 6.07º and 18.24º and other unique medium to low intensity peaks from 10.74º to 55.50º. We can relate some peaks to $Zn(NO_3)_2$ at 15.86º, 18.12º, 25.37º, 27.70º, 29.49º, 32.87º, 35.28º and 48.00º, some to TPT at 8.22º, 16.77º, 23.40º and 26.70º, and none corresponds to ATA.

Compounds **A14a**, **A14b**, **A14c** and **A14f** don't seem to be physical mixtures of the reagents, as they have their own unique peaks not represented in any of the reagents diffractograms. The hydrothermal **A14a** and the heating-synthesized **A14f** have the best chances to be a metal-organic compound, as both show bands above the 50º. What the FTIR told us about **A14f** is conflicting, as this analysis is more precise and **A14f** is not only TPT as seen in **Figure A.78** in **Annexes**.

The heating conditions and ratios used to synthesize the **A14** compounds, **A14e** and **A14f**, display very different PXRD diffractograms, as the **A14e** appear to be only a physical mixture of the reagents.

2.1.2.4.10 Characterization of A15

The expected structures for **A15** is represented in **Figure 74** and the FTIR spectra for **A15A** and **A15b** are in **Figure 75**.

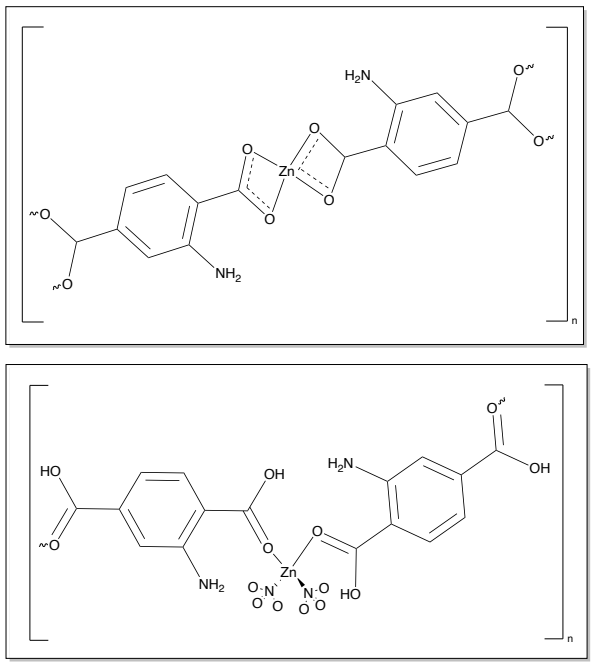

Figure 74. Two possible and expected structures for the **A15** compounds.

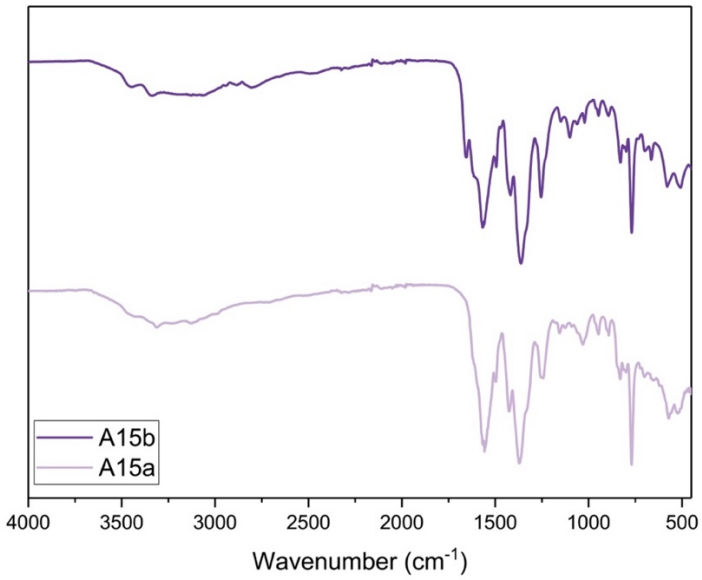

Figure 75. FTIR spectra for the **A15** compounds.

The FTIR spectra (**Figure 75**), representative of the **A15** compounds, shows poorly defined bands from the NH_2 group present in ATA, which usually doesn't form any type of bond to the zinc. **A15b** has those bands at 3442 and 3334 cm^{-1}, and **A15a** has them at 3438 and 3311 cm^{-1}. While **A15a** doesn't seem to have a C=O band from the carboxylic acids, **A15b** has that band at 1653 cm^{-1}. The lack of the characteristic band for that group indicates it was probably reduced, meaning it may have formed a bond to the metal. The asymmetric and symmetric O-C-O stretching vibration bands appear in **A15a** at 1570 and 1369 cm^{-1} and in **A15b** at 1574 and 1361 cm^{-1}, respectively. Those bands did not exist in any of the reagents' spectra. At 1485 cm^{-1}, in both compounds, a band representative of the C=C stretching vibrations from the benzene rings in ATA is present. **A15a** has new bands below 1000 cm^{-1} at 799, 778 and 572 cm^{-1}, while **A15b** has them at 892 and 766 cm^{-1}.

Compound **A15a** seems to be in accordance with the top compound in **Figure 74** and **A15b** to the bottom compound.

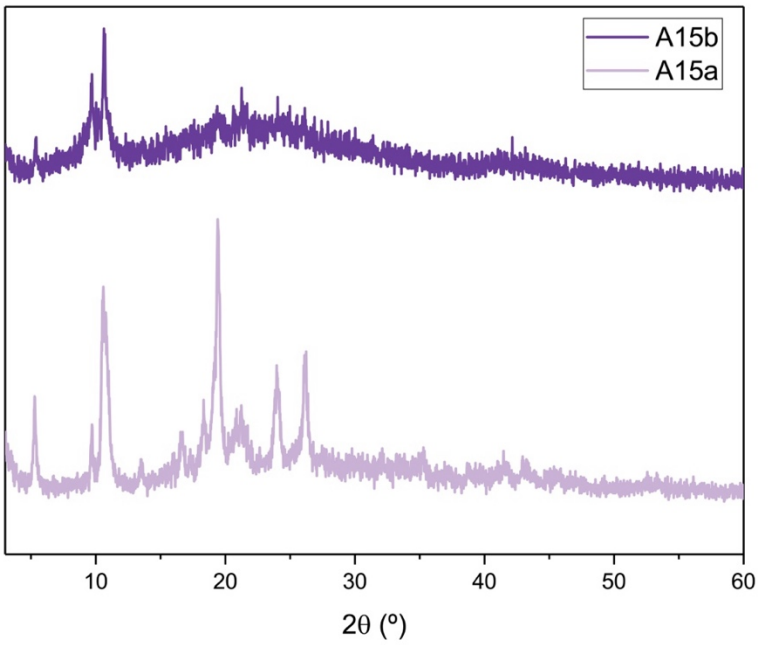

Figure 76. PXRD diffractograms for **A15a** and **A15b**.

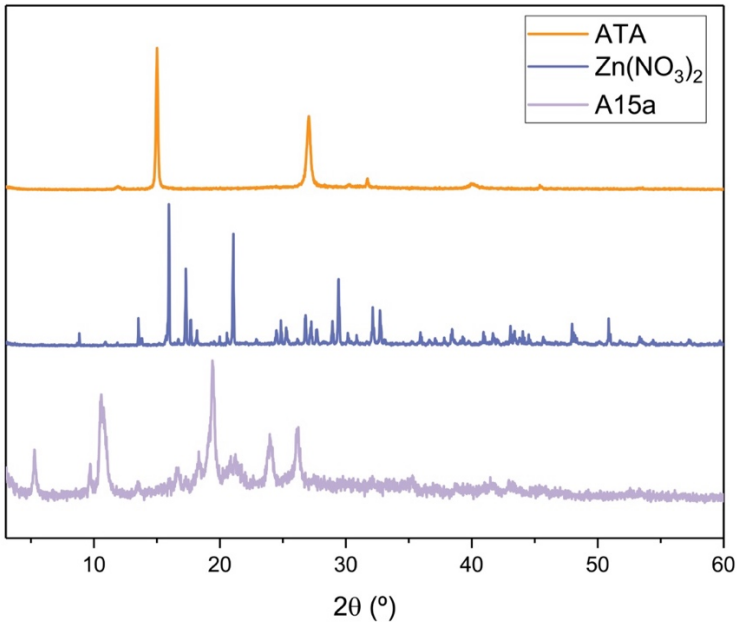

Figure 77. Comparison between PXRD data from **A15a** and the **reagents**.

As we can see in **Figure 76**, both samples present low crystallinity and in **Figure 77**, we have the comparison between the PXRDs from **A15a** *vs.* the reagents.

A15a has two relatively intense peaks at 10.60º and 19.44º and some peaks that are from $Zn(NO_3)_2$ at 13.65º, 18.35º and 26.17º. In the case of **A15b**, it only has three major peaks at 5.38º, 9.72º and 10.66º, but none correspond to the reagents. This indicates that the compounds are not a physical mixture of the reagents.

2.1.2.4.11 Characterization of A16

The only sample worth analyzing further was the **A16**, since the layering techniques only yielded ATA. The expected structure is in **Figure 78** and the FTIR spectrum is represented in **Figure 79**.

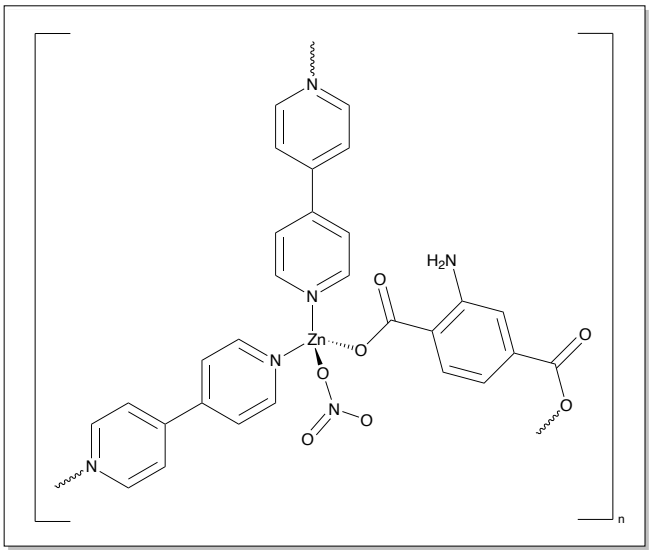

Figure 78. Expected structure for the **A16** compound.

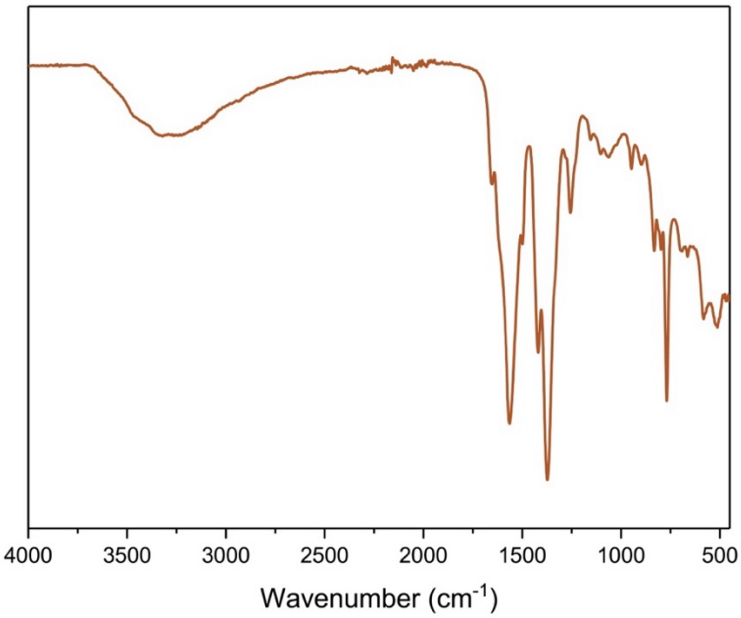

Figure 79. FTIR spectrum for the **A16** compound.

In the spectrum, we can clearly see there is still the presence of water from the synthesis in the broad band at around 3250 cm^{-1}. Since the NH_2 bands also appear around that area, those are not detectable in the spectrum. The carboxylic acid groups from ATA should have three bands for the C=O, C-O asymmetric and symmetric vibrations, which **A16** does have at 1652, 1562 and 1372 cm^{-1}, respectively. The C=C bonds from the benzene rings appear at 1498 cm^{-1}. A new band from the N-O bonding in the nitrate appears at 1255 cm^{-1}. There are also new

bands in the 1000-450 cm^{-1} region at 947, 581 and 512 cm^{-1}, which should correspond to Zn-N or Zn-O bonds. The presence of the carbonyl group states that the desired compound was not formed or there is still ATA present in the sample.

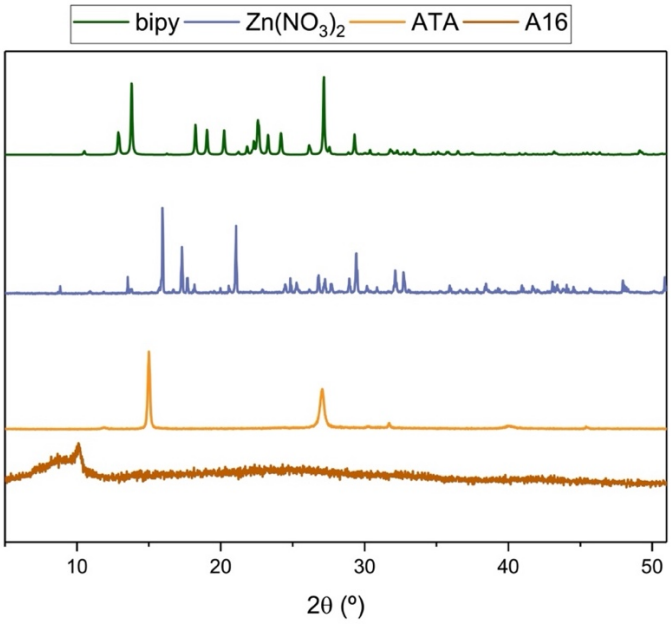

Figure 80. Comparison between PXRD data from **A16** and the reagents.

As observable in **Figure 80**, the sample of **A16** has a very low crystallinity, displayed by the only broad peak at 10.23º, which matches bipy. Since the definition of the diffractogram is very low, we cannot conclude if there are any low intensity peaks above 50º, therefore, we cannot conclude if it has metal present.

2.1.2.4.12 Characterization of A18

Compound **A18** has its expected chemical structure represented in **Figure 81** and FTIR spectrum in **Figure 82**. No PXRD data was traced for this compound due to lack of time.

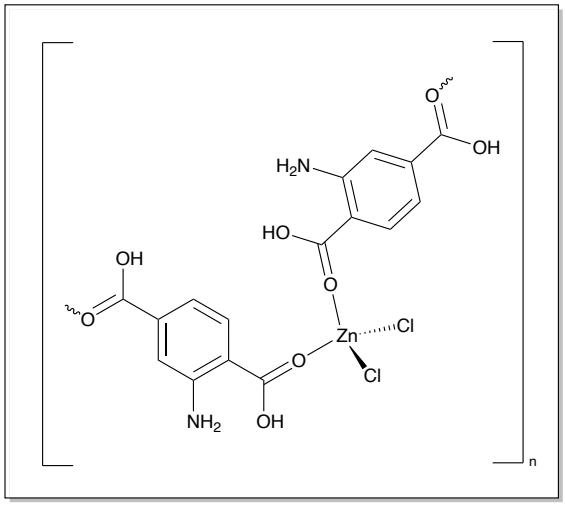

Figure 81. Expected structure for **A18** compounds.

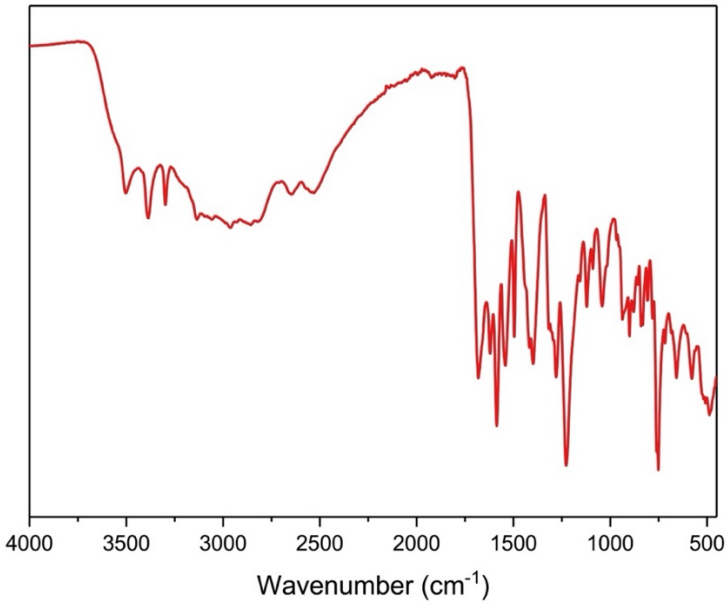

Figure 82. FTIR spectrum for the **A18** compound.

In the FTIR spectrum for compound **A18** (**Figure 82**), we can see the definition of the amine group from ATA bands in 3500-3000 cm^{-1} area (3500 and 3386 cm^{-1}). It has a C=O defining band at 1682 cm^{-1} and the C-O asymmetric and symmetric stretching vibration bands at 1586 and 1396 cm-1. New and thin bands are formed in the 1000-450 cm^{-1} region at 901, 858, 809, 761, 715, 655, 576 and 518 cm^{-1}.

A PXRD should have been performed, but the compound was still wet, even after 2H under vacuum.

2.1.2.4.13 Characterization of A19

The **A19** compounds were generated through microwave-assisted reactions, and since they didn't crystallize, they were analyzed by FTIR and PXRD. The expected structure is represented in **Figure 83** and the FTIR is represented in **Figure 84** and the PXRD in **Figure 85**.

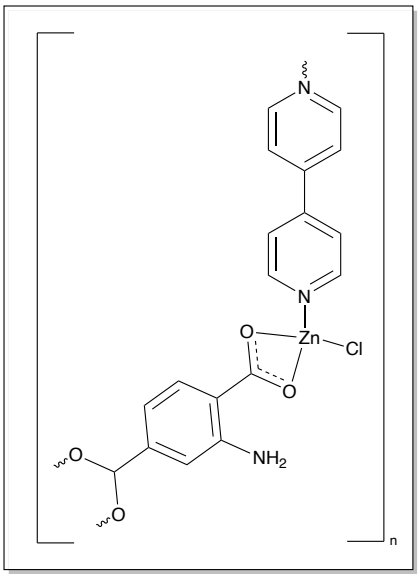

Figure 83. Expected structure for the **A19** compound.

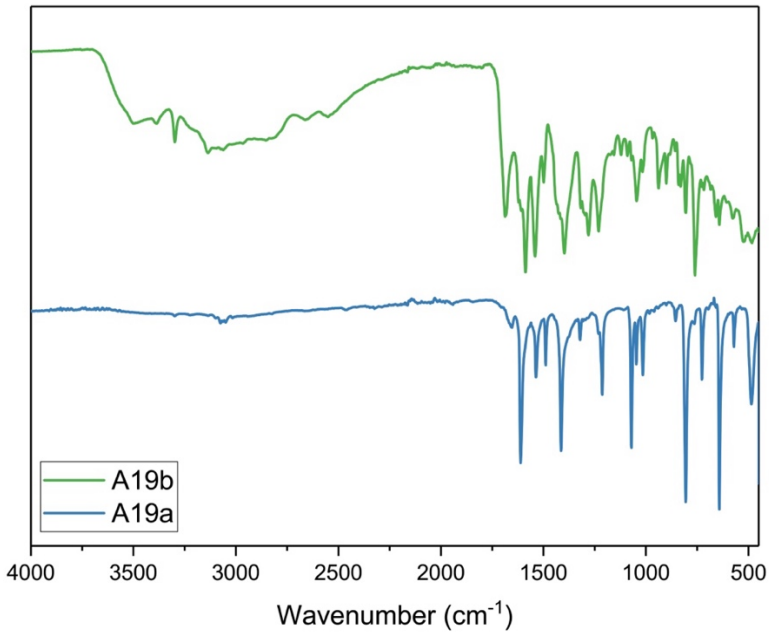

Figure 84. FTIR spectra for compounds **A19**.

The first noticeable aspect in **A19a**'s FTIR spectrum is the lack of NH_2 bands from the ATA. It has the C=O, C-O asymmetric and symmetric stretching vibrations at 1644, 1599 and 1408 cm^{-1}. Indices of bipy's presence appear in the bands at 1540, 1224, 1072, 854 and 570 cm^{-1}, which are close to the free ligand's bands. It also has new bands at 1224, 1014 and 643 cm^{-1}.

However, **A19b** does have the NH_2 bands at 3501 and 3385 cm^{-1}. The ones at 1619, 1586 and 1395 cm^{-1} are related, respectively to the C=O, C-O asymmetric and symmetric bands from the ATA. But this compound could be a mixture of reagents and product, as it has a band at 1683 cm^{-1}, which corresponds to the C=O in ATA, and formation of new bands below 1000 cm^{-1} at 832, 762, 715, 574 and 521 cm^{-1}.

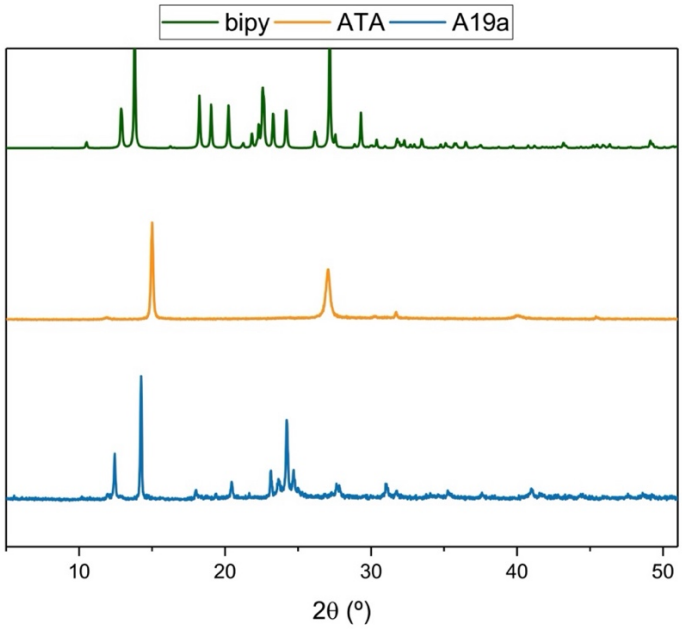

Figure 85. Comparison between PXRD data from **A19a** and the reagents.

We were only able to analyze sample **A19a** by PXRD because **A19b** was still not entirely dried at the time of the measurements, as observable by the OH peak in the FTIR. Also, $ZnCl_2$ was not analyzed. Thus, the **A19a** was only compared to ATA.

A19a has their most intense peaks at 12.46º, 14.25º, 23.12º and 24.22º, which don't belong neither to ATA nor bipy. There are two peaks that correlate to ATA's, the one at 27.77º and 31.72º, and three belonging to bipy at 23.69º, 31.08º and 35.26º. This compound also has a low-definition peak at 52.59º.

2.1.2.4.14 Characterization of B3

The compounds **B3** were characterized firstly by FTIR and then by PXRD. Its expected structure is represented in **Figure 86**.

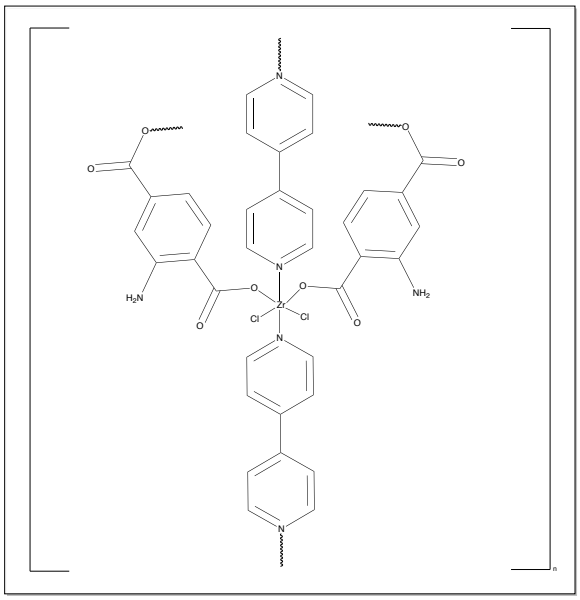

Figure 86. Expected structure for the **B3** compounds.

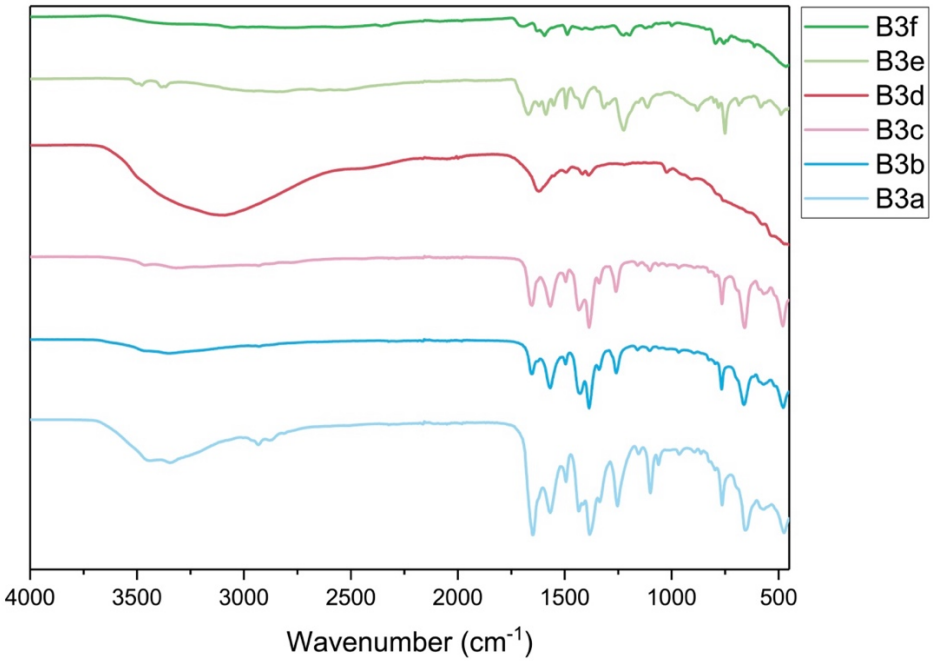

Figure 87. FTIR spectra for the **B3** compounds.

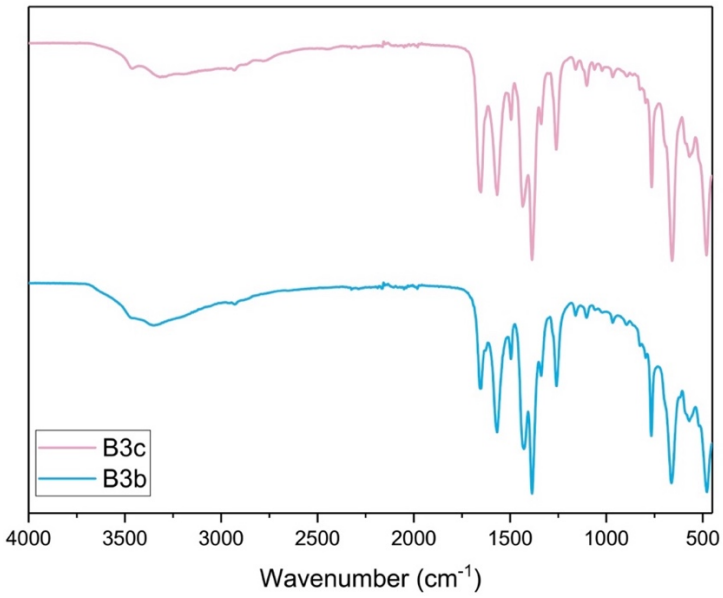

Figure 88. Comparison between the FTIR spectra for **B3b** and **B3c**.

The FTIR spectra for all **B3** compound is represented in **Figure 87** and the differences between the microwave-assisted samples in **Figure 88**.

B3a has a broad band in the 3000 cm^{-1} area, but it is possible to recognize the presence of two bands at 3450 and 3339 cm^{-1} from the NH_2 group in ATA. The C=O, C-O asymmetric and symmetric stretching vibrations bands are new and appear at 1647, 1565 and 1381 cm^{-1}, respectively. Other new bands are at 1060, 791, 651 and 565 cm^{-1}. We cannot confirm the presence of bipy in this compound as it does not have any band in common.

The microwave-assisted **B3b** also does not have the amine bands, but it has new bands at 1657, 1581 and 1384 cm^{-1} corresponding to the carbonyl group, the C-O asymmetric and symmetric vibrations. This compound share some small bands that correspond to bipy at 1100 and 966 cm^{-1}, but it also has its own unique and new bands at 765 and 659 cm^{-1}.

Compound **B3c** has the amine bands at 3459 and 3302 cm^{-1}, but they are roughly defined. The carbonyl, C-O asymmetric and symmetric from the ATA appear at 1651, 1566 and 1384 cm^{-1}, respectively. The new bands show at 1060 and 763 cm^{-1}.

For the **B3d** compound has very few bands and one is the broad band at approximately 3091 cm-1, indicating the presence of hydroxyl groups. The bands are at 1622 (C=O) and 1397 (C-O symmetric) that are important, but others are missing, such as the C-O symmetric vibration bands. Luckily, we were able to use SCXRD to see what type of compound this is.

As for **B3e**, the diffusion layering compounds, there is no bands for NH_2. The carbonyl band is at 1667 cm^{-1}, the C-O asymmetric at 1577 cm^{-1} and the C-O symmetric at either 1419 or 1343 cm^{-1}. The spectra doesn't have any new bands, which indicates nothing new was formed.

To conclude the **B3**'s FTIR analysis, we have compound **B3f**. It does not have any new bands not NH_2 bands. The presence of a broadish band at 1693 cm^{-1} is conceded to the C=O bond from the free ATA, as the bonded molecule appears at 1621 cm^{-1} in the spectra, while the C-O asymetric and symmetric show at 1600 and 1377 cm^{-1}.

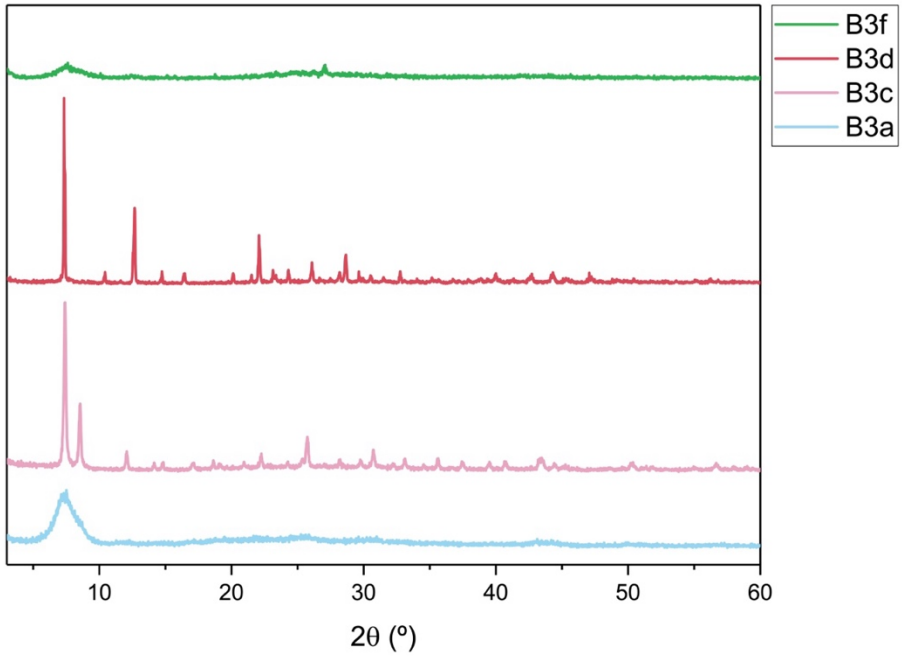

Figure 89. PXRD diffractograms for the **B3** compounds.

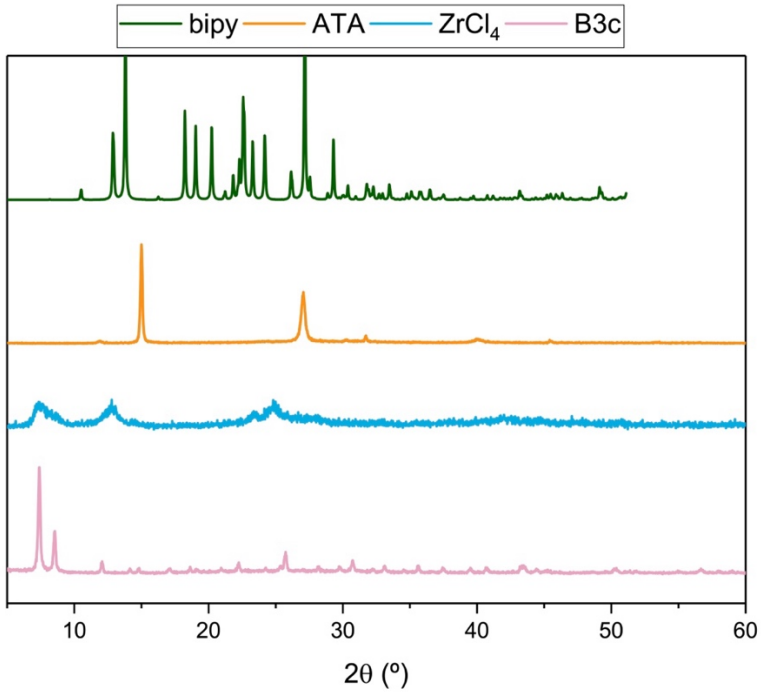

Figure 90. Comparison between the PXRD data for **B3c** and the reagents.

In **Figure 89** is represented the PXRD diffractograms for the **B3** compounds, while in **Figure 90** compound **B3c** is compared to the reagents. Compounds **B3a** and **B3f**, as they only have one or two peaks, were analyzed and their diffractograms are represented in **Annexes A.70** and **A.73**, and compound **B3d**'s is compared against the reagents in **Annexes A.79**.

B3a has very low crystallinity and only one peak at 7.53º that doesn't belong to any reagent. The same happens for **B3f,** but with two peaks at 7.47º and 27.04º, which the first corresponds to $ZrCl_4$ and the second to ATA or bipy.

B3c is a crystalline sample with intense peaks at 7.38º, 8.53º, 25.72º and 30.76º, and other medium to low intensity peaks. None of the peaks correspond to ATA or $ZrCl_4$, but the intense peak at 25.72º matches bipy's diffractogram, as well as some peaks at 18.59º, 20.92º, 22.23º, 29.86º, 34.57º, 35.59º and 45.36º. It also has peaks above 50º at 50.24º and 56.81º. Therefore, we can infer that the sample is probably from a new metalorganic compound.

Finally, for crystalline compound **B3d**, the intense peaks appear at 7.32º, 12.68º, 22.07º, 26.09º and 28.64º, the first two belonging to $ZrCl_4$ plus one at 23.28º, as well as some peaks at 26.09º and 28.64º. The ATA corresponding peaks appear at 27.28º and 31.49º. Bipy matches the peaks at 10.42º, 21.52º, 26.70º, 29.63º, 32.74º, 35.14º and 45.44º. It also has various other unique peaks with medium to low intensity and at 55.28º and 56.14º.

To conclude, **B3f** is a physical mixture of reagents and **B3c** seem promising as a potential new metal-organic material.

The only **B3** compound to be analyzed through SCXRD was **B3d**, as it had big, colorless crystals. The data for this compound was not very good and it showed a great amount disorder. Therefore, it was only identifiable that the compound formed a Zr-cluster, but the final structure and its composition is still undefined.

2.1.2.4.15 Characterization of B6

The **B6** compounds, with the expected structure represented in **Figure 91**, which were synthesized through microwave-assisted and diffusion layering techniques were characterized and compared against each other and against the starting materials.

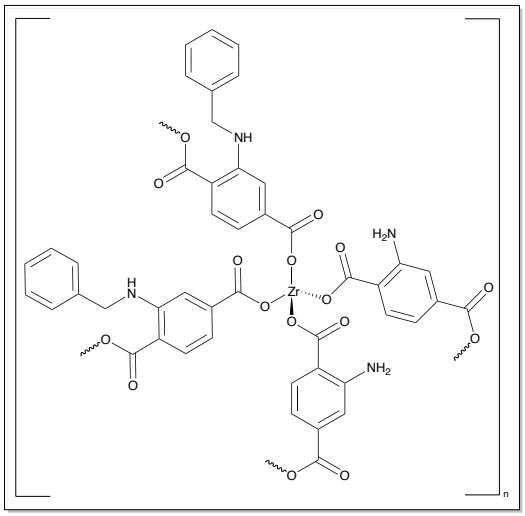

Figure 91. Expected structure for the **B6** compounds.

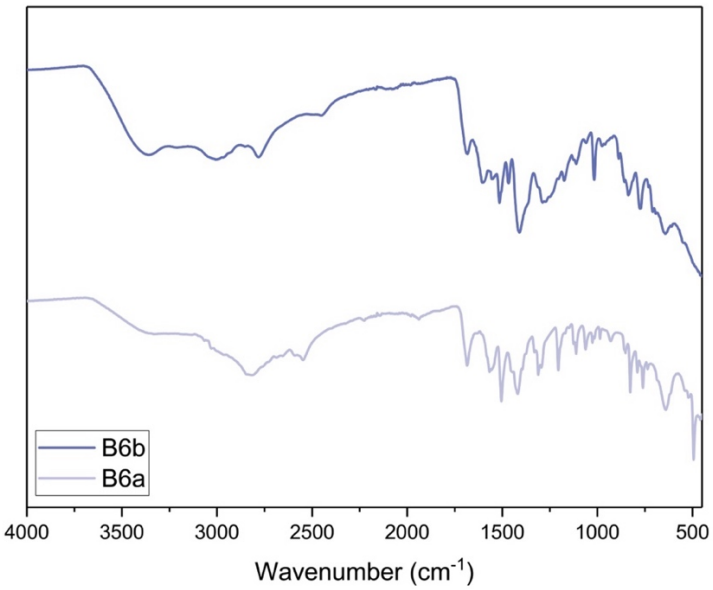

Figure 92. FTIR spectra for the **B6** compounds.

The FTIR spectra for both samples are represented in **Figure 92**. The spectra for both do not differ much in general. Both spectra have a very broad O-H band in the area where the amine bands appear, therefore, those are not appointable. This samples do not seem very promising as new MOFs due to the presence of 1682 (**B6a**) and 1680 cm^{-1} (**B6b**) bands, exactly where the C=O bands for the free ligands are in their spectra, which indicates that the compounds were not formed, and these samples are physical mixtures of reagents.

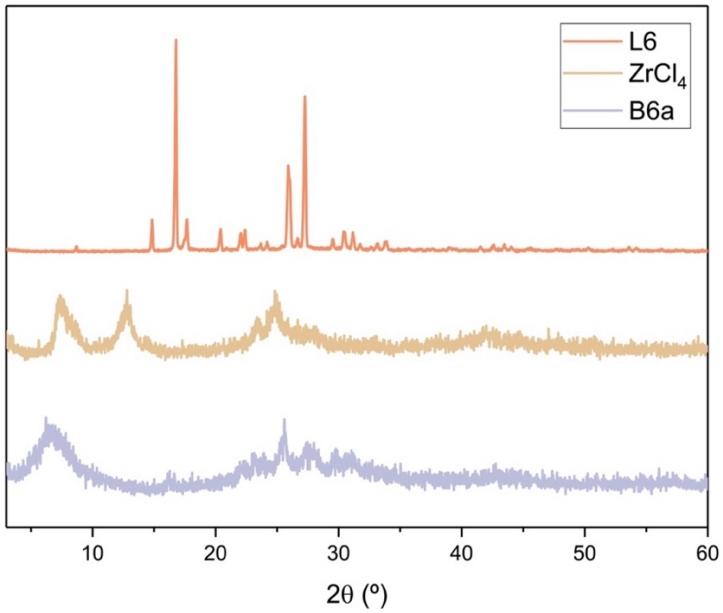

Figure 93. Comparison between the PXRD data for **B6a** and the reagents.

As we can see in **Figure 93**, the compound **B6a** has very low crystallinity and four better defined peaks are roughly around 8.83º, 25.66º, 27.77º and 30.04º. The first two peaks seem to correspond to $ZrCl_4$.

2.1.3 MOFs for Photocatalysis

Under the scope of this master thesis, besides the MOFs and materials synthesized during this project, some Cu-, Co-, Cr-, Zn- and Zr-MOFs prepared by the group of Dr. Salete Balula and Dr. Luís Cunha-Silva at the LAQV-REQUIMTE, Faculdade de Ciências da Universidade do Porto, were received to be tested as photocatalysts for hydrogen production from water splitting. Both pristine MOFs and doped MOFs were tested.

2.1.3.1 Characterization of the Pristine and Doped MOFs

All the materials were characterized by UV/Vis DRS spectroscopy.

2.1.3.1.1 UV/Vis DRS Analysis

Starting with the cobalt material, **ZIF-67**, and the zinc/cobalt MOF doped with a cobalt polyoxometalate (POM), **PW_{11}Co@Co-ZIF-7**, in **Figure 94** is represented the Transformed Kubelka-Munk DRS spectra, while **Figure 95** represents the Tauc's plot of $(f(R)hv)^2$ *versus* energy (eV).

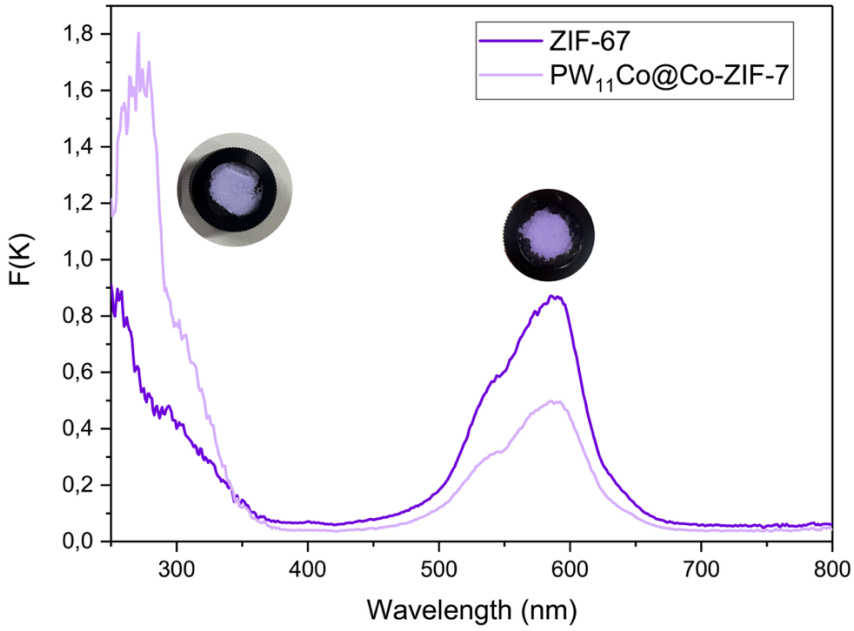

Figure 94. Transformed Kubelka-Munk DRS spectra for **ZIF-67** and **PW_{11}Co@Co-ZIF-7**.

The range of absorption for the pristine MOF, **ZIF-67**, is from 250 to 350 nm and from 500 to 630 nm, absorbing in the UV-B range and in the visible region. For the doped ZIF-7, the range is almost the same, from 250 to 340 nm and from 510 to 630 nm. The color of the compounds didn't differ much, only a slight change in tone, with **PW_{11}Co@Co-ZIF-7** being a lighter purple. Thus, a significant difference in the hydrogen production performance should

not be observable between the two. Their purple color is related to the low absorption area at 390-450 nm.

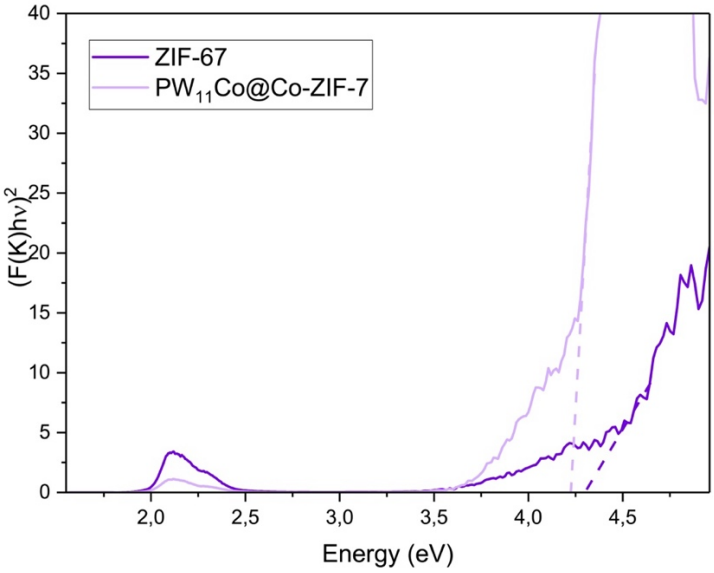

Figure 95. Tauc's plot for **ZIF-67** and **PW_{11}Co@Co-ZIF-7**.

As for the band gap (**Figure 95**), the **ZIF-67** has a band gap of 4.30 eV and **PW_{11}Co@Co-ZIF-7** a value of 4.26 eV. The literature shows that the expected band gap value for **ZIF-67** is 4.3 eV [121], which matches the experimental value, but for the **PW_{11}Co@Co-ZIF-7**, as it is a new material, no value was found.

For the copper material, **Cu-BTC**, **Figure 96** depicts the Transformed Kubelka-Munk DRS spectra and **Figure 97** the Tauc's plot for the band gap calculation.

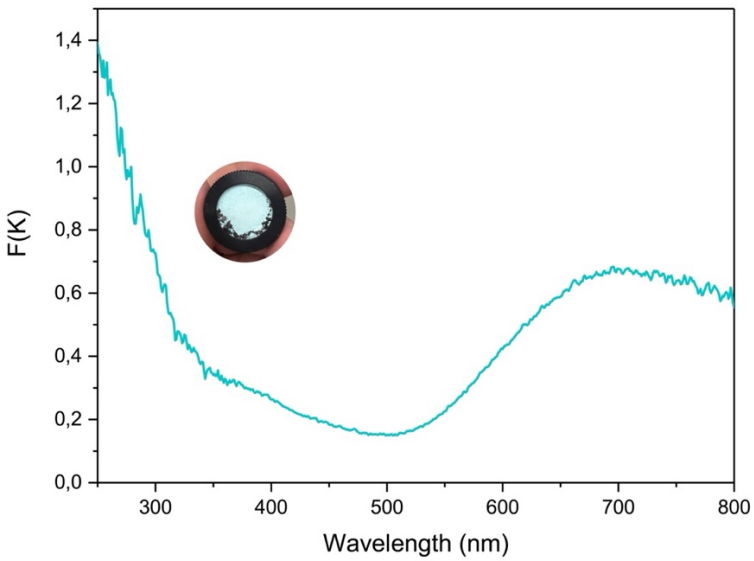

Figure 96. Transformed Kubelka-Munk DRS spectrum for **Cu-BTC**.

The **Cu-BTC** has a range from 250 to 360 nm and from 560 to 800 nm, which translates to it absorbing in the UV and in the visible areas. We can also infer that this compound will

absorb beyond 800 nm, as observable, into the IR range. The blue-green area (470-550 nm), where the compound absorbs very little, corresponds to the color the material has.

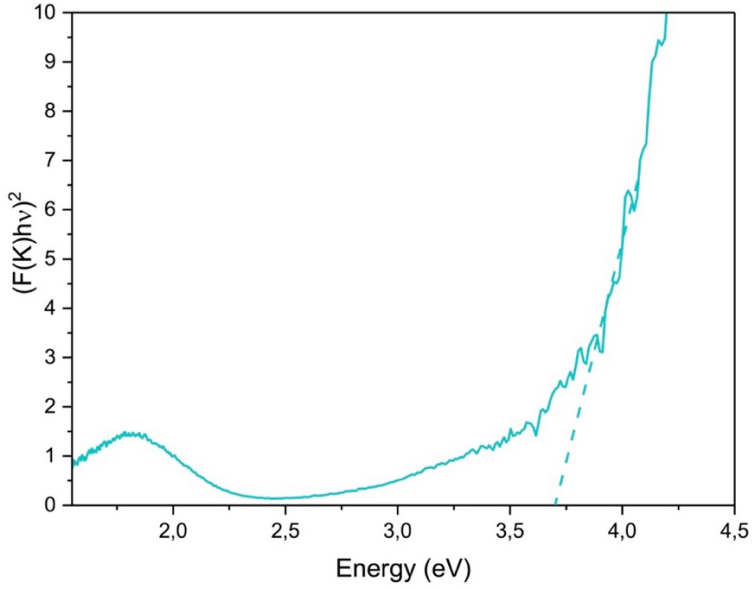

Figure 97. Tauc's plot for **Cu-BTC**.

The band gap for this copper material is 3.69 eV, as seen in the Tauc's plot (**Figure 97**). The value reported in the literature is of 3.68 eV, which is in agreement with the experimental one [122].

As for the pristine Cr-MOF, **MIL-101**, the Transformed Kubelka-Munk DRS spectrum is represented in **Figure 98** and the Tauc's plot in **Figure 99**.

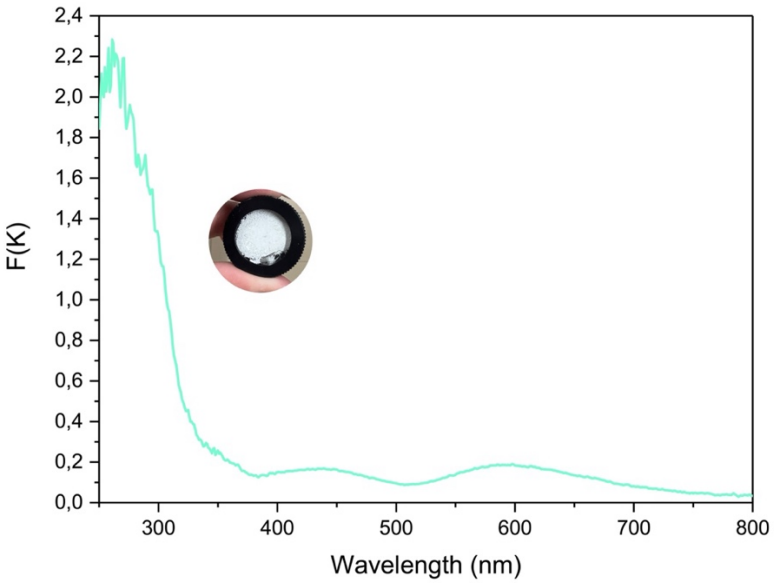

Figure 98. Transformed Kubelka-Munk DRS spectrum for **MIL-101**.

The DRS spectrum with three main bands shows that the material absorbs from 250 to 320 nm, 380 to 480 nm and 520 to 640 nm, which checks with Huyen and coworkers' results

[123]. This indicates that this compound absorbs in the UV range and some small regions of the visible. Its greenish/blue color corresponds to the area of the spectra that the compound absorbs the least (roughly 500-550 nm).

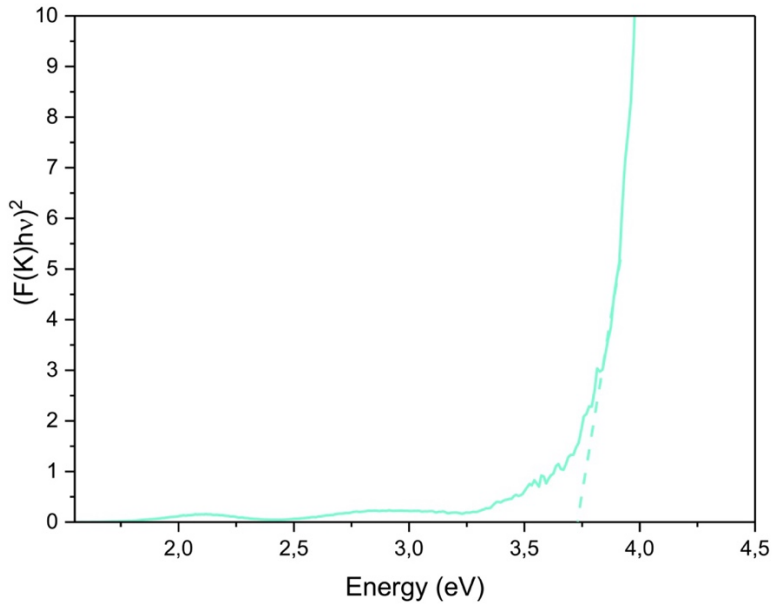

Figure 99. Tauc's plot for **MIL-101**.

As for the Tauc's plot, in **Figure 99**, the band gap for **MIL-101** is 3.73 eV, which is not ideal. In the literature, the value reported by Huyen is of 3.42 eV – 0.31 eV off the experimental value.

Moving to the doped Zr-MOF, **PMo_{12}@MOF-808**, the DRS spectrum is in **Figure 100** and the Tauc's plot is in **Figure 101**.

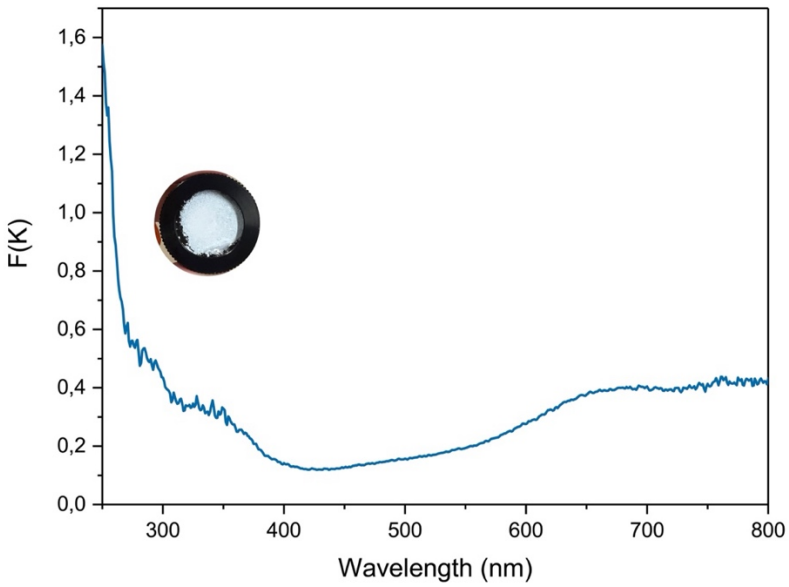

Figure 100. Transformed Kubelka-Munk DRS spectrum for **PMo_{12}@MOF-808**.

PMo_{12}@MOF-808 absorbs in the 250 to 350 nm and in the 620 to 800 nm, roughly, which correlates to the UV and a part of visible light. As the 400-500 nm zone is where the compound absorbs the least, conferring it its blue color.

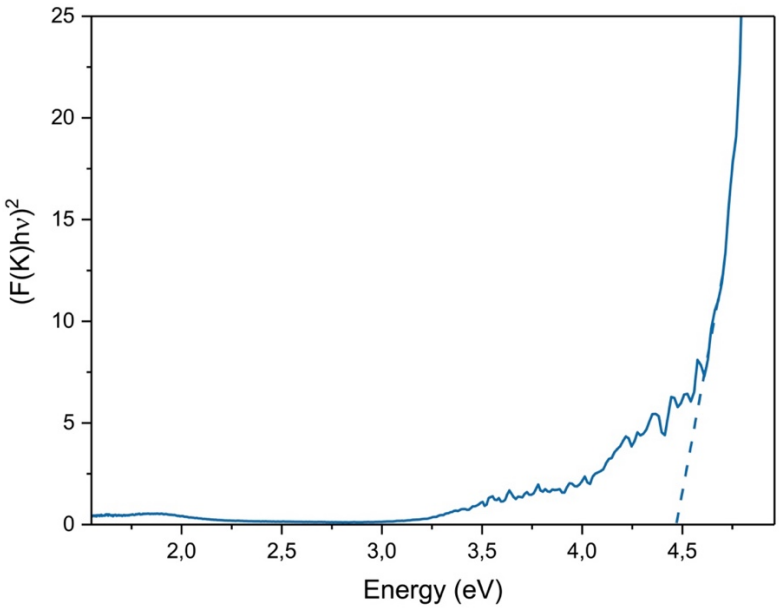

Figure 101. Tauc's plot for **PMo_{12}@MOF-808.**

The band gap for this ferrous material is 4.47 eV, which is higher than the other materials tested.

Rounding all the results up, **Table 32** shows us the band gaps for each material.

Table 32. Band gaps for the pristine and doped MOFs.

Material	Experimental Band Gap Value (eV)	Literature Band Gap Value (eV)
ZIF-67	4.30	4.30
PW_{11}Co@Co-ZIF-7	4.26	--
Cu-BTC	3.69	3.68
MIL-101	3.73	3.42
PMo_{12}@MOF-808	4.47	--

The results state that these materials don't seem very promising as photocatalysts for the hydrogen production by water splitting due to their wide band gap, thus not being able to harvest most of solar light, with values over 3.50 eV. Following the band gaps information, the

pristine MOFs, **Cu-BTC** and the **MIL-101**, are the better candidates out of these materials, so they are expected to perform better than the other metal MOFs.

2.1.4 Reference Photocatalyst

2.1.4.1 Synthesis of 3:2 CdS/ZnS Photocatalyst

The 3:2 CdS/ZnS photocatalyst was used as a reference for the photocatalytic studies performed using the synthesized materials, as it was previously tested in the same conditions with a good performance.

Following a procedure from Antoniadou et al. [124], the photocatalyst was synthesized through the dropwise addition of NaS solution to the heated Cd/Zn solution under stirring, followed by the filtration of the precipitate and its drying in the oven, obtaining an orange solid with a good yield.

2.1.4.2 Characterization of the CdS/ZnS Photocatalyst

With the objective of studying the comparison in the H_2 production between a milled and a non-milled sample of the Cd/ZnS photocatalyst, PXRD and DRS analyses were carried out. This material was obtained as different colored solids: a light orange for the milled sample and a bright orange when the material was not milled. The milling was performed using a Retsch PM 100 in a 50 mL agate jar with three 10 mm balls for 1H at 500 rpm.

2.1.4.2.1 PXRD Analysis

A PXRD analysis was performed for both milled and non-milled samples (**Figure 102**) to see if there was any composition change in the material.

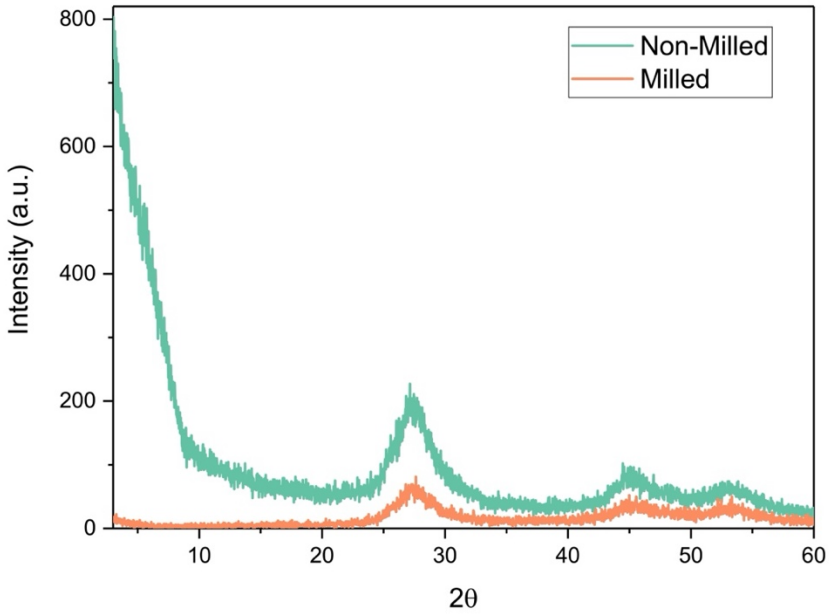

Figure 102. PXRD diffractograms for 3:2 CdS/ZnS Photocatalyst.

No differences were seen in the peaks; therefore, we can conclude that the material didn't suffer any composition changes during the milling process. However, the intensity of the peaks is not similar. In fact, the milled sample shows slightly less intense and broader peaks in its diffractogram, which can be attributed to the fact that the crystallites are smaller, and, therefore, a lower degree of crystallinity. This is in agreement with the more faded color displayed by the material.

2.1.4.2.2 UV-Vis DRS Analysis

Since there was a minor color change after the milling, both samples were analyzed by DRS (**Figure 103**).

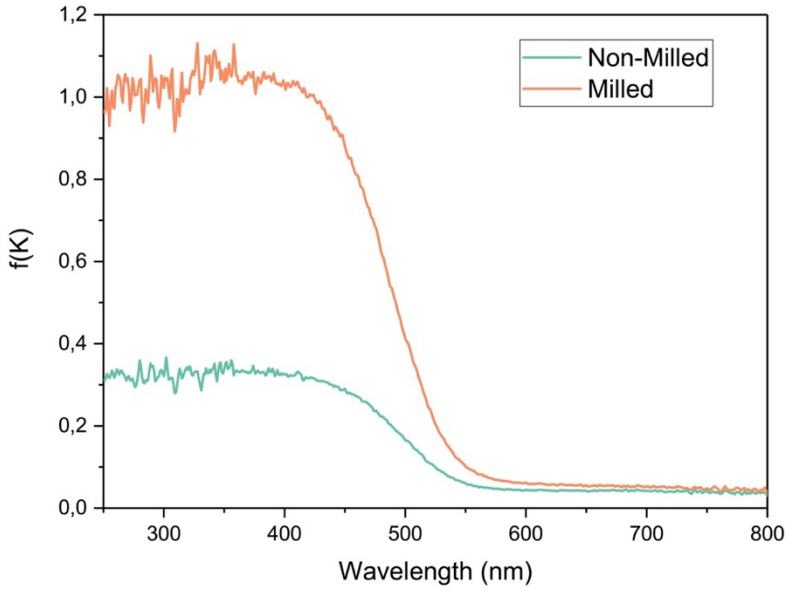

Figure 103. Diffuse reflectance spectra for 3:2 CdS/ZnS photocatalyst.

The small change that can be observed is that the non-milled absorbs in the 250-520 nm range, while the milled absorbs in the 250-540 nm, which can be disregarded.

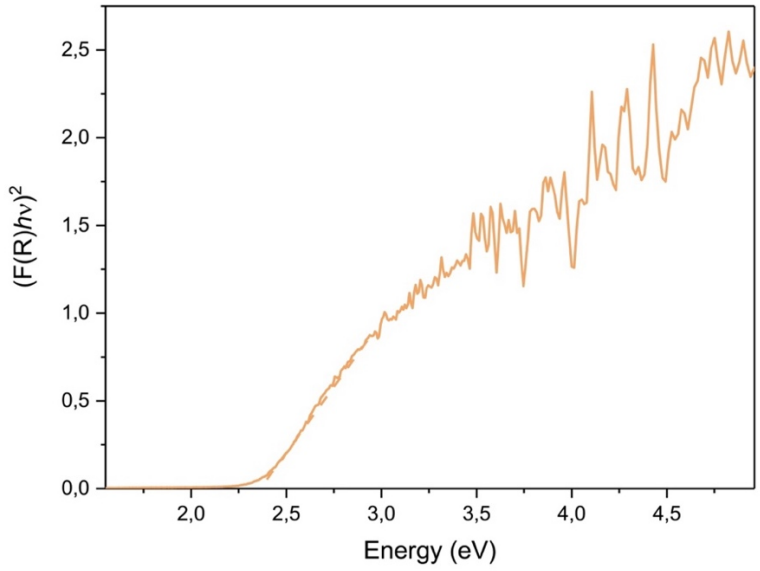

Figure 104. Tauc's plot for 3:2 CdS/ZnS photocatalyst.

The value for the reference photocatalyst's band gap is of 2.37 eV, which is close to the ideal value for a water splitting photocatalyst (2.00 eV), indicating its capacity to efficiently harvest solar light.

2.2 Applications

2.2.1 Structural determination using the Crystalline Sponge Method (CSM)

Resorting to the CSM, Fujita's sponge was used as the host structure for the determination of the molecular structure of compounds which were liquids at room temperature or poorly crystallizable and with no previously reported 3D structure.

The obtention of the 3D data for a guest molecule through the CSM implies its inclusion in the host by soaking for at least three days. The solvent in which the sponge was formed is removed and the crystals are rapidly soaked in the guest, if liquid. If the guest is solid, it is usually dissolved in dichloromethane (DCM) or other solvent for the soaking. The soak must be added fast due to the solventless sponge crystal being unstable and leading to crystals' cracking, diminishing in this way their quality for SCXRD analysis.

Other solvents were trialed for soaking, since not all the compounds dissolve in DCM. Experiments conducted in water prove that crystals typically show cracks within a 24-hour period. In contrast, methanol generally allows for a prolonged stability of the crystals, although some crystals display signs of cracking. Acetonitrile (MeCN) is a better alternative to both, as it maintains crystals of decent to high quality for nearly five days. DCM is identified as the most effective solvent for the soaking process, as it usually preserves the crystals' integrity, even after two weeks of exposure.

Using the CSM, Fujita and co-workers proved the method was valid and reproducible with the inclusion of the 2,6-diisopropylaniline, published on Nature Protocols in 2014 [125]. Therefore, since the *o*-isopropylaniline's structure has a similar nature, is used in the preparation of numerous compounds, and was not reported beforehand, we tried to obtain its absolute structure. Fujita's sponge was then soaked in pure *o*-isopropylaniline for three days before the SCXRD analysis. We were successful in the obtention of its 3D structure (**Figure 105**).

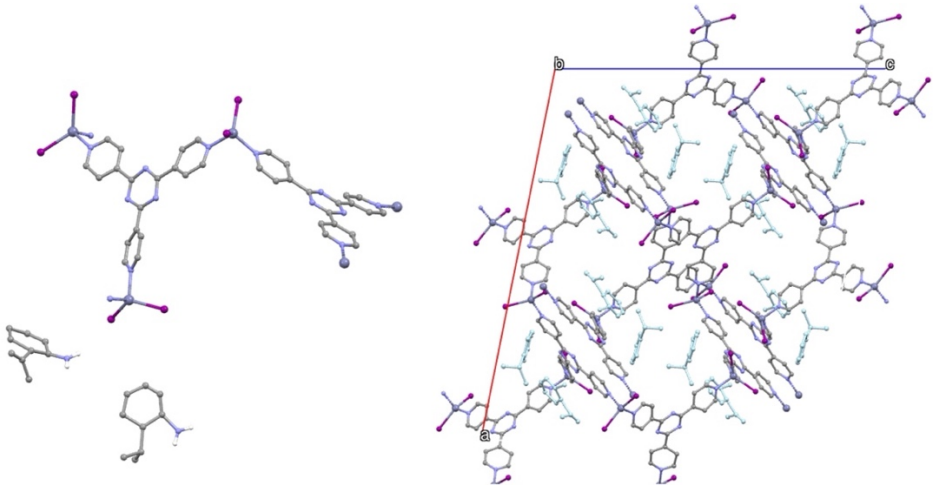

Figure 105. Mercury representation of the inclusion of ***o*-isopropylaniline** (left) and its packing along the *b*-axis (right, light blue).

The host-guest structure crystallized in the monoclinic system, space group $C2/c$, which is the same space group as the vacant Fujita's sponge. The differences between the vacant and the filled-pores is observable in the cell unit dimensions, especially in the *a*-axis. All these alterations are reflected in the volume, as expected, due to the target's presence in the pores. This information can be consulted in detail in **Table 35** (Section 4.3).

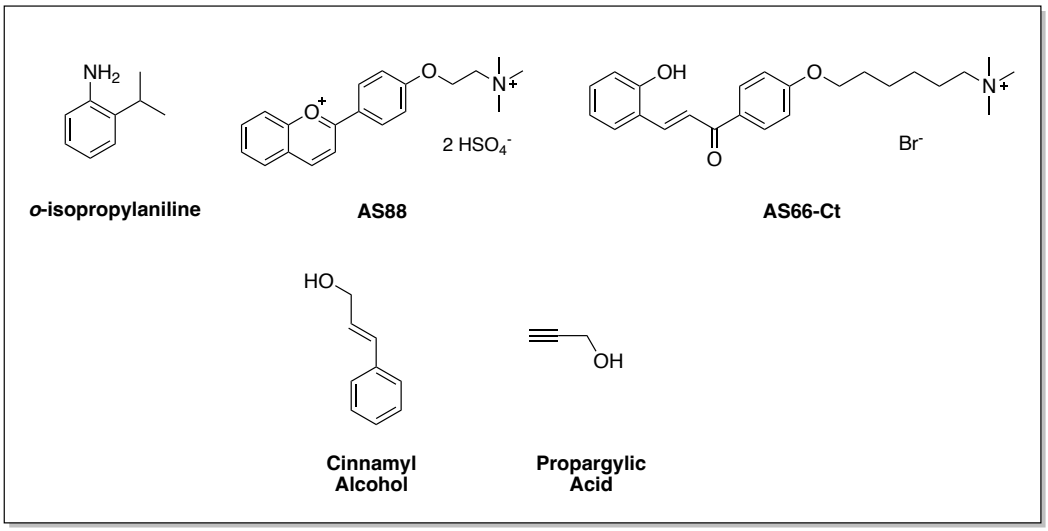

Figure 106. Guest compounds used for CSM.

After the obtention of this structure, we tried to determine the structure of other target compounds, using the same methodology. Those compounds are the flavylium **AS88**, **AS66-Ct**, cinnamyl alcohol and propargylic alcohol (**Figure 106**). **AS88** and **AS66-Ct** are respectively

a flavylium cation and a chalcone, which, although they are solids, are very difficult to crystallize on their own. As for the alcohols, we decided to try to encapsulate them as they are also important compounds in the preparation of relevant organic derivatives, as well as they can also perform as substrates in catalytic oxidation reactions.

The first two compounds exhibit low solubility in "sponge-stable" solvents, i.e., solvents that don't decompose the crystals, such as DCM or chloroform. Consequently, the crystals suspended in MeCN remained stable for four days, while those in methanol lasted about three days; however, only one or two remained intact. Subsequent analysis indicated that the compound was not encapsulated within the sponge.

The cinnamyl alcohol was attempted in two different ways: 1) the pure compound and 2) the compound dissolved in DCM. The SCXRD data was collected, and the unit cell seemed promising. However, it was only possible to modulate the electronic density correspondent to the sponge's structure, as the electronic density inside the pores were very disordered. Therefore, we could not modulate it to confirm the alcohol's presence.

The propargylic alcohol was prepared in a ratio of 10 μL per 100 μL of DCM and used to soak the sponges. The structure was determined in Fujita's sponge and is represented in **Figure 107**.

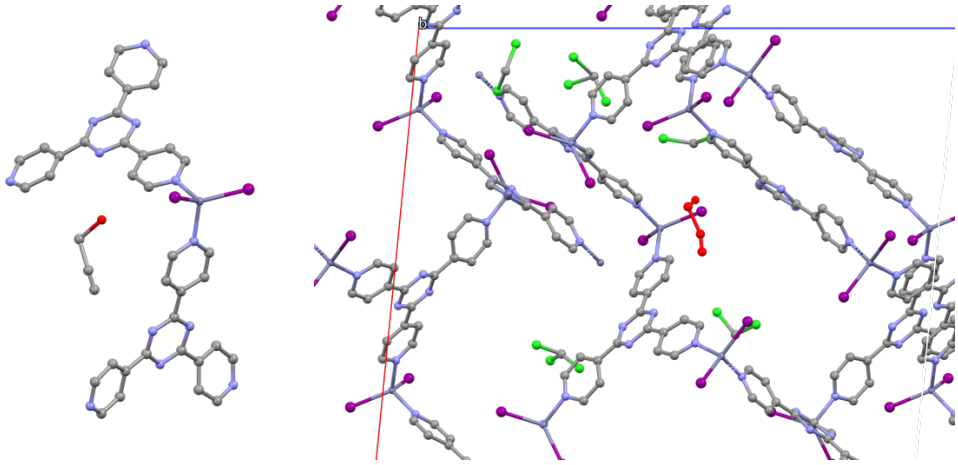

Figure 107. Mercury representation of the inclusion of **propargylic alcohol** (left), with chloroform omitted for clarity, and its packing along the *b*-axis (right, red).

The crystal for this compound is in the monoclinic system comprehended in a $C2/c$ space group. The alterations occur in the dimensions of the network when compared to the sponge with chloroform molecules, such as the *a* and *c*-axis and the β angle, as well as in volume, but, contrary to what its expected, the volume of this crystal diminished in around 1400 $Å^3$. This is due to the pores also containing numerous molecules of solvent besides the alcohol.

MOF1 and **MOF2** were also tested as potential crystalline sponges, using 2,6-diisopropylaniline as the guest molecule, as well as DCM and $CHCl_3$. The use of chlorinated solvents, such as chloroform and dichloromethane, that have a simple and small structure was attempted, as chlorine is a heavy atom, therefore its presence in an electronic density map would be easier to spot if the molecule was encapsulated. The objective was to observe through SCXRD if the materials were microporous or simply had size-limiting pores. Various crystals

were tried, and all showed just the initial structure of the MOF, with no guest inside its pores, confirming their microporous nature.

A zirconium cluster, formed using $ZrCl_4$, bipy and ATA through a microwave-assisted method in H_2O, **B3d**, was attempted to use as a sponge since it had good and stable crystals. The soaking in 2,6-isopropylaniline decomposed the crystals after one day, while soaking with pure cinnamyl alcohol and DCM dissolved cinnamyl alcohol lasted at least two weeks without decomposition or crystal cracking. The crystals of this system (**B3d** with the cinnamyl alcohol) were analyzed by SCXRD, but due to the data collection being performed at room temperature, there was a lot of disorder in the cluster's structure and in the remaining electron density that, so far, was not possible to attribute besides the cluster. Thus, the resolution of the structure remains pending.

2.2.2 Photocatalytic Hydrogen Production by Water Splitting

The synthesized materials were tested as photocatalysts in hydrogen production through water splitting. Two different sacrificial agents were tested in our system: a sulfur-based system and a water/methanol system. The apparent quantum efficiency (AQE) was calculated for each material.

The experiments were conducted with 50 mg of a material in 90 mL of SA in a glass reactor attached to a glass graduated pipette, so the volume increase can be measured and the quantity of H_2 calculated (**Figure 108**).

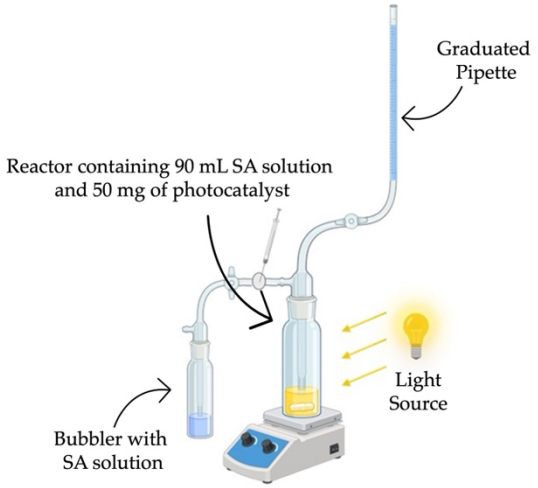

Figure 108. System montage for the hydrogen production by water splitting (Adapted from Sahin and Koca [126]).

2.2.2.1 3:2 CdS/ZnS Photocatalyst

The photocatalyst used for reference, the inorganic material composed of a 3:2 CdS/ZnS ratio, was tested in our system with Na_2S/Na_2SO_3 as a sacrificial agent. Two different samples were used to understand whether the material's milling showed any difference in the production.

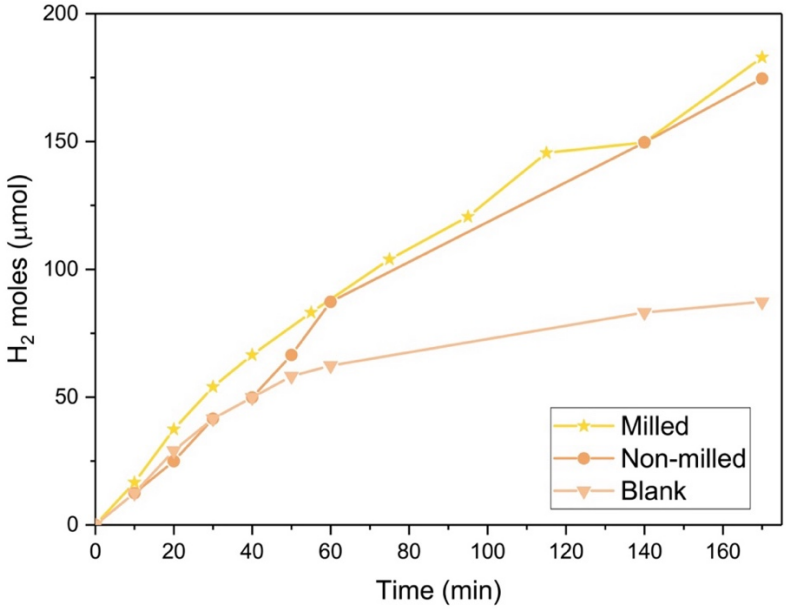

Figure 109. Hydrogen production (moles of H_2 (µmol) *vs.* time (min)) for **3:2 CdS/ZnS** compared to the blank (Na_2S/Na_2SO_3 without photocatalyst).

As observed in **Figure 109**, the non-milled 3:2 CdS/ZnS barely produces less than the milled photocatalyst. After 160 minutes, the milled sample produced 182.91 µmol, while the non-milled produced 174.60 µmol - only a difference of 8.31 µmol. Therefore, we can conclude that the milling of the sample is not required, as it doesn't make a significant difference in the production, overall performing similarly.

2.2.2.2 Reported MOFs

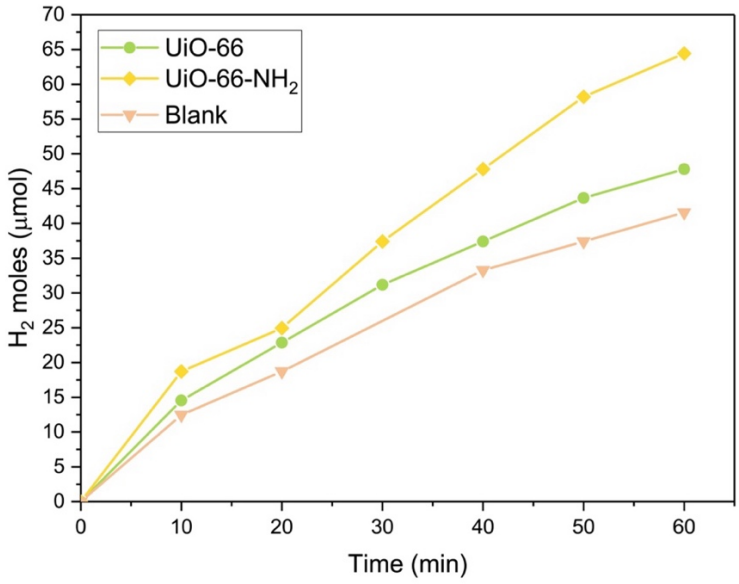

Figure 110. Hydrogen production (moles of H_2 (µmol) *vs* time (min)) for **UiO-66** and **UiO-66-NH_2**. It was compared to the blank (Na_2S/Na_2SO_3).

The graph for the Zr-MOFs, **UiO-66** and its amino-functionalized version, is in **Figure 110**. The quantity produced by **UiO-66-NH$_2$** is bigger than for **UiO-66**. This can be explained by the larger wavelength range in which the UiO-66-NH$_2$ absorbs in, due to the presence of the amino group narrowing the band gap (from 3.92 eV to 2.50 eV) – giving it a boost in solar light harvesting. After an hour, the amino-functionalized compound produces 64.44 μmol and the UiO-66 produces 37.41 μmol, almost half of **UiO-66-NH$_2$** (58%, to be exact).

Using this tendency, we can expect the Zn-MOF **MOF2**, which is also amino-functionalized, to produce more than **MOF1**. Besides the metal, the difference between the Zr-MOFs and the Zn-MOFs, is the presence of two TPT molecules in **MOF1** and **MOF2**'s structure., while the Zr-MOFs are only composed of TA or ATA.

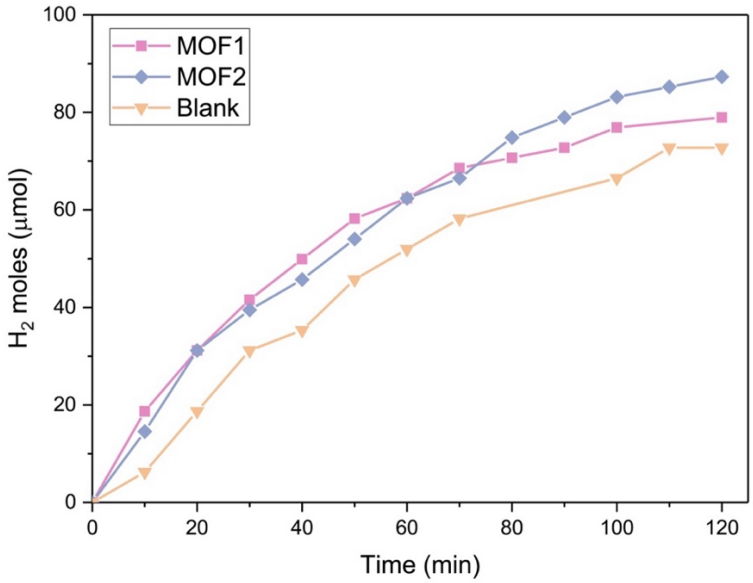

Figure 111. Hydrogen production (moles of H_2 (μmol) *vs* time (min)) for **MOF1** and **MOF2**. It was compared to the blank (Na_2S/Na_2SO_3)

In **Figure 111** is represented the production results of **MOF1** and **MOF2**, in Na_2S/Na_2SO_3 as the SA, are slightly similar to each other after 120 minutes, with the former producing 78.98 μmol and the latter producing 87.30 μmol of hydrogen, a difference of 9.5%. Thus, the disparity in production for the Zr-MOFs is more significant than in the Zn-MOFs.

When compared to the reference photocatalyst in the same conditions, which produces 87.3 μmol after 60 minutes, **MOF2** takes twice that time to obtain the same quantity of hydrogen and **UiO-66-NH$_2$** produces 74% of that value, making in the best hydrogen producing MOF tested in the sulfur-based sacrificial agent. This can best be explained by the 3:2 CdS/ZnS photocatalyst having a narrower band gap (2.37 eV) than the UiO-66-NH$_2$ (2.50 eV) and MOF2 (2.95 eV), meaning that it works better in harvesting the solar light, therefore presenting a better efficiency in the hydrogen production.

The incident photon flux (I_0) was determined by potassium ferrioxalate actinometry. Thus, applicating that value, we were able to calculate the AQE for each material through **Equation 3**.

$$AQE = \frac{2 \times \#\ of\ evoluted\ H_2\ molecules}{\#\ of\ incident\ photons} = \frac{2m}{I_0}$$

Equation 3. Apparent Quantum Efficiency (AQE).

Where m is the slope of the linear regression for the graph representing the quantity of hydrogen (mol) *vs.* time (s), and I_0 is 8.27×10^{-7} mol/s. The AQE values are represented in **Table 33**.

Table 33. AQE percentages for the reported MOFs in aqueous Na_2S/Na_2SO_3.

Material	AQE (%)
UiO-66	4.62
UiO-66-NH_2	4.62
MOF1	6.94
MOF2	6.94

In **Table 33**, we can see that Zn-MOFs, **MOF1** and **MOF2**, have a better efficiency in the sulfur-based system than the Zr-MOFs, **UiO-66** and **UiO-66-NH_2**.

The performance of each MOF as a photocatalyst was also calculated through the quantity of H_2 produced by the 50 mg of compound per hour, as a way to obtain more comparable results. **Table 30** shows the values for the production after 60 and 120 minutes for all the MOFs in Na_2S/Na_2SO_3.

Table 34. Production values in mmol g^{-1} h^{-1} for the tested MOFs.

Material	n(H_2) / mmol g^{-1} h^{-1}
UiO-66	9.56 (60 min) 12.89 (120 min)
UiO-66-NH_2	12.89 (60 min) - (120 min)
MOF1	12.48 (60 min) 15.80 (120 min)
MOF2	12.47 (60 min) 17.46 (120 min)

We can observe in **Table 34** that UiO-66-NH_2 produces the same quantity in one hour that UiO-66 in two, thus we can assume that in two hours it will produce more than the non-

amine-functionalized MOF. **MOF1** and **MOF2** produce about the same quantity in one hour, but a significant difference can be observed at the two-hour mark with **MOF2** producing more.

Typically, the Na_2S/Na_2SO_3 sacrificial agent system is more effective for materials containing sulfur in its composition, such as the reference photocatalyst [127]. Consequently, a new system was tested using an 80:20 water/methanol (H_2O/MeOH) mixture as the sacrificial agent, given that methanol is the most commonly employed SA for oxide photocatalysts. The enhanced performance exhibited by the amino-functionalized MOFs in the previous sacrificial agent is expected to be reproduced in the new system.

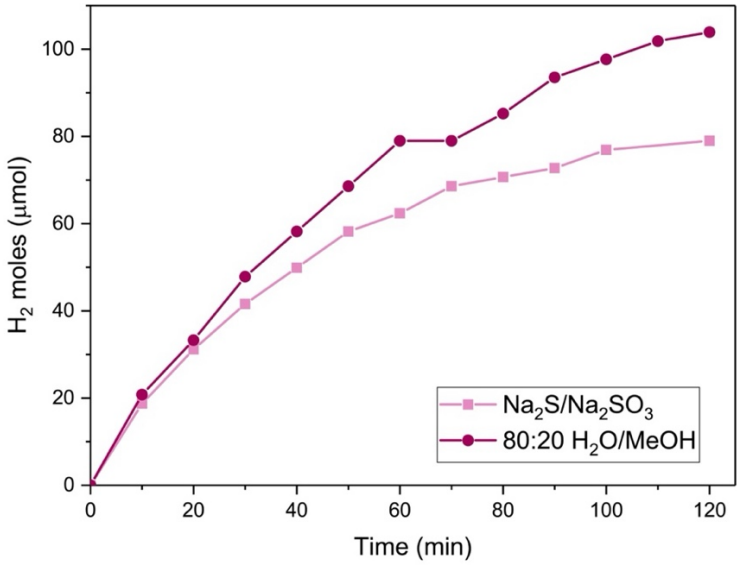

Figure 112. Comparison of **MOF1's** performance in two different sacrificial agent systems: Na_2S/Na_2SO_3 and 80:20 H_2O/MeOH.

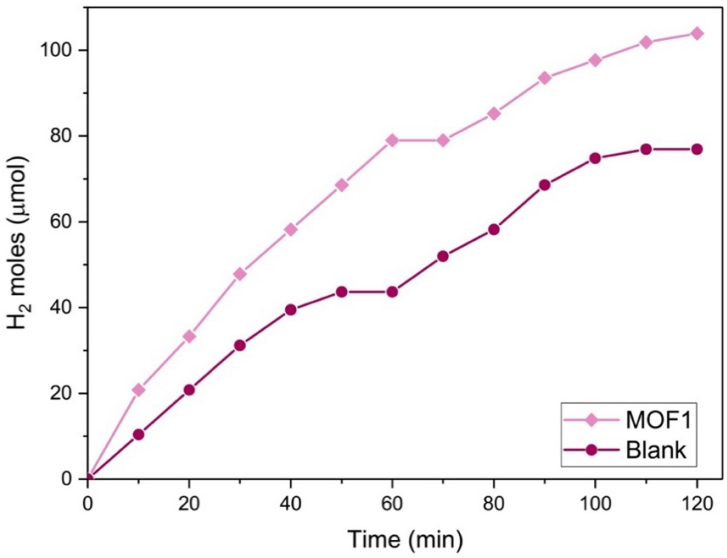

Figure 113. Comparison between the blank (80:20 H_2O/MeOH) and **MOF1** in 80:20 H_2O/MeOH.

The comparison between the sacrificial agents is expressed in **Figure 112** for **MOF1**. We can conclude that the oxide MOFs do, in fact, produce more hydrogen in a methanol

system than in a sulfide one. After 120 minutes, **MOF1** produces 78.98 μmol in the sulfide system and 103.93 μmol in the methanol system, an increase in hydrogen of 31.6%. We can also see the difference between the blank run (using only 80:20 H_2O/MeOH) and **MOF1** in that media in **Figure 113**.

Following the first run in the aqueous methanol system, **MOF1**'s usual yellowish tone completely changed to a lilac color. We found this phenomenon very interesting and decided to perform a FTIR and PXRD analysis to see which modifications the compound went through.

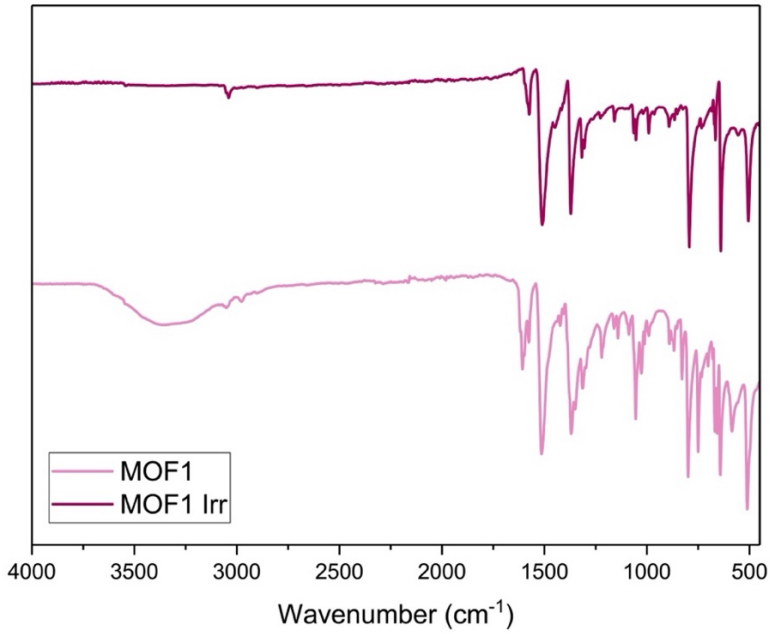

Figure 114. FTIR comparison between **MOF1** and MOF1 after irradiation (**MOF1 Irr**).

The FTIR for both compounds is represented in **Figure 114**. No new bands are visible, but some of the previously existing disappeared or lost intensity. In the normal **MOF1**, we can see the band at 1609 cm^{-1} represents the C=O bond of the TA ligand's carboxylate group, but this band is not observable in the irradiated **MOF1**, possibly indicating the reduction of the carbonyl group. At 1575 cm^{-1}, both samples have bands that correspond to the C-O asymmetric stretching vibrations from TA, but also from C=C stretching of the TPT rings. The C=N stretching vibration of TPT and C=C stretching of the TA's benzene ring appear at 1511 and 1514 cm^{-1}, while C-C mode's ring deformation for TPT and C-O symmetric stretching vibrations in TA appear at 1371 and 1369 cm^{-1} for **MOF1 Irr** and **MOF1**, respectively. In the Zn-O modes zone (1000-400 cm^{-1}), bands such as the ones at 1050, 867, 734, 667 and 585 cm^{-1} diminished in intensity when compared to the ones in **MOF1**, while some remained the same such as the bands at 992, 794, 640 and 505 cm^{-1}.

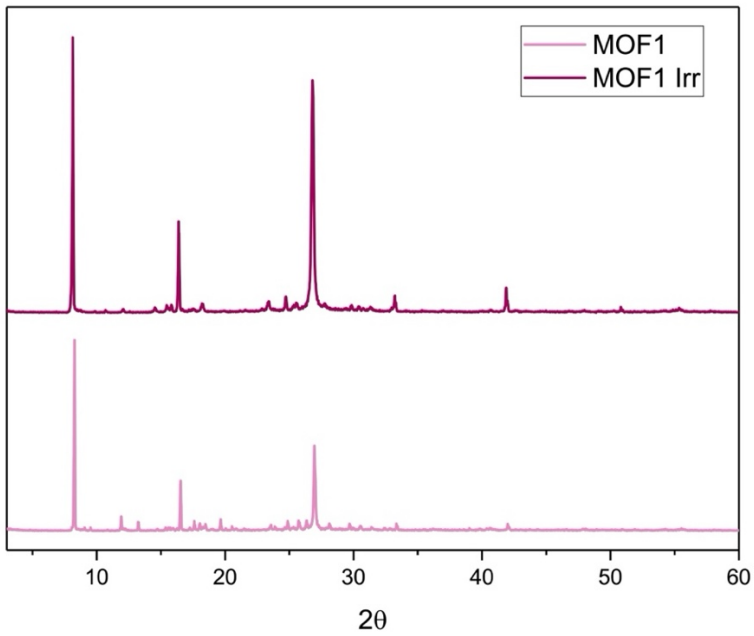

Figure 115. PXRD comparison between **MOF1** and the irradiated **MOF1** (**MOF1 Irr**).

In the PXRD, some differences are also observable in **Figure 115**. Almost all peaks from the **MOF1 Irr** correspond to some on the **MOF1**, only the peaks at 10.64º, 12.03º, 27.83º and 50.83º are unique to this compound. **MOF1** has medium to low intensity bands that don't correlate to its irradiated version, such as 9.06º, 11.91º, 20.55º, 26.93º and 40.71º, for example. This means the compounds are not exactly the same and **MOF1**, when exposed to the radiation, suffered chemical changes.

After these very successful experiments, we decided to test the other MOFs used in the Na_2S/Na_2SO_3 system in 80:20 H_2O/MeOH, starting with the **UiO-66**. **UiO-66-NH_2** could not be tested as the quantity did not reach the desired amount and there was no time left to synthesize again.

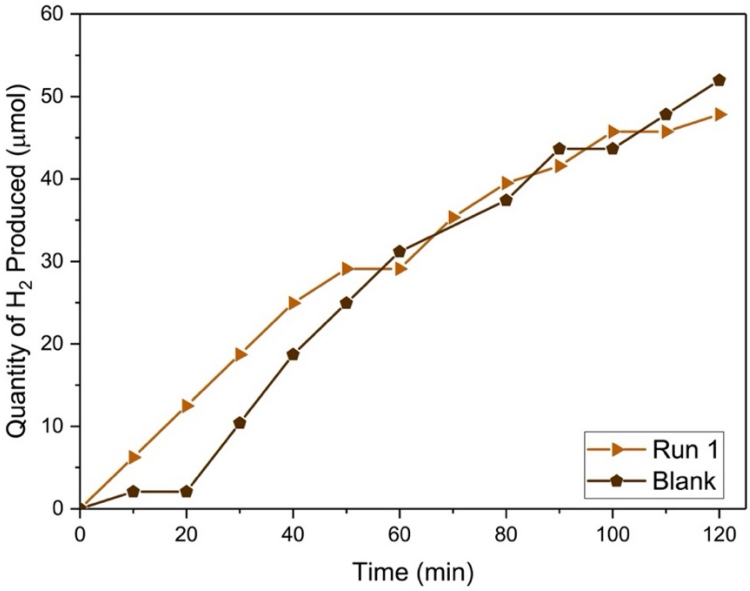

Figure 116. Comparison between the blank (80:20 H_2O/MeOH) and **UiO-66** in 80:20 H_2O/MeOH.

In **Figure 116**, a comparison between the first run for **UiO-66** in the 80:20 H2O/MeOH sacrificial agent and the blank run for only the SA. As seen, the blank run produces more moles of hydrogen than the SA with the MOF. This was not expected, as UiO-66 performed well in the sulfate SA. The data for this run is this way due to a leak in the system during the experiment, when even a slight movement made the volume drop, disturbing the volume analysis. Therefore, this run must not be considered as valid data due to the complications during the measurements.

The values started to feel lower than usual, so another actinometry was performed after proceeding with the tests for **MOF2**. This showed a drop in the incident photon flux, thus influencing the amount of incident light over the reactor and MOF. Still, two runs were performed for **MOF2** in these conditions.

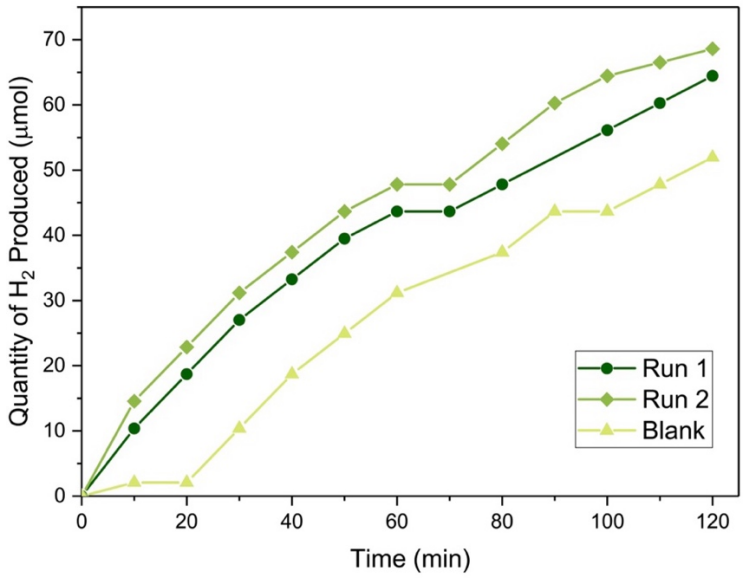

Figure 117. Comparison between the blank (80:20 H_2O/MeOH without photocatalyst) and the runs of **MOF2** in 80:20 H2O/MeOH.

It was expected that **MOF2** acted as a better photocatalyst than **MOF1**, as happened in the other SA system. The issue is: we cannot compare those runs as they were performed under different light intensity conditions. So, the results for each one are comparable between runs of each other and the blank.

MOF2's runs – represented in **Figure 117** – we can clearly see that both produce a bigger quantity of H_2 than the blank. In this system, the difference between the catalyzed production and the blank (without catalyst) production is 16.93 µmol and for the Na_2S/Na_2SO_3 system is 14.55 µmol. Even though the difference is small, we can see that the 80:20 water/methanol system works better for this type of compounds.

2.2.2.3 MOFs for Photocatalysis

Since the 80:20 H_2O/MeOH system worked better for the Zn-MOF, **MOF1**, the same system was applied to the MOFs sent by the Faculdade de Ciências da Universidade do Porto. We started by testing the Co-, Zn/Co- and Cr-MOFs. **ZIF-67** didn't have enough quantity to test in our system, so we advanced to test the **PW_{11}Co@Co-ZIF-67** (**Figure 118**) and **MIL-101** (**Figure 119**). Unfortunately, due to time constraints we were unable to test the remaining compounds. Besides **MOF1**, no other compound suffered any physical changes. Also, these tests were performed after a drop in intensity of the 300W Xe-lamp from 8.42 x 10^{-7} to 2.36 x 10^{-7} mol/s, which could have a direct influence on the quantity of hydrogen produced.

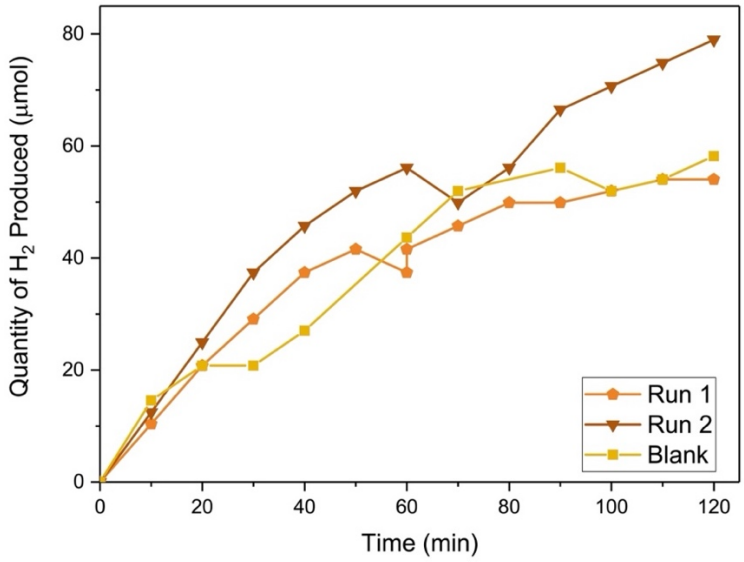

Figure 118. Hydrogen production (moles of H_2 (µmol) *vs* time (min)) for two runs of **PW_{11}Co@Co-ZIF-7** against a blank (80:20 H_2O/MeOH without photocatalyst).

In **Figure 118**, two runs for the **PW_{11}Co@Co-ZIF-67** were reported with 24H of rest in between them. In both runs, a drop in the quantity was observed around 60/70 minutes. In the case of Run 1, the sacrificial solution's volume dropped completely, so it had to be risen again, and, in the case of Run 2, the volume dropped a little bit at the 70-minutes mark. Still, at the end of the 2 hours, Run 2 produced a significant amount of H_2 moles more than Run 1, as it was expected. Since Run 1 didn't work very well due to the volume decreasing issue, the higher production from the blank is no surprise. Thankfully, Run 2 went smoothly and we can observe that the MOF produced more than the blank at the end of 120 minutes in about 20 µmols of surplus.

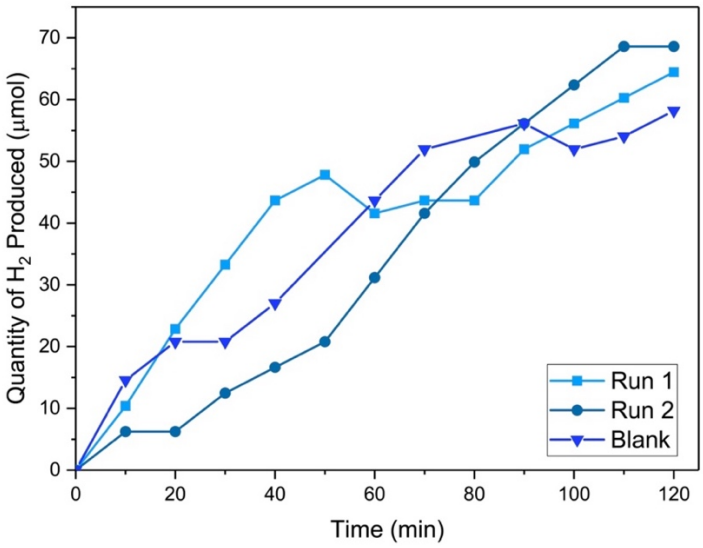

Figure 119. Hydrogen production (moles of H_2 (µmol) vs time (min)) for two runs of **MIL-101**.

In **Figure 119** are represented two runs for the Cr-MOF, **MIL-101**. In Run 1, a decay of volume happens around 60 minutes and stays consistent until the 80-minute mark, then rising again. This behavior doesn't happen with Run 2, the quantity always increases until the last 10 minutes, where it stays consistent. Run 2 produces more at the end of 120 minutes, but, at the end of 60, we can see that in Run 1 more moles were produced. The blank produces more than both runs at 60 minutes, but when two hours have passed, Run 2 produced a larger quantity.

It was expected for **MIL-101** to act better as a photocatalyst, producing more moles, than **PW_{11}Co@Co-ZIF-7** due to their band gaps, the first with a band gap of 3.73 eV and the latter with one of 4.26 eV. This difference in bandgaps can explain the better performance. However, this was not observable in the results, as **PW_{11}Co@Co-ZIF-7** produces more due to its higher absorption in visible light (500 to 650 nm).

We can compare all these results using the mmol g^{-1} h^{-1} calculation (**Table 35**), as to see which material works best in our 80:20 H_2O/MeOH system.

Table 35. Production values in mmol g^{-1} h^{-1} for the tested MOFs.

Material	mmol g^{-1} h^{-1}
UiO-66	5.82 (60 min) 9.56 (120 min)
MOF1	15.80 (60 min) 20.79 (120 min)
MOF2	9.56 (60 min) 13.72 (120 min)
PW_{11}Co@Co-ZIF-7	11.22 (60 min) 15.80 (120 min)
MIL-101	8.31 (60 min) 12.89 (120 min)

As seen in **Table 35**, the result for **UiO-66** is significantly worse than for the other compounds. This is due to a leak in the system during the hydrogen production trial, since the volume was dropping every now and then. The leak plus the intensity of the lamp diminishing gave a low result. As mentioned beforehand, **MOF1** was the only one tested while the lamp presented a good value of intensity, justifying its higher values of production, which is higher than for the Na_2S/Na_2SO_3 system.

We were expecting, in normal circumstances, that **MOF2** produced more moles of H_2 than **MOF1** due to the presence of the amine group. We cannot conclude anything from these results as the runs for **MOF2** were performed after the drop in intensity and there was not enough **MOF1** left to test in the same conditions.

3

CONCLUSION AND FUTURE PERSPECTIVES

The ligands were synthesized using a diverse set of techniques and varying in size, chain length, substituents, aromatic rings, and others. Alternating between ligand combinations and metal salts, we tried to form new MOFs to test as crystalline sponges if adequate and as photocatalysts for hydrogen production.

During several attempts through diffusion layering co-crystallizations of the ligands were obtained as well. Promising yellowish crystals were obtained for **A7**, but the analysis could not be performed as they would not stay fixed on the loop.

Inspired by Fujita's MOF, a new Zn-MOF (**MOF3**) bearing three tpt ligands and two triflate molecules was synthesized and analyzed by SCXRD. During attempts to synthesize more of the new Zn-MOF, the structure for two polymorphs of a cationic complex with two water molecules, two methanol molecules and 2 TPTs in an octahedral arrangement was determined. Following the CSM with Fujita's MOF, we were able to determine the absolute crystalline structure of *o*-isopropylaniline and propargylic alcohol, both liquid compounds at room temperature. Attempts with cinnamyl alcohol were made in Fujita's sponge, but no extra electronic density was detected. A flavylium cation and a chalcone, which never crystallized through regular crystallization techniques dissolved in various solvents, but their insolubility in "sponge-safe" solvents was an issue. Therefore, when the crystals were analyzed, no electronic density was found related to these compounds. **MOF1** and **MOF2** were experimented to evaluate if they could be used as crystalline sponges, but neither 2,6-isopropylaniline nor DCM nor $CHCl_3$ were encapsulated, due to their microporous nature.

During an attempt at synthesizing a new Zr-MOF, a pink solution was left to evaporate for five days and yielded big colorless crystals. After SCXRD analysis, an unreported Zr-O cluster was formed (but the structure is not yet fully refined). This MOF was analyzed as a potential crystalline sponge in 2,6-diisopropylaniline, which decomposed the crystals. When cinnamyl alcohol was employed, extra electron density and disorder were detected during structure solution and refinements, but, so far, we were unable to unambiguously attribute it to the guest, cinnamyl alcohol.

MOF1 and **MOF2** were not reported to being previously tested as photocatalysts in any hydrogen production system, while **UiO-66** and **UiO-66-NH_2** were studied beforehand in a water/methanol as a sacrificial agent system, but not in a Na_2S/Na_2SO_3 system. The results for the hydrogen production using the Na_2S/Na_2SO_3 were good, but we can conclude that the NH_2 functionalized MOFs performed better and, in general, the Zn-MOFs, **MOF1** and **MOF2**, have a higher production of H_2 quantity (15.80 and 17.46 mmol g^{-1} h^{-1} in 120 minutes, respectively). UiO-66-NH_2 has a better performance of all in the first 60 minutes of the experiment (12.89 mmol g^{-1} h^{-1}) but was not evaluated for the full 120 minutes, but we can infer that it would have produced more than the others, as 12.50 mmol g^{-1} h^{-1} is the rounded value for **MOF1** and **MOF2** in 60 minutes.

We expected higher results with the switch to the 80:20 H_2O/MeOH system, as oxide photocatalysts usually perform better. This was confirmed when tests were performed for **MOF1**, which produced 20.79 mmol g^{-1} h^{-1} – a difference of 5 mmol g^{-1} h^{-1} when compared to the production in the other system. The **MOF2** and **UiO-66** were also analyzed, as well as two of the materials sent from the FCUP. However, following new actinometry results, we could observe a very significant decrease in the incident photon flux (I_0), therefore, decreasing the production. **UiO-66** experiment suffered from a leak (due to time constraints we were not able to repeat the experiment), which lowered its production values (5.82 and 9.56 mmol g^{-1} h^{-1} in 60 and 120 minutes, respectively) and **MOF2** produced less than in the Na_2S/Na_2SO_3 system (9.56 and 13.73 mmol g^{-1} h^{-1} in 60 and 120 minutes, respectively). The zinc/cobalt, **PW_{11}Co@Co-ZIF-7**, and chromium, **MIL-101**, materials were tested, with the former having a higher production than the latter (15.80 mmol g^{-1} h^{-1} *vs.* 12.89 mmol g^{-1} h^{-1} in 120 minutes). This was expected according to the absorption ranges expressed in the DRS, as **PW_{11}Co@Co-ZIF-7** absorbs strongly from 500 to 650 nm and **MIL-101** has very low absorption in the visible range, absorbing strongly in the UV zone, even if chromium material's band gap has a better value than the cobalt.

In the future, different solvents or combinations can be used for MOF synthesis, as well as different techniques can be applied, so single crystals can be obtained. Other techniques such as XPS, elemental analysis, SEM and DSC/TGA can be used to confirm the synthesized materials structure. New hydrogen production tests should be performed in the same conditions, so the sacrificial agent systems can be compared. The remaining materials from FCUP are weighed and should be evaluated in our system, as the other two showed promising results even in non-ideal conditions.

4

EXPERIMENTAL PROCEDURES

4.1 Chemicals and Solvents

The metal salts used in the materials' synthesis were obtained commercially. Zinc iodide and zinc trifluoromethanesulfonate are from Sigma Aldrich, and zirconium chloride and zirconium dichloride oxide (octahydrate) were obtained from TCI. The reagents for the preparation of new ligands were also obtained commercially, while some of them were also used as ligands without further modifications. The 2-aminoterephthalic acid, *p*-nitrobenzoic acid, and (1,1'-biphenyl)-4,4'-dicarboxylic acid were bought from BLD Pharm, 4-aminobenzoic acid was purchased from TCI, the 4-formylbenzoic acid from Aldrich and BLD Pharm, *p*-phenylenediamine was obtained from VWR, terephthalic acid and 4,4'-bipyridine was obtained from Alfa Aesar.

The reference photocatalyst was also synthesized from commercial reagents. The cadmium nitrate hexahydrate and zinc nitrate hexahydrate were obtained from Fluka and Merck, respectively. For the preparation of the sacrificial agent, sodium sulfite from Honeywell and sodium sulfide from Alfa Aesar were used.

4.2 General Experimental Conditions

Thin-layer chromatography (TLC) was performed using pre-coated aluminum sheets ALUGRAM® Xtra silica gel 60 with fluorescent indicator UV254 and observed under 254 nm light.

Mechanochemistry reactions were performed in a Retsch PM 100 ball mill, in a 50 mL agate jar with 10 mm or 7 mm agate balls or in a 10 mL stainless steel jar with 7 mm balls, at a frequency of 500 rpm.

The ^{1}H NMR spectra were acquired using a Bruker Avance III 400 and a Bruker Avance III 500 at 25ºC using DMSO-d6 as a deuterated solvent. Setting TMS as a reference, the chemical shifts were reported in ppm using the 2.50 ppm signal DMSO-d6 as residual solvent. The signal multiplicities have been abbreviated as s (singlet), d (duplet), t (triplet), q (quartet), m (multiplet), and dd (duplet of duplet). The ^{1}H NMR characterization is described in the

following way: chemical shift (multiplicity, [coupling constant], integration, attribution). The spectra were posteriorly analyzed using MestreNova.

The infrared (IR) spectra were obtained with a FT-IT Spectrum Two from Perkin-Elmer in ATR mode. The intensity of the IR bands is classified as weak (w), medium (m), strong (s) and broad (b).

The crystal structures were determined using LAQV-REQUIMTE (DQ)'s X-ray crystallography service. The single crystals were separated under the microscope, coated with Fomblin oil, and set up in a nylon loop. The data was obtained at 110 K or room temperature using a Bruker D8 Venture diffractometer and a Photon II detector, equipped with an Oxford Cryosystems. It was used Mo-Kα (λ = 0,7173 Å) as monochromatic radiation. The structures were later resolved using Olex2 [128]or WinGX [129] and represented using Mercury [130].

The diffuse reflectance spectroscopy (DRS) data was obtained using a SHIMADZU-UV-2501PC, with a $BaSO_4$ reference cell to correct the baseline (as it has a reflectance close to 100%). The spectra were acquired in the 250-800 nm range. Since some samples were very colorful, they were diluted with barium sulfate ($BaSO_4$).

Photocatalytic experiments were conducted in a 100 mL borosilicate glass reactor attached with a headspace with a glass graduated pipette on one side and an appendage that connects to a bubbler. In a typical photocatalytic experiment, 50 mg of catalyst was suspended in 90 mL of aqueous sacrificial agent solution. With the room temperature set at 20ºC, the reactant mixture was degassed by bubbling N_2 gas for 20 min to remove air and ensure that the reaction system was under anaerobic conditions. Then, the solution is irradiated by a 300 W Xe lamp for H_2 evolution under constant magnetic stirring. These conditions are applied to every single experiment.

4.3 Chemical Actinometry

To determine the efficiency of a photocatalyst in the system and the rate of a photochemical reaction, we can obtain the apparent quantum yield or efficiency (AQE), which is defined by **Equation 4**.

$$\Phi = \frac{\#\ of\ reacted\ molecules\ per\ unit\ of\ time}{\#\ of\ photons\ absorbed\ per\ unit\ of\ time}$$

Equation 4. Quantum yield formula.

So, for the calculation of the AQE, a chemical actinometry was needed beforehand. A chemical actinometer is a reference substance that, when irradiated with light at a certain wavelength, has an accurately known quantum yield. Therefore, it determines the photon flux in a well-defined domain, that works the most favorably when monochromatic light is used [131]. For an actinometer to be considered good, being photoactive is not the only requirement, its quantum yield should also be independent of excitation wavelength, concentration, trace impurities, temperature, and oxygen.

In our study, Hatchard and Parker's ferrioxalate actinometer procedure [132] was followed, since it is considered the most reliable and practical for UV and visible light up until 500 nm. The decomposition of the potassium ferrioxalate under light excitation, represented in **Equation 5**, yields ferrous ions, which are quantified and monitored by conversion to the colored trisphenanthroline complex ($\varepsilon_{510\,nm}$=11100 L mol^{-1} cm^{-1}).

$$Fe(C_2O_4)_3^{3-} \xrightarrow{h\nu} Fe^{2+} + C_2O_4^{\bullet-} + 2C_2O_4^{2-}$$

$$Fe(C_2O_4)_3^{3-} + C_2O_4^{\bullet-} \xrightarrow{\Delta} Fe^{2+} + 2CO_2 + 3C_2O_4^{2-}$$

Equation 5. Ferrioxalate decomposition reactions.

This complex does not absorb at 510 nm and the original ferric ions are not complexed by phenanthroline. The quantity of ferrous ions formed is given by **Equation 6**.

$$n(Fe^{2+}) = \frac{A}{b \times \varepsilon} \times V_{irr}$$

Equation 6. Obtention of the moles of ferrous ions.

Where A is the real absorption of the complex, V_{irr} is the irradiated volume, b is the optical pathlength (b = 1 cm), ε is the molar absorptivity coefficient of $Fe(phen)_3^{2+}$ complex. So, when **Equation 4** is adapted, we have **Equation 7**.

$$\Phi = \frac{A \times Virr}{\varepsilon \times I_0 \times \Delta t}$$

Equation 7. Adapted quantum yield equation.

Where I_0 is the number of absorbed photons per unit of time.

Since the potassium ferrioxalate is light sensitive, the 15 M solution ($K_3[Fe(C_2O_4)_3]$) with 0.05 M sulfuric acid (H_2SO_4) was prepared and the experiment was conducted under red light. Also, a 1 M acetate buffer solution and 0.1% phenanthroline solution were prepared. The potassium ferrioxalate solution is irradiated for 120 seconds, but every 30 seconds, 0.5 mL is taken to an additional 10 mL volumetric balloon containing 0.5 mL acetate buffer solution and 0.5 mL of phenanthroline, prefacing the volume with water.

The absorbance of each sample was recorded in a Carry 100 Bio UV-Vis Spectrofotometer, originating the graph in **Figure 120**.

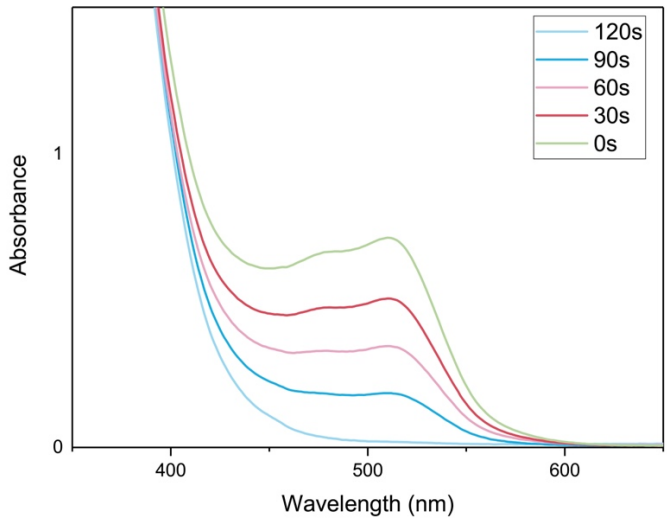

Figure 120. Absorbance *vs.* wavelength (nm) for the trisphenanthroline and respective complexes over a 120 second period.

A linear regression was traced, in **Figure 121**, of the absorbance ate 510 nm in function of the irradiation time (seconds). The absorbance at 510 nm was multiplied by the dilution factor (20).

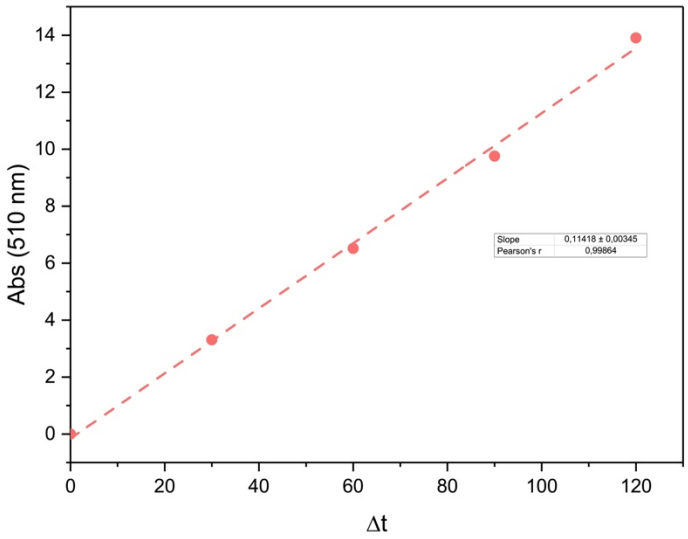

Figure 121. Absorbance at 510 nm *vs.* irradiation time (s).

The slope of the equation (m) is equivalent to $A/\Delta t$ and **Equation 7** was applied to calculate the I_0, obtaining **Equation 8**.

$$I_0 = \frac{m \times Virr}{\varepsilon \times \Phi}$$

Equation 8. Obtention of I_0 from the linear regression.

Where m is the slope from **Figure 117**, V_{irr} is the irradiated volume (v=0,09 L), ε is the molar absorptivity coefficient (ε =11100 L mol^{-1} cm^{-1}) and Φ was given by Hatchard and Parker (Φ = 1).

Therefore, the value of I_0 obtained in these conditions was 8.42x10^{-7} mol/s.

With this value, we are now able to calculate the AQE for these MOFs, using **Equation 9**.

$$\text{AQE} = \frac{\#\ of electron\ that\ react}{\#\ of\ incident\ photons} \times 100\% = \frac{2n(H_2)/t}{\#\ of\ incident\ photons/t} \times 100\%$$

Equation 9. Apparent Quantum Efficiency (AQE) formula.

Where n(H_2) is the number of moles of hydrogen, that is obtained from the hydrogen production graph (number of moles produced (μmol) *vs.* time (min)). The number of incident photons corresponds to the value of I_0, calculated in the chemical actinometry.

4.4 Crystallographic Data

Crystal data and structure refinement were performed for Fujita's sponge, **MOF1**, **MOF2**, **MOF3**, **A9a**, **A9b**, *o*-isopropylaniline and propargylic acid are represented on **Table 36**.

Table 36. Crystallographic data and structure refinement for the appointed materials.

	Fujita's Sponge	MOF1	MOF2	MOF3	A9a	A9b	o-isopropylaniline	Propargylic acid
Formula	$C_{18}H_{12}N_{12}Zn_3I_6$	$C_{17}H_{12}N_6O_4ZnI$	$C_{17}H_{13}N_7O_4ZnI$	$C_{29}H_{18}N_{18}O_6S_2F_6Zn$	$C_{29}H_{18}N_{12}O_4Zn$	$C_{29}H_{18}N_{12}O_4Zn$	$C_{45}H_{37}I_6N_{13}Zn_3$	$C_{29}H_{22}Cl_7I_4N_9Zn_2$
M	1353.6	556.3	571.3	965.6	663.4	663.4	1716.6	1382.9
l (Å)	0.71073	0.71073	0.71073	0.71073	0.71073	0.71073	0.71073	0.71073
T (K)	100	273	296	296(2)	296(2)	110(2)	296(2)	296(2)
Crystal System	Monoclinic	Monoclinic	Monoclinic	Monoclinic	Monoclinic	Monoclinic	Monoclinic	Monoclinic
Space Group	C2/c	$P2_1/c$	$P2_1/n$	C2/c	$P2_1/c$	$P2_1/n$	C2/c	C2/c
Crystal Description	Plate	Prism	Prism	Prism	Prism	Prism	Plate	Plate
Crystal color	Colorless	Colorless	Red	Colorless	Colorless	Colorless	Colorless	Colorless
a (Å)	34.655(3)	9.9777(10)	9.809(2)	23.390(6)	10.891(6)	12.615(5)	35.743(6)	31.384(3)
b (Å)	14.7307(14)	11.4022(11)	11.596(2)	12.418(3)	29.202(16)	29.236(12)	14.653(2)	15.1616(13)
c (Å)	31.081(3)	19.4499(19)	20.754(6)	25.233(8)	7.003(4)	18.314(8)	31.194(5)	29.966(3)
a (Å)	90	90	90	90	90	90	90	90
b (Å)	101.031(2)	98.4750(10)	111.44(3)	117.178(7)	93.70(16)	96.555(14)	101.303(4)	95.626(3)
g (Å)	90	90	90	90	90	90	90	90
V (Å^3)	15573.5	2188.61	2197.31	6520(3)	2223(2)	6710(5)	16021(4)	14190(2)
Z	8	2	2	8	2	2	12	12
ρ_{calc} (g cm^{-3})	-	-	-	2.185	1.623	1.607	2.136	1.958
μ (mm^{-1})	-	-	-	1.001	0.745	0.740	4.850	4.070
θ_{max} (°)	-	-	-	29.176	25.813	28.012	18.851	25.242
Total Data	-	-	-	36185	36185	203200	32396	43171
Unique Data	-	-	-	8758	4238	15053	6227	12627
R_{int}	-	-	-	0.1347	0.3536	0.3759	0.1118	0.0880
R [I>σ(I)]	-	-	-	0.1396	0.0760	0.2560	0.1087	0.0902
wR2	-	-	-	0.3710	0.1357	0.7032	0.2892	0.2453
Goodness of Fit (GoF)	-	-	-	1.293	1.034	1.091	1.052	1.058
ρ_{min}	-	-	-	-1.253	-1.184	5.450	-0.930	-1.965
ρ_{max}	-	-	-	2.251	0.604	3.321	5.741	3.293

4.5 Procedures

4.5.1 Synthesis of Ligands

4.5.1.1 Synthesis and Characterization of 2-(Benzylamino)terephthalic acid

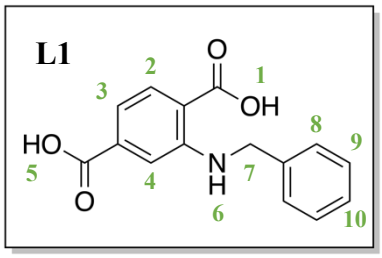

The 2-(benzylamino)terephthalic acid (**Ligand 1, L1**) was obtained using a procedure formerly reported in the literature with a slight modification [104].

In a 250 mL round bottom flask, 2-aminoterephthalic acid (500 mg, 2.80 mmol) was dissolved 40 mL of methanol, stirring for 5 minutes at room temperature. Benzaldehyde (0.70 mL, 2.5 eq.) and triethylamine (1.55 mL, 4 eq.) were added, and the mixture was refluxed for 5H under argon. After cooling to room temperature, it was stirred at 0ºC for 10 minutes. $NaBH_4$ (417 mg, 4 eq.) was slowly added in small quantities and stirred at 0ºC for 2H. After that step, the solution was stirred at room temperature for 20H.

The solvent was evaporated. 14 mL of water and 6 mL of methanol were added to dissolve the product and then 2 mL of acetic acid was added to precipitate. The precipitate was filtered and washed with water (η=72%). The characterization is in accordance with the reported in the literature [104].

^{1}H NMR (400 MHz, DMSO) δ (ppm): 7.90 (d, J = 8.0 Hz 1 H), 7.35 (m, 4 H), 7.27 (m, 1 H), 7.22 (s, 1 H), 7.10 (dd, J = 8 Hz, 1 H), 4.51 (s, 2 H).

IR ATR ν max (cm^{-1}): 3378, 2860 (b), 2642 (b), 1668 (s), 1575, 1516, 1453, 1421, 1317, 1236 (s), 922, 874, 747 (s), 695.

4.5.1.2 Synthesis and Characterization of (*E*)-4-((4-carboxybenzylidene)amino)benzoic acid

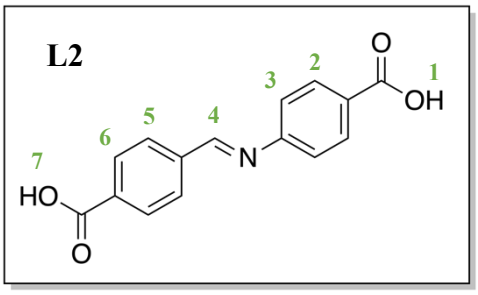

The (*E*)-4-((4-carboxybenzylidene)amino)benzoic acid (**Ligand 2, L2**) was obtained using two different procedures: (**a**) reflux [105] and (**b**) microwave-assisted synthesis.

(a) Reflux: In separated beakers, 4-aminobenzoic acid (1.4 g, 10 mmol) was added to one and 4-formylbenzoic acid (1.5 g, 10 mmol) to another, also adding 50 mL of methanol to each, and stirred until dissolved. Both were added to a 250 mL round bottom flask and refluxed for 3H under consistent stirring. After cooling at room temperature, the solid was filtered and washed with methanol.

(b) Microwave-assisted: 4-aminobenzoic acid (210 mg, 1.15 mmol) and 4-formylbenzoic acid (225 mg, 1.50 mmol) were added to 15 mL methanol in a 30 mL wide neck glass vial. The solution was placed in the microwave with a hold time of 10 minutes at

80ºC. After cooling at room temperature, the precipitate was filtered and washed with methanol and diethyl ether (η=77%). The ^{1}H NMR obtained matches the one described in the literature [105].

^{1}H NMR (400 MHz, DMSO) δ (ppm): 8.75 (s, 1 H, H4), 8.08 (m, 4 H, H2 and H3), 8.00 (m, 2 H, H5), 7.37 (d, 2 H, H3).

IR ATR ν max (cm^{-1}): 2819 (b), 2656, 2537 (b), 1673 (s), 1629 (-C=N-), 1593, 1423, 1283 (s), 1168, 945, 862, 778, 698, 531.

4.5.1.3 Synthesis and Characterization of (*E*)-4,4'-(diazene-1,2-diyl)dibenzoic acid

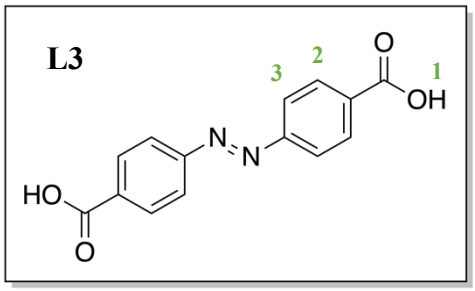

The (*E*)-4,4'-(diazene-1,2-diyl)dibenzoic acid (**Ligand 3, L3**) was prepared using a reported protocol [106].

In a 250 mL round bottom flask, *p*-nitrobenzoic acid (5.5 g, 33 mmol) and sodium hydroxide (20 g, 500 mmol) were dissolved in 75 mL of water at a controlled temperature of 50ºC. A glucose (45 g in 50 mL, 250 mmol) solution was prepared at 50ºC and added dropwise while hot to the mixture. The solution was air bubbled under stirring overnight. The precipitates were filtered and washed with a saturated NaCl solution. The solid was dissolved in water and 20 mL of acetic acid was carefully added while the mixture was air-bubbled, producing a pink precipitate that was filtered and washed with water.

^{1}H NMR (400 MHz, DMSO) δ (ppm): 8.17 (d, 4 H, H2), 8.02 (d, 4 H, H3).

IR ATR ν max (cm^{-1}): 2817 (b), 2660, 1542 (b), 1675 (s), 1603, 1496 (w), 1423, 1289 (s), 1125, 1011, 931 (m), 869, 780, 696, 538.

4.5.1.4 Synthesis and Characterization of 2,4,6-tri(4-pyridil)-1,3,5-triazine

The 2,4,6-tri(4-pyridil)-1,3,5-triazine (**TPT, L4**) was prepared following two synthetic procedures.

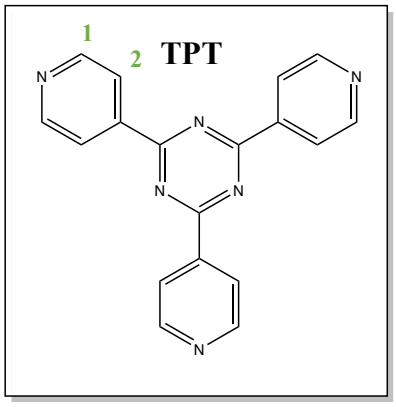

(a) Method 1: 4-cianopyridine (10.0 g, 96.00 mmol) was added to a cup and heated to 50ºC initially and then progressively over time in an ace pressure tube in a sand bath under constant stirring. Afterwards, 0.1 eq. of NaOH (390.0 mg, 9.62 mmol) were added. After all the 4-cianopyridine melted, the tube was left at 150ºC for 24H. The yellowish solid was filtered and washed with PA acetone (3x60 mL) until it becomes whitish and then it was dissolved in 83 mL of an aqueous solution of 2M HCl. The next step was to add activated charcoal and sonicate the mixture for 30 min. The contents were filtered through a porous plate filter with celite and washed with 50 mL of an 5M NaOH aqueous solution, obtaining a

white precipitate, which was then washed with water and acetone and dried under vacuum (η=19%)

(b) Method 2: In a Schlenk tube, 4-cyanopyridine (10.0 g, 96.00 mmol), KOH (240.0 mg, 4.23 mmol), 18-crown-6 (1.03 g, 3.90 mmol) and naphthalene decahydrate (10 mL) were added. The mixture was heated to 200ºC under stirring in an Ar atmosphere for 3H. The solution was decanted, and the precipitate was washed with warm pyridine (3x50 mL) to obtain a white powder, which was later dissolved in 50 mL of 2M HCl and precipitated again with an aqueous solution of NaOH (50 mL). The product was filtered and dried under vacuum (η=20%).

^{1}H NMR (400 MHz, DMSO) δ (ppm): 8.17 (d, 4 H, H1), 8.02 (d, 4 H, H2).

4.5.1.5 Synthesis and Characterization of 4,4'-(1,4-phenylenebis(azaneylylidene)bis(methaneylylidene))dibenzoic acid

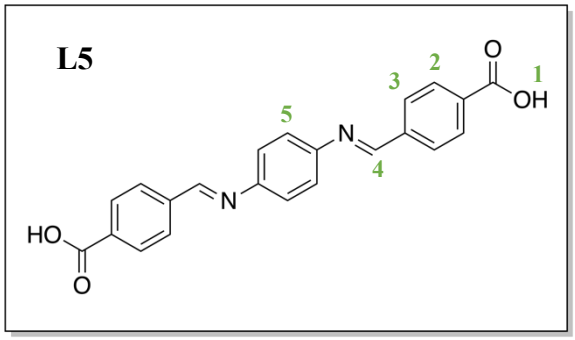

The 4,4'-(1,4-phenylenebis(azaneylylidene)bis(methaneylylidene))dibenzoic acid (**Ligand 5, L5**) was synthesized firstly following **(a)** by reflux and then by **(b)** a protocol reported in the literature [107].

(a) Reflux: In a 50 mL round-bottom flask, *p*-phenylenediamine (108 mg, 1 mmol) in 10 mL ethanol was added and placed under stirring. 4-formylbenzoic acid (300 mg, 2 mmol) in 10 mL ethanol was sonicated and added gradually to the flask. The mixture was refluxed at 65ºC for 3H. The yellow precipitate was filtered and washed with ethanol.

(b) Protocol Synthesis: In a 50 mL round-bottom flask, *p*-phenylenediamine (108 mg, 1 mmol) in 10 mL ethanol was added and placed under stirring. 4-formylbenzoic acid (300 mg, 2 mmol) in 10 mL ethanol was sonicated and added gradually to the flask. The formation of a precipitate was observed with the addition. The mixture was stirred for 1H. The yellow precipitate was filtered and washed with ethanol (η=73%).

^{1}H NMR (400 MHz, DMSO) δ (ppm): 8.81 (s, 2 H, H4), 8.08 (s, 8 H, H2 and H3), 7.44 (s, 4 H, H5).

IR ATR ν max (cm^{-1}): 2985 (b), 2542 (b), 1677 (s), 1619 (m), 1493 (w), 1422 (m), 1285 (s), 857, 768.

4.5.1.6 Synthesis and Characterization of (*E*)-4-((4-aminophenyl)imino)methylbenzoic acid

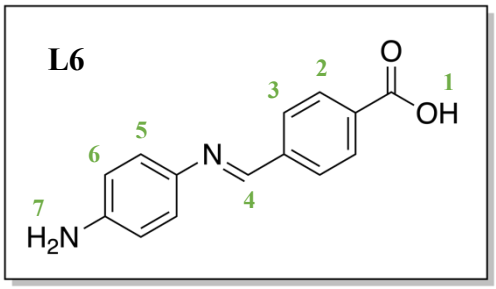

The (*E*)-4-((4-aminophenyl)imino)methylbenzoic acid (**Ligand 6, L6**) was synthesized by reflux, using the following procedure: In a 50 mL round-bottom flask, *p*-phenylenediamine (432 mg, 4 mmol) was added in 10 mL ethanol and stirred.

After sonicating 4-formylbenzoic acid (300 mg, 2 mmol) in 10 mL ethanol for 10 minutes, it was added dropwise to the flask. The mixture was stirred for 1H. The yellowish-green precipitate was collected through filtration and washed with ethanol (η=70%).

^{1}H NMR (400 MHz, DMSO) δ (ppm): 8.70 (s, 1 H, H4), 8.02 (dd, 2H, H2), 8.00 (dd, 2 H, H3), 7.21 (d, 2 H, H5), 6.62 (d, 2 H, H6).

^{13}C {^{1}H} NMR (101 MHz, DMSO) δ (ppm): 153.23, 149.07, 141.12, 139.31, 130.13, 128.30, 123.37, 114.51.

IR ATR ν max (cm^{-1}): 3372 (w), 3292 (w), 2727 (b), 1684, 1625, 1589, 1508, 1414 (w), 1370 (w), 1267, 1227, 1109, 885, 771, 658, 535.

4.5.2 Synthesis of Reported MOFs

The reported MOFs were synthesized following protocols that use different techniques. The Fujita's sponge, $[(ZnI_2)_3(TPT)_2]_n$ was synthesized through Clardy and coworkers' updated protocol and the guest inclusions too [67]. The replication of UiO-66 and UiO-66-NH_2 were synthesized with slight modifications to Taddei et al.'s and Solís et al.'s protocols [110], [111].

4.5.2.1 Synthesis of Fujita's sponge

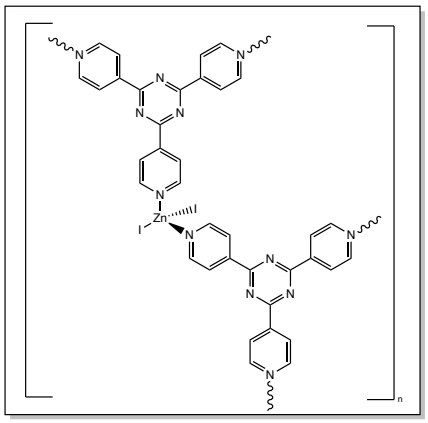

The MOF that acts as Fujita's sponge was synthesized using Clardy and coworkers' procedure by diffusion layering [67]: a 4.2 mL chloroform solution of TPT (TPT = 2,4,6-tri-4-pyridyl-1,3,5-triazine, 0.02 mmol) was added to a screw top tube, then slowly layered with a methanol solution of zinc iodide (ZnI_2, 0.03 mmol). The tube was closed and left to grow crystals for 3 days.

4.5.2.2 Synthesis of UiO-66

UiO-66 was synthesized following the protocol from Taddei et al. [110]. Zr-TA network was synthesized by adding $ZrCl_4$ (1.25 mmol) and terephthalic acid (TA, 1.25 mmol) with 10 mL of DMF to a glass vial. We added acetic acid (2.10 mL, 37.50 mmol) and water (135 mL, 7.50 mmol) were also added to the vial to act as modulators and the solution was stirred for 15 minutes. The vessel was hermetically closed, and microwave irradiated for 30 minutes at

120ºC. The product was centrifuged for 30 minutes, washed with DMF and new DMF was added to soak for 12H. This was performed twice, a third time with acetone but for 24H, and then left to dry at room temperature.

4.5.2.3 Synthesis of UiO-66-NH_2

This Zr-MOF was synthesized through microwave-assisted method following Solís et al's procedure [111]. $ZrOCl_2$ (0.60 mmol) and 2-aminoterephthalic acid (ATA, 0.60 mmol) were added with 17.2 mL DMF to the microwave glass vial and magnetically stirred. In this case, acetic acid (2.80 mL, 49 mmol) and HCl 37% (114,4 mL, 3.67 mmol) were added as modulators and stirred for 15 minutes. The closed vial was placed in the microwave for 30 minutes at 140ºC. The solution was centrifuged for 5 min at 4000 rpm and washed twice with DMF combined with 10 min of centrifuged in between. It was dried in the oven at 80ºC for 16H.

4.5.2.4 Synthesis and Characterization of MOF1

The microporous MOF, $[Zn(TPT)_2(TA)]_n$, was synthesized through solvothermal techniques from Tan et al's procedure [112]. In a 150 mL Teflon-lined stainless-steel autoclave, ZnI_2 (288 mg, 1.5 mmol), TPT (139.5 mg, 0.75 mmol), and TA (81.5 mg, 0.75 mmol) were added with 75 mL of distilled water and 126 μL of triethylamine. The autoclave was screwed shut and placed in the oven for 36H at 160ºC. The solution was filtered and washed with water, ethanol, and diethyl ether.

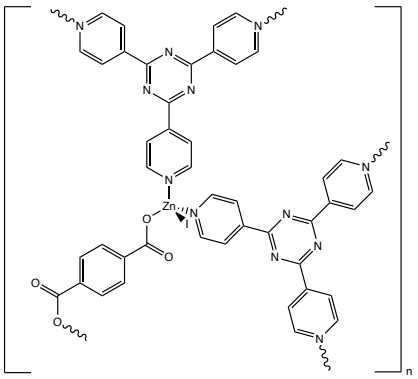

IR ATR ν max (cm^{-1}): 3038 (w), 1575 (m), 1506 (s), 1369 (s), 1316 (m), 1053 (w), 794 (s), 666 (m), 639 (s), 504 (s).

4.5.2.5 Synthesis and Characterization of MOF2

The microporous MOF, $[Zn(TPT)_2(ATA)]_n$, was synthesized the same way as **MOF1**, using the same procedure. In a 150 mL Teflon-lined stainless-steel autoclave, ZnI_2 (480 mg, 1.50 mmol), TPT (232.5 mg, 0.75 mmol), and ATA (135.8 mg, 0.75 mmol) were added with 75 mL of distilled water and 210 μL of triethylamine. The autoclave was sealed and placed in the oven for 72H at 160ºC. Red crystals were collected with a spatula to vial, and the remaining solution was filtered and washed with water, ethanol, and diethyl ether.

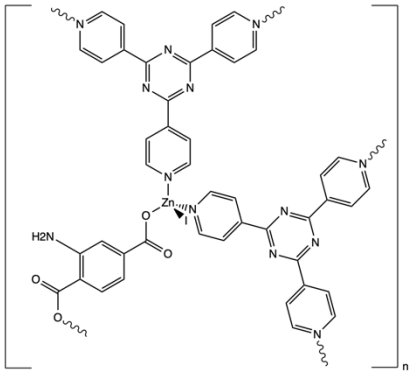

IR ATR ν max (cm^{-1}): 3431 (w), 3313, 3106 (b), 1576, 1514 (s), 1427, 1367 (s), 1253 (w), 773 (s), 654, 512.

4.5.3 Synthesis of New MOFs and Materials

The complexes and MOFs were formed using different techniques: layering, solvothermal, mechanochemistry, microwave, and traditional heating methods.

A. **Layering Protocol**: The ligands were dissolved in two or three different miscible solvents. 4,2 mL of a solution was added to a small round tube, followed by slow addition of 1 mL of another solution, by dripping it through the wall of the tube, forming a thin layer. The lid was closed and left to sit for 3 days without moving or disturbing the tube rack.
B. **Hydro- or Solvothermal Protocol**: In a 150 mL Teflon-lined stainless-steel autoclave, add the reactants to 75 mL of water or N,N-Dimethylformamide (DMF), with possible addition of triethylamine, in some cases. The reactor was sealed shut and then placed in the oven at 160ºC or 120ºC for 24, 36, 48H or 72H. The solid was collected by filtration and washed with solvents. The conditions are the same for a 25 mL autoclave, only changing the quantities of reactants and the volume of the solvent to 17.5 mL.
C. **Mechanochemistry Protocol**: To a milling vessel, add the reactants and the milling balls of choice. If needed, solvent may also be added in very small quantities. The vessel is placed on a planetary ball mill at 500 rpm for a certain time.
D. **Microwave Protocol**: The reactants were added to 15 or 17,5 mL of solvent in a 30 mL wide neck glass vial with a magnetic stirrer. Other acids or bases may also be added. The vial is closed hermetically and placed in the microwave for a determined hold time at a certain temperature. The precipitate can either be obtained through filtration or centrifugation and washed with organic solvents.
E. **Heating**: The reagents are added to a wide neck glass vial with 6 mL of solvent or solvent mixture. The mixture is then sonicated for 10 minutes before being closed hermetically and heated to 110-130ºC for 48H-72H. The contents are filtered, washed and dried.

4.5.3.1 Synthesis and Characterization of the A4 compounds

These compounds were synthesized by different methods: hydro- and solvothermal, microwave-assisted and diffusion layering following the protocols described above.

The conditions were the following for each method:

(a) Hydrothermal: ZnI_2 (112 mg, 0.35 mmol), TPT (54.2 mg, 0.2 mmol) and **L2** (31.7 mg, 0.15 mmol) were added to the reactor with 17.5 mL of distilled water and 49 μL of triethylamine. The reactor was placed in the oven at 160ºC for 72H. The solid was collected by filtration, washed with water, ethanol and diethyl ether and dried at r.t. This reaction yielded a beige microcrystalline powder.

(b) Solvothermal: ZnI_2 (112 mg, 0.35 mmol), TPT (54.2 mg, 0.2 mmol) and **L2** (31.7 mg, 0.15 mmol) were added to the reactor with 17 mL of DMF and 49 μL of triethylamine. The vial was placed in the oven at 120ºC for 72H. The solid was

collected by filtration, washed with DMF and methanol and dried at r.t. This reaction yielded a beige microcrystalline powder.

(c) Microwave-assisted: ZnI_2 (112 mg, 0.35 mmol), TPT (54.2 mg, 0.2 mmol) and **L2** (31.7 mg, 0.15 mmol) were added to a wide neck glass vial with 17.5 mL of distilled water and 49 μL of triethylamine. The reactor was placed in the microwave system at 140ºC for 30 min. The solid was collected by filtration, washed with water, ethanol and diethyl ether and dried at r.t., originating a white powder.

(d) Diffusion Layering: TPT (25.2 mg, 0.08 mmol) was dissolved at 50ºC in 20 mL of chloroform, sonicated and filtered through a cotton filled pipette. ZnI_2 (47.9 mg, 0.15 mmol) and **L2** (20.2 mg, 0.08 mmol) were dissolved in 5 mL of methanol. 4.2 mL of the chloroform solution was added and layered with 1 mL of methanol solution.

(e) Mechanochemistry: ZnI_2 (115 mg, 0.35 mmol), TPT (57 mg, 0.20 mmol) and **L2** (35 mg, 0.15 mmol) were added to a stainless-steel reactor and homogenized with a spatula. Two drops of triethylamine were also added. The reaction was at 500 rpm for 1H, yielding a bright yellow powder.

4.5.3.2 Synthesis and Characterization of the A5 Compounds

The A5 compounds were synthesized by hydrothermal and microwave-assisted methods. Despite the methods used, all the reactions yielded a white powder.

(a) Hydrothermal: ZnI_2 (48 mg, 0.15 mmol), TPT (23.5 mg, 0.08 mmol) and BDC (18.5 mg, 0.08 mmol) were added to the reactor with 12.5 mL of H_2O and 21 μL of triethylamine. The reactor was placed in the oven at 160ºC for 72H. The solid was collected by filtration, washed with water and ethanol and dried at r.t.

(b) Microwave-assisted (H_2O): ZnI_2 (112 mg, 0.35 mmol), TPT (54.2 mg, 0.2 mmol) and BDC (31.7 mg, 0.15 mmol) were added to a wide neck glass vial with 17.5 mL of distilled water and 49 μL of triethylamine. The reactor was placed in the oven at 160ºC for 72H. The solid was collected by filtration, washed with DMF and methanol and dried at r.t.

(c) Microwave-assisted (DMF): ZnI_2 (57.6 mg, 0.18 mmol), TPT (28.2 mg, 0.09 mmol) and BDC (22.1 mg, 0.09 mmol) were added to a wide neck glass vial with 15 mL of DMF. The mixture was stirred for 1H before being placed in the microwave system at 140ºC for 20 min. The solid was collected by filtration, washed with water, ethanol and diethyl ether and dried at r.t., originating a white powder.

4.5.3.3 Synthesis and Characterization of the A6 Compounds

Attempts to synthesize the **A6** compounds were performed once by solvothermal, three times by hydrothermal and twice by microwave-assisted techniques.

(a) Solvothermal: ZnI_2 (319.2 mg, 1 mmol), TPT (156.2 mg, 0.50 mmol) and **L5** (93 mg, 0.25 mmol) were sonicated for 20 minutes in 75 mL of DMF. The reactor was placed

in the oven at 120ºC for 24H. The solid was collected by filtration, washed with DMF and methanol and dried at r.t., yielding only TPT.

(b) Hydrothermal: ZnI_2 (319.2 mg, 1 mmol), TPT (156.2 mg, 0.50 mmol) and **L5** (93 mg, 0.25 mmol) were sonicated for 20 minutes in 75 mL of water. The reactor was placed in the oven at 160ºC for 24H (**A6a**), 48H (**A6b**) or 36H (**A6c**). The solids were collected by filtration, washed with water and methanol and dried at r.t. This reaction yielded white to yellowish powders.

(c) Microwave-assisted (DMF): ZnI_2 (74.4 mg, 0.24 mmol), TPT (36.5 mg, 0.12 mmol) and **L5** (21.7 mg, 0.06 mmol) were added to a wide neck glass vial with 17.5 mL of DMF. The mixture was sonicated for 10 minutes before being placed in the microwave system at 140ºC for 30 min. The solid was collected by filtration, washed with DMF and methanol and dried at r.t., originating only TPT.

(d) Microwave-assisted (H_2O): ZnI_2 (74.4 mg, 0.24 mmol), TPT (36.5 mg, 0.12 mmol) and **L5** (21.7 mg, 0.06 mmol) were added to a wide neck glass vial with 17.5 mL of distilled water. The mixture was sonicated for 10 minutes before being placed in the microwave system at 140ºC for 30 min. The solid was collected by filtration, washed with water and methanol and dried at r.t., giving a brown solid.

4.5.3.4 Synthesis and Characterization of the A7 Compounds

The **A7** compounds were synthesized by diffusion layering and heating methods.

(a) Layering (DMF/MeOH): **L5** (74.5 mg, 0.20 mmol) was dissolved in 20 mL of DMF with sonication, while a 5 mL methanol solution of ZnI_2 (31.9 mg, 0.10 mmol) was prepared. 4.2 mL of the DMF solution was added and layered with 1 mL of methanol solution. This yielded yellow block crystals, which couldn't be analyzed by SCXRD due to the difficulty of keeping them on the loop.

(b) Layering ($CHCl_3$/MeOH): **L5** (74.5 mg, 0.20 mmol) was dissolved in 20 mL of chloroform with sonication and three drops of triethylamine, while a 5 mL methanol solution of ZnI_2 (31.9 mg, 0.10 mmol) was prepared. 4.2 mL of the chloroform solution was added and layered with 1 mL of methanol solution. This reaction only yielded **L5**.

(c) Heating: ZnI_2 (63.8 mg, 0.20 mmol) and **L5** (55.9 mg, 0.15 mmol) were added to a wide neck glass vial with 5 mL DMF and 1 mL NMP. The mixture is then sonicated for 10 minutes before closed hermetically and heated to 130ºC for 72H. The contents are filtered, washed with DMF and methanol and dried, yielding a dark brown solid.

4.5.3.5 Synthesis and Characterization of the A8 Compound

A8 was only tried following the diffusion layering protocol.

(d) Layering: **L6** (48.0 mg, 0.20 mmol) was dissolved in 20 mL of chloroform with sonication, the solution was divided in two: three drops of triethylamine were added to 10 mL, and the other 10 mL were filtered through a cotton filtered pipette. A 5 mL methanol solution of ZnI_2 (31 mg, 0.10 mmol) was prepared. 4.2 mL of the filtered

DMF solution was added to each of two tubes and 4.2 mL of the NEt_3 DMF were each added to another two tubes. Each of the tubes were layered with 1 mL of methanol solution. Both methods ended up precipitating only the **L6**.

4.5.3.6 Synthesis and Characterization of A9 Compounds

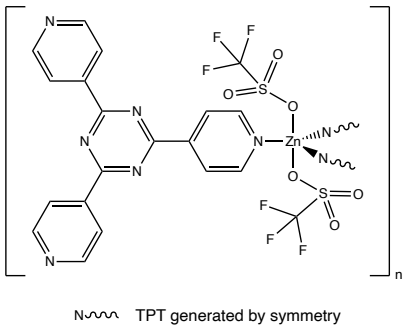

During the preparation of the new MOF, $[Zn(TPT)_3(OTf)_2]_n$, using Fujita's procedure, two side products in the form of cationic complexes were also obtained.

(a) Layering: In a beaker, *p*-methylbis(imino)acenaphthale (*p*-methylBIAN, 12 mg) and TPT (24.9 mg, 0.09 mmol) were added to 20 mL of chloroform. The mixture was stirred at 50ºC, while alternating with cycles of sonification until most of the solids were dissolved. The solution was filtered through a cotton-filled pipette and 4.2 mL of the filtered solution was added to a small round tube, closing the lid. A $Zn(OTf)_2$ 0.03M (54.5 mg, 0.18 mmol) solution was prepared in 5 mL of methanol, adding 1 mL of that solution to the tube slowly. The characterization was done through SCXRD, discovering a new MOF bearing three TPTs and two triflates connected to the zinc molecule and two polymorphs of a cationic complex with the zinc center connected to two methanol, two water and two TPT molecules and two triflate counterions.

4.5.3.7 Synthesis and Characterization of A10

The **A10** was synthesized by various means: diffusion layering, solvothermal and hydrothermal reactions.

(a) Layering: TPT (25.2 mg, 0.08 mmol) was dissolved at 50ºC in 20 mL of chloroform, sonicated and filtered through a cotton filled pipette. $Zn(OTf)_2$ (54.5 mg, 0.15 mmol) and **L2** (20.2 mg, 0.08 mmol) were dissolved in 5 mL of methanol and 0.20 mL of NEt_3 was added. 4.2 mL of the chloroform solution was added and layered with 1 mL of methanol solution.

(b) Solvothermal: $Zn(OTf)_2$ (112.0 mg, 0.30 mmol), TPT (54.2 mg, 0.15 mmol) and **L2** (31.7 mg, 0.15 mmol) were added to the reactor with 17 mL of DMF and 49 µL of NEt_3. The reactor was placed in the oven at 120ºC for 72H. The solid was collected by filtration, washed with DMF and methanol and dried at r.t.

(c) Hydrothermal: $Zn(OTf)_2$ (328.0 mg, 0.90 mmol), TPT (140.9 mg, 0.45 mmol) and **L2** (131.2 mg, 0.45 mmol) were added in 75 mL of water plus 126 µL of NEt_3. The reactor was placed in the oven at 160ºC for 72H. The solids were collected by filtration, washed with water and ethanol and dried at r.t.

4.5.3.8 Synthesis and Characterization of the A11 Compounds

Microwave-assisted and two different diffusion layering systems were used in the attempt to synthesize the **A11** compounds.

(a) Microwave-assisted: $Zn(OTf)_2$ (113.0 mg, 0.30 mmol) and **L5** (116.0 mg, 0.30 mmol) were added to a wide neck glass vial with 17 mL of distilled water and 50 µL of NEt_3. The mixture was sonicated for 15 minutes before being placed in the microwave system at 120ºC for 30 min. The solid was collected by filtration, washed with water and methanol and dried at r.t., yielding a yellow solid.

(b) Layering (DMF/MeOH): L5 (74.5 mg, 0.10 mmol) was dissolved in 20 mL of DMF at 50ºC with sonication and 4.2 mL of solution was added to the tubes. Then, a 5 mL methanol solution of $Zn(OTf)_2$ (36.4 mg, 0.10 mmol) was prepared, and 1 mL of the solution was carefully layered. This reaction yielded a dark brown powder.

(c) Layering ($CHCl_3$/MeOH): The same quantities were used as in the previous point, only changing the DMF for chloroform. This yielded a yellowish brown solid.

4.5.3.9 Synthesis and Characterization of the A12 Compounds

A12 compounds were synthesized only by diffusion layering.

(a) Layering: L6 (48.0 mg, 0.20 mmol) was dissolved in 20 mL of DMF at 50ºC with sonication and 4.2 mL of solution was added to the tubes. Then, a 5 mL methanol solution of $Zn(OTf)_2$ (36.4 mg, 0.10 mmol) was prepared, and 1 mL of the solution was carefully layered. After 1 day, 1 mL of diethyl ether was slowly layered. This reaction yielded a dark powder.

4.5.3.10 Synthesis and Characterization of the A13 Compounds

The **A13** compounds originated clear block crystals using the diffusion layering technique and a clear solution when using the hydrothermal.

(a) Layering: TPT (46.9 mg, 0.15 mmol) was dissolved in 20 mL of DMF at 50ºC with sonication and 4.2 mL of solution was added to the tubes. Then, a 5 mL methanol solution of $Zn(NO_3)_2$ (59.5 mg, 0.20 mmol) was prepared, and 1 mL of the solution was carefully layered. After three days, colorless block crystals had grown in the walls.

(b) Hydrothermal: $Zn(NO_3)_2$ (112.0 mg, 0.38 mmol) and TPT (54.2 mg, 0.19 mmol) were added in 17.5 mL of water plus 49 µL of NEt_3 to the reactor which was placed in the oven at 160ºC for 72H. This reaction yielded a clear colorless solution which didn't precipitate using diethyl ether nor pentane nor a mixture of both in a 1:1 ratio.

4.5.3.11 Synthesis and Characterization of the A14 Compounds

A14's synthesis was done through hydrothermal, microwave-assisted, diffusion layering and heating methods. These yielded different compounds, as observable by the FTIR and PXRD data.

(a) Hydrothermal (1): $Zn(NO_3)_2$ (112.0 mg, 0.38 mmol), TPT (54.2 mg, 0.30 mmol) and ATA (31.8 mg, 0.12 mmol) were added in 75 mL of water plus 126 μL of NEt_3. The reactor was placed in the oven at 160ºC for 72H. The solids were collected by filtration, washed with water and ethanol and dried at r.t. This yield a white and brown, non-uniform solid.

(b) Hydrothermal (2): $Zn(NO_3)_2$ (328.0 mg, 1.10 mmol), TPT (140.9 mg, 0.78 mmol) and ATA (131.2 mg, 0.42 mmol) were added in 17.5 mL of water plus 49 μL of NEt_3. The reactor was placed in the oven at 160ºC for 72H. The solids were collected by filtration, washed with water and ethanol and dried at r.t., yielding a light brown solid.

(c) Microwave-assisted: $Zn(NO_3)_2$ (100.0 mg, 0.34 mmol), TPT (28.4 mg, 0.17 mmol) and ATA (48.9 mg, 0.08 mmol) were added to a wide neck glass vial with 17.5 mL of distilled water and 50 μL of NEt_3. The mixture was stirred for 15 minutes before being placed in the microwave system at 140ºC for 30 min. The solid was collected by filtration, washed with water and ethanol and dried at r.t.

(d) Layering: TPT (25.2 mg, 0.09 mmol) was dissolved in 20 mL of chloroform at 50ºC with sonication, filtered through a cotton-filled pipette and 4.2 mL of solution was added to the tubes. Then, a 5 mL methanol solution of $Zn(NO_3)_2$ (59.5 mg, 0.18 mmol) and ATA (20.2 mg, 0.08 mmol) was prepared and 0.50 mL of NEt_3 was added, and 1 mL of the solution was carefully layered.

(e) Heating (1): $Zn(NO_3)_2$ (91.3 mg, 0.20 mmol), TPT (23.4 mg, 0.10 mmol) and ATA (27.2 mg, 0.10 mmol) were added to a wide neck glass vial with 5 mL DMF and 1 mL NMP. The mixture is then sonicated for 5 minutes before closing hermetically and heated to 130ºC for 48H. The contents were cooled slowly and filtered, washed with DMF and methanol and dried, yielding brown solid.

(f) Heating (2): $Zn(NO_3)_2$ (60.0 mg, 0.30 mmol) TPT (31.3 mg, 0.15 mmol) and ATA (18.1 mg, 0.08 mmol) were added to a wide neck glass vial with 6 mL of a 1:1 DMF/H_2O mixture. The solution is then sonicated for 10 minutes before closed hermetically and heated to 110ºC for 72H. The contents are filtered, washed with DMF and methanol and dried, yielding a pink fluffy solid.

4.5.3.12 Synthesis and Characterization of the A15 Compounds

Solvothermal was the method employed twice in the same conditions for the synthesis of the **A20** compounds.

(a) Hydrothermal: $Zn(NO_3)_2$ (328.0 mg, 1.73 mmol) and ATA (313.7 mg, 1.73 mmol) were added in 75 mL of water. The reactor was placed in the oven at 120ºC for 72H. The solids were collected by filtration, washed with water and methanol and dried at r.t. The reaction yielded a white solid.

4.5.3.13 Synthesis and Characterization of the A16 Compounds

A16 was synthesized through hydrothermal and diffusion layering synthesis.

(a) **Solvothermal**: $Zn(NO_3)_2$ (328.0 mg, 1.73 mmol), bipy (135.0 mg, 0.87 mmol) and ATA (157.0 mg, 0.87 mmol) were added in 75 mL of DMF. The reactor was placed in the oven at 120ºC for 72H. The solids were collected by filtration, washed with DMF and methanol and dried at r.t. This yielded a light brown solid.

(b) **Layering:** $Zn(NO_3)_2$ (38 mg, 0.10 mmol) was dissolved in 5 mL of water and 2 mL were added to the bottom of the tube. ATA (36.2 mg, 0.09 mmol) was dissolved in 5 mL of methanol with 56 μL NEt_3, and 2 mL were layered carefully on top. The same was done for the bipy (15.6 mg, 0.10 mmol) in 5 mL ethanol solution. This led to the precipitation of only ATA.

4.5.3.14 Synthesis and Characterization of the A17 Compounds

A17 was synthesized through diffusion layering in a H_2O/MeOH/EtOH system.

(a) **Layering:** $Zn(NO_3)_2$ (38 mg, 0.20 mmol) was dissolved in 5 mL of water and 2 mL were added to the bottom of the tube. **L1** (36.0 mg, 0.10 mmol) was dissolved in 5 mL of methanol, and 2 mL were layered carefully on top. The same was done for the bipy (31.2 mg, 0.10 mmol) in 5 mL ethanol solution. This led to the precipitation of orange crystals.

4.5.3.15 Synthesis and Characterization of the A18 Compounds

A18 was synthesized using the diffusion layering and microwave-assisted synthetic methods.

(a) **Layering:** $ZnCl_2$ (27.2 mg, 0.20 mmol) was dissolved in 5 mL of water and 2 mL were added to the bottom of the tube. ATA (36.2 mg, 0.10 mmol) was dissolved in 5 mL of methanol, and 2 mL were layered carefully on top. This led to the precipitation of orange crystals.

(b) **Microwave-assisted (DMF)**: $ZnCl_2$ (81.8 mg, 0.60 mmol) and ATA (108.7 mg, 0.60 mmol) were added to a wide neck glass vial with 17.2 mL of DMF, 2.8 mL of acetic acid and 114.4 μL of HCl 37%. The mixture was stirred for 7 minutes before being placed in the microwave system at 140ºC for 30 min. The solution didn't precipitate anything, so 10 mL of diethyl ether were layered. A dark brown solid was obtained.

(c) **Microwave-assisted (H_2O)**: $ZnCl_2$ (81.8 mg, 0.60 mmol) and ATA (108.7 mg, 0.60 mmol) were added to a wide neck glass vial with 17.2 mL of distilled water, and it was stirred for 15 minutes before being placed in the microwave system at 160ºC for 30 min. The reaction only yielded ATA.

4.5.3.16 Synthesis and Characterization of the A19 Compounds

The techniques used for the synthesis of these **A19** compounds were diffusion layering and microwave-assisted method.

(a) **Layering:** $ZnCl_2$ (27.2 mg, 0.10 mmol) was dissolved in 5 mL of water and 2 mL were added to the bottom of the tube. ATA (36.2 mg, 0.10 mmol) was dissolved in 5 mL of methanol, and 2 mL were layered carefully on top. The same was done with 2 mL of

bipy (31.2 mg, 0.20 mmol) in 5 mL of ethanol solution. This led to the formation of small crystals on the walls of a tube.

(b) Microwave-assisted: $ZnCl_2$ (76.5 mg, 0.56 mmol), bipy (43.8 mg, 0.28 mmol) and ATA (50.8 mg, 0.42 mmol) were added to a wide neck glass vial with 17 mL of DMF. The mixture was stirred for 7 minutes before being placed in the microwave system at 120ºC for 30 min. The solution was then precipitated using 10 mL of a 1:1 Diethyl ether/*n*-pentane mixture. A white powder precipitated, was filtered and washed with DMF and MeOH. The waters of the methanol wash also precipitated a white powder, which was recovered, analyzed and compared to the other compound.

4.5.3.17 Synthesis and Characterization of the B3 Compounds

The **B3** compounds were synthesized using all methods, with the only exceptions being the heating and hydrothermal synthesis.

(a) Solvothermal: $ZrOCl_2$ (356.0 mg, 2.00 mmol), bipy (156.0 mg, 1.00 mmol) and ATA (156.0 mg, 1.00 mmol) were added in 75 mL of DMF. The reactor was placed in the oven at 120ºC for 72H. This yielded a salmon orange colored gel, which was filtered and washed with DMF and methanol and dried at r.t, yielding a brick red powder.

(b) Microwave-assisted (DMF, 1): $ZrOCl_2$ (106.9 mg, 0.60 mmol), bipy (93.7 mg, 0.60 mmol) and ATA (108.7 mg, 0.60 mmol) were added to a wide neck glass vial with 17 mL of DMF, 2.8 mL of acetic acid and 114.4 µL of HCl 37%. The mixture was stirred for 15 minutes before being placed in the microwave system at 120ºC for 30 min. The solution was precipitated with 20 mL 1:1 mix of diethyl ether/*n*-pentane.

(c) Microwave-assisted (DMF, 2): $ZrCl_4$ (116.5 mg, 0.50 mmol), bipy (39.0 mg, 0.25 mmol) and ATA (45.3 mg, 0.25 mmol) were added to a wide neck glass vial with 15 mL of DMF and 3 mL of HCl 37%. The mixture was stirred for 15 minutes before being placed in the microwave system at 100ºC for 30 min. The precipitate was centrifuged and washed with DMF four times. Then centrifuged and washed with methanol three times and dried at r.t.

(d) Microwave-assisted (H_2O): $ZrCl_4$ (116.5 mg, 0.50 mmol), bipy (39.0 mg, 0.25 mmol) and ATA (45.3 mg, 0.25 mmol) were added to a wide neck glass vial with 15 mL of distilled water and 3 mL of HCl 37%. The mixture was stirred for 15 minutes before being placed in the microwave system at 120ºC for 30 min. The pink solution was precipitated with 20 mL of the 1:1 diethyl ether mixture, yielding colorless block crystals.

(c) Layering: $ZrOCl_2$ (35.2 mg, 0.05 mmol) was dissolved in 5 mL of water and 2 mL were added to the bottom of the tube. ATA (36.0 mg, 0.05 mmol) was dissolved in 5 mL of methanol, and 2 mL were layered carefully on top. The same was done with 2 mL of bipy (31.2 mg, 0.05 mmol) in 5 mL of ethanol solution. After three days, a single crystal was formed, but yellow solid also deposited at the bottom.

(e) Mechanochemistry: $ZrCl_4$ (600.0 mg, mmol), bipy (201.1 mg, mmol) and ATA (233.0 mg were added to an agate jar, uniformizing with a spatula. Two 10 mm balls and

one 5 mm ball (m = 10.66 g) were added and the agate reactor was placed on the milling machine. The reaction was performed at 500 rpm for three hours. The final product was a purplish or brownish powder.

4.5.3.18 Synthesis and Characterization of the B4 Compounds

The **B4** compound was attempted through diffusion layering using a wide range of combinations for the solvents, yet they still yielded a dark solution, which doesn't precipitate using diethyl ether nor pentane nor a 1:1 mixture of both.

(a) Layering (H_2O/EtOH/MeOH): $ZrOCl_2$ (35.2 mg, 0.15 mmol) was dissolved in 5 mL of water and 2 mL were added to the bottom of the tube. ATA (36.0 mg, 0.20 mmol) was dissolved in 5 mL of ethanol, and 2 mL were layered carefully on top. The same was done with 2 mL of **L1** (36.0 mg, 0.20 mmol) in 5 mL of methanol solution. After three days, a single crystal was formed in one of the tubes.

(b) Layering (EtOH/MeOH): $ZrOCl_2$ (35.2 mg, 0.15 mmol) and **L1** (36.0 mg, 0.20 mmol) were dissolved in 5 mL of ethanol and 2 mL were added to the bottom of the tube. ATA (36.0 mg, 0.20 mmol) was dissolved in 5 mL of methanol, and 2 mL were layered carefully on top.

(c) Layering (DMF/EtOH): $ZrOCl_2$ (35.2 mg, 0.15 mmol) was dissolved in 5 mL of water and 2 mL were added to the bottom of the tube. ATA (36.0 mg, 0.20 mmol) and **L1** (36.0 mg, 0.20 mmol) were dissolved at 40ºC in 5 mL of ethanol plus two drops of NEt_3, and 2 mL were layered carefully on top. The same was repeated using $ZrCl_4$ instead.

(d) Layering (DMF/EtOH): $ZrCl_4$ (46.6 mg, 0.15 mmol) was dissolved in 5 mL of ethanol. Then, ATA (36.0 mg, 0.20 mmol) and **L1** (36.0 mg, 0.20 mmol) were dissolved at 80ºC in 5 mL of ethanol, adding 2 mL to a tube. The Zr solution was afterwards layered on top.

4.5.3.19 Synthesis and Characterization of the B5 Compounds

B5 was also synthesized following the diffusion layering technique.

(a) Layering ($CHCl_3$/MeOH): ATA (36.0 mg, 0.20 mmol) was dissolved in 5 mL of ethanol, and 2 mL were layered carefully on top. The same was done with 2 mL of **L1** (36.0 mg, 0.20 mmol) in 5 mL of methanol solution. $ZrOCl_2$ (50.0 mg, 0.15 mmol) was dissolved in 5 mL of methanol and 2 mL were added to the bottom of the tube. After three days, a single crystal was formed in one of the tubes. All the other tubes yielded only TPT.

4.5.3.20 Synthesis and Characterization of the B6 Compounds

The **B6** compounds followed the microwave-assisted and layering techniques for its synthesis.

(a) Microwave-assisted: $ZrCl_4$ (104.8 mg, 0.45 mmol) and **L6** (108.1 mg, 0.45 mmol) were added to a wide neck glass vial with 17.5 mL of distilled water and 2 mL of acetic

acid. The mixture was stirred for 15 minutes before being placed in the microwave system at 120ºC for 30 min. The tube rested for one day and then the solution was filtered, washed with water and methanol. The compound dissolved in methanol; therefore, we concluded it was just an organic compound, performing an ^{1}H NMR to confirm which. The results was that the compound formed was one of the precursors for **L6**, the 4-formylbenzoic acid.

(b) Layering: $ZrCl_4$ (23.3 mg, 0.01 mmol) was dissolved in 5 mL of water and 2 mL were added to the bottom of the tube. **L6** (48.1 mg, 0.02 mmol) was dissolved in 20 mL of DMF with sonification, layering 2 mL of solution carefully. It yielded a yellow solid.

4.5.4 Synthesis of the Reference Photocatalyst

The 3:2 Cd/Zn photocatalyst was used as a reference for the studies in the H_2 production to compare the MOFs/complexes results. The synthesis of this compound was adapted from the literature [124].

In a beaker, $Cd(NO_3)_2.4H_2O$ (984.5 mg, 4.2 mmol) and $Zn(NO_3)_2.4H_2O$ (525.7 mg, 2.8 mmol) were dissolved in 40 mL of distilled water under stirring and at 70ºC.

An aqueous solution of Na_2S (1.66 mg) was prepared in 40 mL of distilled water and added dropwise to the Cd/Zn solution, followed by vigorous stirring at 70ºC for 30 minutes. The yellow mixture was filtered and washed with water. The solid was dried at 80ºC for 20H.

IR ATR ν max (cm^{-1}): 3291 (b), 1622, 1363, 1111, 997.

BIBLIOGRAPHY

[1] J. Ceramella *et al.*, "A Look at the Importance of Chirality in Drug Activity: Some Significative Examples," *Appl Sci*, vol. 12, no. 21, p. 10909, Oct. 2022, doi: 10.3390/app122110909.

[2] S. Liu *et al.*, "Design of metal-organic framework-based photocatalysts for hydrogen generation," *Coord Chem Rev*, vol. 413, p. 213266, Jun. 2020, doi: 10.1016/j.ccr.2020.213266.

[3] Y. Qin *et al.*, "Metal–organic frameworks for photocatalysis," *Interface of Science and Technology*, Elsevier, vol. 31 2020, pp. 541–579. doi: 10.1016/B978-0-08-102890-2.00017-8.

[4] A. E. Baumann *et al*, "Metal-organic framework functionalization and design strategies for advanced electrochemical energy storage devices," *Commun Chem*, vol. 2, no. 1, p. 86, Jul. 2019, doi: 10.1038/s42004-019-0184-6.

[5] C. P. Raptopoulou, "Metal-Organic Frameworks: Synthetic Methods and Potential Applications," *Materials*, vol. 14, no. 2, p. 310, Jan. 2021, doi: 10.3390/ma14020310.

[6] S. R. Batten *et al.*, "Terminology of metal–organic frameworks and coordination polymers (IUPAC Recommendations 2013)," *Pure Appl Chem*, vol. 85, no. 8, pp. 1715–1724, Jul. 2013, doi: 10.1351/PAC-REC-12-11-20.

[7] O. M. Yaghi *et al.*, "Selective binding and removal of guests in a microporous metal–organic framework," *Nature*, vol. 378, no. 6558, pp. 703–706, Dec. 1995, doi: 10.1038/378703a0.

[8] S. Øien-Ødegaard *et al.*, D. S. Wragg, and K. P. Lillerud, "Pitfalls in metal–organic framework crystallography: towards more accurate crystal structures," *Chem Soc Rev*, vol. 46, no. 16, pp. 4867–4876, 2017, doi: 10.1039/C6CS00533K.

[9] J. L. C. Rowsell *et al.*, "Metal–organic frameworks: a new class of porous materials," *Microporous Mesoporous Mater*, vol. 73, no. 1–2, pp. 3–14, Aug. 2004, doi: 10.1016/j.micromeso.2004.03.034.

[10] O. M. Yaghi *et al.*, "Mutually Interpenetrating Sheets and Channels in the Extended Structure of [Cu(4,4′-bpy)Cl]," *Angew Chem Int Ed Eng*, vol. 34, no. 2, pp. 207–209, Feb. 1995, doi: 10.1002/anie.199502071.

[11] X. Feng *et al.*, "Generating Catalytic Sites in UiO-66 through Defect Engineering," *ACS Appl Mater Interfaces*, vol. 13, no. 51, pp. 60715–60735, Dec. 2021, doi: 10.1021/acsami.1c13525.

[12] H. Li *et al.*, "Design and synthesis of an exceptionally stable and highly porous metal-organic framework," *Nature*, vol. 402, no. 6759, pp. 276–279, Nov. 1999, doi: 10.1038/46248.

[13] A. Dhakshinamoorthy *et al.*, "Catalysis and photocatalysis by metal organic frameworks," *Chem Soc Rev*, vol. 47, no. 22, pp. 8134–8172, 2018, doi: 10.1039/C8CS00256H.

[14] S. T. Meek *et al.*, "Metal-Organic Frameworks: A Rapidly Growing Class of Versatile Nanoporous Materials," *Adv Mater*, vol. 23, no. 2, pp. 249–267, Jan. 2011, doi: 10.1002/adma.201002854.

[15] Y. Qin *et al.*, "Metal–organic frameworks for photocatalysis," 2020, pp. 541–579. doi: 10.1016/B978-0-08-102890-2.00017-8.

[16] T. Devic *et al.*, "High valence 3p and transition metal based MOFs," *Chem Soc Rev*, vol. 43, no. 16, pp. 6097–6115, 2014, doi: 10.1039/C4CS00081A.

[17] T.-F. Liu *et al.*, "Topology-Guided Design and Syntheses of Highly Stable Mesoporous Porphyrinic Zirconium Metal–Organic Frameworks with High Surface Area," *J Am Chem Soc*, vol. 137, no. 1, pp. 413–419, Jan. 2015, doi: 10.1021/ja5111317.

[18] B. Wang *et al.*, "Highly Stable Zr(IV)-Based Metal–Organic Frameworks for the Detection and Removal of Antibiotics and Organic Explosives in Water," *J Am Chem Soc*, vol. 138, no. 19, pp. 6204–6216, May 2016, doi: 10.1021/jacs.6b01663.

[19] S. T. Meek *et al.*, "Metal-Organic Frameworks: A Rapidly Growing Class of Versatile Nanoporous Materials," *Adv Mater*, vol. 23, no. 2, pp. 249–267, Jan. 2011, doi: 10.1002/adma.201002854.

[20] S. Yuan *et al.*, "Stable Metal–Organic Frameworks: Design, Synthesis, and Applications," *Advanced Materials*, vol. 30, no. 37, Sep. 2018, doi: 10.1002/adma.201704303.

[21] N. Kornienko *et al.*, "Metal–Organic Frameworks for Electrocatalytic Reduction of Carbon Dioxide," *J Am Chem Soc*, vol. 137, no. 44, pp. 14129–14135, Nov. 2015, doi: 10.1021/jacs.5b08212.

[22] H. P. Nguyen Thi *et al.*, "Size-Control and Surface Modification of Flexible Metal-Organic Framework MIL-53(Fe) by Polyethyleneglycol for 5- Fluorouracil Anticancer Drug Delivery," *ChemistrySelect*, vol. 4, no. 8, pp. 2333–2338, Feb. 2019, doi: 10.1002/slct.201803887.

[23] B. J. Deibert *et al.*, "A distinct reversible colorimetric and fluorescent low pH response on a water-stable zirconium–porphyrin metal–organic framework," *Chem Comm*, vol. 50, no. 68, pp. 9636–9639, 2014, doi: 10.1039/C4CC01938E.

[24] Y. Fu *et al.*, "An Amine-Functionalized Titanium Metal–Organic Framework Photocatalyst with Visible-Light-Induced Activity for CO2 Reduction," *Angew Chem Int Ed*, vol. 51, no. 14, pp. 3364–3367, Apr. 2012, doi: 10.1002/anie.201108357.

[25] M. A. Nasalevich *et al.*, "Co@NH2-MIL-125(Ti): cobaloxime-derived metal–organic framework-based composite for light-driven H2 production," *Energy Environ Sci*, vol. 8, no. 1, pp. 364–375, 2015, doi: 10.1039/C4EE02853H.

[26] H. Furukawa *et al.*, "Water Adsorption in Porous Metal–Organic Frameworks and Related Materials," *J Am Chem Soc*, vol. 136, no. 11, pp. 4369–4381, Mar. 2014, doi: 10.1021/ja500330a.

[27] K. Wang *et al.*, "Pyrazolate-Based Porphyrinic Metal–Organic Framework with Extraordinary Base-Resistance," *J Am Chem Soc*, vol. 138, no. 3, pp. 914–919, Jan. 2016, doi: 10.1021/jacs.5b10881.

[28] O. K. Farha *et al.*, "Rational Design, Synthesis, Purification, and Activation of Metal−Organic Framework Materials," *Acc Chem Res*, vol. 43, no. 8, pp. 1166–1175, Aug. 2010, doi: 10.1021/ar1000617.

[29] N. M. Padial *et al.*, "Highly Hydrophobic Isoreticular Porous Metal–Organic Frameworks for the Capture of Harmful Volatile Organic Compounds," *Angew Chem Int Ed*, vol. 52, no. 32, pp. 8290–8294, Aug. 2013, doi: 10.1002/anie.201303484.

[30] T. Tsuruoka *et al.*, "Nanoporous Nanorods Fabricated by Coordination Modulation and Oriented Attachment Growth," *Angew Chem Int Ed*, vol. 48, no. 26, pp. 4739–4743, Jun. 2009, doi: 10.1002/anie.200901177.

[31] M. Zhang *et al.*, "Symmetry-Guided Synthesis of Highly Porous Metal–Organic Frameworks with Fluorite Topology," *Angew Chem Int Ed*, vol. 53, no. 3, pp. 815–818, Jan. 2014, doi: 10.1002/anie.201307340.

[32] J. H. Cavka *et al.*, "A New Zirconium Inorganic Building Brick Forming Metal Organic Frameworks with Exceptional Stability," *J Am Chem Soc*, vol. 130, no. 42, pp. 13850–13851, Oct. 2008, doi: 10.1021/ja8057953.

[33] A. Schaate *et al.*, "Modulated Synthesis of Zr-Based Metal–Organic Frameworks: From Nano to Single Crystals," *Chem Eur J*, vol. 17, no. 24, pp. 6643–6651, Jun. 2011, doi: 10.1002/chem.201003211.

[34] A. Umemura *et al.*, "Morphology Design of Porous Coordination Polymer Crystals by Coordination Modulation," *J Am Chem Soc*, vol. 133, no. 39, pp. 15506–15513, Oct. 2011, doi: 10.1021/ja204233q.

[35] BM. Omkaramurthy *et al.*, "Two new Zn (II) bdc Metal-Organic Frameworks based on benzene 1, 4-dicarboxylic acid: Synthesis, Crystal structures, Luminescent properties and Electrochemical studies," *Mater Today Proc*, vol. 22, pp. 2179–2190, 2020, doi: 10.1016/j.matpr.2020.03.298.

[36] P. Horcajada *et al.*, "Porous metal–organic-framework nanoscale carriers as a potential platform for drug delivery and imaging," *Nat Mater*, vol. 9, no. 2, pp. 172–178, Feb. 2010, doi: 10.1038/nmat2608.

[37] R. Safdar Ali *et al.*, "Zinc-Based Metal-Organic Frameworks in Drug Delivery, Cell Imaging, and Sensing," *Molecules*, vol. 27, no. 1, p. 100, Dec. 2021, doi: 10.3390/molecules27010100.

[38] M. Sohail *et al.*, "A new water stable zinc metal organic framework as an electrode material for hydrazine sensing," *New J Chem*, vol. 42, no. 15, pp. 12486–12491, 2018, doi: 10.1039/C8NJ01507D.

[39] J. Lan *et al.*, "A facile fabrication of a multi-functional and hierarchical Zn-based MOF as an efficient catalyst for CO_2 fixation at room-temperature," *Inorg Chem Front*, vol. 8, no. 12, pp. 3085–3095, 2021, doi: 10.1039/D1QI00104C.

[40] S. Kalhor *et al.*, "Application of Functionalized Zn-Based Metal–Organic Frameworks (Zn-MOFs) with CuO in Heterocycle Synthesis via Azide–Alkyne Cycloaddition," *Inorg Chem*, vol. 63, no. 11, pp. 4898–4914, Mar. 2024, doi: 10.1021/acs.inorgchem.3c03988.

[41] W. Li *et al.*, "Microporous metal–organic frameworks constructed by Cu(I)/Zn(II), Tpt and 1,4-benzenedicarboxylate," *Inorg Chem Commun*, vol. 10, no. 7, pp. 753–756, Jul. 2007, doi: 10.1016/j.inoche.2007.03.026.

[42] R. Pepinsky, "Crystal Engineering: New Concepts in Crystallography," *Phys. Rev.*, vol. 100, no. 971, 1955.

[43] G. M. J. Schmidt, "Photodimerization in the solid state," *Pure Appl Chem*, vol. 27, no. 4, pp. 647–678, Jan. 1971, doi: 10.1351/pac197127040647.

[44] G. R. Desiraju, *Crystal Engineering: The Design of Organic Solids*, 1st ed. Elsevier Science, 1989.

[45] K. Biradha, "Crystal engineering: from weak hydrogen bonds to co-ordination bonds," *Cryst Eng Comm*, vol. 5, no. 66, p. 374, 2003, doi: 10.1039/b309903b.

[46] J.-P. Zhang *et al.*, "Supramolecular isomerism in coordination polymers," *Chem Soc Rev*, vol. 38, no. 8, p. 2385, 2009, doi: 10.1039/b900317g.

[47] T. L. Hennigar *et al.*, "Supramolecular Isomerism in Coordination Polymers: Conformational Freedom of Ligands in [Co(NO3)2(1,2-bis(4-pyridyl)ethane)1.5]n," *Angew Chem Int Ed Eng*, vol. 36, no. 9, pp. 972–973, May 1997, doi: 10.1002/anie.199709721.

[48] P. Ball, "Scandal of crystal design...," *Nature*, vol. 381, no. 6584, pp. 648–650, Jun. 1996, doi: 10.1038/381648a0.

[49] B. Moulton *et al.*, "From Molecules to Crystal Engineering: Supramolecular Isomerism and Polymorphism in Network Solids," *Chem Rev*, vol. 101, no. 6, pp. 1629–1658, Jun. 2001, doi: 10.1021/cr9900432.

[50] S. M. Cohen, "Postsynthetic Methods for the Functionalization of Metal–Organic Frameworks," *Chem Rev*, vol. 112, no. 2, pp. 970–1000, Feb. 2012, doi: 10.1021/cr200179u.

[51] S. Yuan *et al.*, "Linker Installation: Engineering Pore Environment with Precisely Placed Functionalities in Zirconium MOFs," *J Am Chem Soc*, vol. 138, no. 28, pp. 8912–8919, Jul. 2016, doi: 10.1021/jacs.6b04501.

[52] M. Kalaj *et al.*, "Postsynthetic Modification: An Enabling Technology for the Advancement of Metal–Organic Frameworks," *ACS Cent Sci*, vol. 6, no. 7, pp. 1046–1057, Jul. 2020, doi: 10.1021/acscentsci.0c00690.

[53] M. Hoshino *et al.*, "The crystalline sponge method updated," *IUCrJ*, vol. 3, no. 2, pp. 139–151, Mar. 2016, doi: 10.1107/S2052252515024379.

[54] W. J. Gee, "The growing importance of crystalline molecular flasks and the crystalline sponge method," *Dalton Trans*, vol. 46, no. 46, pp. 15979–15986, 2017, doi: 10.1039/C7DT03136J.

[55] H. Furukawa *et al.*, "The Chemistry and Applications of Metal-Organic Frameworks," *Science (1979)*, vol. 341, no. 6149, Aug. 2013, doi: 10.1126/science.1230444.

[56] F. Gándara *et al.*, "Crystallography of metal–organic frameworks," *IUCrJ*, vol. 1, no. 6, pp. 563–570, Nov. 2014, doi: 10.1107/S2052252514020351.

[57] H. R. Abid *et al.*, "Physicochemical characterization of metal organic framework materials: A mini review," *Heliyon*, vol. 10, no. 1, p. e23840, Jan. 2024, doi: 10.1016/j.heliyon.2023.e23840.

[58] J. Martí-Rujas, "Structural elucidation of microcrystalline MOFs from powder X-ray diffraction," *Dalton Trans*, vol. 49, no. 40, pp. 13897–13916, 2020, doi: 10.1039/D0DT02802A.

[59] R. W. Frei, "Diffuse reflectance spectroscopy; applications, standards, and calibration (with special reference to chromatography)," *J Res Natl Bur Stand A Phys Chem*, vol. 80A, no. 4, p. 551, Jul. 1976, doi: 10.6028/jres.080A.055.

[60] P. Bajpai, "Optical Properties of Paper," in *Biermann's Handbook of Pulp and Paper*, Elsevier, 2018, pp. 237–271. doi: 10.1016/B978-0-12-814238-7.00011-8.

[61] Y. Inokuma *et al.*, "X-ray analysis on the nanogram to microgram scale using porous complexes," *Nature*, vol. 495, no. 7442, pp. 461–466, Mar. 2013, doi: 10.1038/nature11990.

[62] G. S. Nolas, *The Physics and Chemistry of Inorganic Clathrates*. Spinger, 2014.

[63] J. L. C. Rowsell *et al.*, "Metal–organic frameworks: a new class of porous materials," *Microporous Mesoporous Mater*, vol. 73, no. 1–2, pp. 3–14, Aug. 2004, doi: 10.1016/j.micromeso.2004.03.034.

[64] S. Kitagawa *et al.*, "Functional Porous Coordination Polymers," *Angew Chem Int Ed*, vol. 43, no. 18, pp. 2334–2375, Apr. 2004, doi: 10.1002/anie.200300610.

[65] Y. Inokuma *et al.*, "X-ray analysis on the nanogram to microgram scale using porous complexes," *Nature*, vol. 495, no. 7442, pp. 461–466, Mar. 2013, doi: 10.1038/nature11990.

[66] T. R. Ramadhar *et al.*, "Analysis of rapidly synthesized guest-filled porous complexes with synchrotron radiation: practical guidelines for the crystalline sponge

method," *Acta Crystallogr A Found Adv*, vol. 71, no. 1, pp. 46–58, Jan. 2015, doi: 10.1107/S2053273314019573.

[67] N. Zigon *et al.*, "Structural Elucidation of Trace Amounts of Volatile Compounds Using the Crystalline Sponge Method," *Chem Asian J*, vol. 12, no. 10, pp. 1057–1061, May 2017, doi: 10.1002/asia.201700515.

[68] N. Zigon *et al.*, "Where is the Oxygen? Structural Analysis of α-Humulene Oxidation Products by the Crystalline Sponge Method," *Angew Chem Int Ed*, vol. 54, no. 31, pp. 9033–9037, Jul. 2015, doi: 10.1002/anie.201502302.

[69] S. Yoshioka *et al.*, "X-ray Structure Analysis of Ozonides by the Crystalline Sponge Method," *J Am Chem Soc*, vol. 138, no. 32, pp. 10140–10142, Aug. 2016, doi: 10.1021/jacs.6b05817.

[70] Y. Hayashi *et al.*, "Crystalline sponge-laser desorption ionization (CS-LDI) of unsaturated cyclic organic compounds encapsulated in different electronic environments in pores," *Anal Chim Acta*, vol. 1064, pp. 80–86, Aug. 2019, doi: 10.1016/j.aca.2019.03.011.

[71] X.-F. Gu *et al.*, "Differentiation of volatile aromatic isomers and structural elucidation of volatile compounds in essential oils by combination of HPLC separation and crystalline sponge method," *J Chromatogr A*, vol. 1474, pp. 130–137, Nov. 2016, doi: 10.1016/j.chroma.2016.10.072.

[72] W. M. Bloch *et al.*, "X-ray Crystallography in Open-Framework Materials," *Angew Chem Int Ed*, vol. 54, no. 44, pp. 12860–12867, Oct. 2015, doi: 10.1002/anie.201501545.

[73] G.-H. Ning *et al.*, "A saccharide-based crystalline sponge for hydrophilic guests," *Chem Comm*, vol. 52, no. 43, pp. 7013–7015, 2016, doi: 10.1039/C6CC03026B.

[74] K. Rissanen, "Crystallography of encapsulated molecules," *Chem Soc Rev*, vol. 46, no. 9, pp. 2638–2648, 2017, doi: 10.1039/C7CS00090A.

[75] F. Habib *et al.*, "Applications of the crystalline sponge method and developments of alternative crystalline sponges," *Mater Today Proc*, vol. 56, pp. 3766–3773, 2022, doi: 10.1016/j.matpr.2022.01.018.

[76] K. Ohara *et al.*, "The Catalytic Z to E Isomerization of Stilbenes in a Photosensitizing Porous Coordination Network," *Angew Chem Int Ed*, vol. 49, no. 32, pp. 5507–5509, Jul. 2010, doi: 10.1002/anie.201001902.

[77] E. G. Derouane *et al.*, "Confinement effects in the adsorption of simple bases by zeolites," *Microporous Mesoporous Mater*, vol. 35–36, pp. 425–433, Apr. 2000, doi: 10.1016/S1387-1811(99)00239-5.

[78] G. Sastre *et al.*, "The confinement effect in zeolites," *J Mol Catal A Chem*, vol. 305, no. 1–2, pp. 3–7, Jun. 2009, doi: 10.1016/j.molcata.2008.10.042.

[79] E. Sanna *et al.*, "Macrocyclic Tetraimines: Synthesis and Reversible Uptake of Diethyl Phthalate by a Porous Macrocycle," *J Org Chem*, vol. 81, no. 12, pp. 5173–5180, Jun. 2016, doi: 10.1021/acs.joc.6b00768.

[80] S.-Y. Zhang *et al.*, "Structural Insight into Guest Binding Sites in a Porous Homochiral Metal–Organic Material," *J Am Chem Soc*, vol. 137, no. 37, pp. 12045–12049, Sep. 2015, doi: 10.1021/jacs.5b06760.

[81] V. Duplan *et al.*, "In Situ Observation of Thiol Michael Addition to a Reversible Covalent Drug in a Crystalline Sponge," *Angew Chem Int Ed*, vol. 55, no. 16, pp. 4919–4923, Apr. 2016, doi: 10.1002/anie.201509801.

[82] K. Ikemoto *et al.*, "X-ray Snapshot Observation of Palladium-Mediated Aromatic Bromination in a Porous Complex," *J Am Chem Soc*, vol. 136, no. 19, pp. 6892–6895, May 2014, doi: 10.1021/ja502996h.

[83] A. Dhakshinamoorthy *et al.*, "Metal–Organic Framework (MOF) Compounds: Photocatalysts for Redox Reactions and Solar Fuel Production," *Angewandte Chemie International Edition*, vol. 55, no. 18, pp. 5414–5445, Apr. 2016, doi: 10.1002/anie.201505581.

[84] J. C. Scaiano *et al.*, "Intrazeolite Photochemistry: Toward Supramolecular Control of Molecular Photochemistry," *Acc Chem Res*, vol. 32, no. 9, pp. 783–793, Sep. 1999, doi: 10.1021/ar9702536.

[85] J.-W. Grimaldo-Guerrero *et al.*, "A Review of History, Production and Storage of Hydrogen," *J Eng Sci Tech Rev*, vol. 14, no. 5, pp. 121–134, Oct. 2021, doi: 10.25103/jestr.145.14.

[86] J. M. Ogden, "Hydrogen: The Fuel of the Future?," *Phys Today*, vol. 55, no. 4, pp. 69–75, Apr. 2002, doi: 10.1063/1.1480785.

[87] A. Fujishima *et al.*, "Electrochemical Photolysis of Water at a Semiconductor Electrode," *Nature*, vol. 238, no. 5358, pp. 37–38, Jul. 1972, doi: 10.1038/238037a0.

[88] L. Zeng *et al.*, "Metal–Organic Frameworks: Versatile Materials for Heterogeneous Photocatalysis," *ACS Catal*, vol. 6, no. 11, pp. 7935–7947, Nov. 2016, doi: 10.1021/acscatal.6b02228.

[89] X. Chen *et al.*, "Titanium Dioxide Nanomaterials: Synthesis, Properties, Modifications, and Applications," *Chem Rev*, vol. 107, no. 7, pp. 2891–2959, Jul. 2007, doi: 10.1021/cr0500535.

[90] T. Hisatomi *et al.*, "Recent advances in semiconductors for photocatalytic and photoelectrochemical water splitting," *Chem. Soc. Rev.*, vol. 43, no. 22, pp. 7520–7535, Jan. 2014, doi: 10.1039/C3CS60378D.

[91] L. Jiao *et al.*, "Metal–Organic Frameworks as Platforms for Catalytic Applications," *Adv Mater*, vol. 30, no. 37, Sep. 2018, doi: 10.1002/adma.201703663.

[92] H. Furukawa *et al.*, "Ultrahigh Porosity in Metal-Organic Frameworks," *Science (1979)*, vol. 329, no. 5990, pp. 424–428, Jul. 2010, doi: 10.1126/science.1192160.

[93] X. Lang *et al.*, "Heterogeneous visible light photocatalysis for selective organic transformations," *Chem Soc Rev*, vol. 43, no. 1, pp. 473–486, 2014, doi: 10.1039/C3CS60188A.

[94] C. A. Downes *et al.*, "Evaluation of the H2 Evolving Activity of Benzenehexathiolate Coordination Frameworks and the Effect of Film Thickness on H2

Production," *ACS Appl Mater Interfaces*, vol. 10, no. 2, pp. 1719–1727, Jan. 2018, doi: 10.1021/acsami.7b15969.

[95] Y. Gong *et al.*, "Metal(II)-Induced Coordination Polymer Based on 4-(5-(Pyridin-4-yl)-4H-1,2,4-triazol-3-yl)benzoate as an Electrocatalyst for Water Splitting," *Cryst Growth Des*, vol. 14, no. 2, pp. 649–657, Feb. 2014, doi: 10.1021/cg401529u.

[96] C. H. Hendon *et al.*, "Engineering the Optical Response of the Titanium-MIL-125 Metal–Organic Framework through Ligand Functionalization," *J Am Chem Soc*, vol. 135, no. 30, pp. 10942–10945, Jul. 2013, doi: 10.1021/ja405350u.

[97] C. Gomes Silva *et al.*, "Water Stable Zr–Benzenedicarboxylate Metal–Organic Frameworks as Photocatalysts for Hydrogen Generation," *Chem Eur J*, vol. 16, no. 36, pp. 11133–11138, Sep. 2010, doi: 10.1002/chem.200903526.

[98] Z. Lionet *et al.*, "Linker Engineering of Iron-Based MOFs for Efficient Visible-Light-Driven Water Oxidation Reaction," *J Phys Chem C*, vol. 123, no. 45, pp. 27501–27508, Nov. 2019, doi: 10.1021/acs.jpcc.9b06838.

[99] L.-L. Dang *et al.*, "Stable Zinc-Based Metal-Organic Framework Photocatalyst for Effective Visible-Light-Driven Hydrogen Production," *Molecules*, vol. 27, no. 6, p. 1917, Mar. 2022, doi: 10.3390/molecules27061917.

[100] Q. Wang *et al.*, "Recent advances in MOF-based photocatalysis: environmental remediation under visible light," *Inorg Chem Front*, vol. 7, no. 2, pp. 300–339, 2020, doi: 10.1039/C9QI01120J.

[101] J. F. Reber *et al.*, "Photochemical production of hydrogen with zinc sulfide suspensions," *J Phys Chem*, vol. 88, no. 24, pp. 5903–5913, Nov. 1984, doi: 10.1021/j150668a032.

[102] J. Zhang *et al.*, "Visible Light Photocatalytic H2 -Production Activity of CuS/ZnS Porous Nanosheets Based on Photoinduced Interfacial Charge Transfer," *Nano Lett*, vol. 11, no. 11, pp. 4774–4779, Nov. 2011, doi: 10.1021/nl202587b.

[103] Q. Li *et al.*, "Zn1–xCdxS Solid Solutions with Controlled Bandgap and Enhanced Visible-Light Photocatalytic H_2 -Production Activity," *ACS Catal*, vol. 3, no. 5, pp. 882–889, May 2013, doi: 10.1021/cs4000975.

[104] A. Chatz-Giachia *et al.*, "Detection of nitrophenols with a fluorescent Zr(IV) metal–organic framework functionalized with benzylamino groups," *J Mater Chem C Mater*, vol. 10, no. 34, pp. 12307–12315, 2022, doi: 10.1039/D2TC02494B.

[105] S. Yuan *et al.*, "Exposed Equatorial Positions of Metal Centers via Sequential Ligand Elimination and Installation in MOFs," *J Am Chem Soc*, vol. 140, no. 34, pp. 10814–10819, Aug. 2018, doi: 10.1021/jacs.8b04886.

[106] J. Li *et al.*, "An 'Ingredients' Approach to Functional Self-Synthesizing Materials: A Metal-Ion-Selective, Multi-Responsive, Self-Assembled Hydrogel," *Chem Eur J*, vol. 20, no. 48, pp. 15709–15714, Nov. 2014, doi: 10.1002/chem.201404977.

[107] P. Ghamari Kargar *et al.*, "Simple synthesis of the novel Cu-MOF catalysts for the selective alcohol oxidation and the oxidative cross-coupling of amines and alcohols," *Appl Organomet Chem*, vol. 34, no. 12, Dec. 2020, doi: 10.1002/aoc.5965.

[108] Y. Zhou *et al.*, "Schiff Base-functionalized cobalt-based metal organic framework microspheres with a sea urchin-like structure for supercapacitor electrode material," *J Electroanal Chem*, vol. 847, p. 113248, Aug. 2019, doi: 10.1016/j.jelechem.2019.113248.

[109] C. Karunakaran *et al.*, "Conversion of anilines into azobenzenes in acetic acid with perborate and Mo(VI): correlation of reactivities," *Chem Pap*, vol. 73, no. 2, pp. 375–385, Feb. 2019, doi: 10.1007/s11696-018-0599-z.

[110] M. Taddei *et al.*, "Efficient microwave assisted synthesis of metal–organic framework UiO-66: optimization and scale up," *Dalton Trans*, vol. 44, no. 31, pp. 14019–14026, 2015, doi: 10.1039/C5DT01838B.

[111] R. R. Solís *et al.*, "Highly stable UiO-66-NH2 by the microwave-assisted synthesis for solar photocatalytic water treatment," *J Environ Chem Eng*, vol. 10, no. 2, p. 107122, Apr. 2022, doi: 10.1016/j.jece.2021.107122.

[112] Y. Tan *et al.*, "A layered amino-functionalized zinc-terephthalate metal organic framework: Structure, characterization and catalytic performance for Knoevenagel condensation," *Inorg Chem Commun*, vol. 14, no. 12, pp. 1966–1970, Dec. 2011, doi: 10.1016/j.inoche.2011.09.022.

[113] Z. Jin *et al.*, "Exploration of Zr–Metal–Organic Framework as Efficient Photocatalyst for Hydrogen Production," *Nanoscale Res Lett*, vol. 12, no. 1, p. 539, Dec. 2017, doi: 10.1186/s11671-017-2311-6.

[114] J. Ma *et al.*, "Composite ultrafiltration membrane tailored by MOF@GO with highly improved water purification performance," *Chem Eng J*, vol. 313, pp. 890–898, Apr. 2017, doi: 10.1016/j.cej.2016.10.127.

[115] Q. Liu *et al.*, "Removal of methyl orange wastewater by Ugi multicomponent reaction functionalized UiO-66-NS," *Environ Sci Pollut Res*, vol. 29, no. 51, pp. 76833–76846, Nov. 2022, doi: 10.1007/s11356-022-21175-0.

[116] X.-Q. Zhan *et al.*, "Ligands-Coordinated Zr-Based MOF for Wastewater Treatment," *Nanomaterials*, vol. 8, no. 9, p. 655, Aug. 2018, doi: 10.3390/nano8090655.

[117] J. Wang *et al.*, "Single- and few-layer BiOI as promising photocatalysts for solar water splitting," *RSC Adv*, vol. 7, no. 39, pp. 24446–24452, 2017, doi: 10.1039/C7RA01723E.

[118] Y. L. Wang *et al.*, "UiO-66-based metal organic frameworks for the photodegradation of acetaminophen under simulated solar irradiation," *J Environ Chem Eng*, vol. 9, no. 5, p. 106087, Oct. 2021, doi: 10.1016/j.jece.2021.106087.

[119] S. Hayami *et al.*, "Crystal Structure of a Molecular Building Block with π-π Intermolecular Interaction," *Mol Cryst Liq Crys*, vol. 379, no. 1, pp. 371–376, Jan. 2002, doi: 10.1080/713738628.

[120] R. Pritchard *et al.*, "CCDC 1977900: Experimental Crystal Structure Determination," 2020. doi: 10.5517/ccdc.csd.cc24d57z.

[121] K. T. Butler *et al.*, "Designing porous electronic thin-film devices: band offsets and heteroepitaxy," *Faraday Discuss*, vol. 201, pp. 207–219, 2017, doi: 10.1039/C7FD00019G.

[122] M. S. Samuel *et al.*, "Synthesis of a copper (II) metal–organic framework for photocatalytic degradation of rhodamine B dye in water," *Environ Sci Pollut Res*, vol. 28, no. 30, pp. 40835–40843, Aug. 2021, doi: 10.1007/s11356-021-13571-9.

[123] A. Dang *et al.*, "Embed CdS into MIL-101 to Boost the Photocatalytic Activity for Methylene Blue and Methyl Orange Degradation in the Visible Range," *Water Air Soil Pollut*, vol. 235, no. 2, p. 156, Feb. 2024, doi: 10.1007/s11270-024-06969-x.

[124] M. Antoniadou *et al.*, "Photocatalysis and photoelectrocatalysis using (CdS-ZnS)/TiO2 combined photocatalysts," *Appl Catal B*, vol. 107, no. 1–2, pp. 188–196, Aug. 2011, doi: 10.1016/j.apcatb.2011.07.013.

[125] Y. Inokuma *et al.*, "Preparation and guest-uptake protocol for a porous complex useful for 'crystal-free' crystallography," *Nat Protoc*, vol. 9, no. 2, pp. 246–252, Feb. 2014, doi: 10.1038/nprot.2014.007.

[126] M. Sahin *et al.*, "Photocatalytic Hydrogen Production by Direct Sunlight: A Laboratory Experiment," *J Chem Educ*, vol. 80, no. 11, p. 1314, Nov. 2003, doi: 10.1021/ed080p1314.

[127] V. Kumaravel *et al.*, "Photocatalytic Hydrogen Production: Role of Sacrificial Reagents on the Activity of Oxide, Carbon, and Sulfide Catalysts," *Catalysts*, vol. 9, no. 3, p. 276, Mar. 2019, doi: 10.3390/catal9030276.

[128] O. V. Dolomanov, *et al.*, "OLEX2: a complete structure solution, refinement and analysis program," *J Appl Crystallogr*, vol. 42, no. 2, pp. 339–341, Apr. 2009, doi: 10.1107/S0021889808042726.

[129] L. J. Farrugia, "WinGX and ORTEP for Windows: an update," *J Appl Crystallogr*, vol. 45, no. 4, pp. 849–854, Aug. 2012, doi: 10.1107/S0021889812029111.

[130] C. F. Macrae *et al.*, "Mercury 4.0: from visualization to analysis, design and prediction," *J Appl Crystallogr*, vol. 53, no. 1, pp. 226–235, Feb. 2020, doi: 10.1107/S1600576719014092.

[131] M. Montalti *et al.*, *Handbook of Photochemistry*. CRC Press, 2006. doi: 10.1201/9781420015195.

[132] C. G. Hatchard *et al.*, "A new sensitive chemical actinometer - II. Potassium ferrioxalate as a standard chemical actinometer," *Proc R Soc Lond A Math Phys Sci*, vol. 235, no. 1203, pp. 518–536, Jun. 1956, doi: 10.1098/rspa.1956.0102.

A

ANNEXES

A.1 Ligands Spectra

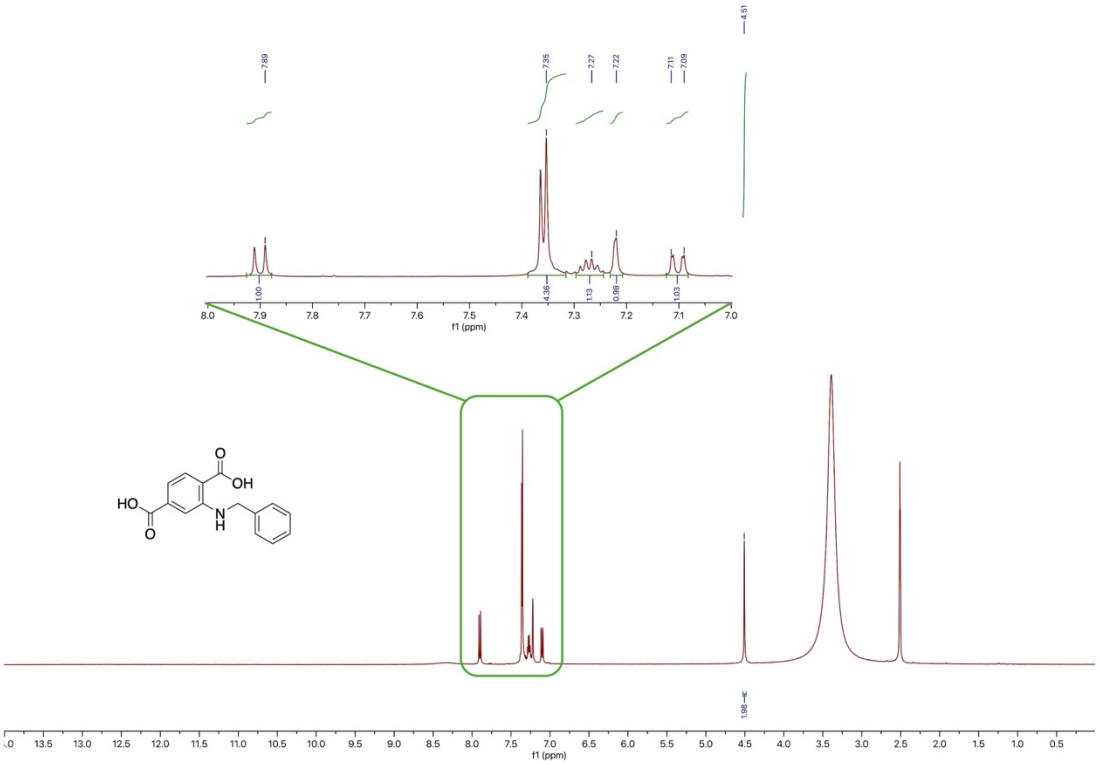

Figure A.1. ^{1}H NMR in DMSO of the synthesized **L1**.

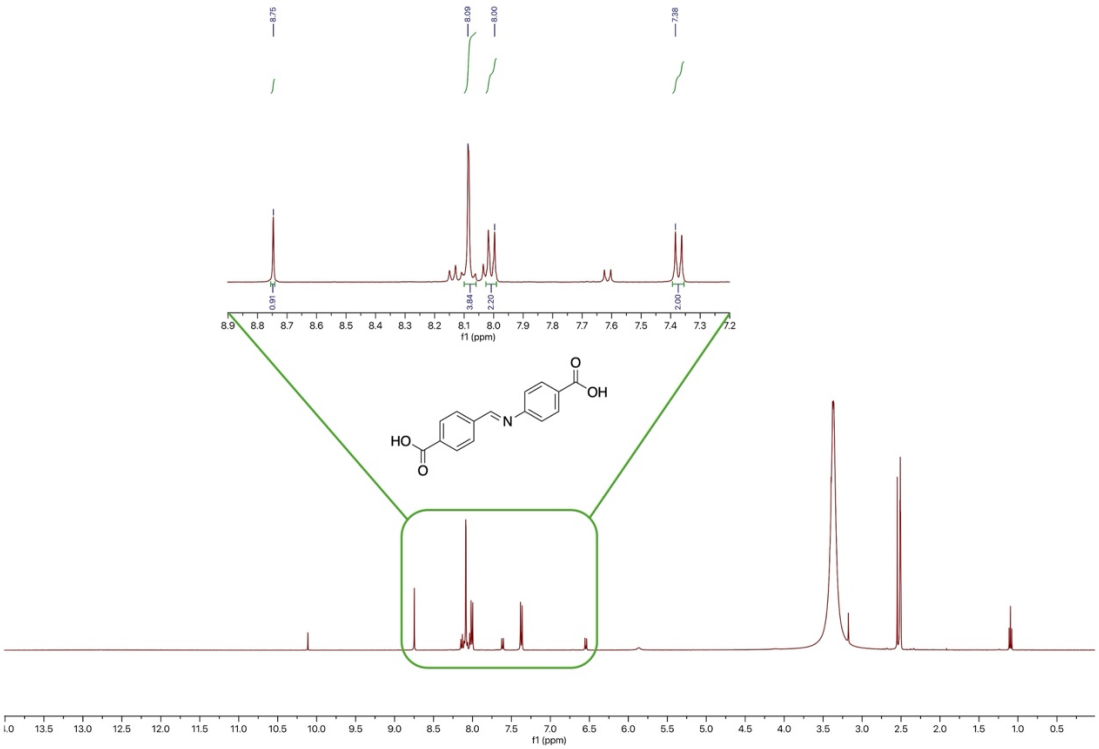

Figure A.2. ^{1}H NMR in DMSO of the synthesized **L2**.

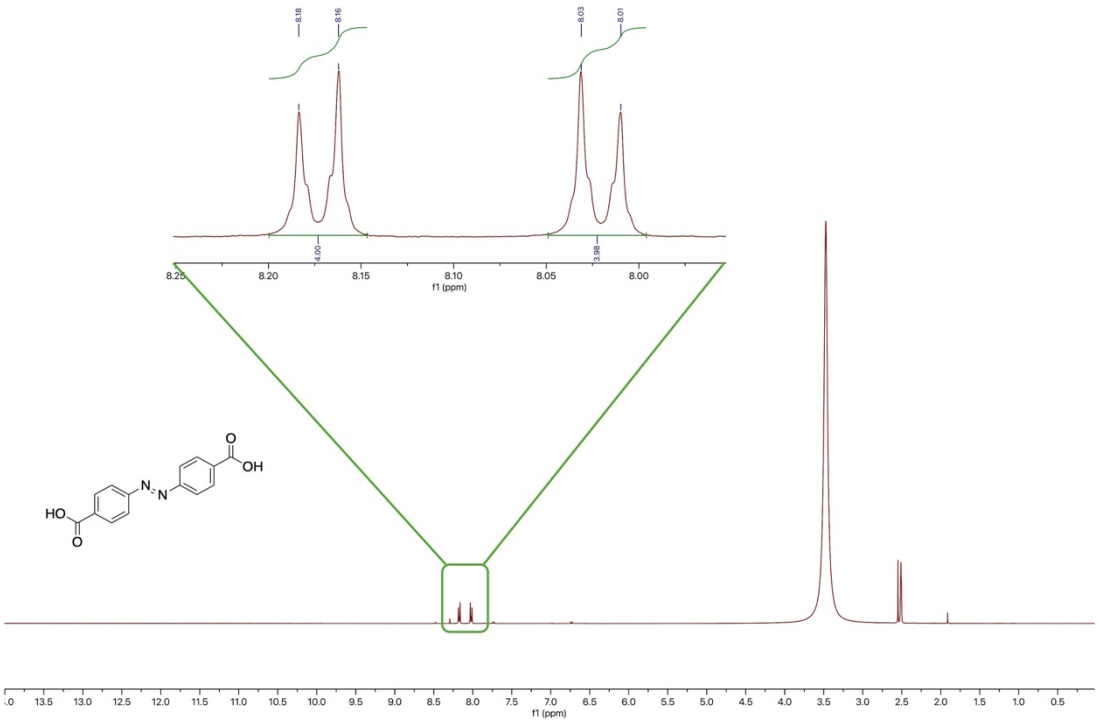

Figure A.3. ^{1}H NMR in DMSO of the synthesized **L3**.

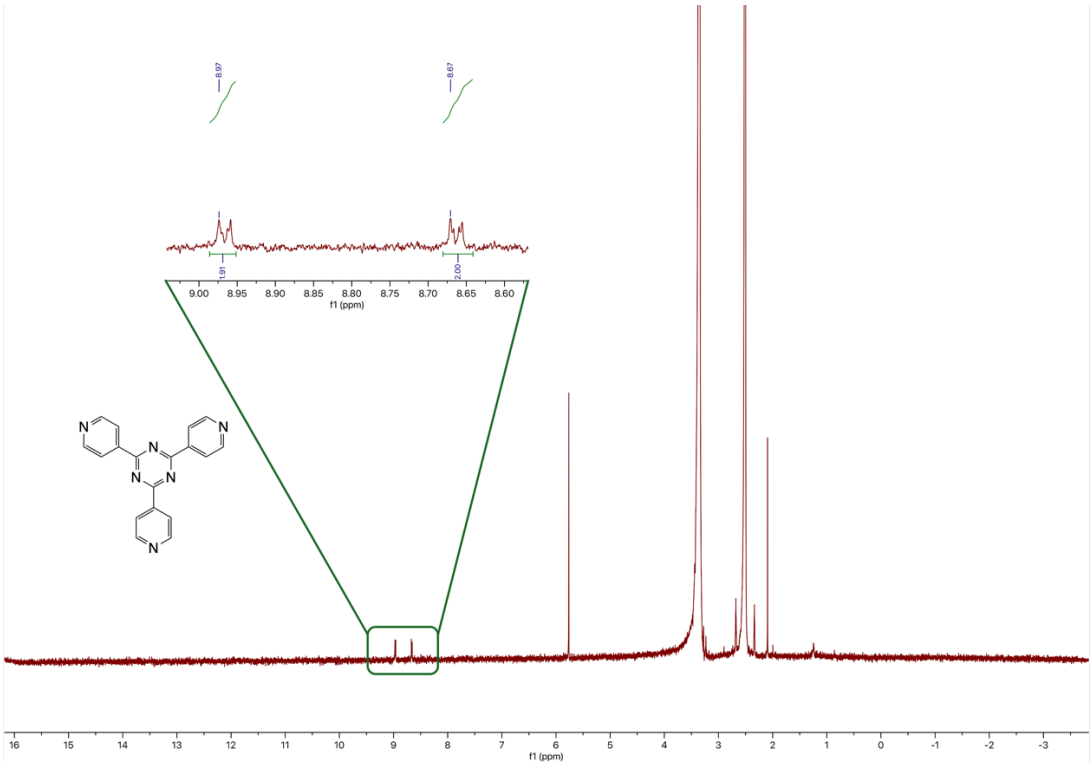

Figure A.4. [1]H NMR in DMSO of the synthesized TPT. (**L4**).

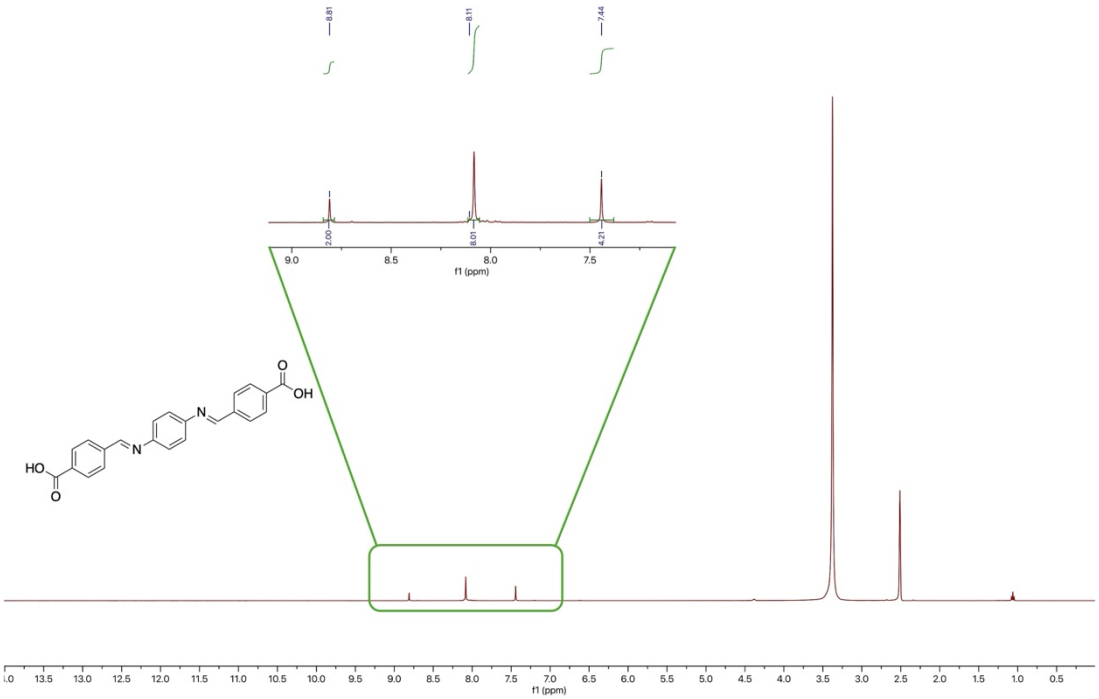

Figure A.5. [1]H NMR in DMSO of the synthesized **L5**.

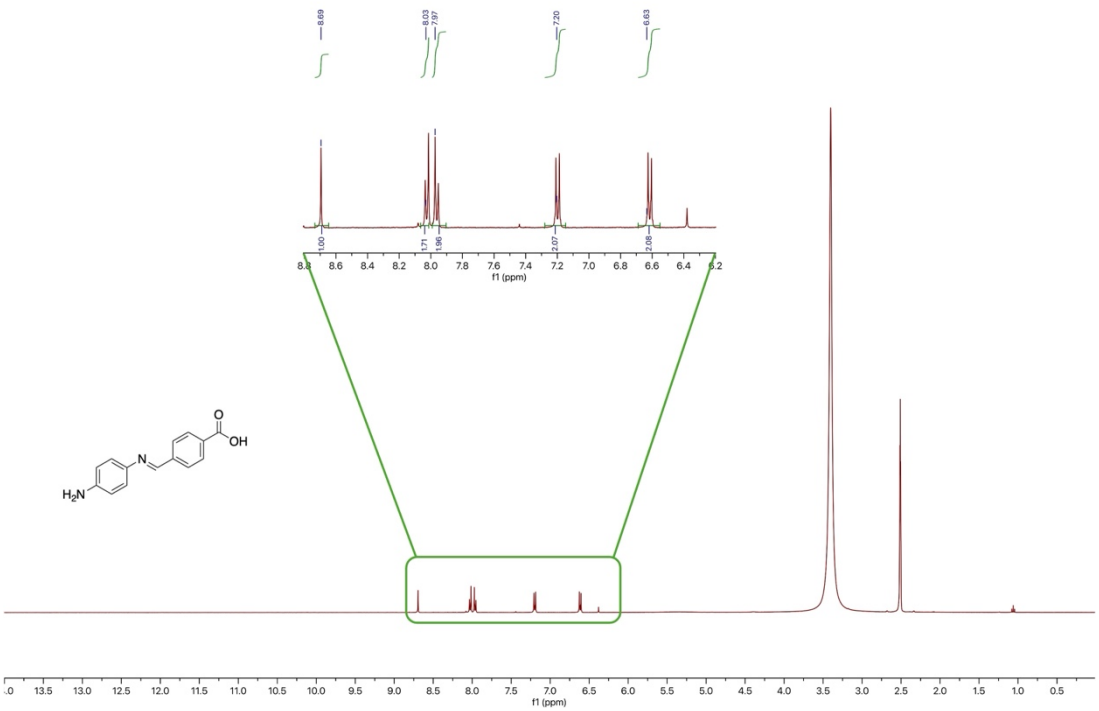

Figure A.5. ^{1}H NMR in DMSO of the synthesized **L6**.

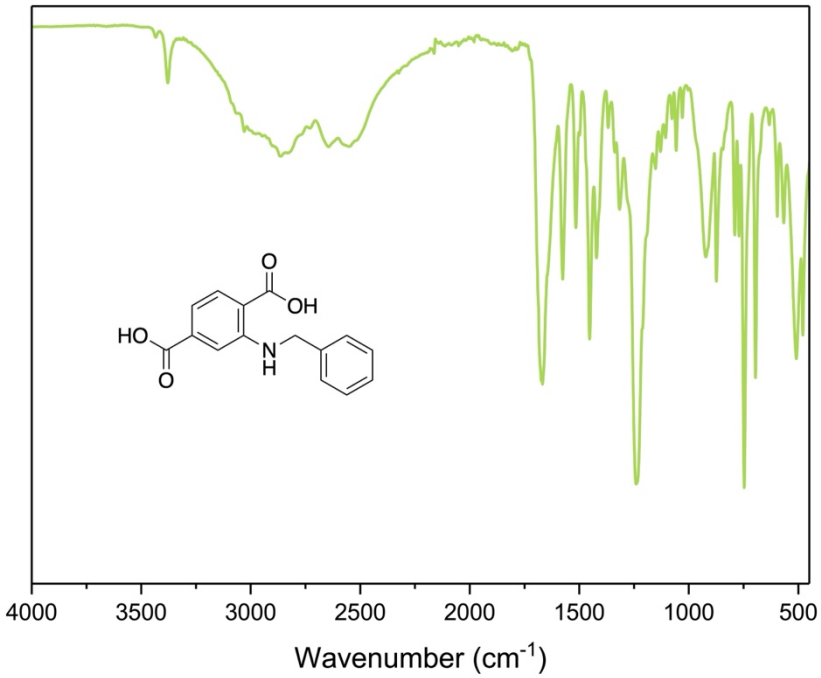

Figure A.6. FTIR spectrum for ligand **L1**.

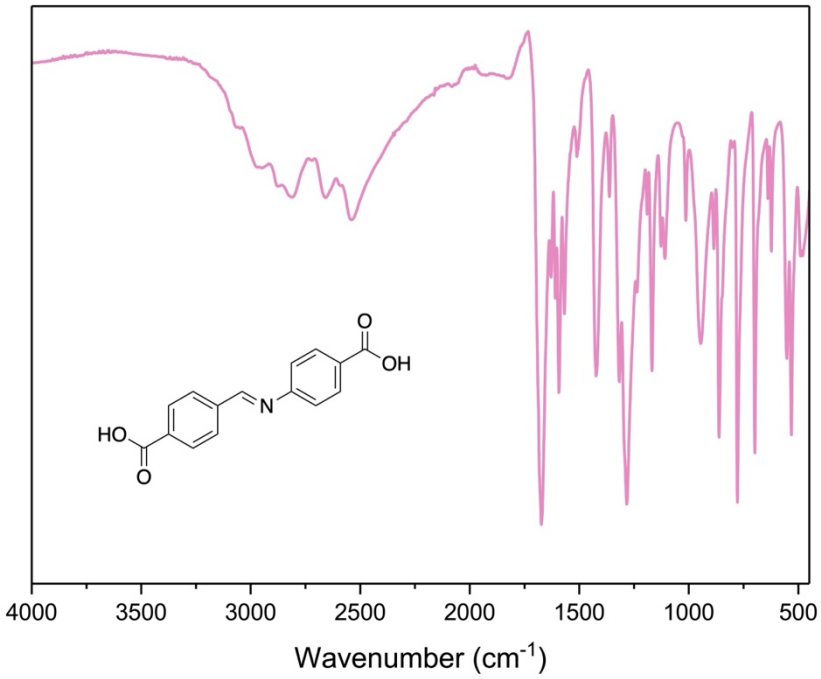

Figure A.7. FTIR spectrum for ligand **L2**.

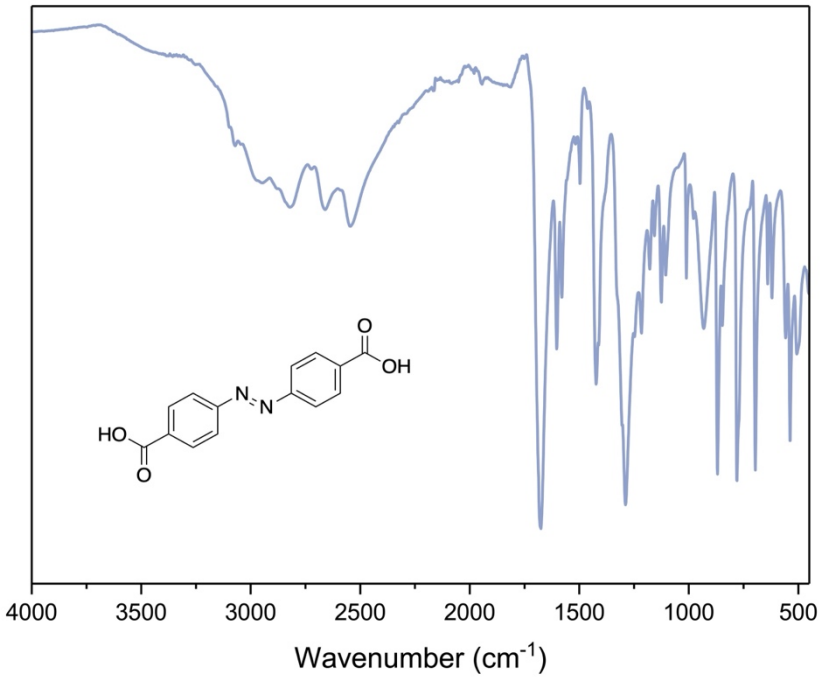

Figure A.8. FTIR spectrum for ligand **L3**.

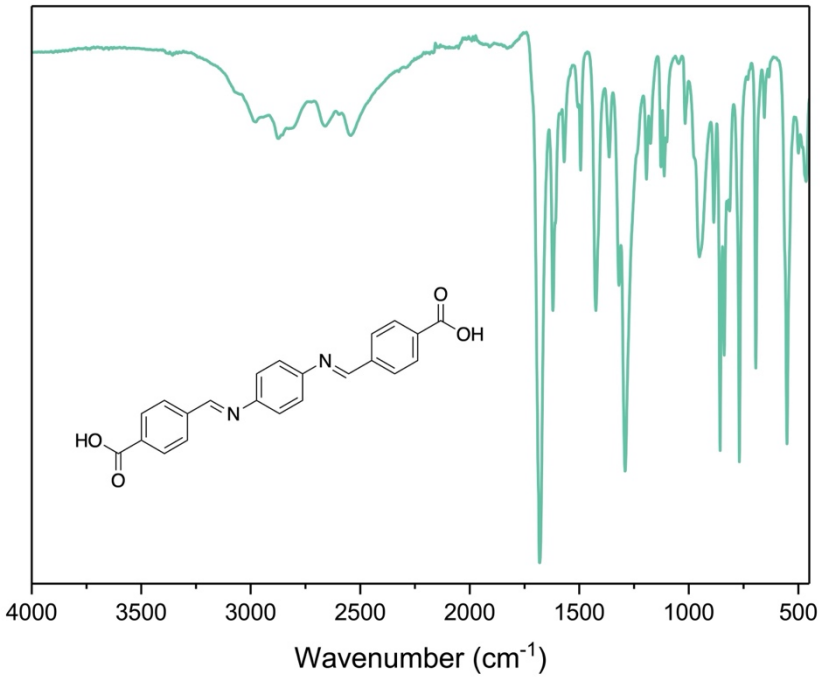

Figure A.9. FTIR spectrum for ligand **L5**.

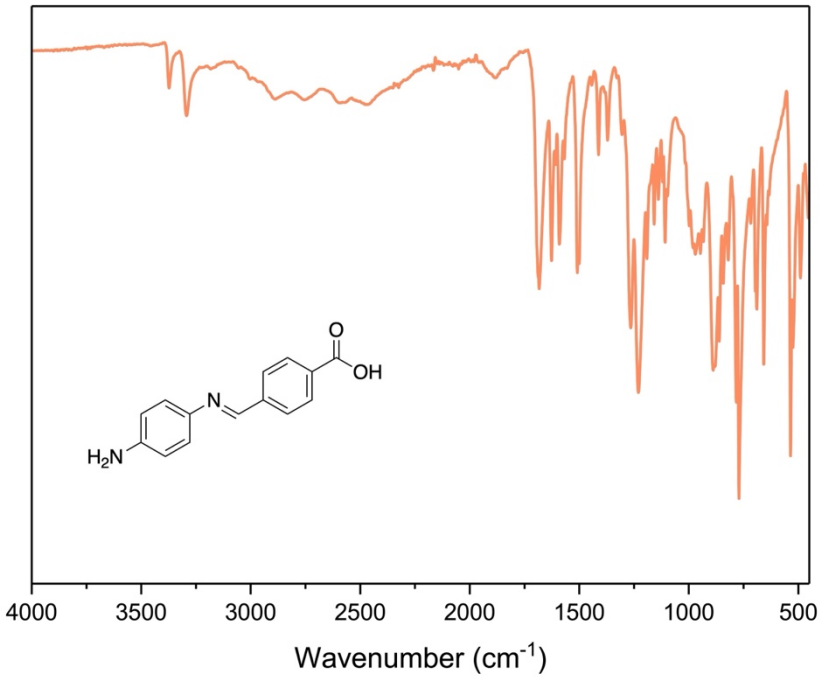

Figure A.10. FTIR spectrum for ligand **L6**.

A.2 Compounds Spectra

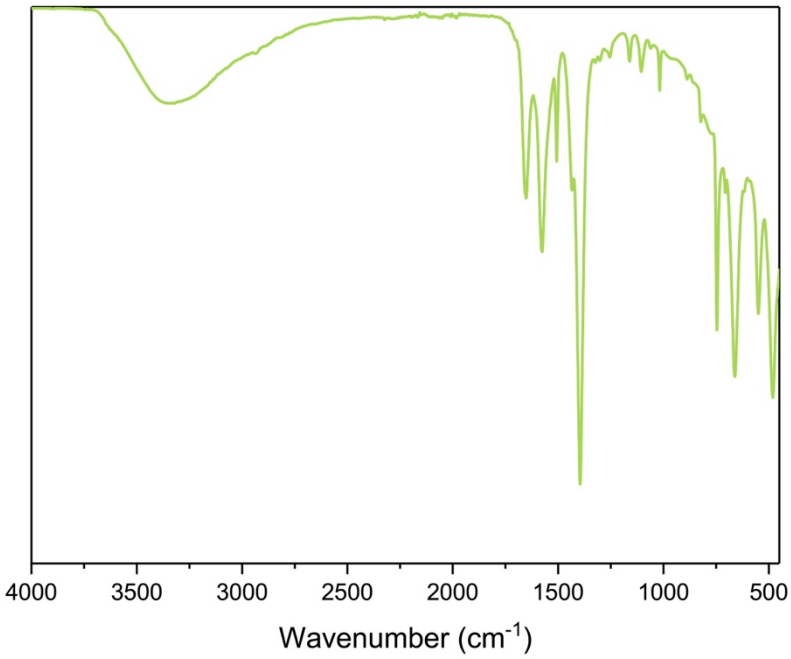

Figure A.11. FTIR spectrum for **UiO-66**.

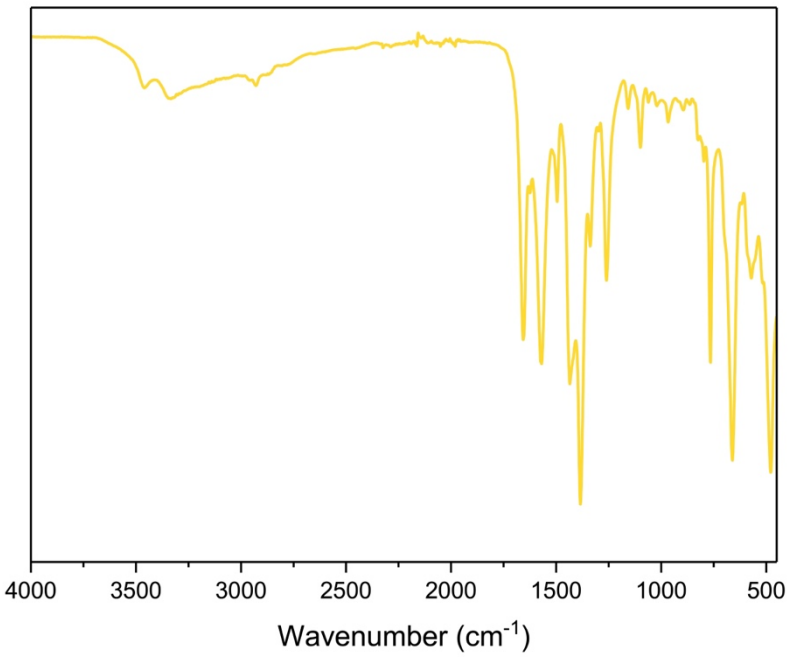

Figure A.12. FTIR spectrum for **UiO-66-NH_2**.

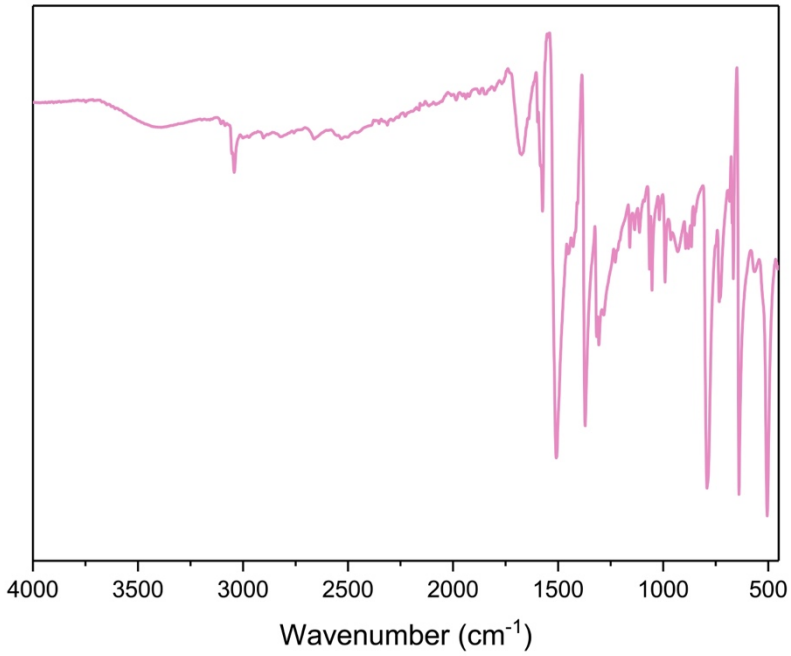

Figure A.13. FTIR spectrum for **MOF1**.

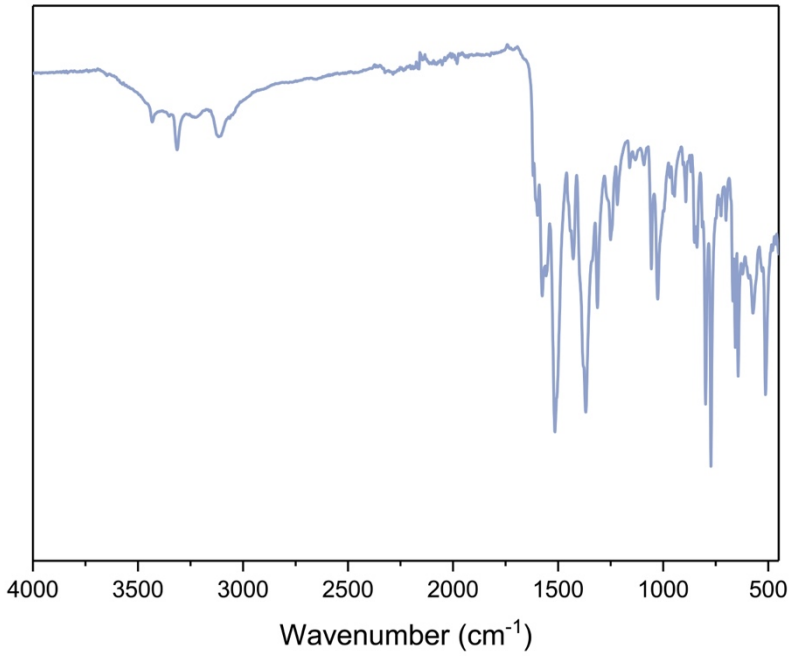

Figure A.14. FTIR spectrum for **MOF2**.

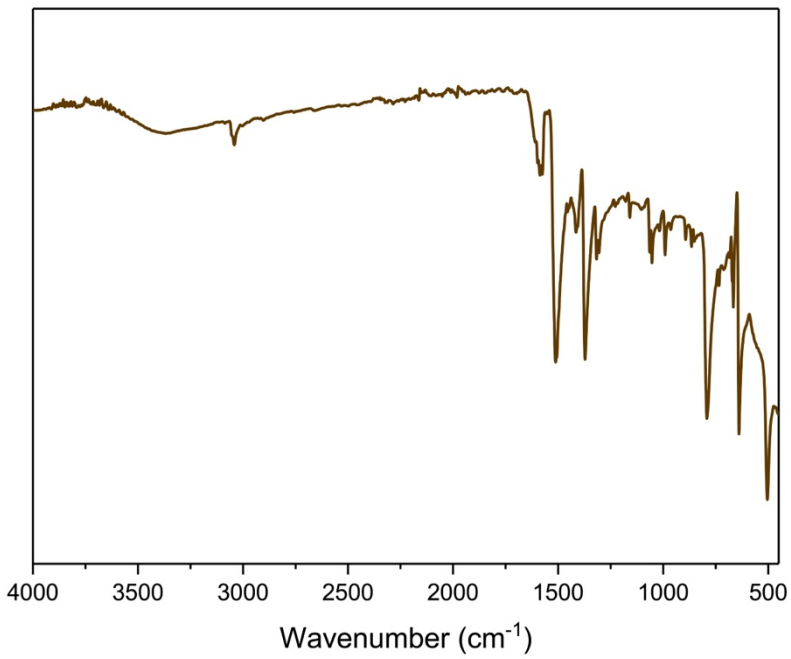

Figure A.15. FTIR spectrum for **A4a**.

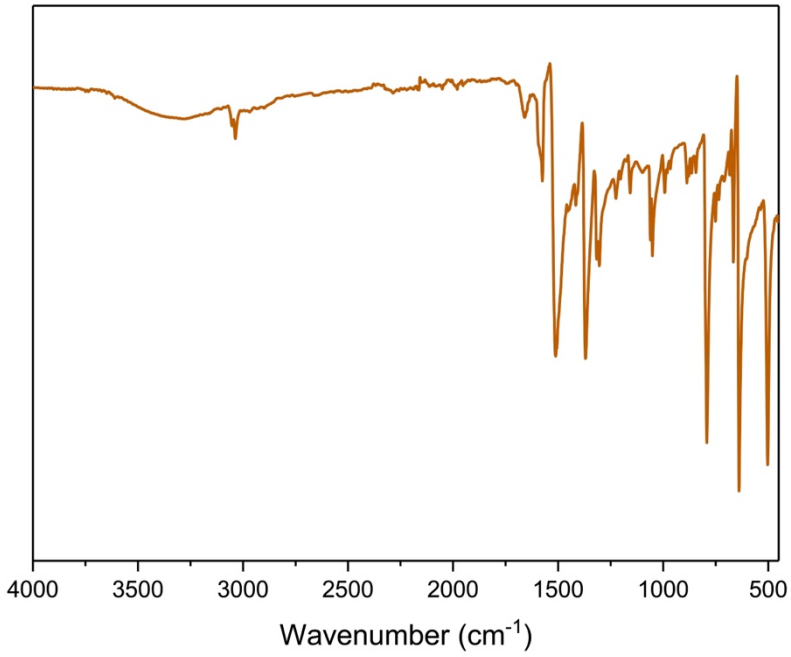

Figure A.16. FTIR spectrum for **A4b**.

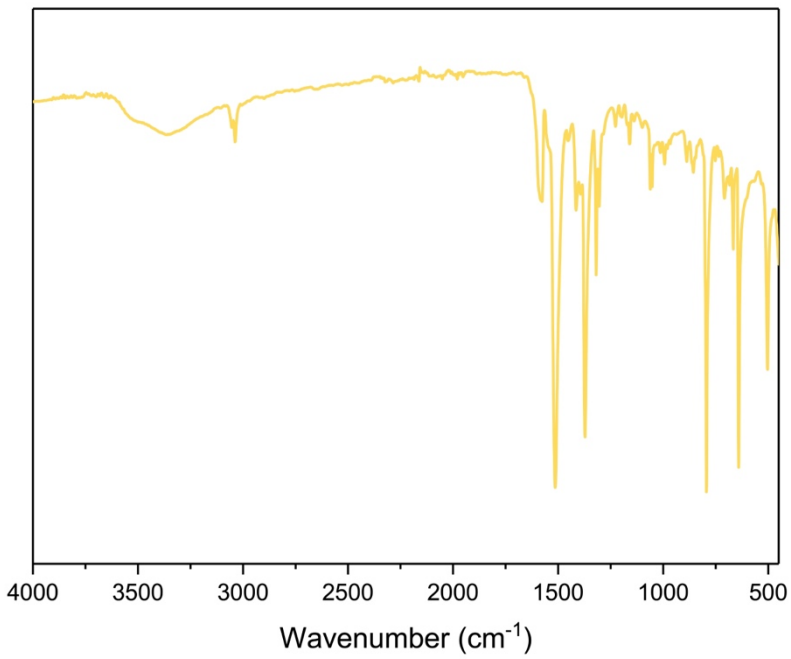

Figure A.17. FTIR spectrum for **A4c**.

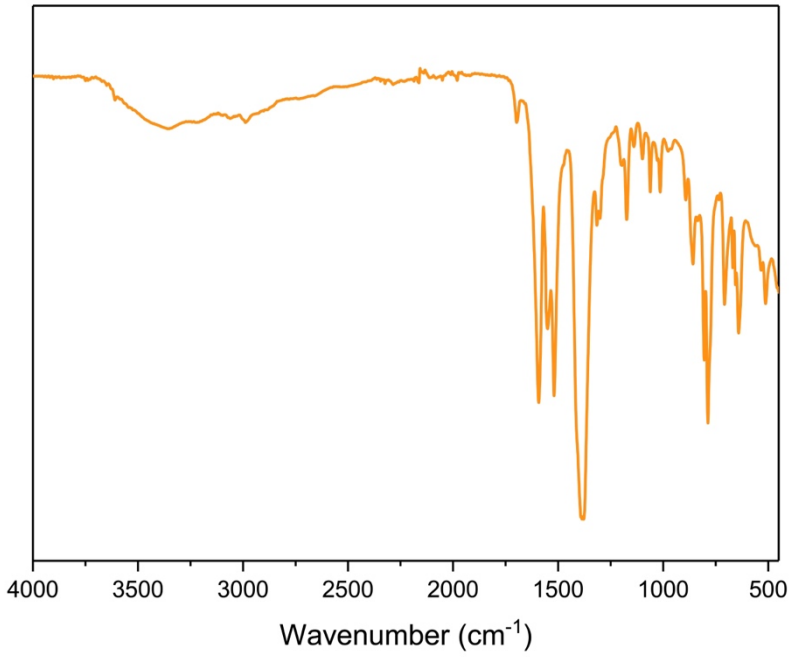

Figure A.18. FTIR spectrum for **A4d**.

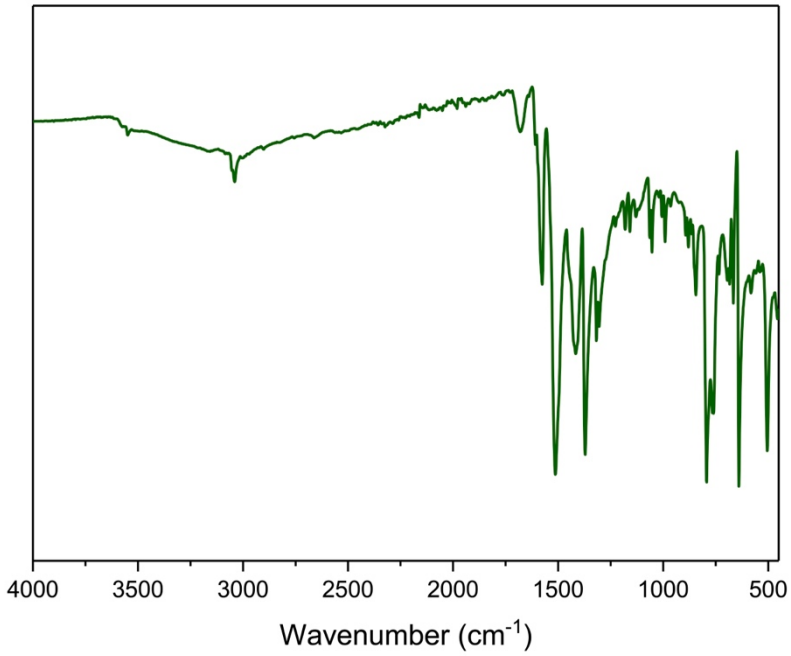

Figure A.19. FTIR spectrum for **A5a**.

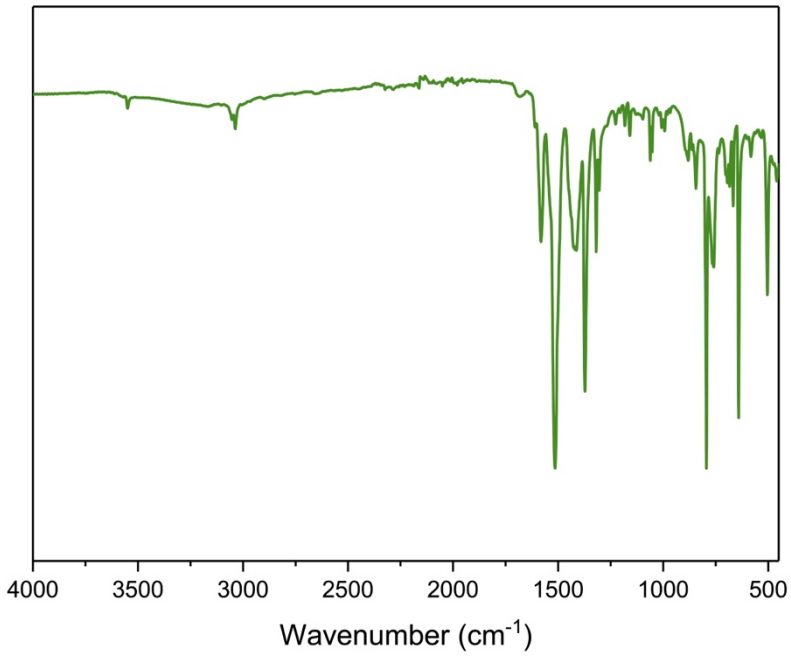

Figure A.20. FTIR spectrum for **A5b**.

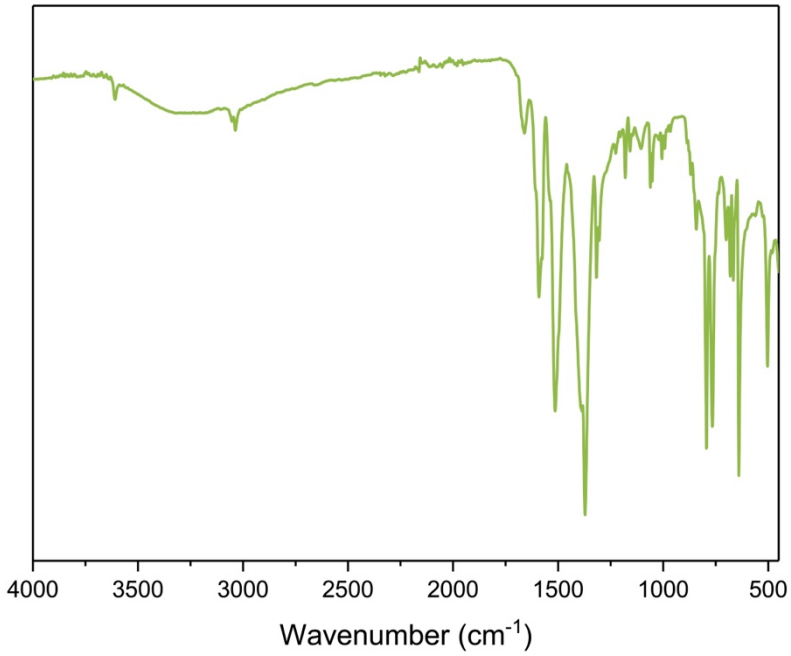

Figure A.21. FTIR spectrum for **A5c**.

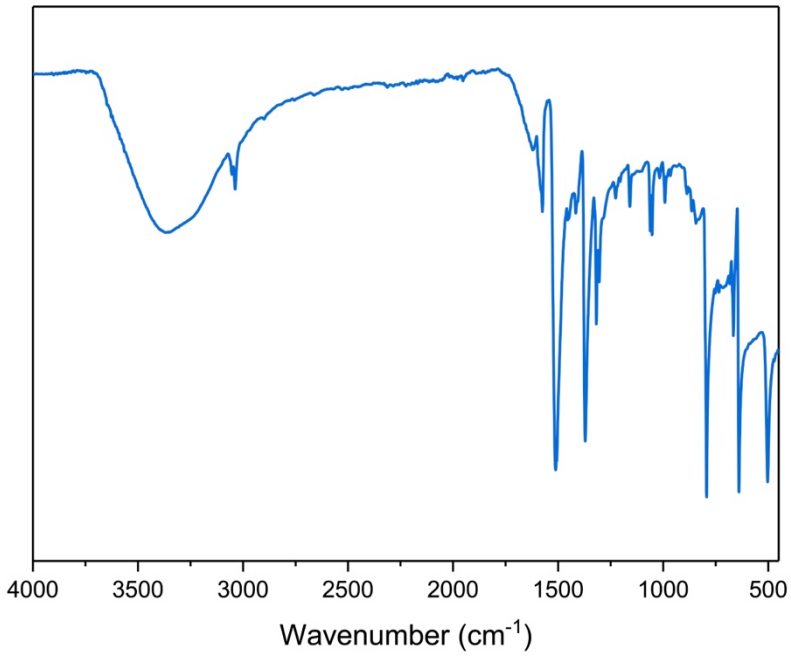

Figure A.22. FTIR spectrum for **A6a**.

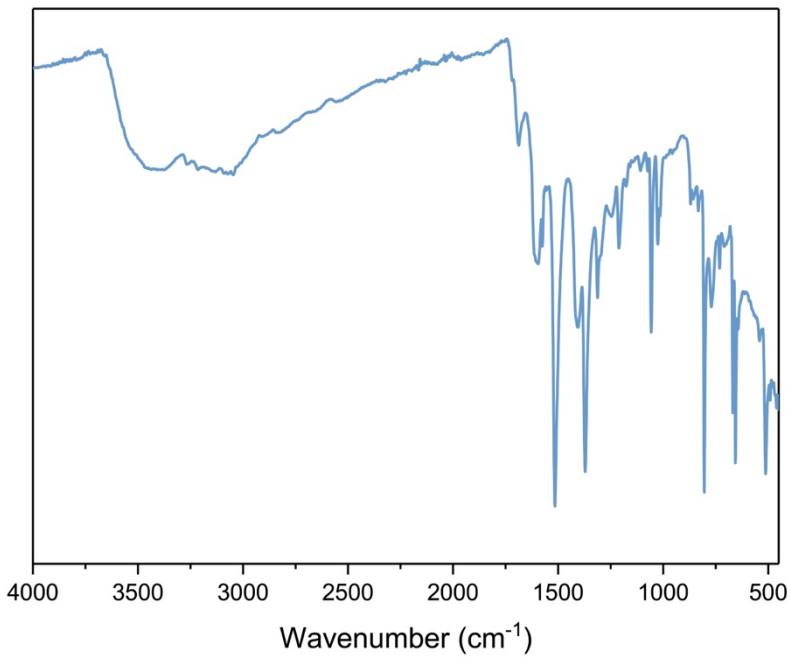

Figure A.23. FTIR spectrum for **A6b**.

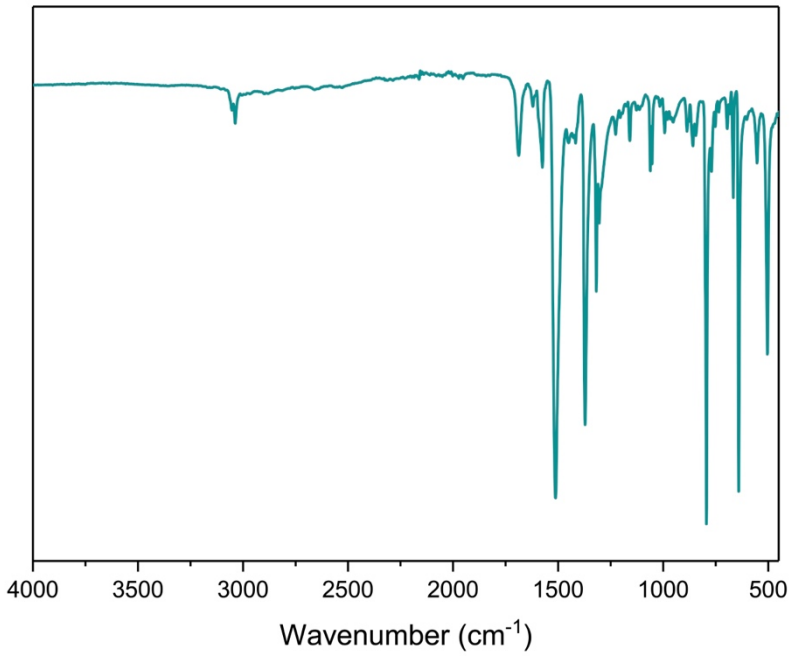

Figure A.24. FTIR spectrum for **A6c**.

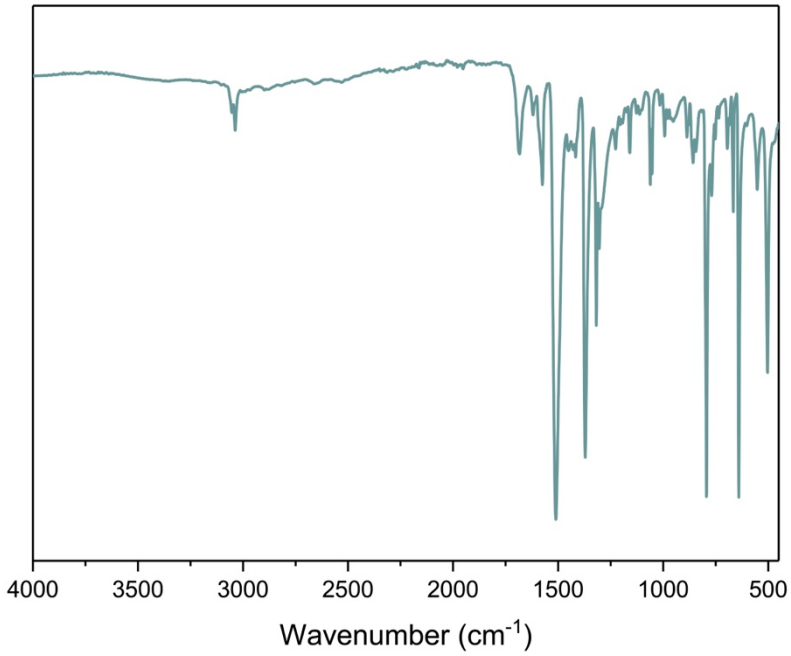

Figure A.25. FTIR spectrum for **A6d**.

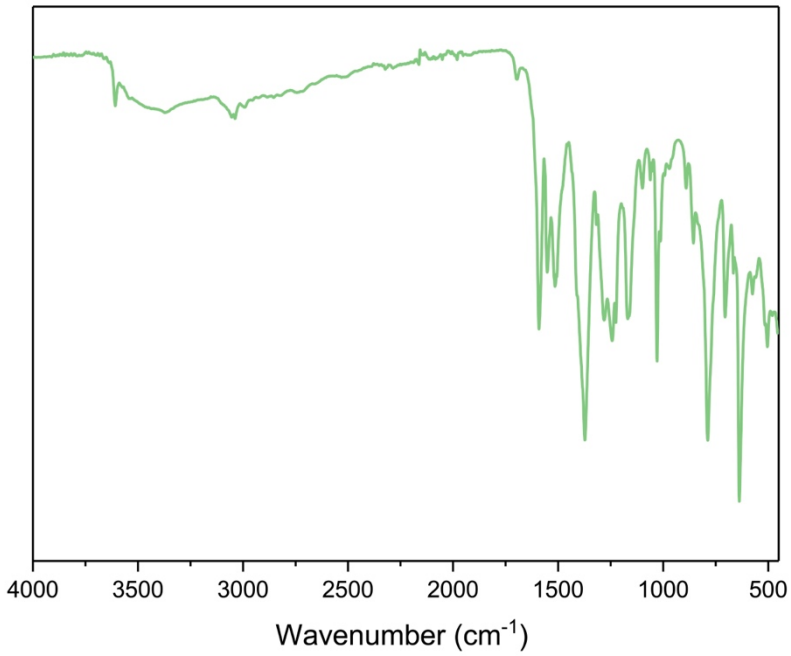

Figure A.26. FTIR spectrum for **A10a**.

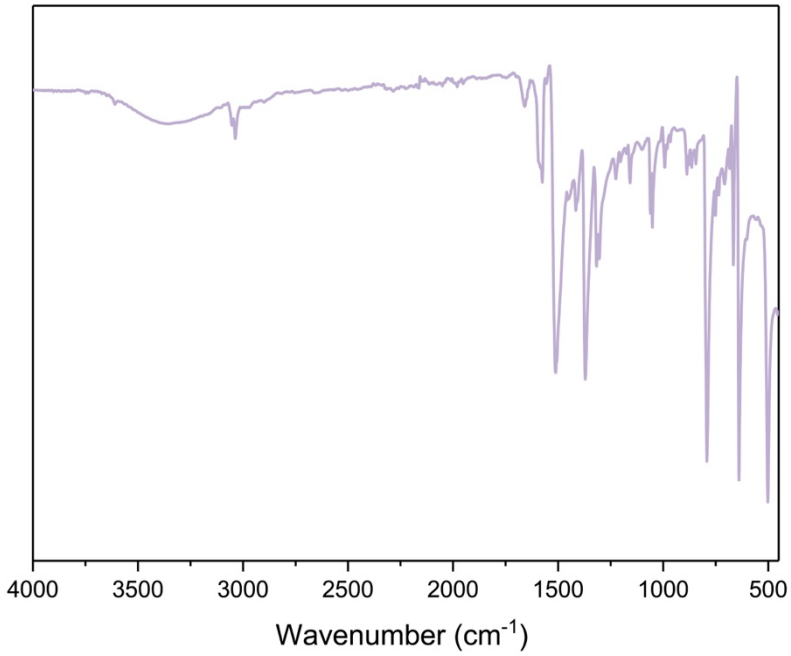

Figure A.27. FTIR spectrum for **A10b**.

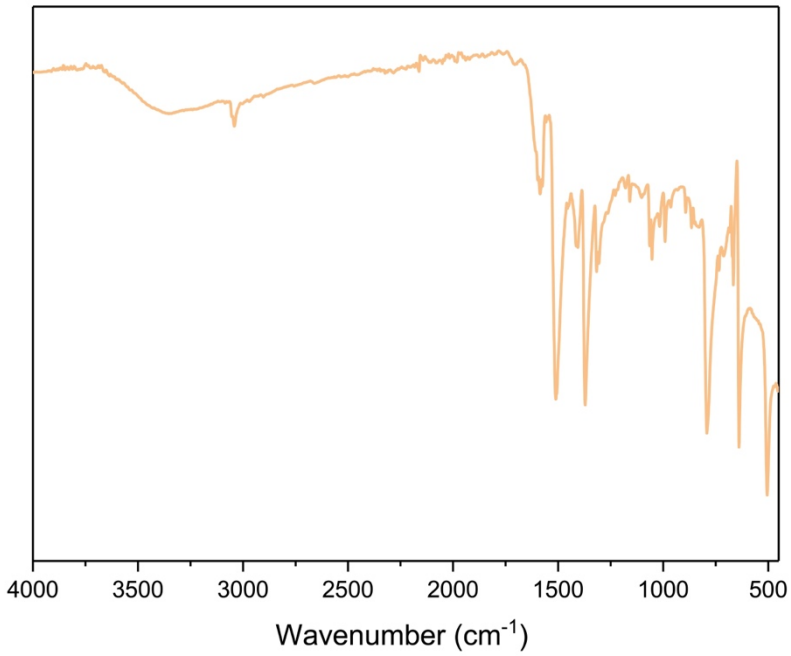

Figure A.28. FTIR spectrum for **A10c**.

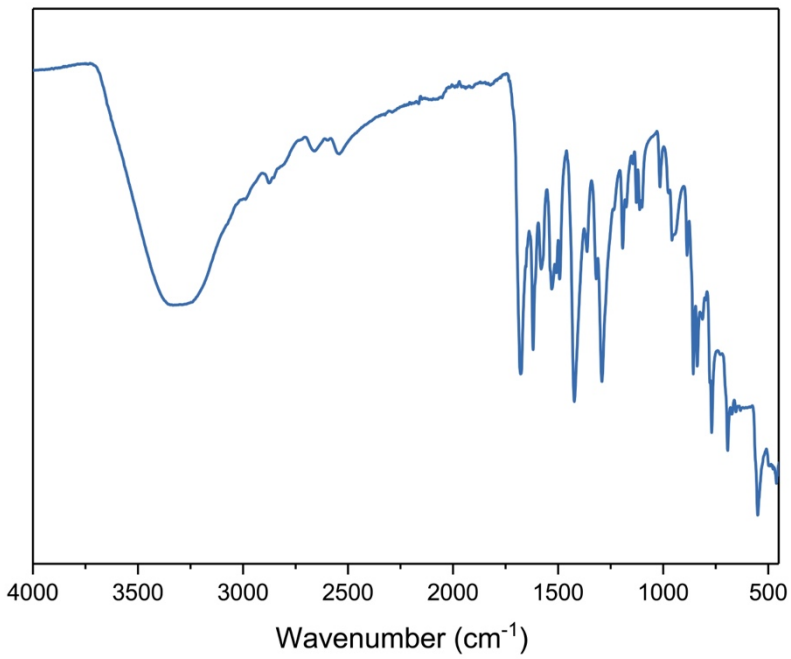

Figure A.29. FTIR spectrum for **A11a**.

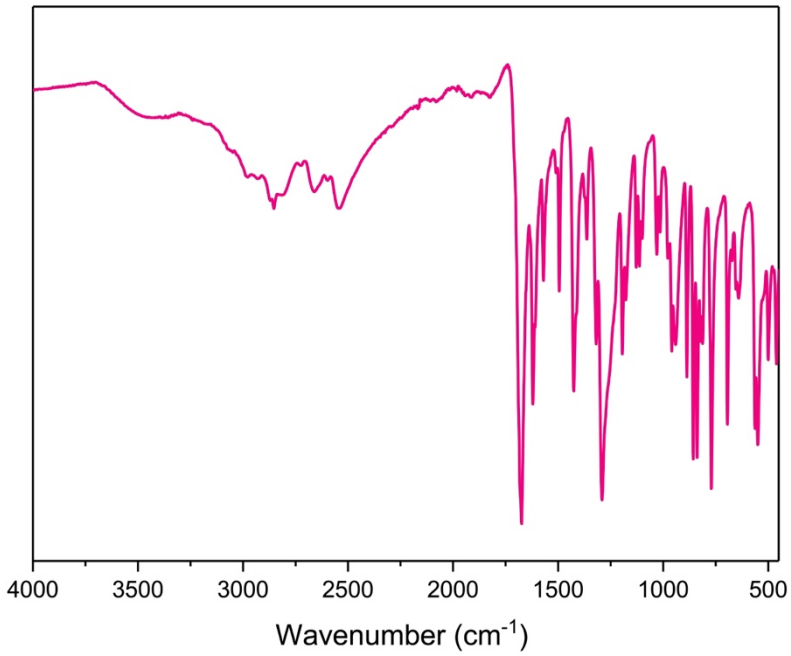

Figure A.30. FTIR spectrum for **A11b**.

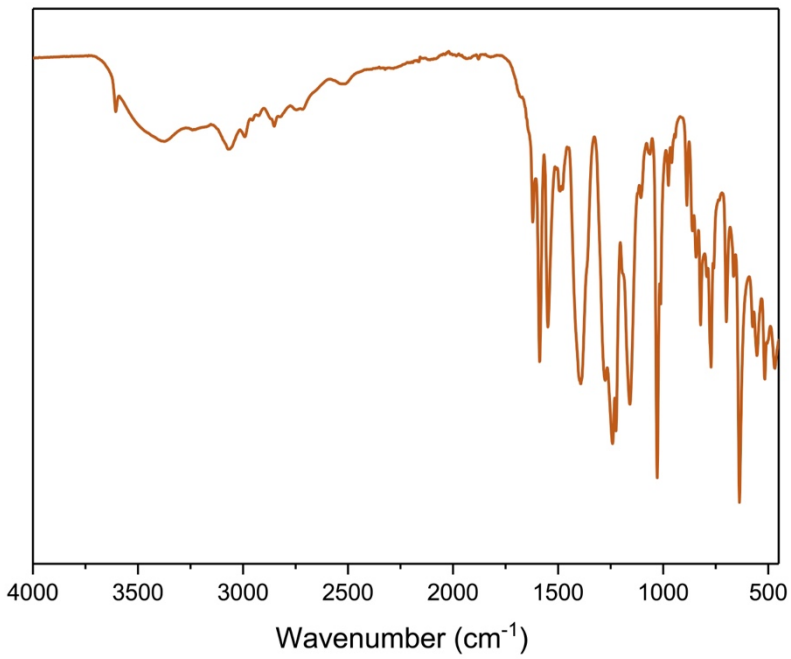

Figure A.31. FTIR spectrum for **A11c**.

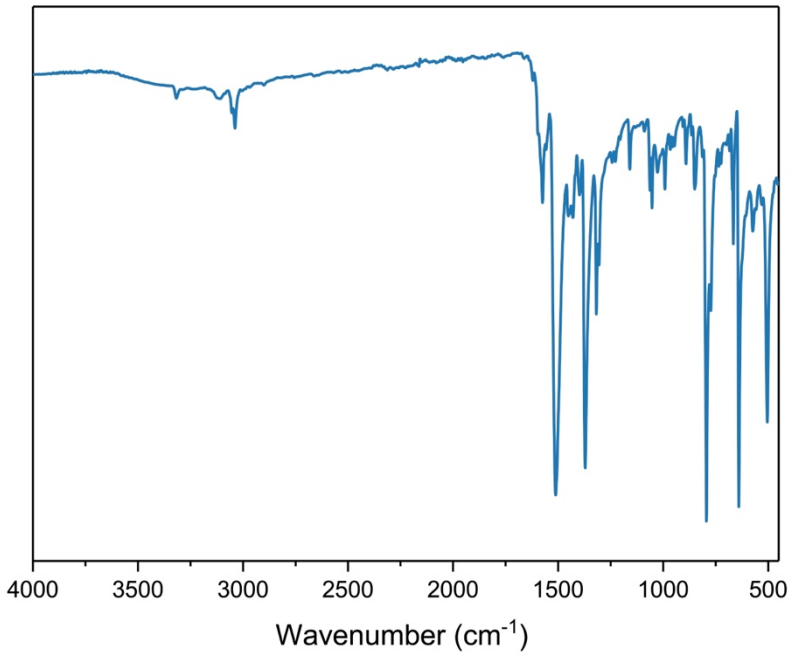

Figure A.32. FTIR spectrum for **A14a**.

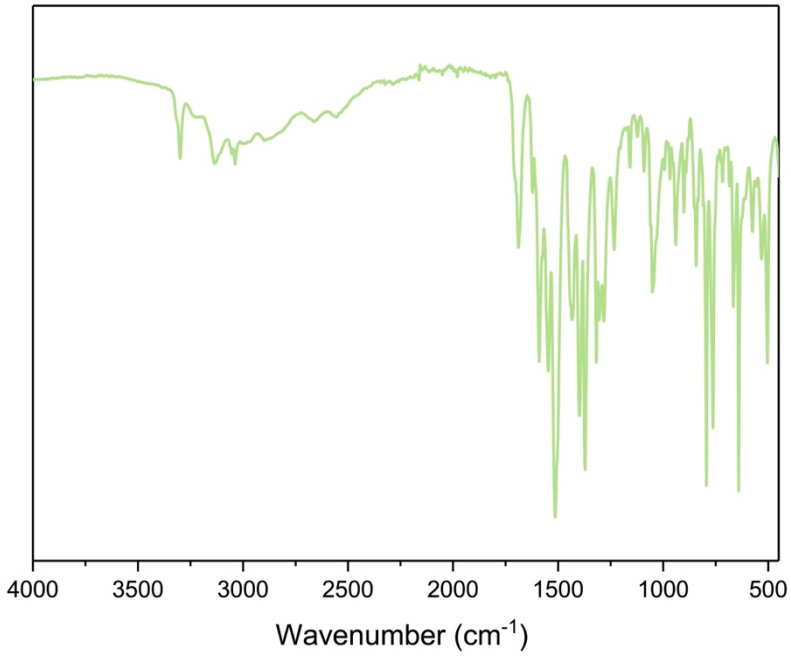

Figure A.33. FTIR spectrum for **A14b**.

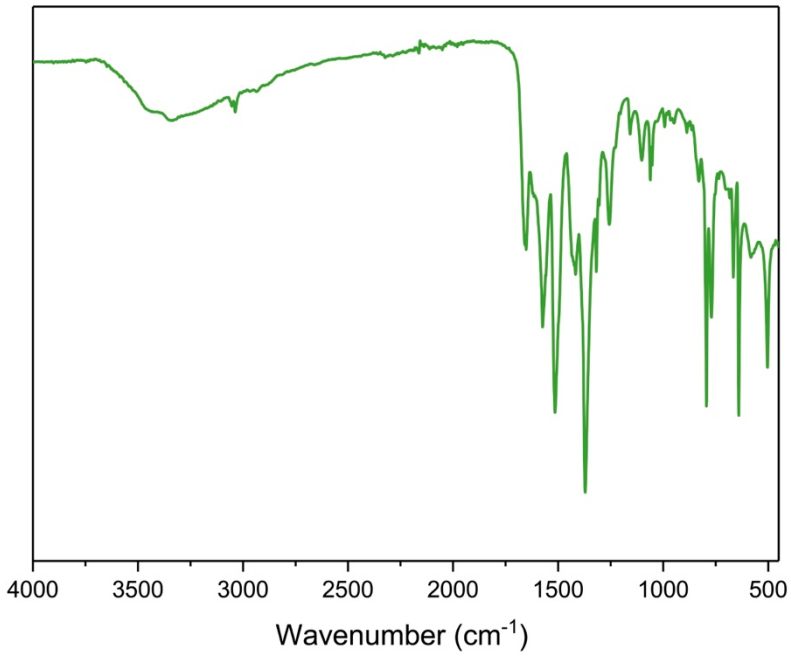

Figure A.34. FTIR spectrum for **A14c**.

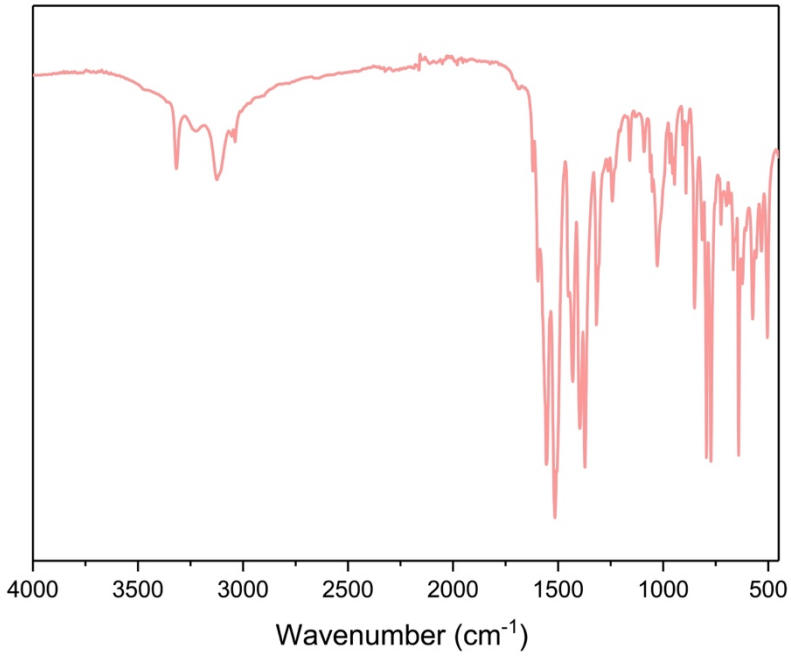

Figure A.35. FTIR spectrum for **A14d**.

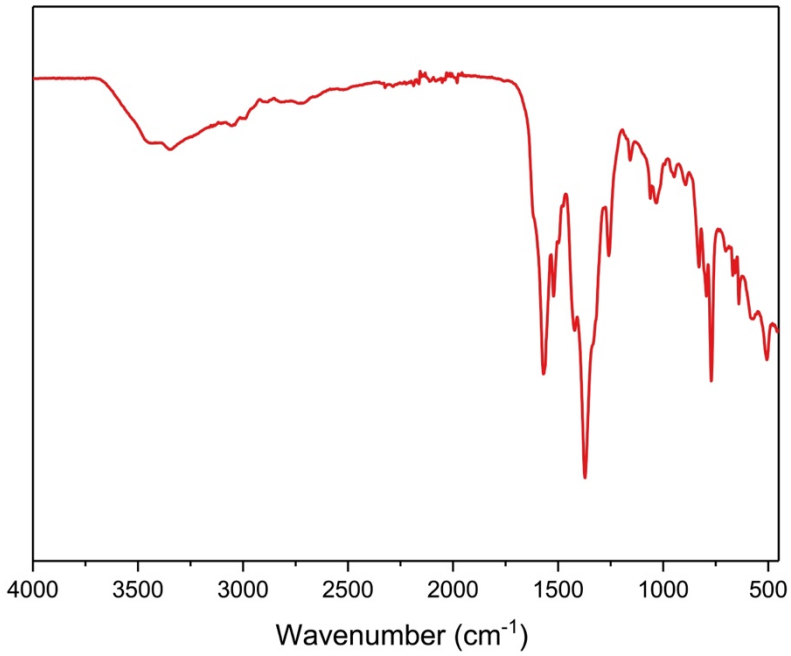

Figure A.36. FTIR spectrum for **A14e**.

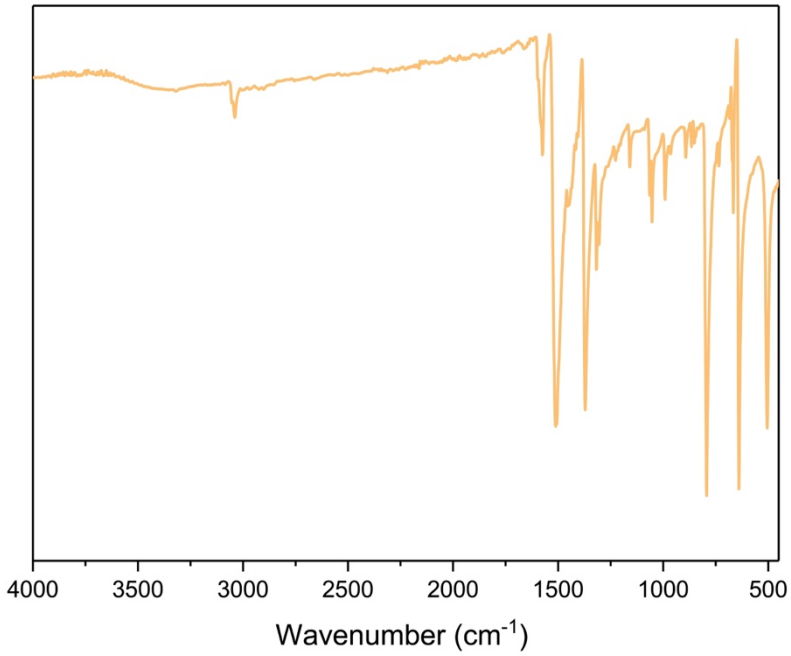

Figure A.37. FTIR spectrum for **A14f**.

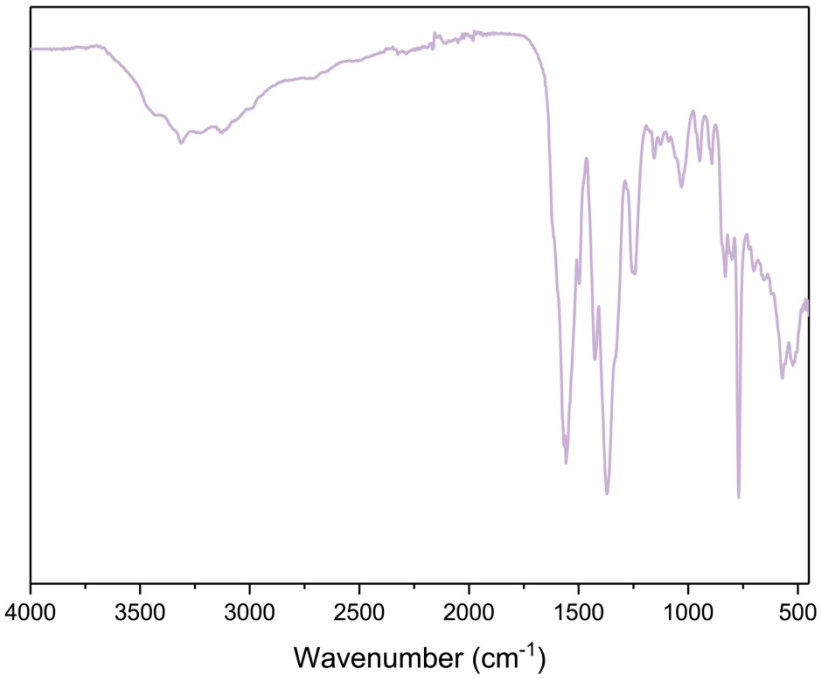

Figure A.38. FTIR spectrum for **A15a**.

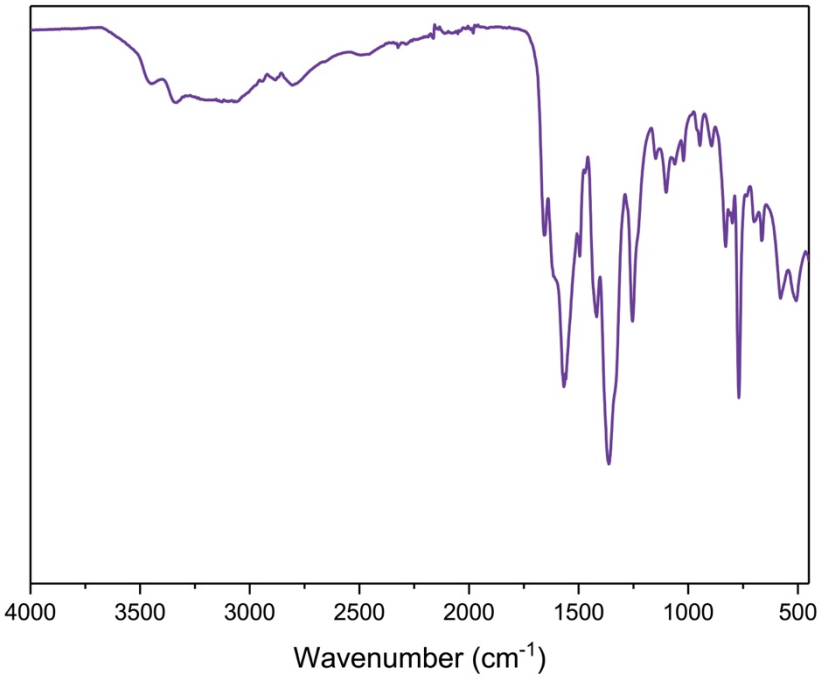

Figure A.39. FTIR spectrum for **A15b**.

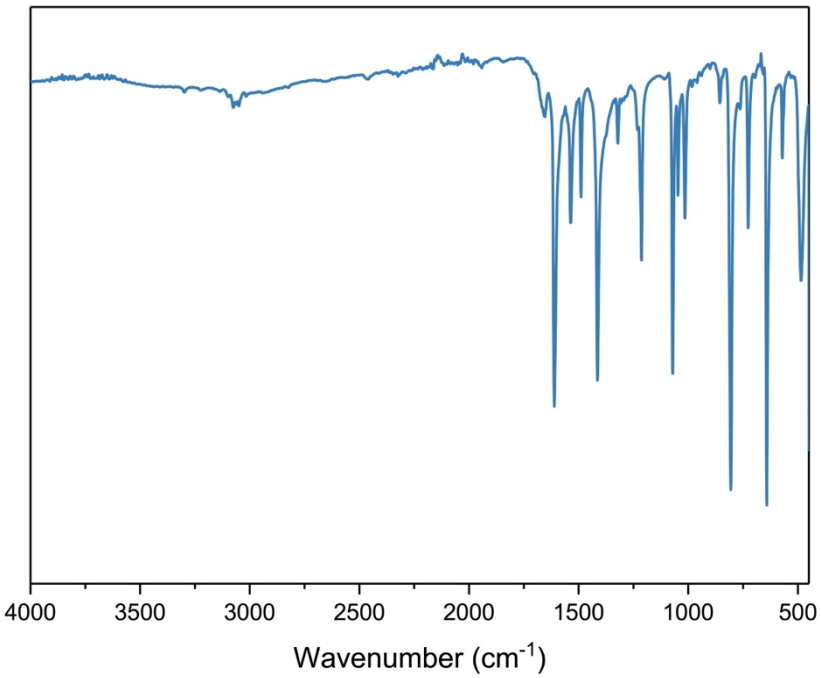

Figure A.40. FTIR spectrum for **A19a**.

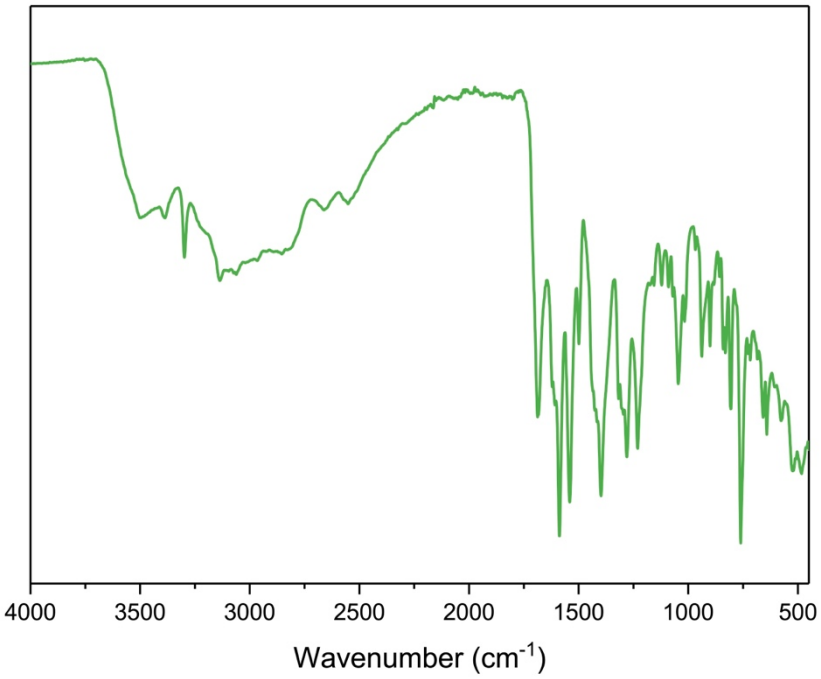

Figure A.41. FTIR spectrum for **A19b**.

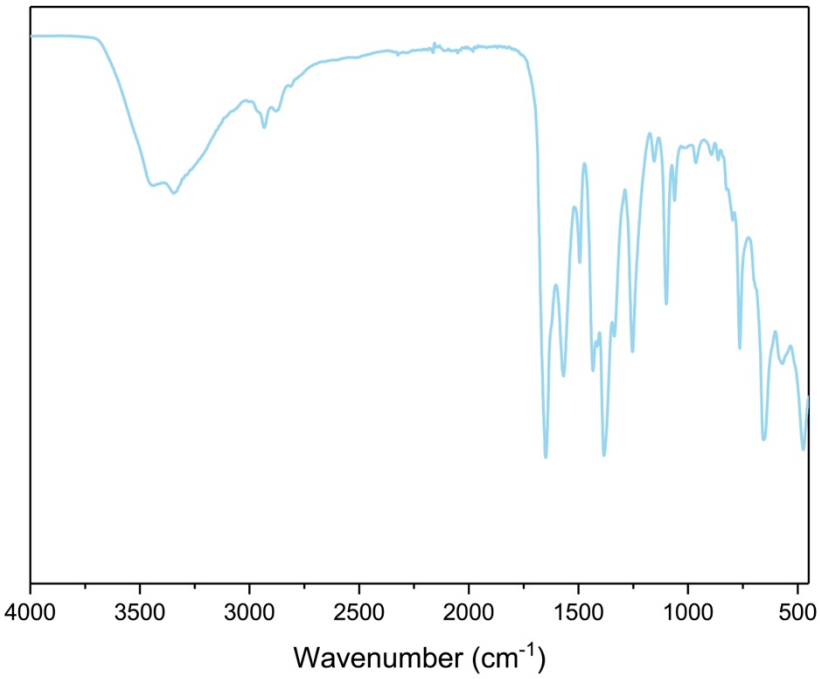

Figure A.42. FTIR spectrum for **B3a**.

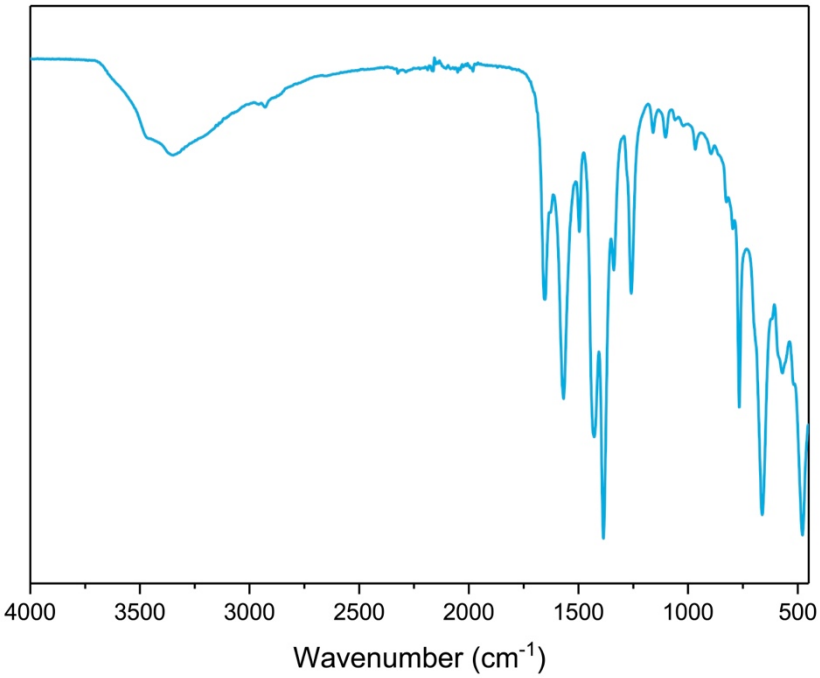

Figure A.43. FTIR spectrum for **B3b**.

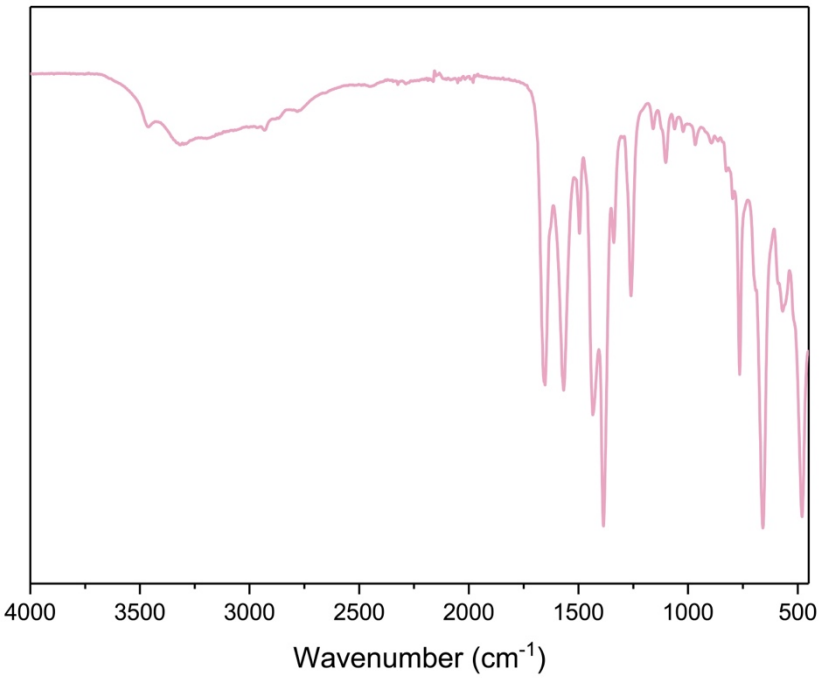

Figure A.44. FTIR spectrum for **B3c**.

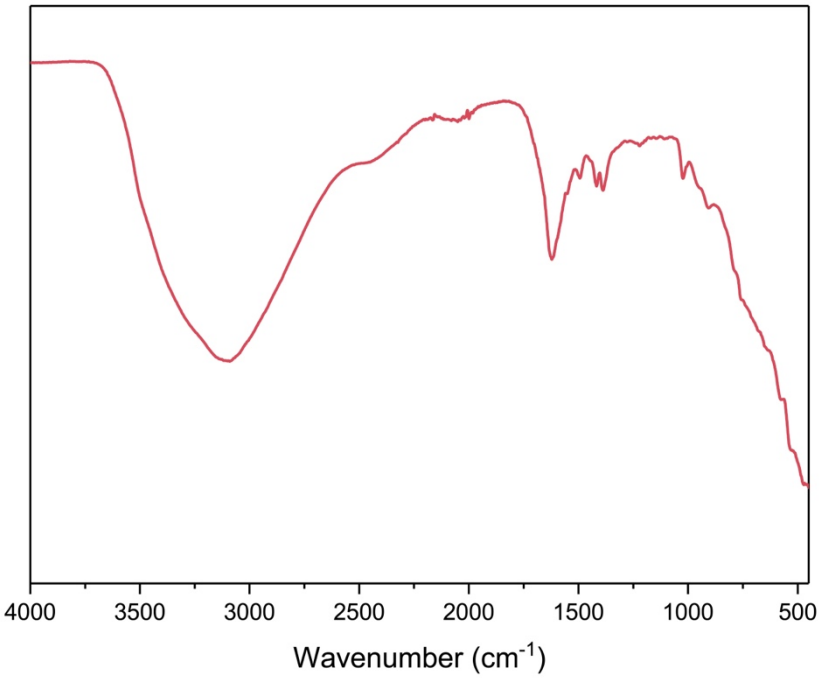

Figure A.45. FTIR spectrum for **B3d**.

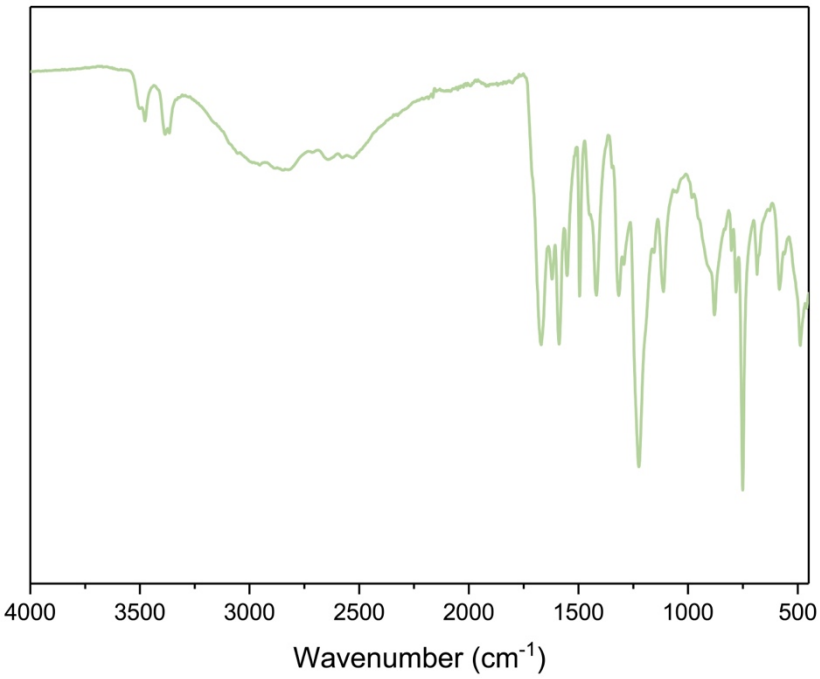

Figure A.46. FTIR spectrum for **B3e**.

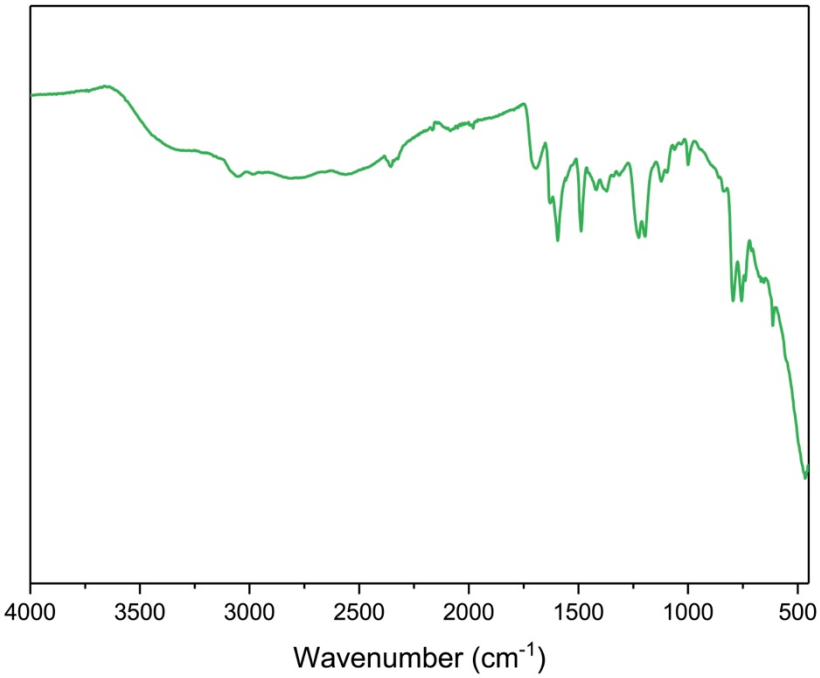

Figure A.47. FTIR spectrum for **B3f**.

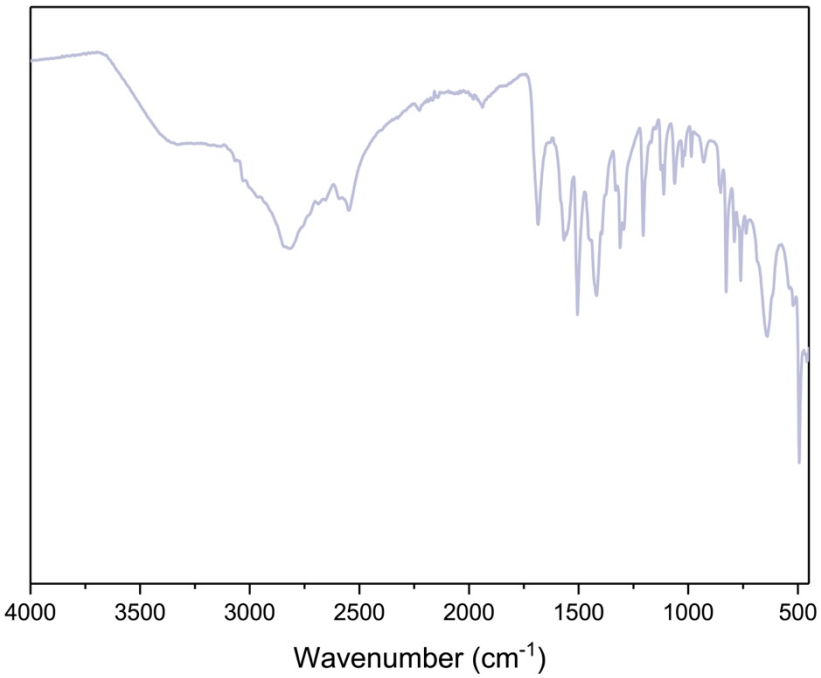

Figure A.48. FTIR spectrum for **B6a**.

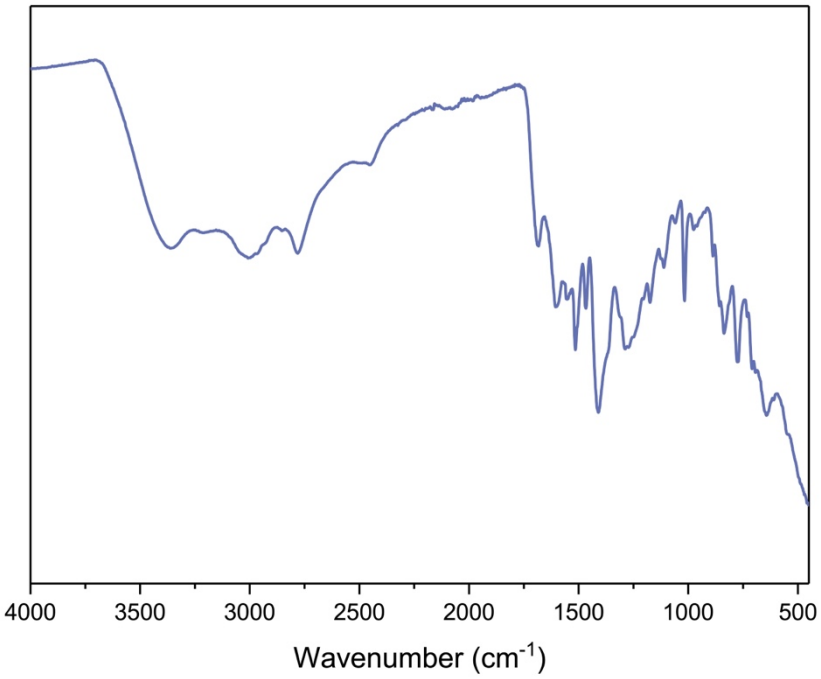

Figure A.49. FTIR spectrum for **B6b**.

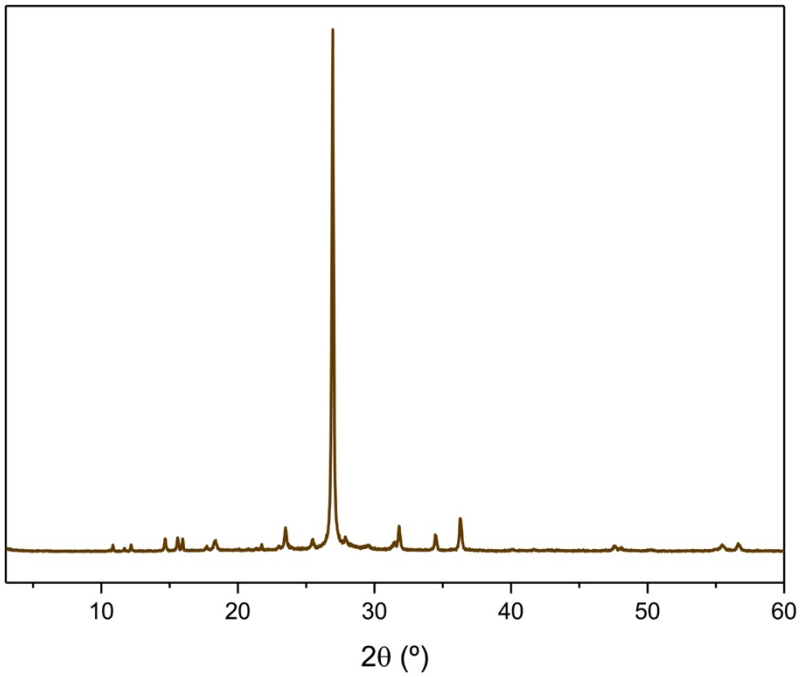

Figure A.50. PXRD spectrum for **A4a**.

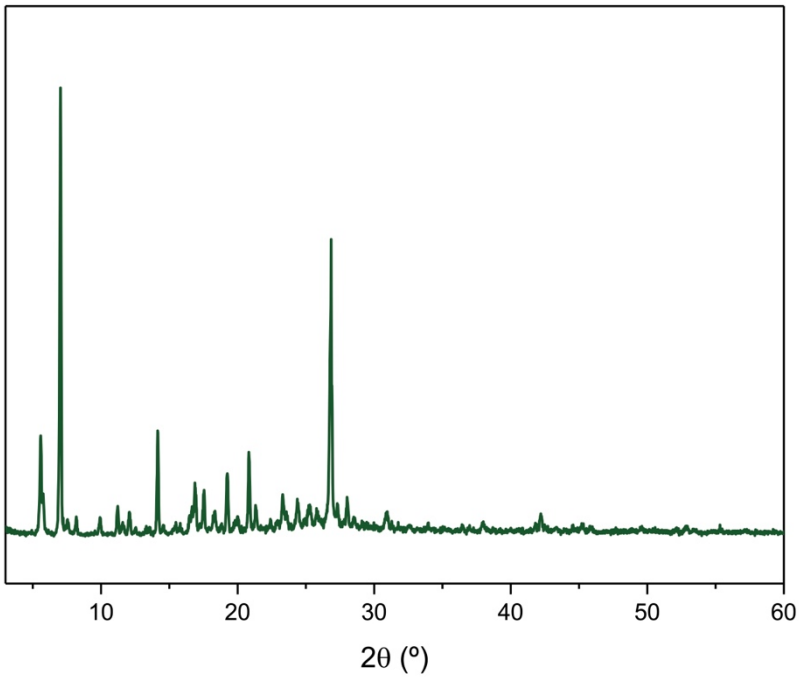

Figure A.51. PXRD spectrum for **A5a**.

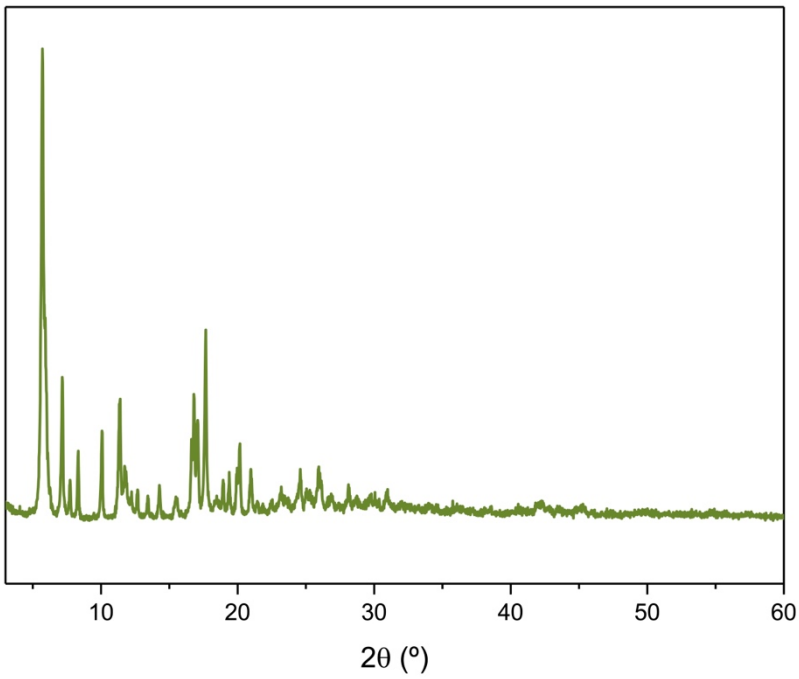

Figure A.52. PXRD spectrum for **A5b**.

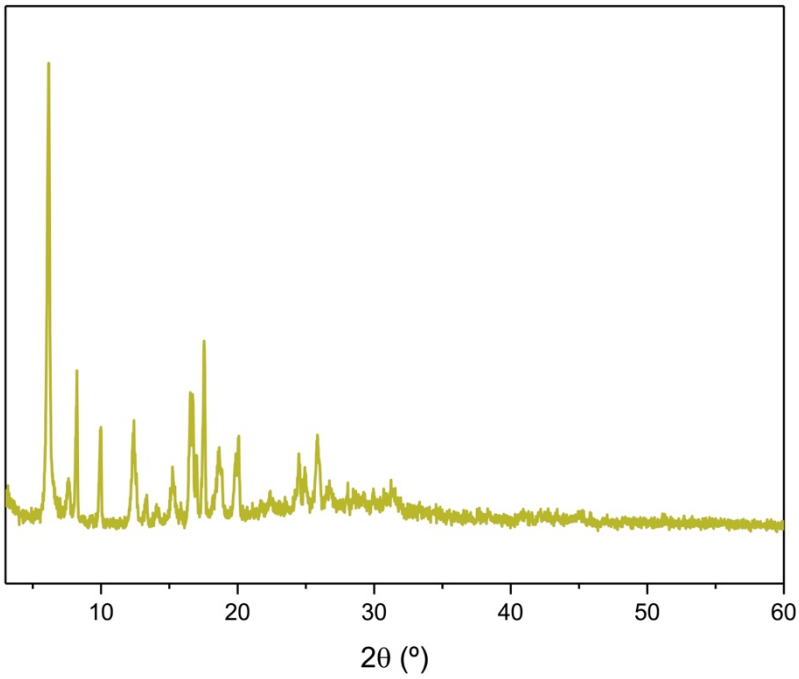

Figure A.53. PXRD spectrum for **A5c**.

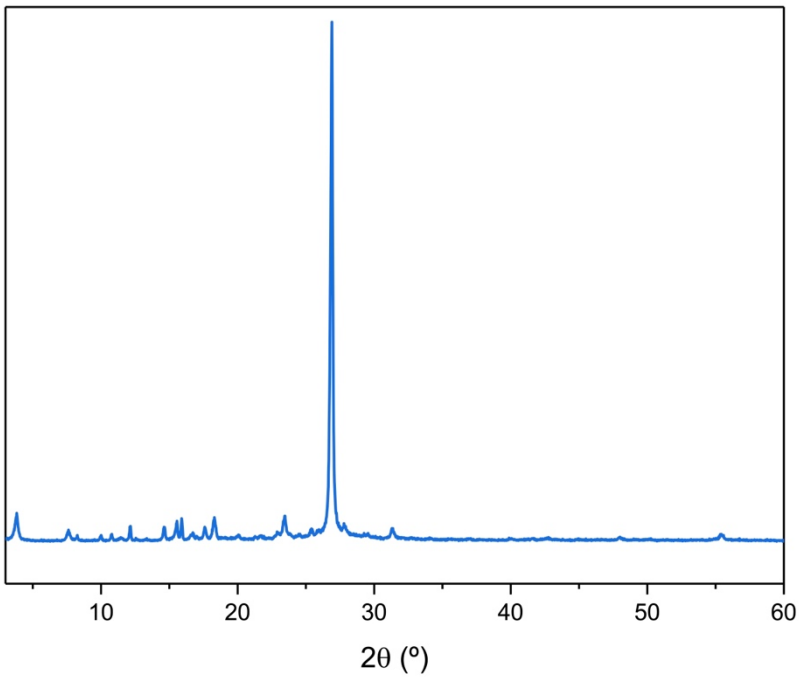

Figure A.54. PXRD spectrum for **A6a**.

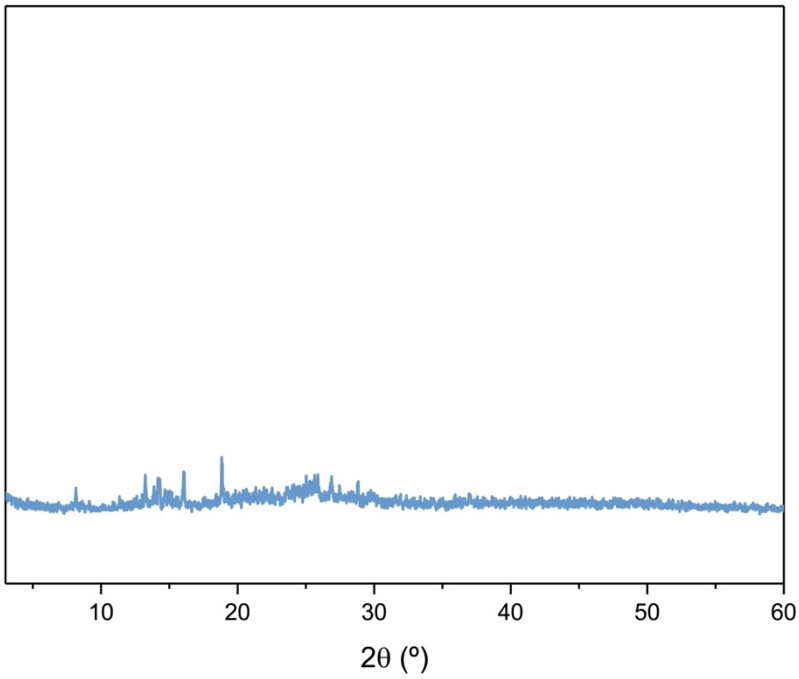

Figure A.55. PXRD spectrum for **A6b**.

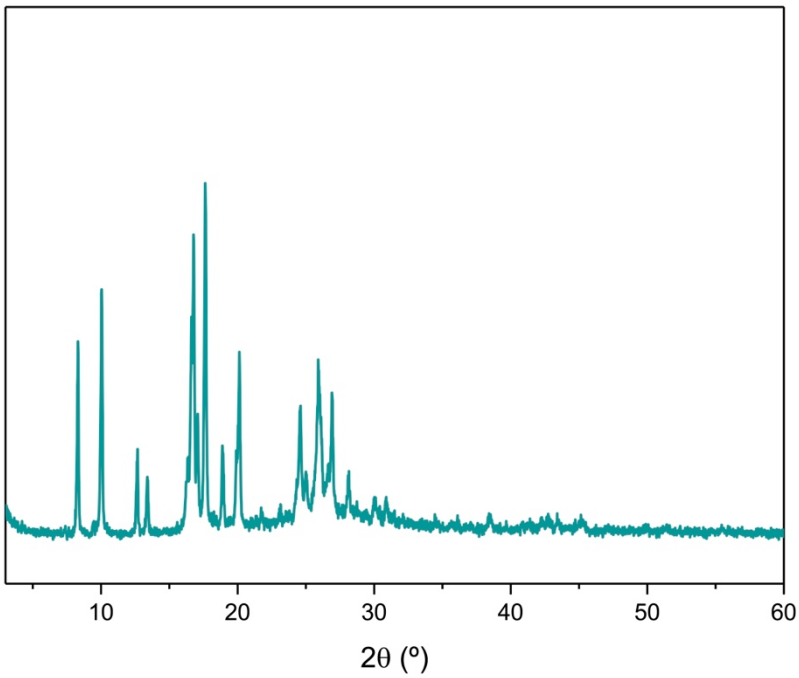

Figure A.56. PXRD spectrum for **A6c**.

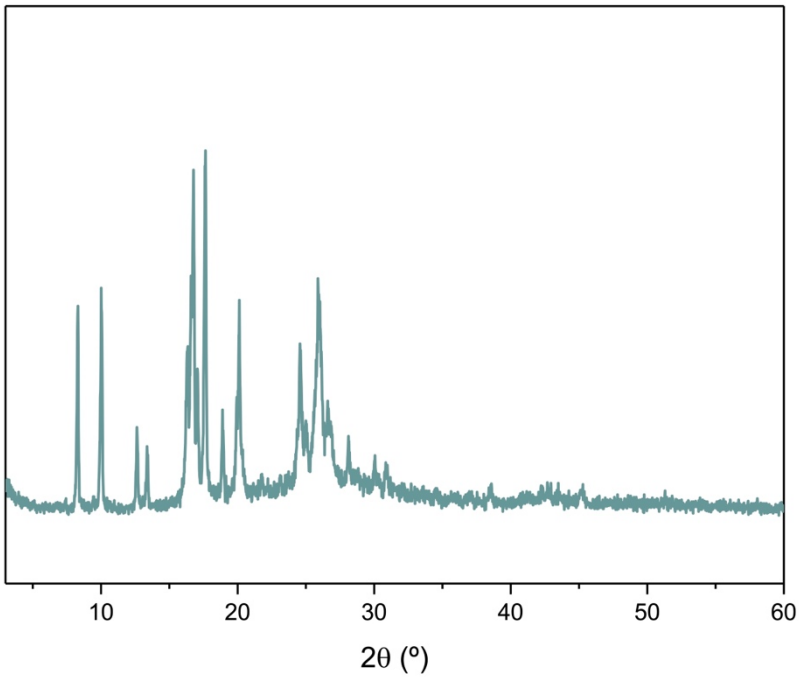

Figure A.57. PXRD spectrum for **A6d**.

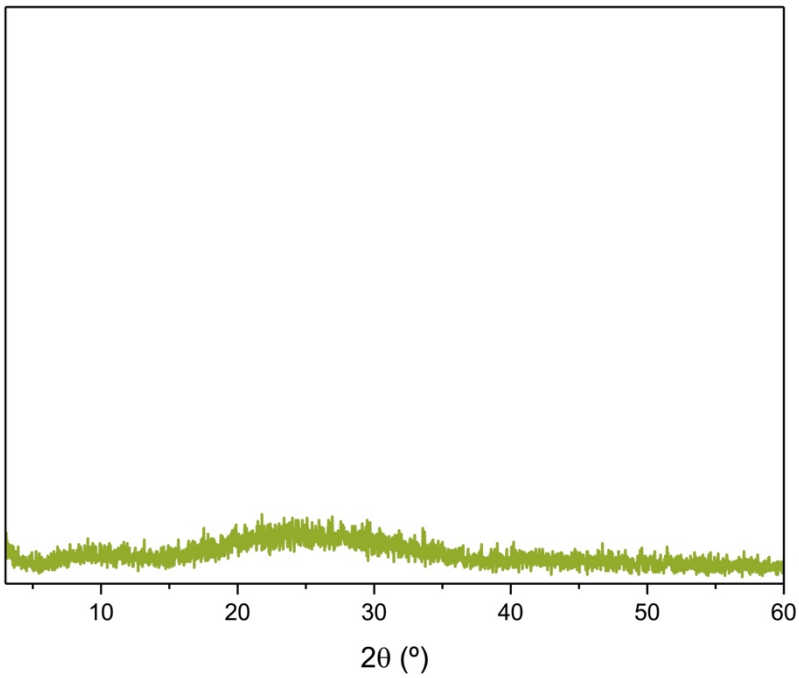

Figure A.58. PXRD spectrum for **A7**.

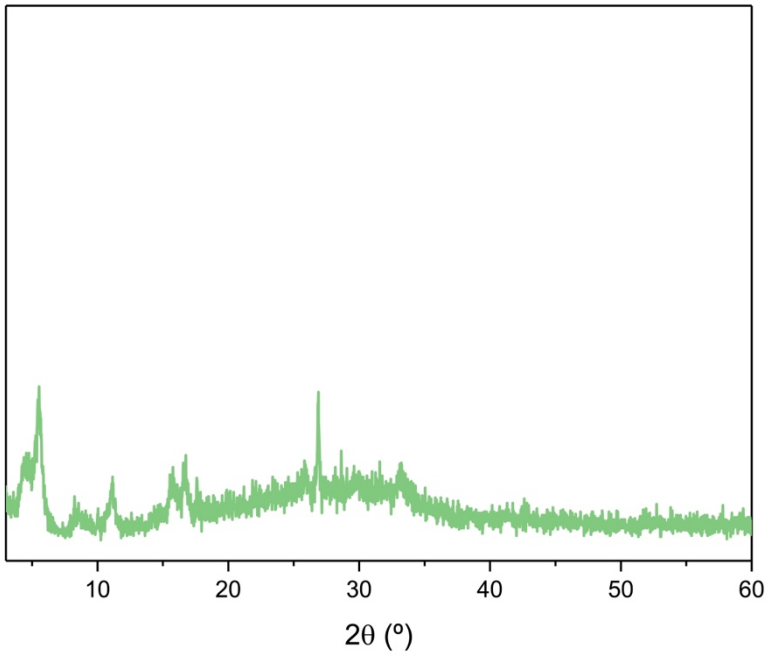

Figure A.59. PXRD spectrum for **A10a**.

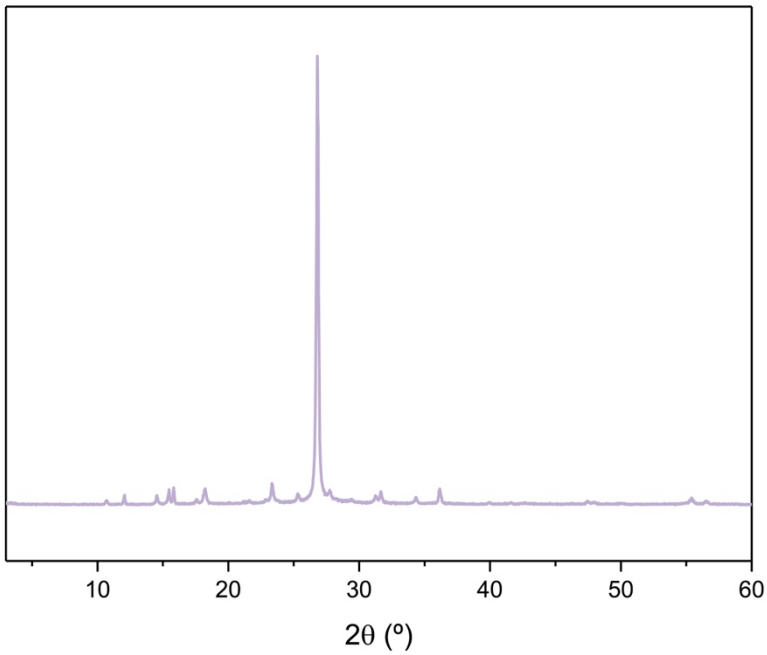

Figure A.60. PXRD spectrum for **A10b**.

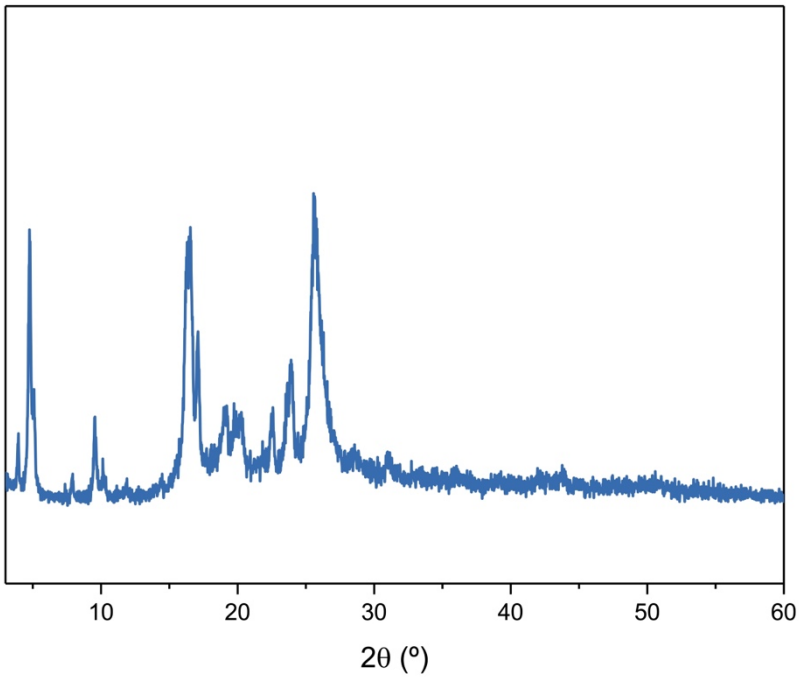

Figure A.61. PXRD spectrum for **A11a**.

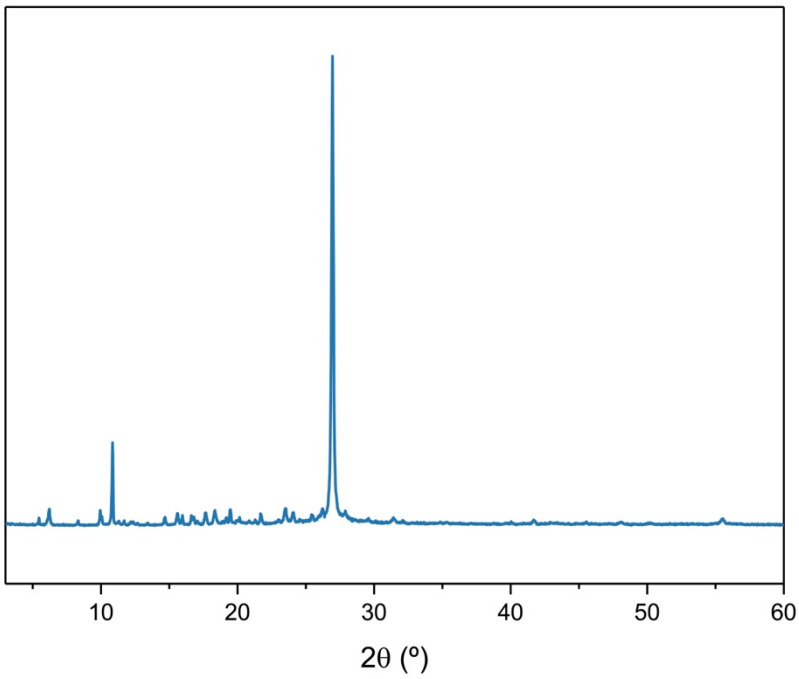

Figure A.62. PXRD spectrum for **A14a**.

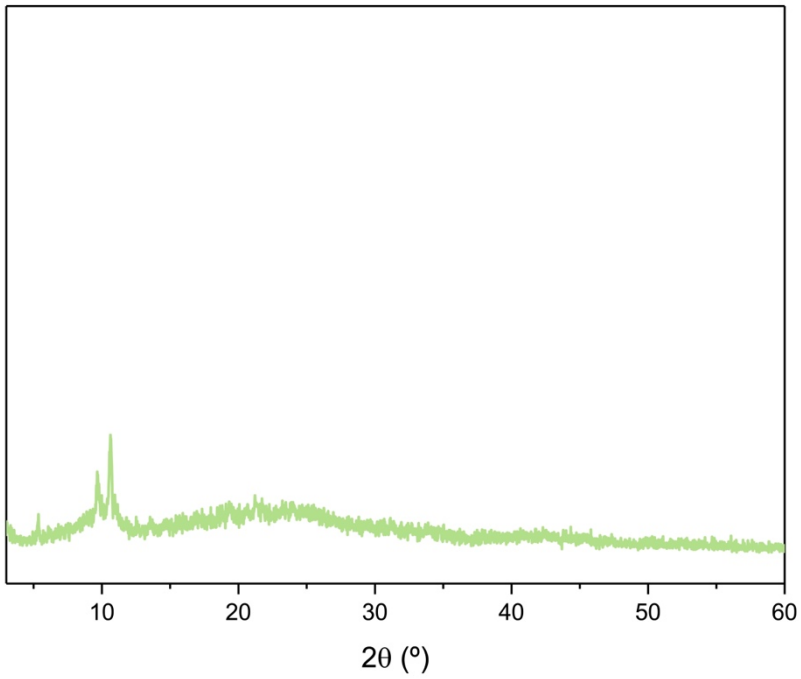

Figure A.63. PXRD spectrum for **A14b**.

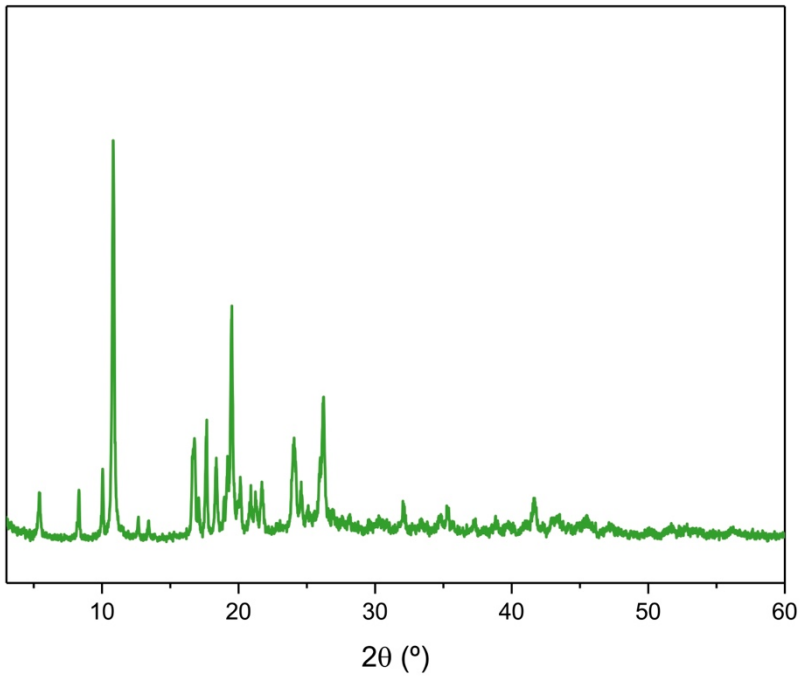

Figure A.64. PXRD spectrum for **A14c**.

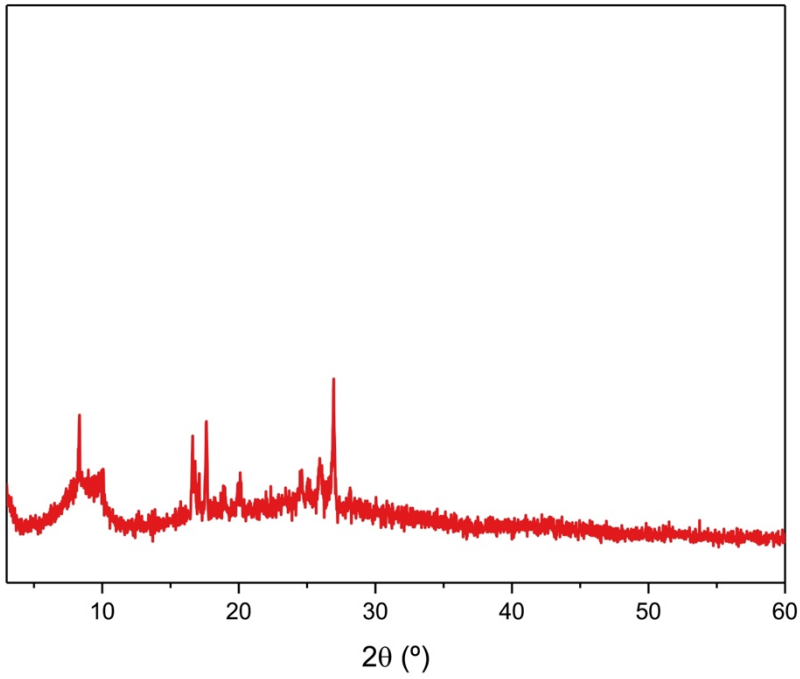

Figure A.65. PXRD spectrum for **A14e**.

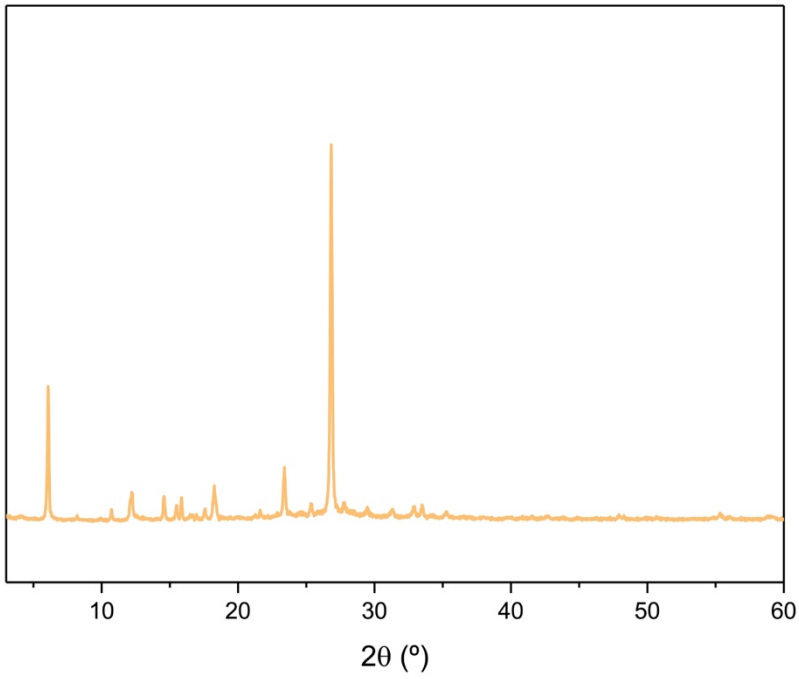

Figure A.66. PXRD spectrum for **A14f**.

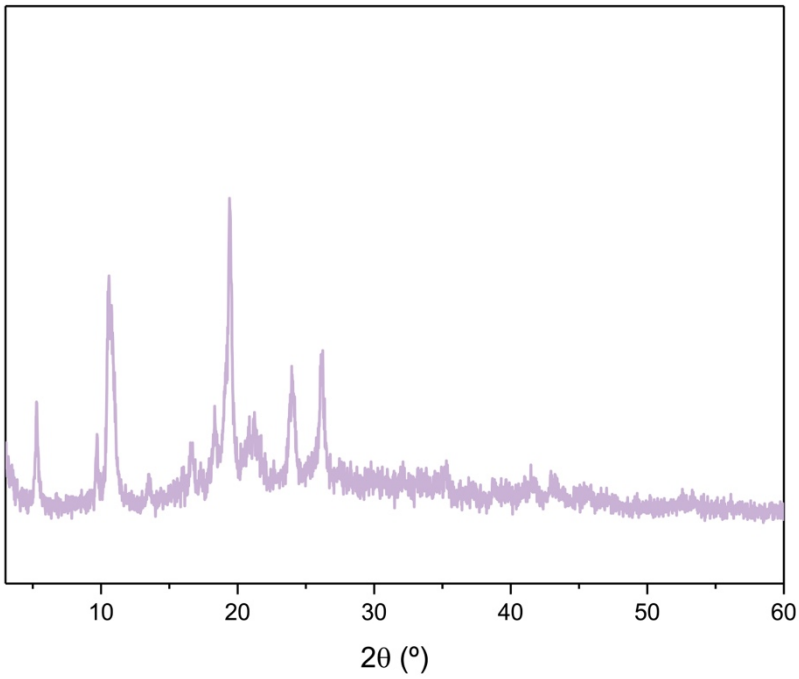

Figure A.67. PXRD spectrum for **A15a**.

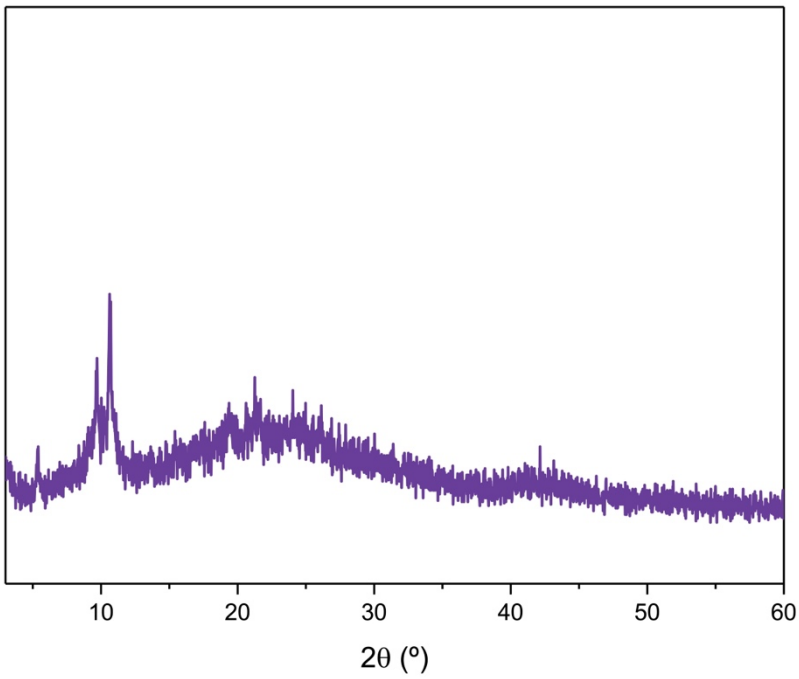

Figure A.68. PXRD spectrum for **A15b**.

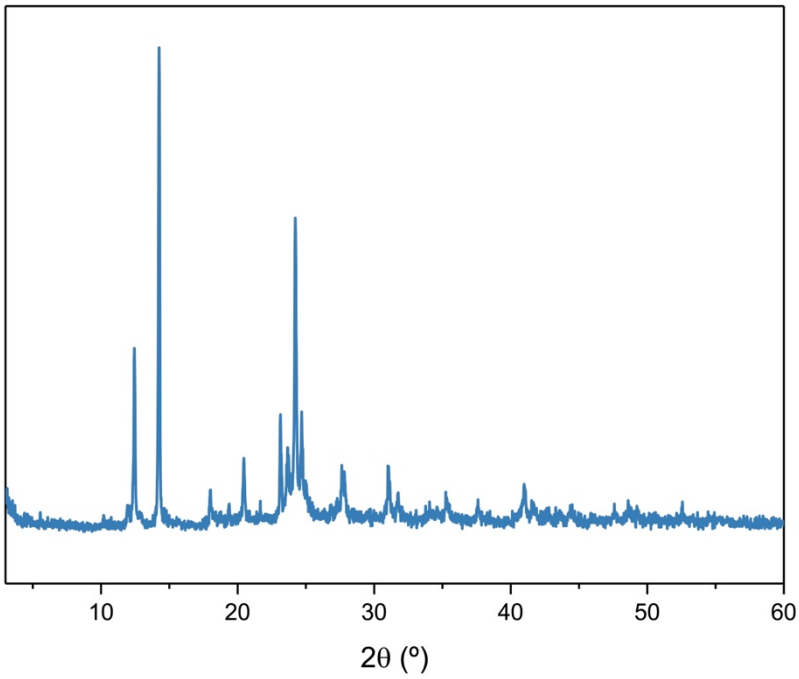

Figure A.69. PXRD spectrum for **A19a**.

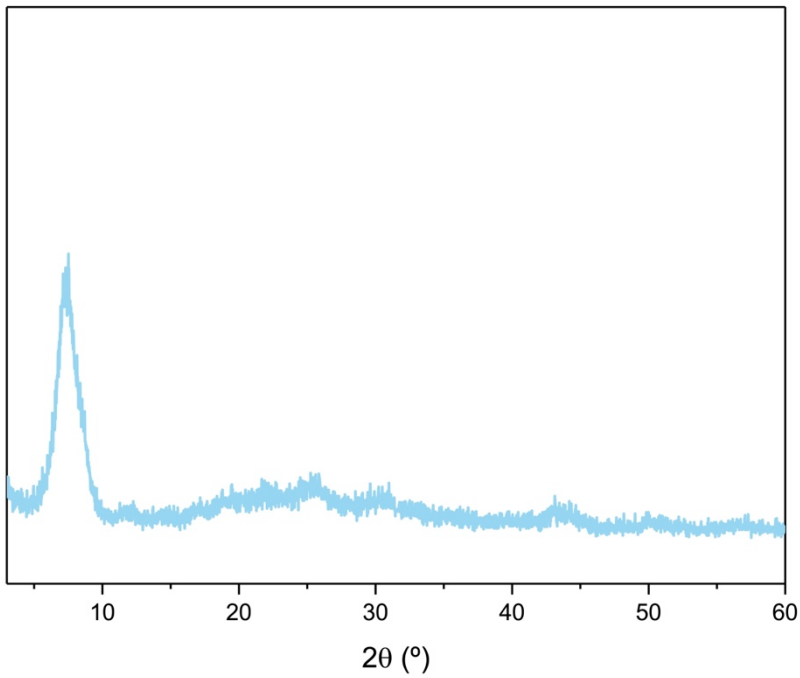

Figure A.70. PXRD spectrum for **B3a**.

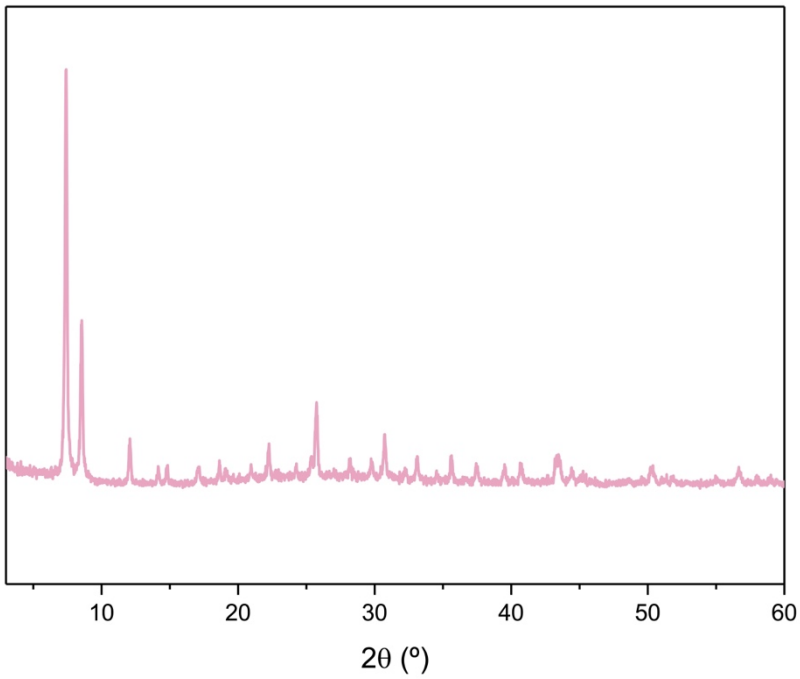

Figure A.71. PXRD spectrum for **B3c**.

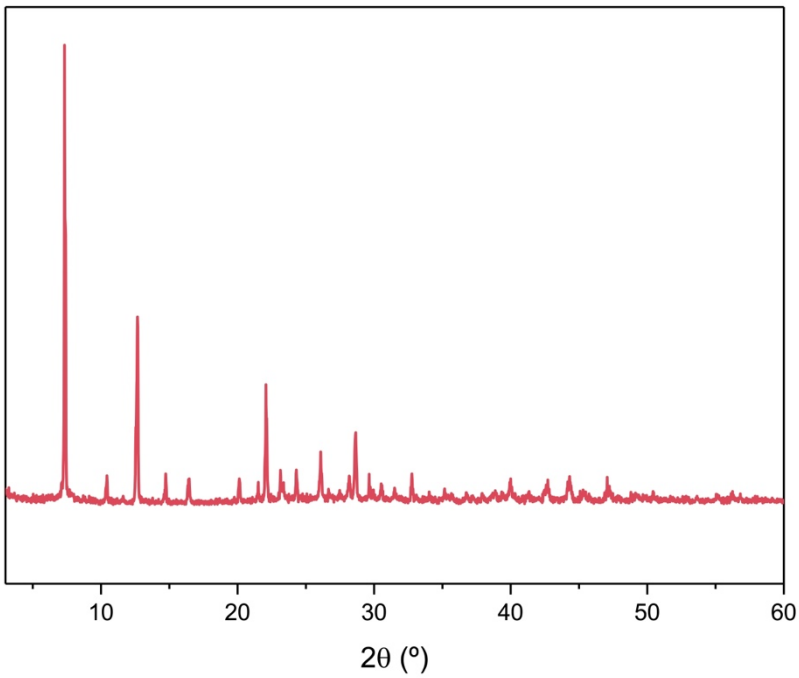

Figure A.72. PXRD spectrum for **B3d**.

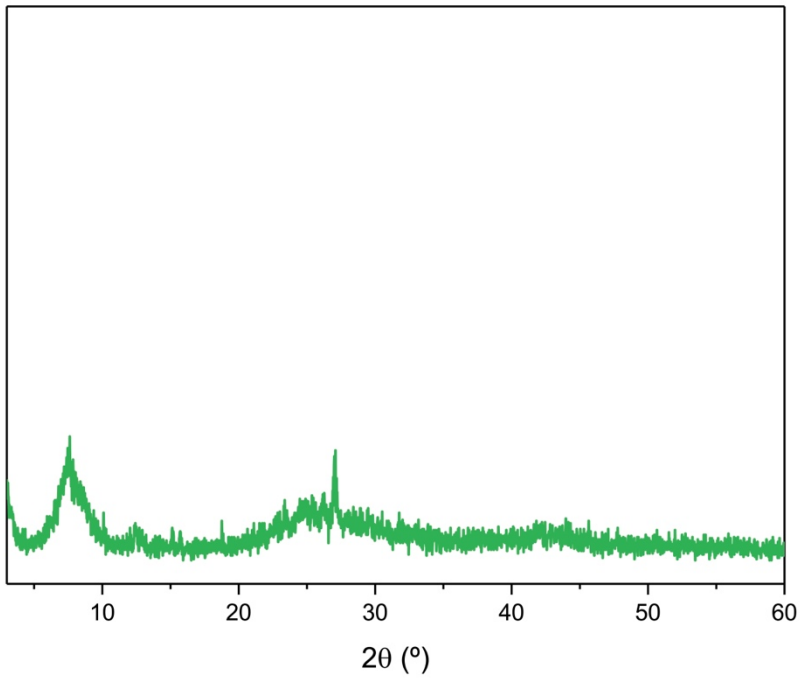

Figure A.73. PXRD spectrum for **B3f**.

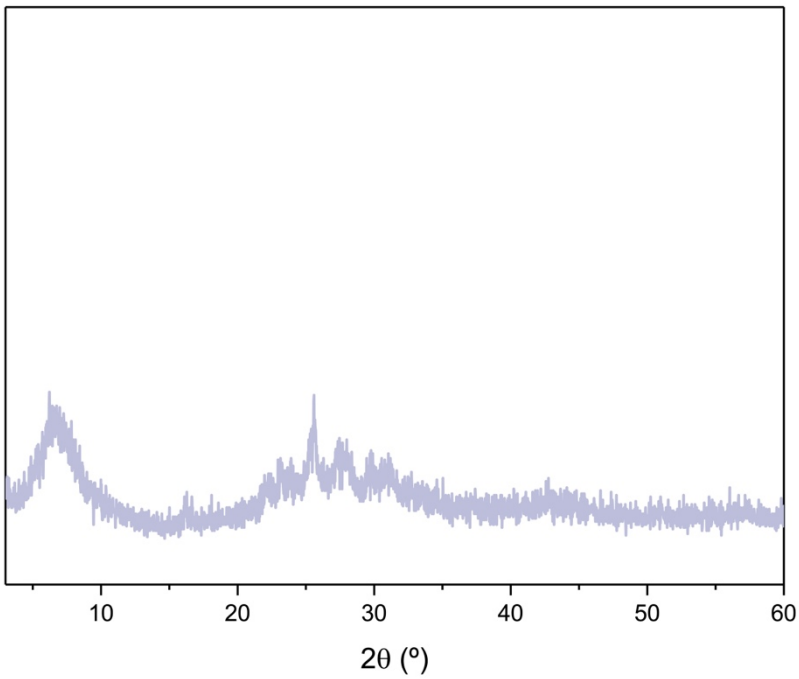

Figure A.74. PXRD spectrum for **B6a**.

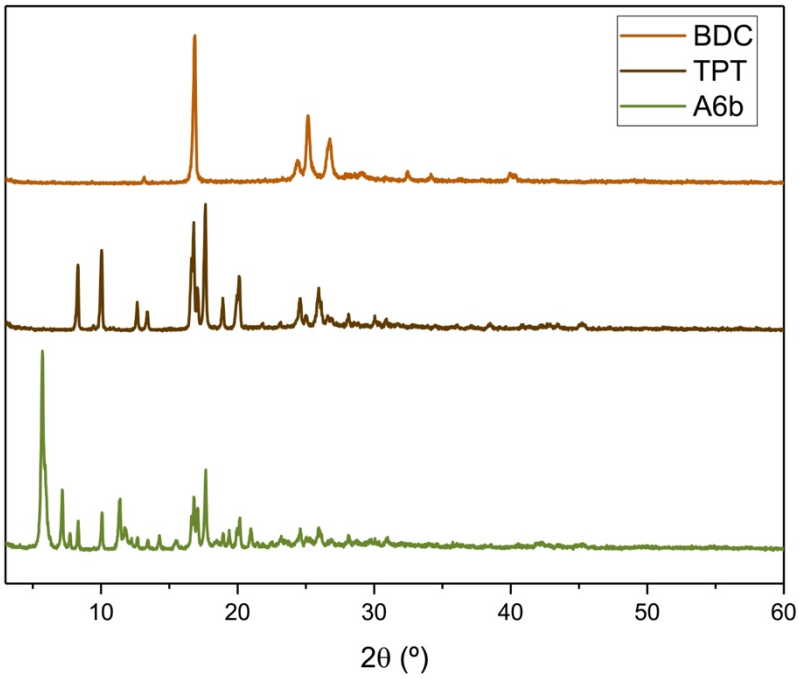

Figure A.75. Comparison between the PXRD data for **A5b** and the reagents.

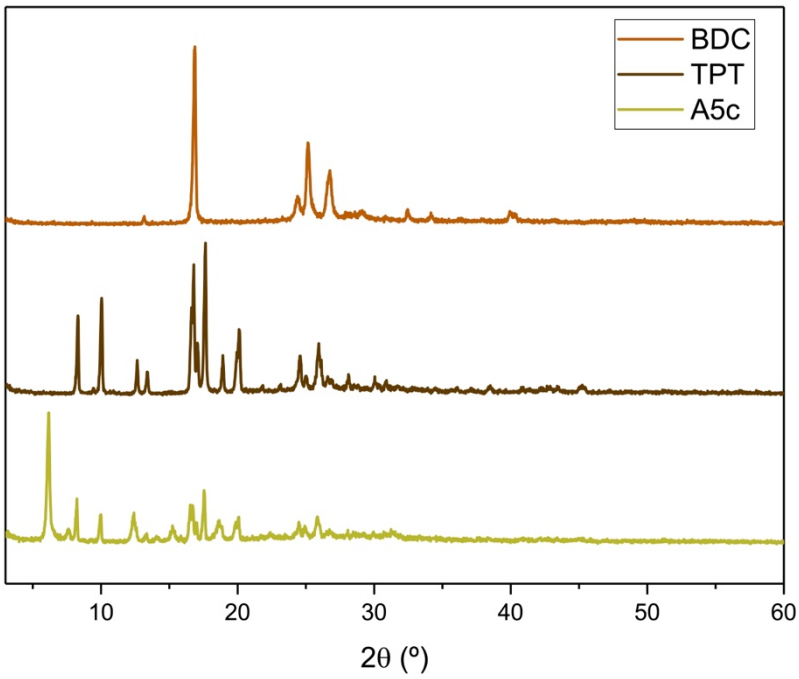

Figure A.76. Comparison between the PXRD data for **A5c** and the reagents.

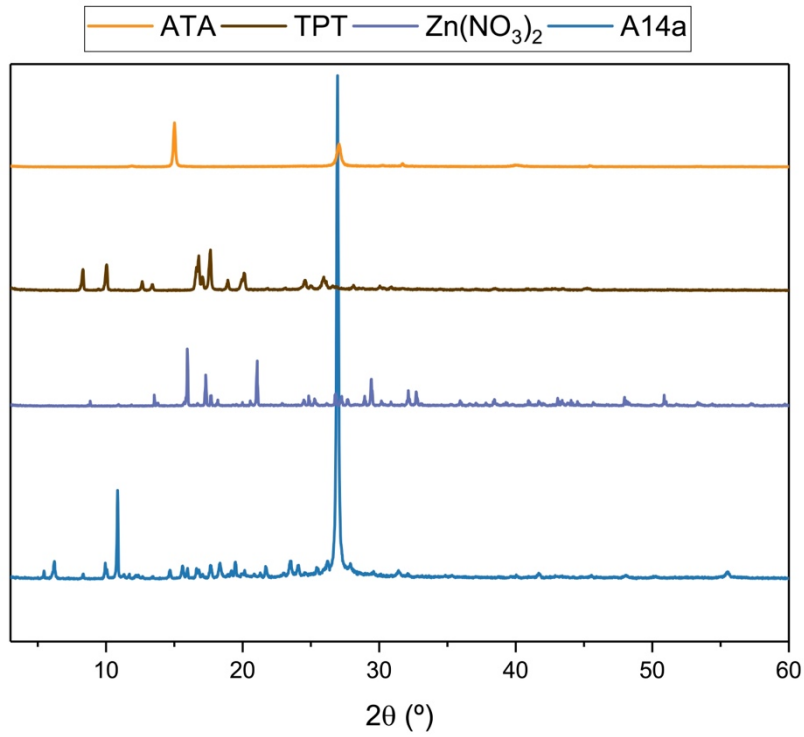

Figure A.77. Comparison between the PXRD data for **A14a** and the reagents.

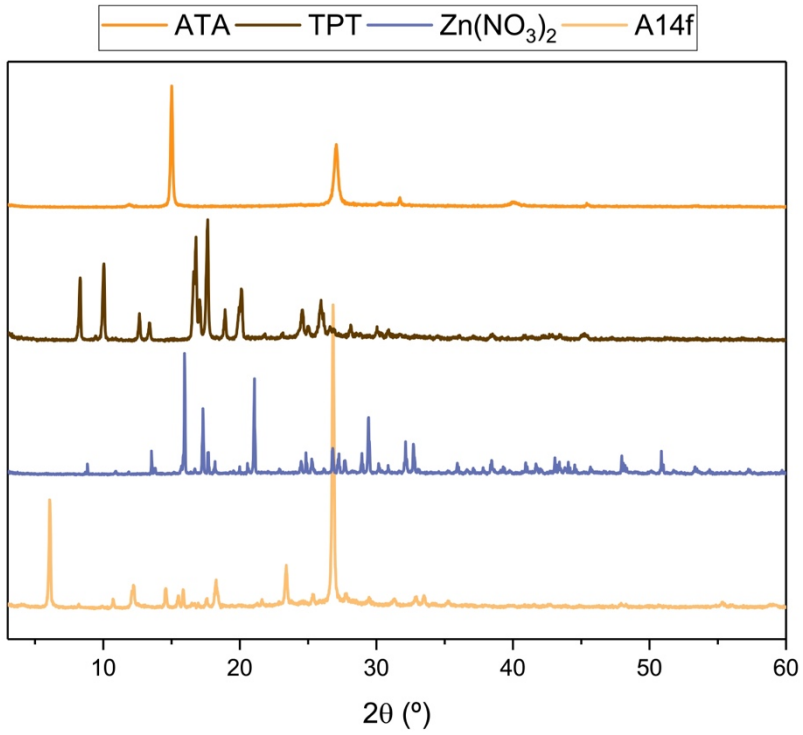

Figure A.78. Comparison between the PXRD data for **A14f** and the reagents.

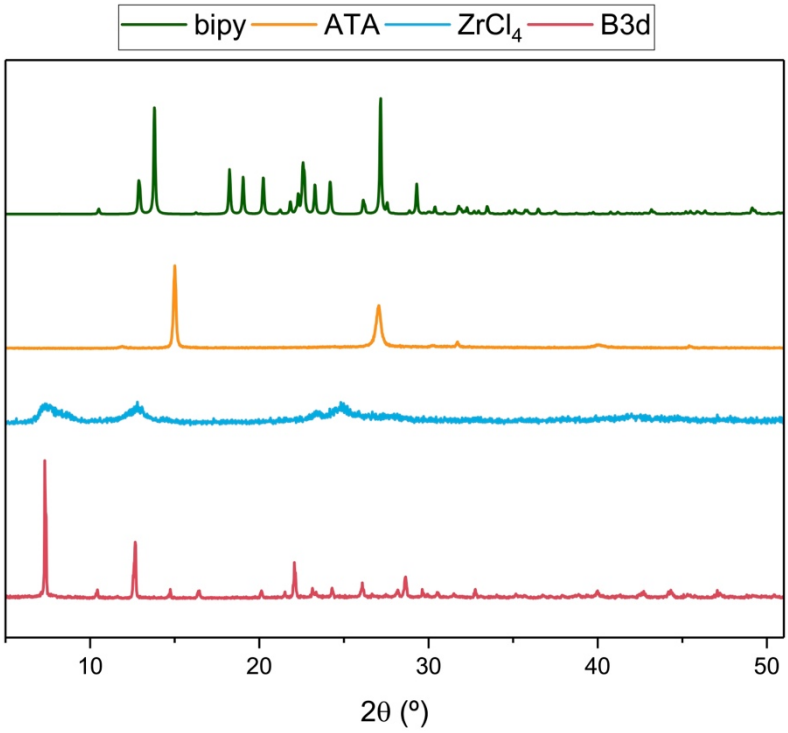

Figure A.79. Comparison between the PXRD data for **B3d** and the reagents.

List of Compounds

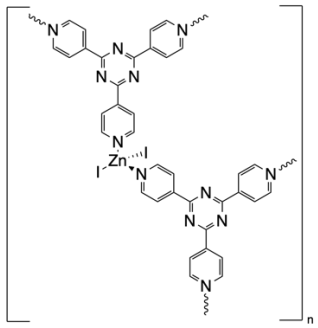

Fujita's Sponge

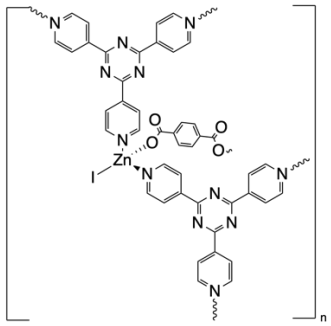

MOF1

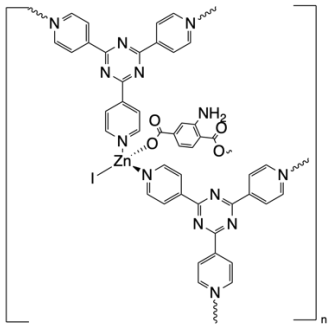

MOF2

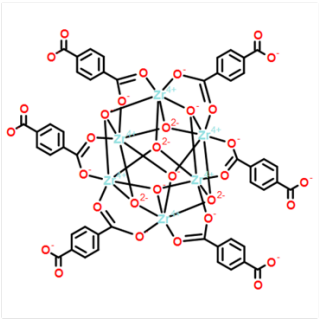

UiO-66

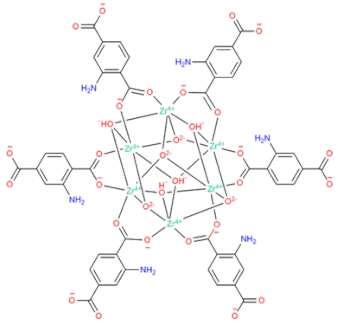

UiO-66-NH_2

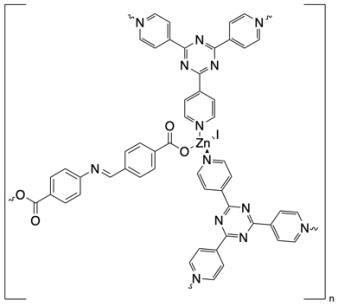

A4

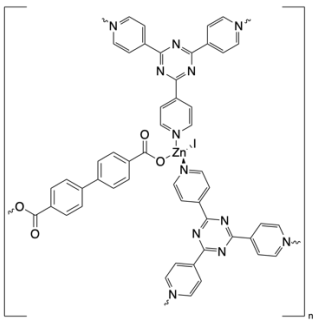

A5

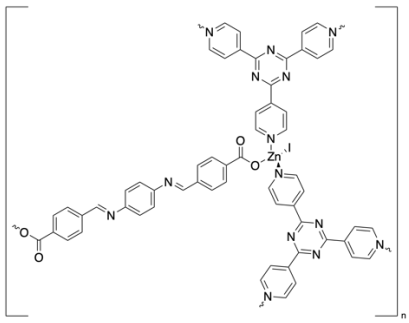

A6

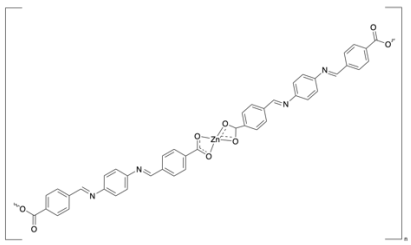

A7

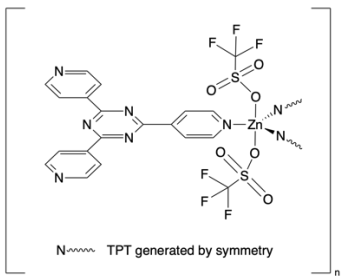

MOF3

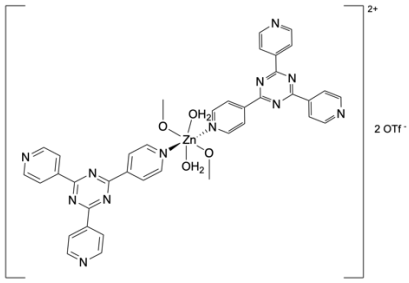

A9a&A9b

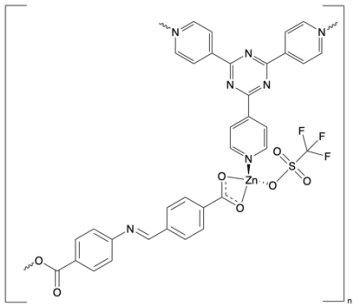

A10

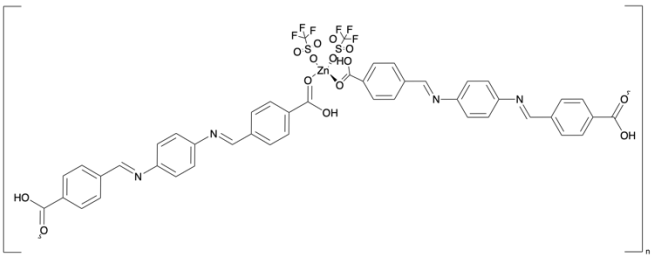

A11

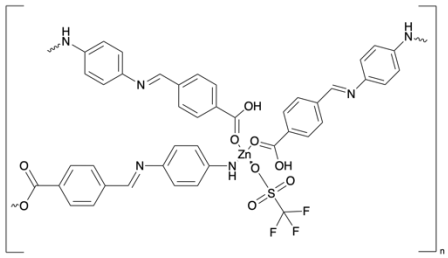

A12

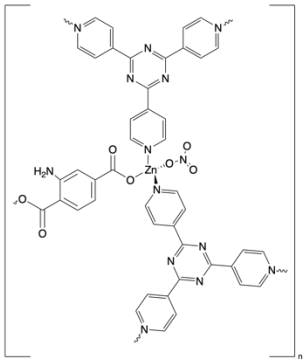

A14

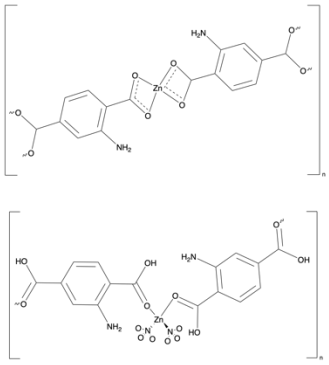

A15

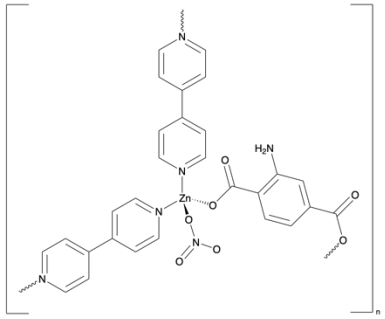

A16

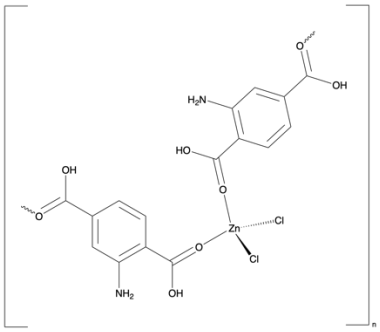

A18

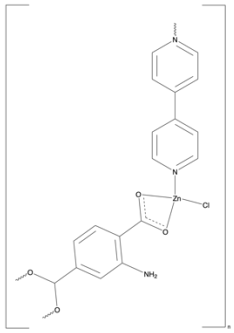

A19

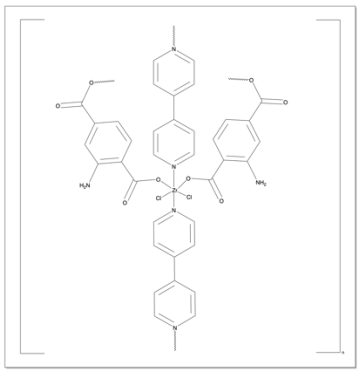

B3

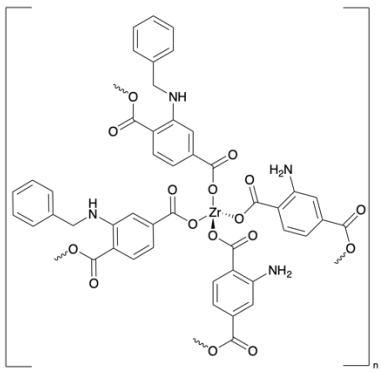

B6